THÈSE

En vue de l'obtention du
DOCTORAT DE L'UNIVERSITÉ DE TOULOUSE
Délivré par l'Université Toulouse 3 - Paul Sabatier

Présentée et soutenue par

Charaf Eddine MERZOUGUI

Le 14 décembre 2021

Interactions des protéines sanguines avec interfaces polymères modifiées

Ecole doctorale : **MEGEP - Mécanique, Energétique, Génie civil, Procédés**

Spécialité : **Génie des Procédés et de l'Environnement**

Unité de recherche :
LGC - Laboratoire de Génie Chimique

Thèse dirigée par
Christel CAUSSERAND et Patrice BACCHIN

Jury

M. Damien QUEMENER , Rapporteur
M. Stéphane PEZENNEC , Rapporteur
Mme Murielle RABILLER-BAUDRY, Examinatrice
Mme Christelle GUIGUI, Examinatrice
Mme Christel CAUSSERAND, Directrice de thèse
M. Patrice BACCHIN, Co-directeur de thèse

Acknowledgements

First of all, I would like to acknowledge the Agence Nationale de la Recherche (MOST-ANR International Program: ANR 17-CE08- 0041) for the financial support, and FERMaT Federation FR3089 for providing the Small Angle X-ray Scattering laboratory facility.

During this PhD journey I have met and interacted with several wonderful people weather it was for work, exchange discussions or just share some convivial moments and whom I would like to acknowledge. Foremost, I would like to express my warmest gratitude to my supervisors, Pr. Christel Causserand, Dr. Pierre Aimar and Pr. Patrice Bacchin for their invaluable guidance, constant involvement through regular meetings and discussions, but also for encouraging and motivating me throughout the entire duration of the thesis, which helped me completing well my PhD. It is also a true pleasure to acknowledge Dr Pierre Roblin, whom I consider as my scientific mentor for his willing to provide me the required assistance specially to perform the SAXS experiments and to process the data, and I would like to thank him also for all the fruitful discussions that helped me to develop my knowledge.

I would like to thank all the members of the committee defence of my thesis, Dr. Damien Quemener, Dr. Stéphane Pezennec, Pr. Murielle Rabiller-Baudry and Pr. Christelle Guigui, first for accepting to evaluate my thesis work, but also for their insightful comments and for making the discussion that pleasant.

Within the framework of this PhD, I had the chance to travel to Taiwan as an invited research student for 6 weeks in the Research and Development Center for Membrane Technology (Chung Yuan Christian University, ChungLi, Taiwan). Thus, I thank Pr. Chang Yung, Pr. Antoine Venault and all the students of the lab for welcoming me and helping me to carry out my experiments in the best possible conditions.

Special thanks to Corrine Routaboul of the Toulouse Institute of Chemistry (ICT) for having trained me on the ATR-FTIR microscopes, and for facilitating my access to the instruments.

I would like to acknowledge also the entire LGC staff, professors, engineers, technicians, administrative officers and especially the students, among whom I have made friends, for the three pleasant years I have shared with them, and for all the good convivial moments. I thank in particular my very good friend Dihia, for being there through the ups and downs and for her support, as well as Nabiil and Fatma for also being good friends to me and for all the things we shared together.

My special thanks also go to all the trainees who worked with me (Abigail Rosales, Sharath Jayakumar and Ema Louati), for their contribution to the progress of this project.

Words are not enough and will never be enough to thank the people who are dearest to me, my parents, to whom I owe my existence, my happiness and all the success belongs to them in the first place. I would like to express my deep sense of thanks to them for their encouragements, their unconditional trust, endless love that raised me up again when I got weary and for believing in me and being behind me whatever the circumstances are. With my parents always come my brothers Habib and Abdelhamid and my lovely sister Besma who also fill me with their unconditional love and support, I would like to thank them simply for being the best family I could have, and I also thank all the other members of the family for their support.

Finally, I would like to dedicate this thesis to my family and especially to my dear uncle Abdou and my dear aunt Zahra, two people who meant a lot to me and who suddenly passed away together because of the COVID pandemic, without giving me the chance to see them one last time, I hope they rest in peace in heaven.

Summary

The selective separation of blood proteins and cells is of a major importance to address some target diseases and for several medical applications such as wound healing. The challenge is to provide the most efficient and cost-effective technology that can ensure that. Among many other technologies, membranes processes have been revealed as promising techniques. However, their nonspecific interactions with proteins make them prone to biofouling, which in turn limits their application in biomedical fields. Therefore, the aim of this work is to design tailored membrane for blood proteins screening via surface modification. This latter is performed by coating onto the membrane surface some functional groups such as polystyrene-poly acrylic acid (PS-PAA) and polystyrene-poly ethylene glycol (PS-PEG) copolymers, either to promote a specific interaction with target proteins or to reduce their non-specific interaction. First, the potential interactions that could take place between PAA, PEG brushes and some abundant proteins in plasma such as human serum albumin (HSA) and ɣ-globulin (IgG) have been investigated in solution using Small Angle X-ray Scattering (SAXS) combined to chromatography. Thus, PAA has been found to form complexes with HSA in some specific physicochemical conditions of pH and ionic strength. This HSA-PAA binding has then been revealed to be reversible depending on the pH and the ionic strength of the medium and its stoichiometry was shown to be related to the PAA size. Whereas IgG did not exhibit the same behaviour as HSA towards PAA, it was found to be partially aggregated in our conditions. PEG did not display any interaction with both proteins. After that, Fourier Transform Infrared spectroscopy (FTIR) mapping showed that surface modification of the membranes by copolymers coating was successful, although the distribution of copolymer was heterogeneous over the membrane surface. The static adsorption of HSA onto membranes coated with PS-PAA was found to be also correlated to the pH and ionic strength as it was in solution, while that of IgG was not. Then, the adsorption of HSA onto a membrane coated with PS-PEG has been shown to be mitigated. Eventually, filtration experiments disclosed the same trend of HSA adsorption in dynamic mode even though the membrane permeability was reduced by the increase of the size of the copolymers brushes deposited onto the surface.

Overall, this study enabled us to understand the behaviour of some abundant blood proteins in contact of some functional groups either in solution or at the interface of a modified membrane.

Résumé

La séparation sélective des protéines et des cellules sanguines est d'une importance capitale pour traiter certaines maladies cibles et pour plusieurs applications médicales telles que la cicatrisation des plaies. Le défi consiste à fournir la technologie la plus efficace et la plus rentable qui puisse garantir cette séparation. Parmi de nombreuses autres technologies de séparation, les technologies membranaires se sont révélées être prometteuses. Cependant, leurs interactions non spécifiques avec les protéines les rendent vulnérables au bio-colmatage, ce qui limite leur application dans le domaine biomédical. Par conséquent, l'objectif de ce travail est de concevoir une technologie membranaire adaptée pour le dépistage des protéines sanguines en utilisant la modification de surface. Cette dernière est réalisée en déposant certains groupements fonctionnels sur la surface de la membrane, tels que des copolymères polystyrène-poly acrylique acide (PS-PAA) et polystyrène-polyéthylène glycol (PS-PEG), soit pour favoriser une interaction spécifique avec des protéines cibles ou pour réduire leur interaction non spécifique. Dans un premier temps, les interactions potentielles qui pourraient avoir lieu entre les brosses de PAA, PEG et certaines protéines abondantes dans le plasma telles que la sérum-albumine humaine (HSA) et la ɣ-globuline (IgG) ont été étudiées en solution en utilisant la Diffusion des rayons-X aux petits angles (Acronyme anglais : SAXS) combinée à la chromatographie. Ainsi, nous avons constaté que le PAA forme des complexes avec l'HSA dans certaines conditions physico-chimiques spécifiques de pH et de force ionique. Cette liaison HSA-PAA s'est ensuite révélée réversible en fonction du pH et de la force ionique du milieu, et il a été démontré que sa stœchiométrie était liée à la taille du PAA. En revanche, l'IgG n'a pas présenté le même comportement que l'HSA vis-à-vis du PAA, mais elle s'est avérée être partiellement agrégée. Quant au PEG, il n'a montré aucune interaction avec les deux protéines. Ensuite, la cartographie par spectroscopie infrarouge à transformée de Fourier (FTIR) a confirmé le succès de la modification de surface par dépôt de copolymères sur la surface de la membrane, bien que la distribution du copolymère y soit hétérogène. L'adsorption statique de l'HSA sur les membranes revêtues de PS-PAA s'est avérée également corrélée au pH et à la force ionique comme elle l'était en solution, alors que celle de l'IgG ne l'était pas. Ensuite, il a été démontré que l'adsorption de l'HSA sur la membrane recouverte de PS-PEG était réduite. Enfin, les expériences de filtration ont révélé la même tendance à l'adsorption de l'HSA en mode dynamique, même si la perméabilité de la membrane était réduite par l'augmentation de la taille des brosses de copolymères déposées sur la surface.

Globalement, cette étude nous a permis de comprendre le comportement de certaines protéines sanguines abondantes au contact de certains groupes fonctionnels que ce soit en solution ou à l'interface d'une membrane modifiée.

Contents

List of figures

List of tables

Glossary

ATR	Attenuated total reflectance
BSA	Bovine serum albumin
CAGR	Compound annual growth rate
DLS	Dynamic light scattering
EDS	Energy-dispersive X-ray Spectroscopy
$EtOH_{abs}$	Absolute ethanol
FTIR	Fourier Transform Infrared spectroscopy
HEPES	Hydroxyethyl piperazin ethanesulfonic acid
HPLC	High performance liquid chromatography
HSA	Human serum albumin
ID	Immersion-Drying
IDW	Immersion-Drying-Washing
IgG	Immunoglobulin G
IR	Infrared spectroscopy
ITC	Isothermal titration calorimetry
IWD	Immersion-Washing-Drying
LCST	Lower critical solution temperature
MES	2-(N-morpholino)ethanesulfonic acid
M_w	Molecular weight
PAA	Poly(acrylic acid)
PBS	Phosphate buffered saline
PDGF	Platelets derived growth factor
PDI	Polydispersity index
PEG	Poly(ethylene glycol)
PES	Polyethersulfone
PNIPAAM	Poly(N-isopropylacrylamide)
PPO-b-PSBMA	poly(propylene oxide)-block-poly (sulfobetaine methacrylate)
PRP	Platelets rich plasma
PS	Polystyrene
PS-b-PAA	Polystyrene-block-poly(acrylic acid)
PS-b-PEG	Polystyrene-block-poly(ethylene glycol)

PS-b-PEO	Polystyrene-block-poly(ethylene oxide)
PS-r-PSBMA	Polystyrene-random-poly(sulfobetaine methacrylate)
PS-r-PEGMA	Polystyrene-random-poly(ethylene glycol methacrylate)
PVDF	Polyvinylidene fluoride
RBC	Red blood cells
SANS	Small angle neutron scattering
SAXS	Small angle X-ray scattering
SEC	Size exclusion chromatography
THF	Tetrahydrofuran
Tris base	Tris(hydroxymethyl)aminomethane
VDW	Van der Waals
WBC	White blood cells
XPS	X-ray Photoelectron Spectroscopy

Chapter I.

General introduction:

State of the art

This chapter constitutes a state of the art on the use of membrane technology in separation processes in different fields for versatile applications, especially medical ones. Besides, in this chapter are reported the different membrane materials, how they can be tailored and functionalized depending on the application, as well as how to characterise them. It also introduces the concept of smart biomedical membranes for blood separation and the application behind. Eventually, the positioning of the PhD project with regards to the application, and the different parts constituting this work and structuring the manuscript are presented.

1. Membrane technology for medical applications

A membrane is a thin layer of semipermeable material that could be used for separation processes in liquid or gas phase as a driven force is applied across the membrane (pressure, electrical potential, etc.). It is an interphase between two adjacent phases acting as a selective barrier, regulating the transport of substances between two compartments. In this manuscript, membranes for liquid phase separations operated under pressure are mainly reported. In fact, membrane separation technology could be used to purify some solutes contained in a mixture due to the difference of their properties such as their size or of a specific interaction that they exhibit towards the membrane. The main advantages of membrane technology as compared with other unit operations in (bio)chemical engineering are related to the transport selectivity that could possess the membrane. Separations with membranes do not require additives, and they can be performed isothermally without change of state, hence at low temperatures and at low energy consumption compared to other thermal separation processes [1]. Certain properties of membrane separation technology, such as durability, porosity, permeability, stability, and selectivity, make them an indispensable element in various industrial applications [2]. In addition, upscaling and downscaling of membrane processes as well as their integration into other separation or reaction processes are easy.

Membrane technologies have now been industrially established on an impressively large scale, after a long period of inspiration by biological membranes and scepticism about the ultimate technical feasibility [3]. This technology is widely used for commercial and industrial purposes. The markets are rather diverse from medicine to the chemical industry and the most important industrial market segments are food and beverages, water treatment, and medical devices (Figure 1. 1).

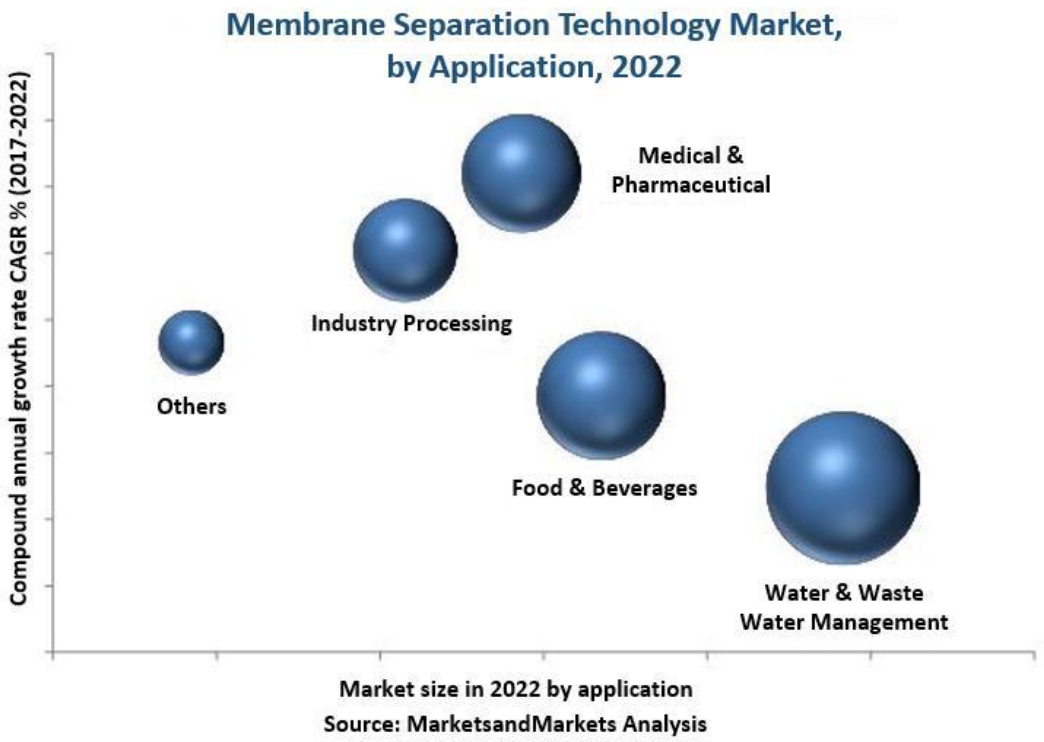

Figure 1. 1. Membrane Separation Technology Market by Application - Global Forecast 2022 | MarketsandMarkets.

The Medical Membranes market is supposed to reach USD 3.31 billion by 2022 growing from USD 2.13 billion in 2017, registering a CAGR (Compound annual growth rate) of 9.2% from 2017 to 2022 [4]. Increasing incidences of diseases, advancement in medicines, growing pharmaceutical and healthcare industry, demand for high purity products and medicines are some major driving forces that are anticipated to drive the global medical membrane market for pharmaceutical filtration. The commercial application of artificial membranes in medicine and especially in dialysis has started many years ago and is still growing steadily. Hemodialysis is now among the dominant therapeutic applications in which membranes are widely used and where improvement of biocompatibility remains a challenge [5]. Blood oxygenators and filters for infusion solutions represent also a large group with respect to membrane consumption for medical devices. Among other medical applications, membranes are used for liver support systems, artificial pancreas, therapeutic apheresis and plasma donation [6]. Membranes are also used in drug delivery systems and diagnostic devices [7]. Those applications for membranes are by far not all, there is a continuous development of devices for specific separation applications. Considering only extracorporeal devices containing membranes for blood purification several new therapy devices are emerging.

Thereby, artificial membranes are used in medicine to treat blood for a broad variety of therapeutic purposes. In most treatments, blood is continuously withdrawn from the patient's blood circulation and brought in extracorporeal circulation into direct contact with the membranes assembled in the device. Membranes are used as permselective barriers to permit transport of selected solutes to/from the blood, while hindering the loss of essential blood constituents, and to regulate the rate at which solutes are transferred across the membrane so as to maintain the patient's homeostasis [8].

For such processes rather complex, a number of factors contribute to make the development of adequate membranes and devices, among which are the physical-chemical properties of the species to be transported or rejected, the interactions between membranes and body fluids that continuously modify both membrane and blood properties, and the need for materials with suitable properties.

2. Membrane materials

Membrane materials lie at the center of membrane technology by determining membrane separation performance, cost, operational stability, and process design. That's because the material a membrane is made of determines its physical and chemical properties, for example, its physical strength and workability; its resistance to temperature and chemicals, which determines the sterilization methods that can be used without altering its structure and separation properties; and its biocompatibility in the case of biomedical applications.

The membrane process conditions must be engineered very carefully, but the performance limits are clearly determined by the membrane itself. Depending on the application the membrane is used for, this last could be formed of different materials.

Extensive research efforts have been dedicated to investigating novel membrane materials leading to the emergence of three major membrane material categories: organic (polymeric), inorganic (ceramic) materials, and biological materials [9]. Polymeric membranes dominate the present separation market due to their relatively low cost and excellent mechanical strength.

Organic membranes are either cellulose based or composed of modified polymers. The main polymers constituting the organic membranes include Polyamide (PA), Polysulfone (PSf), Polyethersulfone (PES), Polyvinylidene fluoride (PVDF), and Polypropylene (PP).

Those materials are less resistant to high temperature and aggressive chemicals compared to inorganic or metallic membranes. However, they are still widely used due to easy preparation, reasonable expense (low cost), high efficiency, lower energy requirement and flexibility in membrane configuration [1]. For that reason, polymeric membranes are attractive materials for various applications, such as filtration, microelectronic devices, biomaterials, and so on. For instance, polymeric materials have been widely applied in the biomedical field such as in dental/bone materials, implants, wound dressing, prosthetic materials, drug carriers, and tissue engineering scaffolds. This is owing to their desired mechanical and physical properties, manufacturability into various shapes, sterilizing capability, and ease of modification with multiple functionalities [10].

The performance of polymeric materials in many applications relies largely upon the combination of bulk (e.g. mechanical) properties and the properties of their surfaces [11]. However, those materials very often do not possess both the surface properties needed for these applications and good mechanical properties at the same time, which is critical for their successful application.

Due to this dilemma, surface modification of membrane without changing the bulk properties has been a topical aim in research for many years, mostly because surface modification provides a potentially easier route to obtain new surface properties than other techniques (e.g. polymer blending) [11]. Another advantage of surface modification is that it permits to enhance or prevent specific interactions (affinity) during separation processes. The field is still receiving extensive attention as new applications of polymeric materials emerge rapidly, especially in the fields of biotechnology, bioengineering, and nanotechnology [12].

3. Membrane fouling and surface modification

Fouling is the deposition of retained particles, colloids, macromolecules, salts, etc., at the membrane surface or inside the pores which either temporarily or permanently alters their transport properties such as their permeability or selectivity. The foulants could be inorganic, organic, or biological substances depending on the application the membrane is used for. They not only physically interact with the membrane surface but also chemically degrade the membrane material sometimes [13]. In the case of membranes for biomedical applications we talk more about biofouling by biological substances like proteins, human cells, bacteria, etc. For such applications synthetic hydrophobic materials are often chosen as matrix materials but their hydrophobicity makes them prone to biofouling, which in turn limits their application [14].

This phenomenon could be minimized by periodical washing with chemicals, but it results in the simultaneous degradation of the membrane material's lifetime, and it could involve additional environmental and economic costs.

The management of fouling involves different strategies: improvement of pre-treatment processes, optimisation of cleaning protocols, amelioration of membrane module design, and development and modification of membranes taking into consideration different parameters such as hydrophilicity, charge and the roughness of the surface [13].

Since the separation process by membrane is essentially a surface phenomenon, it is a natural consequence to modify membrane surface for reducing the fouling. Surface modification of membranes is thought to be equally important to the membrane industry as membrane material and process development [15].

In membrane manufacturing, surface functionalization of membranes has already become a key technology. The aims of surface modification of a membrane are essentially two-fold [16]. First, improvement of the selectivity as shown in Figure 1. 2.B, or even the formation of entirely novel separation functions. The second fold is the minimization of undesired interactions (adsorption or adhesion, or in more general terms membrane fouling) that reduce the performance as illustrated in Figure 1. 2.B. This can be achieved via the introduction of additional (tailored) interactions (affinity and responsiveness). Novel membranes with a high selectivity, e.g. for special biomolecules are in high demand. Consequently, particular attention is paid to truly molecule-selective separations, i.e. advanced nanofiltration and ultrafiltration membranes [17]. In addition, a membrane selectivity that can be switched by an external stimulus or can adapt to the environment/ process conditions would be an important feature.

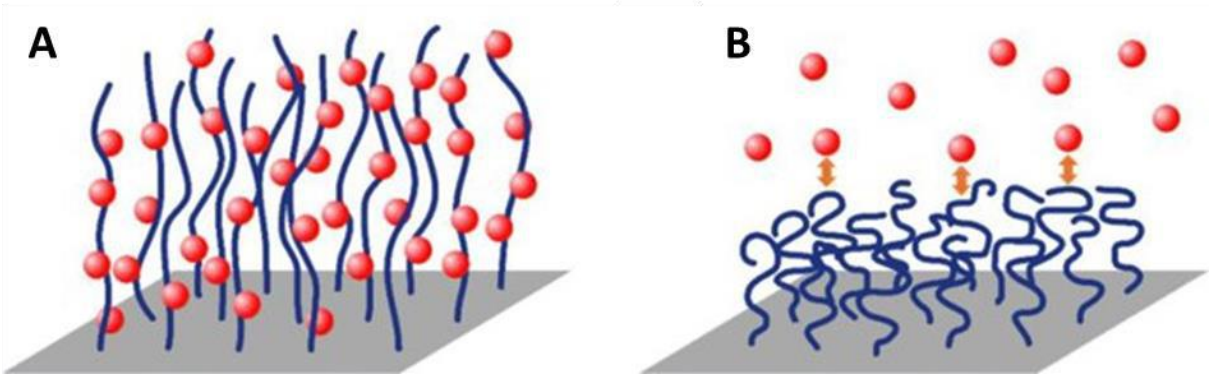

Figure 1. 2. Illustration of a/ improvement of protein adsorption on modified membrane with polymer brushes and b/ minimization of undesired interactions depending on the polymer brushes nature. Adopted from [16].

In the overall process of membrane modification, many factors need to be considered, such as uniformity, reproducibility, stability, process control, and reasonable cost, together with precise control over functional groups, which is a big challenge [12]. Among the surface modification techniques developed to date, grafting and coating are common processes as it allows control of grafting or coating density, thickness of the modifying layer, and chemistry (through polymer material choice) without significantly changing the structure of the membrane.

Grafting processes establish covalent bonding between the surface modifier and the membrane surface through "grafting from" or "grafting to" techniques, illustrated by the scheme in Figure 1. 3 adopted from [18]. It creates stronger interactions resulting in better stability than coating processes. In grafting from, polymer grows from the membrane surface by putting the membrane in contact with a monomer solution given that there is additional energy supplied to initiate the polymerization and to activate the membrane. While in grafting to, a known composition of polymer covalently bonds to the surface activated membrane. Both grafting methods require additional energy and time-consuming multiple step process which generates high costs. In addition, membrane pretreatment with alkali solution or irradiation can damage the properties and structure of the membrane, thereby affecting the membrane's performance.

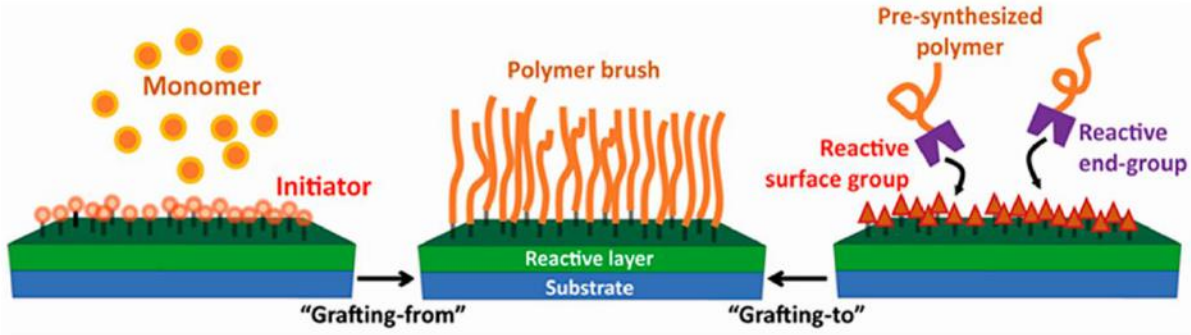

Figure 1. 3. Scheme depicting the two processes "grafting from" or "grafting to" used for surface modification [18].

Conversely, coating is readily achieved through immersion, spray coating, dip-coating, and spin coating making it suitable for large-scale production at a reduced cost. In this process, surface-modifying molecules self-assemble on the surface of membrane establishing non-covalent (hydrophobic, electrostatic, etc.) interactions [11]. For example, it could be a functional copolymer with hydrophobic groups forming a strong affinity with a hydrophobic

membrane. Since surface modifiers interact with the membrane through non-covalent interactions, it may not be stable resulting in detachment from the membrane surface. Thus, the success of the coating depends on the extent of interaction between the surface modifier and the membrane surface.

4. Membrane surface functionalization by polymers adsorption

The adsorption of soluble polymers at solid interfaces is a highly complex phenomenon with a vast number of possible configurations of the molecules at the surface. The driving forces of adsorption processes are numerous including covalent or chemical bonding forces, interactions between polar molecules, electrostatic interactions, hydrogen binding, hydrophobic and hydrophilic interactions, etc. [19]. As illustrated in Figure 1. 4, depending on the nature of these interactions we distinguish between chemisorption that involve covalent bonding formation, and physisorption related to van der Waals forces between dipoles, to electrostatic attractions or to hydrophobic interactions, etc. [20]. This latter does not imply a significant change in the electronic orbital patterns of the species involved in the adsorption. It is a reversible phenomenon that involves low adsorption energies of the order of a few kilocalories per mole, and it is a process generally favoured by low temperatures.

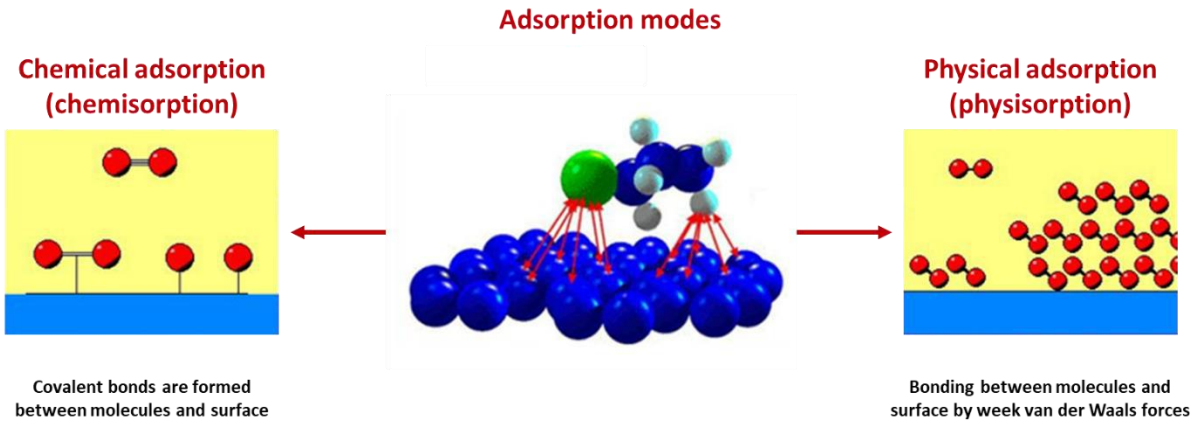

Figure 1. 4. Illustration of possible configuration of molecules attachment onto a surface during the chemisorption and physisorption.

The effect of the adsorption processes is shown by the resulting surface properties (stability, chemical and physical properties), and it strongly depends on the adsorption mechanism described by adsorption isotherms and the nature of the effective interaction forces.

A quantitative description of adsorption of solved molecules onto solid surfaces at constant temperature and at equilibrium is given by the so called adsorption isotherms reported below in

section 4.1. The interactions that could be involved in protein adsorption on membrane surfaces are pointed out in section 4.2, as well as the way to characterise this adsorption onto surfaces and in solution (section 4.3).

4.1. Adsorption isotherms

A multiplicity of adsorption isotherms that describe the adsorption of solved substances at solid surfaces has been reported in the literature [21]. They were classified by Giles and al, and later a theoretical basis was given to the classification adopted [22]. Thus, the several equations that have been proposed to model isotherms have either theoretical or empirical foundations [23]. The most common isotherm model is the L class described by Langmuir equation, where interactions between adsorbate molecules are considered as negligible. This model describes the monolayer adsorption and it assumes that the surface is energetically homogeneous, that no interactions between the adsorbed molecules take place, that the molecules remain fixed once adsorbed, and that the thickness of the monolayer corresponds to that of a molecule [21].

If the driving forces for adsorption are strong (e.g. electrostatic interactions in the case of polyelectrolytes), if the behaviour of the adsorbate is not ideal, e.g. multilayer adsorption, or if equilibrium conditions are not reached during measurement, deviations from this isotherm may happen [19]. Overall, Langmuir law is considered as applicable in the case of physisorption only where the driving force is van der Waals interactions. A special variant of the L class is the H class that represents high interaction forces between adsorbate molecules. In this case, we speak about cooperative adsorption.

Isotherms of the C class are characterised by a constant partition of the solute between the solid surface and the solution and it can be observed in the case of penetration of adsorbate molecules in the surface region of the solid. Linearity means that new sites are created during adsorption. This is interpreted by the fact that the initially adsorbed molecules have caused the expansion of the pores of the solid, which allows other molecules to penetrate.

In the case of long-chain molecules like polymers, effects from the adsorbed molecules must be observed including configuration effects [24], aggregation effects, micelles formation, multilayer adsorption, molar weight, chain stiffness [25].

4.2. Interactions of functionalized membrane with proteins

Polymer-coated surfaces have been widely studied to control material interactions with the biological environment. Thereby, the understanding of bio-physicochemical interactions at the nano-biointerface and the driving forces is of paramount importance. Wherefore, several studies have sought to investigate the forces leading to these interactions [26], [27]. It has been reported in many studies that among all possible parameters, water-mediated hydrophobic and hydration forces are considered to be the major players in protein adsorption [26]. Thus, it has been disclosed that proteins should not be able to displace water from the surface and adsorb on hydrophilic surfaces, whereas the opposite behaviour is expected for hydrophobic surfaces. However, this concept was not enough to explain all experimental results, where several drawbacks remained, as the involvement of these forces in causing adsorption in the case of small proteins [28], [29]. Besides, this concept does not consider the competitive adsorption of different mutually interacting proteins.

Further studies recognized that protein adsorption was governed by various polar and nonpolar interplay mechanisms. The latter include nonspecific electrostatic and ionic screening effects as well as more local noncovalent interactions such as salt bridges or hydrogen bonds. The polar interactions can be manipulated by a change in pH or salt concentration. Nonpolar interactions include van der Waals and solvent-mediated phenomena such as hydrophobic attraction [28] or hydration repulsion [29].

Nel et al. [27] have listed the main possible forces involved in proteins adsorption from biological systems, and they explain their origin and nature, as well as the possible impact it could have on the interface as shown in Table 1. 1.

Table 1. 1. Main forces governing the interfacial interactions between nanomaterials and biological systems. Adopted from Nel et al. [27].

Force	**Origin and nature**	**Possible impact on the interface**
Hydrodynamic and Brownian interactions	Convective drag, shear, lift and Brownian diffusion are often hindered or enhanced at nanoscale separations between interacting interfaces.	Increase the frequency of collisions between nanoparticles and other surfaces responsible for transport.
Electrodynamic interactions	VDW interactions arising from each of the interacting materials and the intervening media.	Universally attractive in aqueous media; substantially smaller for biological media and cells owing to high water content.
Electrostatic interactions	Charged interfaces attract counter-ions and repel co-ions through Coulombic forces, giving rise to the formation of an electrostatic double layer.	Overlapping double layers are generally repulsive as most materials acquire negative charge in aqueous media, but can be attractive for oppositely charged materials.
Solvent interactions	Lyophilic materials interact favourably with solvent molecules.	Lyophilic materials are thermodynamically stable in the solvent and do not aggregate.
Steric interactions	Polymeric species adsorbed to inorganic particles or biopolymers expressed at the surfaces of cells give rise to spring-like repulsive interactions with other interfaces.	Generally increase stability of individual particles but can interfere in cellular uptake, especially when surface polymers are highly water-soluble.
Polymer bridging interactions	Polymeric species adsorbed to inorganic particles or biopolymers expressed at the surfaces of cells containing charged functional groups can be attracted by oppositely charged moieties on a substrate surface.	Generally, promote aggregation or deposition, particularly when charge functionality is carboxylic acid and dispersed in aqueous media containing calcium ions.

4.3. Methods for characterization of functionalized membranes and protein adsorption

The surface modification efficiency could be judged only by assessing the performance of the membrane regarding the purpose for which the modification was performed. Thus, it is essential to determine the modified membrane surface properties (chemical composition, surface wettability, modification layer density, and morphology) through surface characterization to understand its performance and stability. There are numerous characterization methods and they can be thermodynamic, spectroscopic or imaging methods [19]. Among thermodynamic techniques the following ones can be listed [19]: calorimetry, volumetry, gravimetry, inverse gas chromatography, electrokinetics and wetting measurements.

The spectroscopic techniques are often used for surface chemical analysis, and it includes mainly infrared spectroscopy (ATR-FTIR), surface plasmon resonance spectroscopy, fluorescence spectroscopy, X-ray photoelectron spectroscopy, Raman spectroscopic and energy dispersive X-ray spectroscopy.

Other methods such as contact angle measurements can be used for determination of membrane wettability, microscopy techniques for analysis of surface morphology, and characterization of surface charge.

Furthermore, the evaluation of the membrane permeability to the solvent and its retention rate during filtration process are among methods that allow to assess the performance of the membrane. The methodology to assess these parameters is explicitly detailed in chapter IV where dead-end filtration experiments are discussed. Thus, as stated in section 3.2 of chapter IV, the permeability can be calculated using the Darcy law given by equation 4.1, while the retention could be evaluated using the equation 4.3.

4.3.1. Surface chemical analysis

Determination of the membrane surface chemical composition is essential to verify the presence of coating and adsorbed foulants. Their amount can be correlated to assess the modified membrane’s performance and stability. As stated above, there are several characterization techniques for this purpose, and the most frequently used according to the literature are summarized in Table 1. 2. However, it should be considered that membranes are generally used in their wet state while some characterization techniques only allow analysis using samples in its dry state. Thus, it is important to keep in mind that membranes could behave differently depending on the characterization technique used.

Table 1. 2. Spectroscopic methods used in membrane surface characterization [30].

	Infrared Spectroscopy (IR)	Raman Spectroscopy	Energy Dispersive X-ray Spectroscopy (EDS)	X-ray Photoelectron Spectroscopy (XPS)
Detection of elements	No	Yes	Yes, Be-U	Yes, H-U
Detection of functional groups	Yes	Yes	No	No
Detection of chemical bonds	Yes	Yes	No	Yes
Determination of crystallinity	Yes	Yes	No	No
Qualitative analysis	Yes	Yes	Yes	Yes
Quantitative analysis	Yes	Yes	Yes	Yes
Mapping/imaging of the chemical composition possible	Yes	Yes	Yes	Yes
Depth profiling of the chemical composition possible	Yes	Yes	No	Yes
Analysis in vacuum	No	No	Yes	Yes
Wet samples can be analyzed	No	Yes	No	No
Special sample pretreatment	No	No	Yes	No
Sample destructive technique	No	Yes/No	Yes	No
Analysis depth	1–100 μm (PAS) 1–10 μm (ATR)	1–5 μm	0.5–5 μm	1–3 nm
Spatial resolution	0.5–1 μm (ATR, PAS)	0.5–1 μm (confocal Raman)	0.5–5 μm	5–50 μm
Detection limit	1 atom% (ATR)	[a]	0.1 atom%	1 atom%

[a] A general value is not available because the detection limit depends strongly on the equipment and the measuring conditions.

In infrared spectroscopy (IR), the sample is irradiated with infrared light. When the frequency of the incident light matches the vibration of the molecules in the sample, the molecules absorb the radiation. The remaining transmitted light is detected and converted to a spectrum showing the changes in the infrared intensity as a function of frequency (or wavenumber) [30]. The peaks in the spectrum correspond to bond stretching or deformation specific to functional groups present in the sample and its intensity could be correlated to the amount.

Raman spectroscopy uses a monochromatic light source that can be in UV, visible, or near-infrared regions. This technique uses the concept of Raman scattering to generate a spectrum with intensity of the scattered light as a function of Raman shift (energy difference between the incident and Raman scattered photons). Groups with double and triple C-C bonds, disulfide bonds, and C-H bonds are detected easily with Raman spectrometer, while it is the opposite for water [30]. Consequently, this is interesting for membrane characterization as it allows analysis of wet samples. Raman spectroscopy is complementary to FTIR (Fourier Transform Infrared spectroscopy) since bands that are strong in infrared spectrum are weak in Raman spectrum and vice versa.

In X-ray Photoelectron Spectroscopy (XPS), the sample is placed under ultrahigh vacuum and is irradiated with focused X-rays resulting in photoemissions. The emitted electrons and their binding energies unique for each element will be detected allowing identification of the elements present in the sample. Results are presented as spectrum with intensity as a function of binding energy. In addition, the peak intensity is proportional to the quantity of the element in the sample. This method is non-destructive and non-conducting samples, such as polymeric membranes, can be analysed without conductive coating. However, the membranes should be analysed in their dry state, and the analysis time should be kept short since increased exposure period could lead to sample deterioration [30].

Energy-dispersive X-ray Spectroscopy (EDS) is coupled with an electron microscope where the sample is irradiated with an electron beam followed by X-ray generation which is unique for each element [31]. However, this technique requires that the sample chamber is under vacuum condition, thus, membranes must be analysed in their dry state. In addition, non-conducting samples, such as polymeric membranes, should be coated with a conductive material prior to the analysis. There is also a possibility of alteration in the composition of polymeric samples upon exposure to the electron beam.

Fluorescence microscopy could be useful when it comes to studying the presence of foulants such as proteins on a membrane surface. Indeed, when multiple proteins are present on a sample surface, FTIR technique may not be able to distinguish them from one another due to their almost similar composition. Fluorescence microscopy uses laser of a specific wavelength as the incident light source that will excite the fluorescent molecules or fluorophores in the sample. The sample will then emit fluorescent light of another wavelength in which the observer can view through the fluorescent microscope. This method can visualize auto-fluorescent specimens on a surface [32]. For samples that have either extremely faint or bright, nonspecific fluorescence, they can be attached with fluorescent stains or fluorescent-tagged antibodies. This technique is capable of detecting a single molecule. Using multiple fluorescence labelling and different probes, it can also simultaneously identify several target molecules. Thus, fluorescence microscopy could be advantageous to observe the competitive adsorption of proteins on the modified membrane surface.

4.3.2. Membranes wettability

Surface wetting mostly governs the interactions between solid surfaces and fluids. Thus, this phenomenon is essential when investigating membrane processes since it influences flux, rejection, and fouling. The most common method to determine the degree of wetting is through the measurement of the contact angle formed by a droplet of liquid on membrane surface (Figure 1. 5). It depends on the interfacial tensions of all the interfaces involved. For instance, when a drop of water is put on a solid surface under air, the shape of the drop changes under the pressure of the different surface-interfacial tensions until equilibrium is reached [30]. A hydrophilic surface will favour the interaction with water, thus, the water droplet spreads on the surface and the measured contact angle is small. Conversely, a hydrophobic surface will repel water, thus, to minimize their interaction, the contact angle formed will be high.

It is important to note that on porous substrates such as porous membrane, the effect of some factors such as liquid absorption, pore structure, surface roughness and drop size should be considered [33]. It should also be considered that the contact angle of a sample could change depending on the environment implying that measured contact angles could be different for dry and wet states. For instance, polymeric membranes tend to reorganize their structure to adapt to the surrounding medium [34]. Consequently, its surface properties will vary depending on the environment it is currently in. Since membranes are generally used in their wet state, it would be more interesting to observe its surface wetting properties in an environment similar to its working condition that is their wet state. Moreover, the contact angle measurement requires a number of precautions to be used effectively, including surface cleanliness, liquid purity, temperature control, multiple measurements, etc.

Contact angle analysis is a convenient tool to characterize grafted polymer surfaces, because contact angles are very sensitive to changes in surface chemistry [31]. Eventually, there are several methods to measure contact angle – sessile drop method, captive bubble/drop method, and Wilhelmy plate method [30].

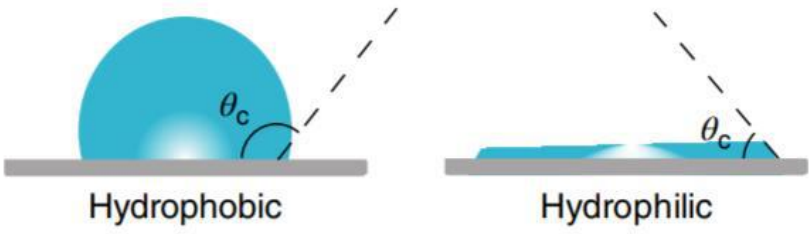

Figure 1. 5. Illustration of contact angle over a flat surface [31].

4.3.3. Assessment of the modification layer density

4.3.3.1. Difference of dried mass

Several studies quantified the amount of the deposited brushes on a membrane surface using the difference of mass [35]. It is done by measuring the weight difference between the modified (W_M), and unmodified (W_D), dry membranes with respect to membrane surface area ($A_{membrane}$) (equation 1.1).

$$Coating\ density = \frac{W_M - W_D}{A_{membrane}} \quad (1.1)$$

Although this method is fast and simple, it is not a very sensitive method. In fact, a previous study revealed that coating density started to reach a plateau at copolymer concentrations beyond 3-5 mg·mL^{-1} when FTIR imaging showed that there was still an observable difference between 5 and 10 mg·mL^{-1} concentration [35]. Thus, this method exhibits some inaccuracies due to the non-consideration of the humidity during measurement. Besides. Besides, it cannot verify the homogeneity of the coating. It does not consider the contribution of the pores to the surface area and the amount of modifying functions that penetrate the pores during modification process. Lastly, membranes could potentially absorb moisture when exposed to air, which could lead to overestimation of the measured weights. Thus, it is recommended to consider the coating density trend instead of the actual value [35].

4.3.3.2. Mass balance in solution using UV Visible spectroscopy

UV Visible spectroscopy is an analytical technique where a sample is irradiated with light of different wavelengths in the visible, ultraviolet, and near-infrared regions [32]. Depending on the content of the sample, the light is partially absorbed. The remaining transmitted light will be detected and recorded as a function of wavelength creating the sample's UV-visible spectrum, which can be used to identify or quantify the content of the sample. Generally, the results are presented as absorbance as a function of wavelength since the intensity of the absorbance is directly proportional to the concentration of the analyte. Also, the concentration can be obtained quantitatively by measuring absorptions of multiple standard solutions with known concentration followed by the application of Beer-Lambert's Law.

Since the initial copolymer concentration is known, then the difference in concentration before and after the immersion is the amount adsorbed on the surface. Some researchers used UV-visible spectrophotometer to quantify the adsorbed amount of BSA and lysozyme on PVDF

membranes. The remaining concentration of the protein on the solution after the immersion process was determined by measuring the absorbance at 280 nm [36]. However, this method does not consider the amount of coating that penetrated the pores.

4.3.4. Characterization of protein adsorption in solution

A way to better understand proteins adsorption on membrane surfaces is to study in solution the interactions with the polymers or the functional groups used for the membrane surface functionalization. Another method that was revealed to be effective for proteins adsorption study in solution was the use of colloidal core-shell particles that exhibit a large surface to allow the adsorption of a high amount of protein in small volumes [37].

Thus, a wide variety of methods can be added to those listed previously to characterize proteins adsorption [26]. Among these methods calorimetry utilizes the enthalpic effect generated by the binding of proteins to polymers in solution to provide direct thermodynamic information that is not available on planar surfaces [38].

If the concentrations are not too high, spectroscopic techniques such as fluorescence spectroscopy can be applied to monitor adsorption of fluorescent-labeled proteins [37]. Another spectroscopic technique is FTIR, that can be used to determine the secondary structure of adsorbed proteins with great precision, because it is not hampered by the turbidity of these aqueous suspensions [26].

Scattering methods as small-angle X-ray and neutron scattering (SAXS, SANS), have been also extensively used for the analysis of proteins uptake by polyelectrolyte brushes in solution [37]. Proteins have a strong X-ray contrast in water, which leads to a marked change of the scattering curves caused by their adsorption or uptake by other solutes. Besides, investigation of scattering data could furnish information about the radial distribution of the adsorbed proteins within the layer and the total amount of adsorbed protein.

Added to those stated above, others techniques can be used to characterize proteins-polymers systems in solution. For instance, dynamic light scattering (DLS) is used for the evaluation of the hydrodynamic diameter of the proteins-polymers system, size exclusion chromatography (SEC) determines the molecular weight, while UV-visible spectroscopy allows to estimate the amount of adsorbed protein [26].

5. Smart biomedical membranes for blood separation

5.1. Blood separation

Blood is a fluid transported in the vascular system through veins and arteries that supply nutrients and oxygen to different parts of the body, which is necessary for its survival and development while carrying away metabolic waste. It is 55% plasma (91% water and 9% proteins, ions, nutrients, wastes, etc.) and 45% erythrocytes (red blood cells), leukocytes (white blood cells) and thrombocytes (platelets). Erythrocytes carry the oxygen, leukocytes are for immune response, and thrombocytes' main function is to stop bleeding through blood clot formation after adhesion to the wall of the damaged vessel [39].

Whole blood can be delivered directly to patients suffering from active bleeding after major trauma without undergoing separation [40]. However, it can also be separated into different specific fractions (e.g. red blood cells concentrates and platelets concentrates), some of which can address direct blood conditions.

Red blood cells concentrates are essential to patients who suffer from severe bleeding or during surgical operations [41]. They are also commonly provided to premature infants to address symptoms of anemia [42]. The importance of red blood cells in oncology has also been shown recently, as membrane-modified red blood cells could act as natural chemotherapy drug carriers to specifically target cancer cells [43].

As for platelets, their transfusion is necessary for patients undergoing intensive medication (chemotherapy), hematological disease, and surgery [44]. In addition, the platelets concentrate or usually called Platelets Rich Plasma (PRP) play an important role in many processes such as coagulation, immune response, angiogenesis and the healing of damaged tissues. That's because platelets, are an important reservoir of proteins called growth factors that regulate cell growth and division. Those proteins contained in the granules of platelets include platelet-derived growth factor (PDGF), transforming growth factor (TGF), platelet factor interleukin (IL), platelet-derived angiogenesis factor (PDAF), vascular endothelial growth factor (VEGF), epidermal growth factor (EGF), insulin-like growth factor IGF and fibronectin [45].

From above it can be concluded that separation of blood components, and the use of each fraction alone could be better for more targeted applications.

The separation of blood components is often done by centrifugation, a fast technique but energy demanding. It uses the action of gravitational force to separate blood into three major

fractions: erythrocytes in the bottom of the centrifugation tube, plasma as the supernatant, and a mixture of leukocytes and thrombocytes (platelets) in between [46]. Thus, centrifugation remains ineffective to separate white cells from platelets because they have almost the same density. Adding to that, if it is not done in proper conditions, it can lead to hemolysis of red blood cells (RBC) resulting in contamination of plasma [47].

A slower alternative technology but less energy demanding, is separation by porous membranes in which the separation is primarily based on size differences. But after membrane functionalization by introducing some smart groups into the surface to control interactions with different components, both the particle size and the particle's affinity for the membrane material are ruling criteria for the separation process [5].

Globally, blood filtration can be conducted without necessarily designing smart membranes, but by controlling the structure of the membrane and its wetting properties, as it has been done for many years with dialysis membranes aimed at purifying blood [48]. However, when it comes to separating blood components from whole blood, the introduction of some smart functions into the surface of the membrane could permit to control specific interactions with the desired blood component that has to be retained.

5.2. Concept of smart membranes

The supporting layer of membranes used for blood separation are now mostly synthetic hydrophobic polymers such as PVDF. They are chosen for their outstanding bulk properties that prevent membrane structure damages during the manufacture or sterilization steps. However, being hydrophobic makes them easy to interact with plasma proteins partly hydrophobic leading to some unwanted phenomena as platelet activation [5]. Thus, to enhance their hemocompatibility it is necessary to introduce some smart functions onto these membranes surface that can improve their resistance to nonspecific proteins adsorption and prevent or reduce the biofouling blood cells. Among materials minimizing the interactions with blood components, the neutral poly(ethylene glycol) (PEG) and its derivatives such as poly(ethylene glycol methacrylate) (PEGMA) have been proved to do it well [49].

Another route was proved to improve the hemocompatibility of hydrophobic membrane, it consists on coating or grafting charged moieties either positively and negatively in the surface which forms the so called zwitterionic systems [50].

In addition to hydrophobic nature of polymeric membranes leading to biofouling, this phenomenon could be also due to electrostatic interactions in the case of membranes with surface charge deviating from electroneutrality. This could happen due to the local charge density bared by the cells and proteins that is likely different from zero because they carry both positively and negatively charged functional groups. Furthermore, if the pH of the surrounding medium in which blood flows is different of the isoelectric point of the proteins, coated and grafted membranes, that is, membranes with a local charge bias, will undergo nonspecific proteins adsorption [5]. This issue can be turned into an advantage in the development of smart biomedical membranes. Indeed, those charged materials could be used to interact specifically with some blood cells and proteins, while being totally blind to others. The cells separation in this case will be no longer based on their size but rather on their surface charge.

The stimuli-responsive materials are among the functions that could be also incorporated onto the membranes surfaces. The physical behaviour of this variety of brushes in solution can be controlled by altering the environmental conditions. A typical example of stimuli-responsive materials is poly(N-isopropylacrylamide), which can expand or shrink by tuning the temperature, thereby affecting the membranes' pore size [51].

Only one of these interactions is not enough to ensure an interesting membrane property in regard to the complexity and the multiple components of the blood. Thus, the combination of two or more functional groups among those mentioned above could be promising for the development of smart biomedical membranes for blood separation (Figure 1. 6). Indeed, it can provide a more refined control of interactions between blood cells and membranes materials. While one functional group establishes electrostatic-based interactions with the targeted cells, the other functional group prevents the adhesion of the plasma proteins and other cells contained in the blood. The adhesion could be then reversible using stimuli-responsive brushes to release for example the cells already captured before.

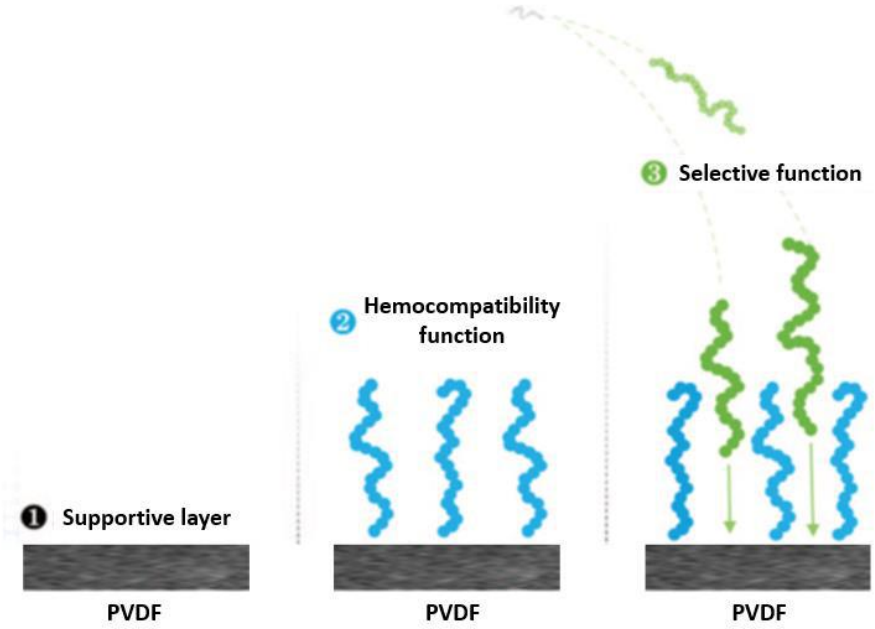

Figure 1. 6. Architecture of a smart membrane for blood separation composed of a polymeric supporting layer surface modified with antifouling brushes and smart functional groups for selective trapping [5].

5.3. PVDF as supporting material for blood separation systems

Membranes are widely used as supporting materials for separation processes in biomedical applications and research on their use in blood-contacting devices is growing steadily. For instance, their application in the separation of plasma and viruses from whole blood, the concentration and de-mineralization of blood plasma using ultrafiltration membranes have been under investigation [49]. However, when the blood is in contact with the material outside the human body, some biological responses are likely to happen such as the activation of blood coagulation system at the blood/material interface. Then a response of the immune system arising from the blood/material contact and other tissues responses occurs [49]. Therefore, the choice of materials that can be used to design membranes for blood contacting devices is limited by their lack of hemocompatibility and biofouling resistance.

Synthetic polymeric membranes, such as polyvinylidene fluoride (PVDF) among others, are usually chosen for blood separation research [52]. The main advantages of PVDF are sufficient thermal and mechanical resistance preventing damages during the manufacture and sterilization steps [5]. In addition, some studies have confirmed that PVDF porous membranes can be used in biomedical application such as artificial blood vessel, tissue engineering and blood purification [53].

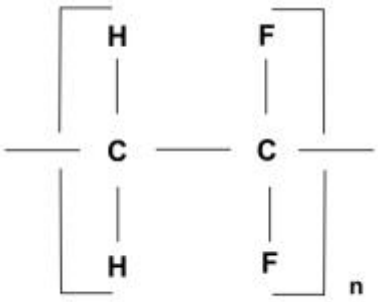

Figure 1. 7. Structure of the PVDF molecule

Nowadays, PVDF (Figure 1. 7) is one of the most popular material for ultrafiltration and microfiltration membrane manufacturing. This material provides robust membranes due to its structural and chemical stability. Further, reasonable cost compared to other membrane materials, add to the popularity of this polymer [54].

Unfortunately, PVDF is a hydrophobic material, with a relatively low surface energy and high water contact angle, which make it easy to adsorb blood plasma proteins and blood cells thus triggering coagulation, hemolysis and other immune responses [53], so that one may assume that it cannot be used as a hemocompatible material. Yet, modifying the surface of PVDF membrane directly in contact with blood might be an interesting path to take advantage of the excellent bulk properties of this material.

In order to capitalize on the usefulness of PVDF membranes in filtration operations, many studies have investigated (surface) modification of this material to make it polar and less hydrophobic [14], [17]. Many of the modification methods are aiming to structure a hydration layer to improve the anti-hemolysis property of PVDF membrane or to establish a heparin/heparin-like anticoagulant layer to prolong the blood coagulation time when blood contact membrane materials [8].

Chang et al. modified commercial PVDF membranes by grafting zwitterionic polymer, and unveiled that blood compatibility was obtained when overall charge neutrality of the hydrated layer was achieved [55]. They also used poly(ethylene glycol) methacrylate (PEGMA) to modify the surface of PVDF membranes and proved an increase of the resistance to proteins adsorption or blood cells adhesion. Other studies proposed a surface glycosylation of PVDF microporous membranes to improve their anti-biofouling properties along with their resistance to platelet adhesion [56].

5.4. Surface-Modifying functional groups

Hydrophilic polymer polyethylene glycol (PEG), called also polyethylene oxide (PEO) when it is large (> 20 kDa), and its derivatives are one of the most studied polymers to prevent adsorption of blood proteins, blood cells, and bacteria. PEGylated copolymers on membranes enhance the trapping of water at its surface through hydrogen bonding leading to the formation of hydration layer which gives a physical and energetic barrier against protein, cells, and bacteria [5]. Consequently, biofouling on the membrane is reduced. To ensure the stability of these polymers on the membrane surface, they are usually combined with a hydrophobic block that will interact with the hydrophobic membrane surface. In some studies the polystyrene (PS) block was used to anchor the hydrophilic poly(ethylene glycol) methacrylate (PEGMA) block to the hydrophobic PVDF surface which made the membrane resistant to bovine serum albumin (BSA) adsorption [57]. Other studies have shown that PVDF membrane modified with PS/PEGMA block copolymer reduces the adhesion of platelets, erythrocytes, leukocytes, and fibrinogen [49]. Tuning the amount of the polymer blocks coated on the membrane surface allows control of the hydrophobic/hydrophilic balance resulting in tunable fouling resistance.

Poly(N-isopropylacrylamide) (PNIPAAM) is a temperature-responsive polymer that undergoes a rapid transition from a hydrophilic to a hydrophobic structure in water at its lower critical solution temperature (LCST) between 30 and 35^{o}C [51]. It swells (hydrophilic) at temperatures below its LCST due to hydrogen bonding between the water and PNIPAAM molecules, and it collapses (hydrophobic) at temperatures above its LCST due to preferred intramolecular interaction among PNIPAAM molecules. This means that its hydrophilicity and consequently, cell, protein, and bacterial adhesion behaviour can be regulated with temperature which can be further controlled through the incorporation of other anti-fouling functional groups as demonstrated by several studies [58].

Poly(acrylic acid) (PAA) is a negatively charged bioactive polymer in aqueous medium which is widely used to modify polymeric surfaces for drug release and protein immobilization [59]. AA is a hydrophilic monomer that allows to introduce carboxyl groups (–COOH) which react with the amino groups from proteins. It has been shown that this polymer binds to blood proteins at some specific conditions of pH and ionic strength. Other studies demonstrated that albumin polymer could be conjugated with fibrinogen and successfully attached to a platelet-immobilized surface [60]. Thus, it would be interesting to investigate the interactions of blood proteins (HSA, fibrinogen, and globulin) with PAA and verify the potential use of protein modified PAA to selectively interact with platelets.

The variety of properties of functional groups may provide an opportunity to develop new membrane materials with specific affinities and interactions with complex biological fluids like blood.

6. PhD strategy and positioning

The PhD thesis has been conducted as part of the MOSAIC-3D project, which is an international collaboration between Laboratoire de Génie Chimique (UMR 5503, Université de Toulouse, CNRS, INPT, UPS, Toulouse, France) and the Research and Development Center for Membrane Technology (Chung Yuan Christian University, ChungLi, Taiwan). The funding for this project was provided by the Agence Nationale de la Recherche (ANR 17-CE08-0041) and by the Ministry of Science and Technology in Taiwan (MOST 107-2923-E-033-001) for a budget of 250 k€ each, which makes a total budget of 500k.

Within this framework, a 6-weeks stay was made in the Research and Development Center for Membrane Technology (Chung Yuan Christian University, ChungLi, Taiwan), where training on copolymer synthesis and membrane surface modification was initiated. The visit was concluded with a workshop between the two groups and a participation to the International Membrane Conference in Taipei (2019).

6.1. Context and objectives

This project aims at designing and developing smart membrane technologies to address several critical needs related to blood cells screening and the concentration of a growth factor stored inside the granules of platelets and expressed after their activation. This growth factor namely platelet-derived growth factor (PDGF) is a mitogen among those numerous growth factors mentioned earlier in section 5.1. It is used particularly to help heal diabetic ulcers, in orthopedic surgery and periodontics as an alternative to bone autograft to stimulate bone regeneration and repair. To allow that to happen, thrombocytes (platelets) need first to be separated from other blood cells.

The current PDGF extraction and purification methods are centrifugation [5] and chromatography [61]. Centrifugation is fast but energy demanding. Besides, it does not allow to separate thrombocytes from leukocytes. Chromatography is effective on separation, but its discontinuous mode and its low yield and productivity hamper its use on a large scale production [62]. Wherefore, this project proposes to use smart membranes tailored at the nanoscale as an efficient alternative to facilitate the reversible adhesion and activation of

platelets. The membranes can be functionalized through surface modification allowing it to specifically interact with the targeted components resulting in selective separation.

Thus, the main challenges of this project are:

- The design of tailored functional groups (brushes of copolymer to be grafted onto the membrane surface) to have switchable control between attachment and detachment of proteins and cells.
- Control of the membrane architecture through surface modification with the aim to enhance its selectivity or non-adhesive properties.
- Tuning of operating conditions by the analysis and the control of interface properties during filtration to have the best performance of the developed membranes.

6.2. Strategy

The strategy is based on designing and testing different membrane systems in order to (1) purify platelets from whole blood (separation of blood components) and (2) enable the activation of platelets and release of PDGF (Figure 1. 8). Thus, the systems schematized below allow to consider several routes for the production of PDGF. The first one to select platelets, release the platelets and activate them in solution to induce the formation of growth factor (Membrane I). The second option is to select the platelets and purify the growth factors at the interface (Membrane II). Finally, for a comparative study, the third route is to select erythrocytes and leukocytes, let the platelets permeate through the membrane and activate them in solution similarly as in (1) (Membrane III).

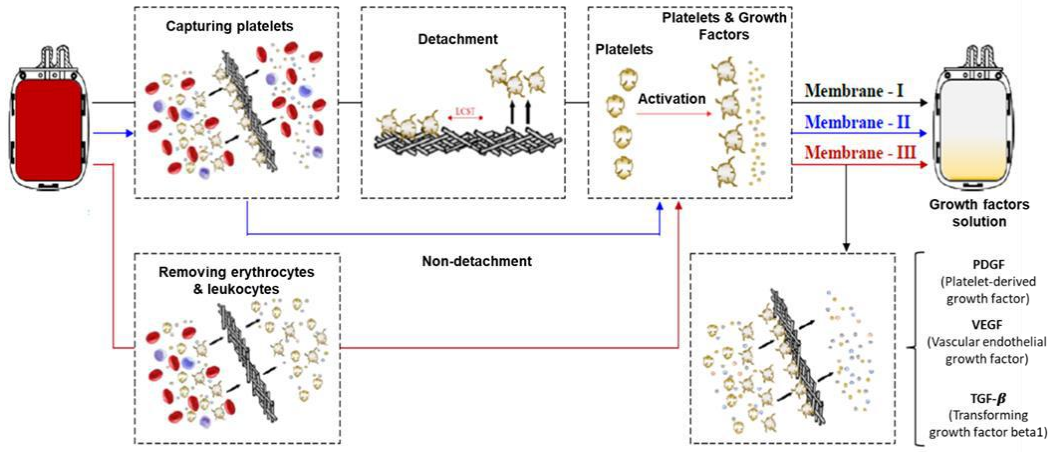

Figure 1. 8. Design of different membrane systems to purify platelets from whole blood (separation of blood components) and enable the activation of platelets and purification of growth factor.

6.3. Contribution of PhD thesis

The research target is the preparation of an interface/membrane that can selectively capture platelets from human whole blood (Figure 1. 9). This design represents the ultimate design goal and it involves the grafting of three different functional groups: one type of functional group for the selection of platelets, one functional group to provide bio-inert properties to the system, and the last group is to release platelets. Thus, there should be specific biofouling of the membrane system.

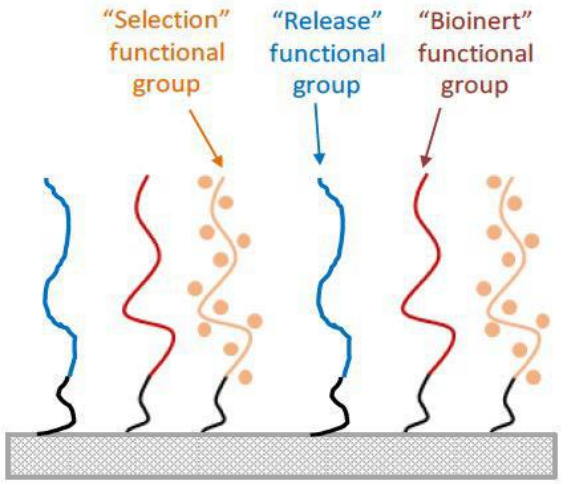

Figure 1. 9. Schematic representation of a membrane for selection and release of the platelets.

For that reason, different copolymers were used in this study to modify hydrophobic PVDF membrane surface. The polymers used for the surface modification are chosen from a range of polymers known to have limited or specific interaction with other target solutes. Polystyrene-block-poly(acrylic acid) (PS-b-PAA) copolymer was used to investigate its interaction with blood proteins. PAA is considered as bioactive polymer that can be conjugated with blood proteins which could induce platelet capture and activation. Then the polystyrene-block-poly(ethylene glycol) (PS-b-PEG) should avoid unwanted interactions with other blood proteins. Finally, the polystyrene-block- poly(N-isopropylacrylamide) (PS-b-PNIPAAM) role is to release platelets by changing the temperature.

In order to test the copolymers mentioned above, some primary experiments on the capture of platelets from PRP solutions (Platelets Rich Plasma on polystyrene (PS) well plates modified with triblock PS-PAA and random PS-PEG polymers have been conducted. The copolymers used for modification were synthetized in the Research and Development Center for Membrane Technology (Chung Yuan Christian University, ChungLi, Taiwan), and the experiments were carried out during my visit to the center.

The quantitative analysis (Tables given in **Appendix A**) of the obtained confocal microscope images (Figure 1. 10) showed a potential increase of the number of platelets captured on the PS-PAA modified PS well plate, while their presence was mitigated in the presence of PS-PEG.

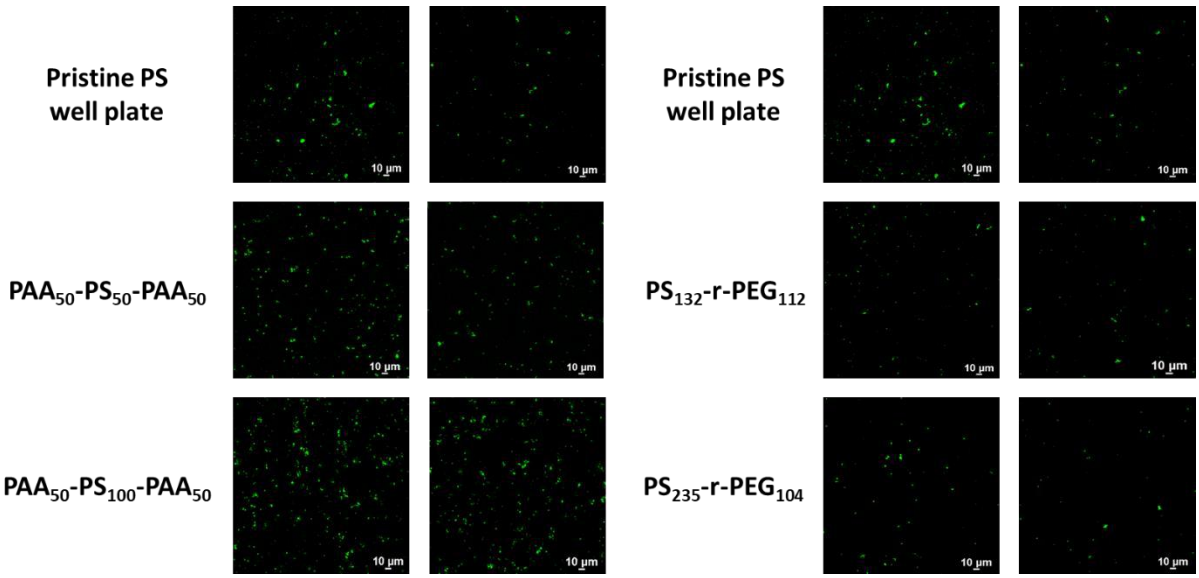

Figure 1. 10. Confocal microscope images of blood platelets adhering onto the PS well plates surfaces modified with triblock PS-PAA and with random PS-PEG.

These very preliminary results confirmed the potential of the polymers to influence the adhesion of platelets, though a lot remained to be understood before getting full control of this capture mechanism.

In particular, the efficacy of a surface modification may be jeopardized if the functionalized surface is poisoned by unexpected interactions with other solutes or colloids than the target ones. In the specific case of the extraction of platelets from blood, the presence of various proteins especially those at high concentration such as human serum albumin (HSA) which is well known to adsorb on a wide variety of surfaces, maybe an issue. A comprehensive understanding of the interactions between blood proteins and the polymers candidate for surface modification was therefore considered as a prerequisite, in the project strategy. From that arises the objectives of this PhD thesis given below and illustrated in Figure 1. 11.

- Understand and control the local interactions (electrostatic, hydrophobic …) between the selected moieties (PAA, PEG) with major human blood proteins (albumin, ɣ-globulin, and fibrinogen). That's why, the second chapter of this manuscript is dedicated to present an explicit study of these interactions in batch in different physicochemical conditions using mostly Small Angle X- ray Scattering (SAXS) as a tool of investigation.

- Study the functionalization of PVDF membranes using the copolymers mentioned previously, and then investigate the static adhesion of human blood proteins on the copolymer. For that, the third chapter discuss the optimization of the modification process for each copolymer. It also presents the different interactions that could take place but at the modified interface this time.

- Assess the performance of the functionalized membranes for filtration processes. This point is detailed in the fourth chapter that presents all the experiments related to filtration tests. Indeed, the filtration of pure water was first performed to validate the operating conditions of the modification process discussed in the third chapter. Then, dead-end filtrations of protein solutions were conducted to investigate the adhesion of blood proteins on modified surfaces but this time in dynamic mode.

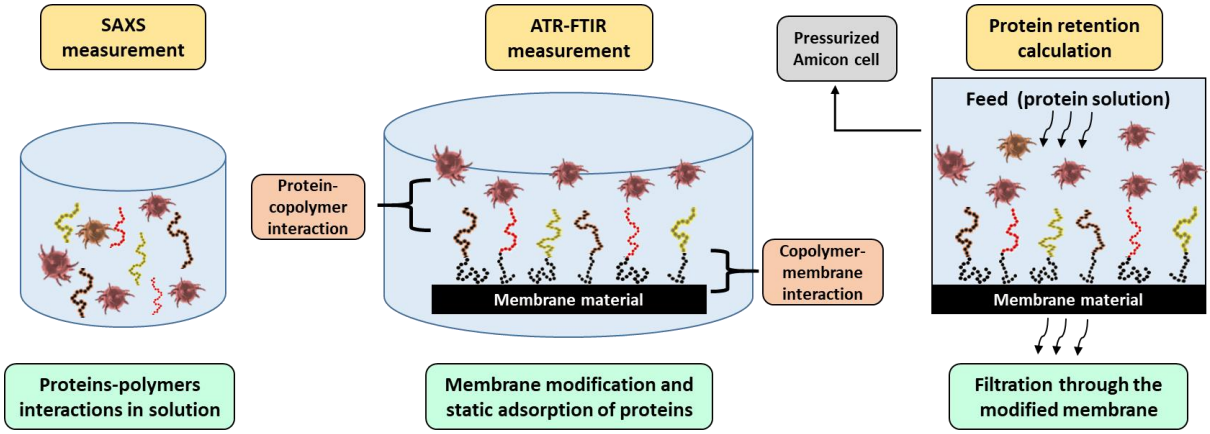

Figure 1. 11. Illustration of the different steps and studies conducted to achieve the objectives of PhD thesis.

7. References

[1] A. J. Jose, J. Kappen, et M. Alagar, « 2 - Polymeric membranes: Classification, preparation, structure physiochemical, and transport mechanisms », in *Fundamental Biomaterials: Polymers*, 2018, p. 21-35.

[2] N. N. Li, A. G. Fane, W. S. W. Ho, et T. Matsuura, *Advanced Membrane Technology and Applications*. John Wiley & Sons, 2011.

[3] « Overview of Membrane Science and Technology », in *Membrane Technology and Applications*, John Wiley & Sons, Ltd, 2004, p. 1-14.

[4] https://www.marketsandmarkets.com/

[5] A. Venault, C.-C. Yeh, N.-T. Hsieh, et Y. Chang, « Chapter 14: Smart Biomedical Membranes for Blood Separation », in *Smart Membranes*, 2019, p. 389-413.

[6] B. Krause *et al.*, « Polymeric Membranes for Medical Applications », *Chemie Ingenieur Technik*, vol. 75, nº 11, p. 1725-1732, 2003.

[7] D. F. Stamatialis *et al.*, « Medical applications of membranes: Drug delivery, artificial organs and tissue engineering », *Journal of Membrane Science*, vol. 308, nº 1, p. 1-34, 2008.

[8] G. Catapano et J. Vienken, « Biomedical Applications of Membranes », in *Advanced Membrane Technology and Applications*, John Wiley & Sons, Ltd, 2008, p. 489-517.

[9] M. Ulbricht, « Advanced functional polymer membranes », *Polymer*, vol. 47, nº 7, p. 2217-2262, mars 2006.

[10] X. Chen et J. Li, « Bioinspired by cell membranes: functional polymeric materials for biomedical applications », *Materials Chemistry Frontiers*, vol. 4, nº 3, p. 750-774, 2020.

[11] N. Nady, M. C. R. Franssen, H. Zuilhof, M. S. M. Eldin, R. Boom, et K. Schroën, « Modification methods for poly(arylsulfone) membranes: A mini-review focusing on surface modification », *Desalination*, vol. 275, nº 1-3, p. 1-9, 2011.

[12] R. Gopal, M. Zuwei, S. Kaur, et S. Ramakrishna, « Surface Modification and Application of Functionalized Polymer Nanofibers », in *Molecular Building Blocks for Nanotechnology: From Diamondoids to Nanoscale Materials and Applications*, 2007, p. 72-91.

[13] D. Rana et T. Matsuura, « Surface Modifications for Antifouling Membranes », *Chemical Reviews*, vol. 110, nº 4, p. 2448-2471, 2010.

[14] C.-H. Hsu *et al.*, « Toward Antibiofouling PVDF Membranes », *Langmuir*, vol. 35, nº 20, p. 6782-6792, 2019.

[15] K. C. Khulbe, C. Feng, et T. Matsuura, « The art of surface modification of synthetic polymeric membranes », *Journal of Applied Polymer Science*, vol. 115, n° 2, p. 855-895, 2010.

[16] C. Czeslik et A. Wittemann, « Adsorption mechanism, secondary structure and local distribution of proteins at polyelectrolyte brushes », *Colloid Polym Sci*, vol. 298, n° 7, p. 775-789, 2020.

[17] J. Hong et Y. He, « Effects of nano sized zinc oxide on the performance of PVDF microfiltration membranes », *Desalination*, vol. 302, p. 71-79, 2012.

[18] M. Kim, S. K. Schmitt, J. W. Choi, J. D. Krutty, et P. Gopalan, « From Self-Assembled Monolayers to Coatings: Advances in the Synthesis and Nanobio Applications of Polymer Brushes », *Polymers*, vol. 7, n° 7, p. 1346-1378, 2015.

[19] C. Bellmann, « Surface Modification by Adsorption of Polymers and Surfactants », in *Polymer Surfaces and Interfaces: Characterization, Modification and Applications*, Springer, 2008, p. 235-259.

[20] L. W. Bruch, M. W. Cole, et E. Zaremba, *Physical Adsorption: Forces and Phenomena*. Courier Dover Publications, 2007.

[21] M. A. Al-Ghouti et D. A. Da'ana, « Guidelines for the use and interpretation of adsorption isotherm models: A review », *Journal of Hazardous Materials*, vol. 393, p. 122383, 2020.

[22] C. H. Giles, D. Smith, et A. Huitson, « A general treatment and classification of the solute adsorption isotherm. I. Theoretical », *Journal of Colloid and Interface Science*, vol. 47, n° 3, p. 755-765, 1974.

[23] C. H. Giles, A. P. D'Silva, et I. A. Easton, « A general treatment and classification of the solute adsorption isotherm part. II. Experimental interpretation », *Journal of Colloid and Interface Science*, vol. 47, p. 766-778, 1974.

[24] R. HOGG, « Evaluation of a Macroscopic Model for Polymer Adsorption », in *Polymer Adsorption and Dispersion Stability*, vol. 240, p. 23-37, American Chemical Society, 1984.

[25] E. Papirer, *Adsorption on Silica Surfaces*. CRC Press, 2000.

[26] Q. Wei *et al.*, « Protein Interactions with Polymer Coatings and Biomaterials », *Angewandte Chemie International Edition*, vol. 53, n° 31, p. 8004-8031, 2014.

[27] A. E. Nel *et al.*, « Understanding biophysicochemical interactions at the nano-bio interface », *Nat Mater*, vol. 8, n° 7, p. 543-557, 2009.

[28] D. Chandler, « Interfaces and the driving force of hydrophobic assembly », *Nature*, vol. 437, n° 7059, p. 640-647, 2005.

[29] M. Kanduč, E. Schneck, et R. R. Netz, « Hydration Interaction between Phospholipid Membranes: Insight into Different Measurement Ensembles from Atomistic Molecular Dynamics Simulations », *Langmuir*, vol. 29, n° 29, p. 9126-9137, 2013.

[30] M. Kallioinen et M. Nyström, « Membrane Surface Characterization », in *Advanced Membrane Technology and Applications*, John Wiley & Sons, Ltd, 2008, p. 841-877.

[31] M. A. Rufin et M. A. Grunlan, « Surface-Grafted Polymer Coatings », in *Functional Polymer Coatings*, John Wiley & Sons, Ltd, 2015, p. 218-238.

[32] W. Chen, C. Qian, K.-G. Zhou, et H.-Q. Yu, « Molecular Spectroscopic Characterization of Membrane Fouling: A Critical Review », *Chem*, vol. 4, n° 7, p. 1492-1509, 2018.

[33] S. Krainer et U. Hirn, « Contact angle measurement on porous substrates: Effect of liquid absorption and drop size », *Colloids and Surfaces A: Physicochemical and Engineering Aspects*, vol. 619, p. 126503, 2021.

[34] W. Zhang, M. Wahlgren, et B. Sivik, « Membrane Characterization by the Contact Angle Technique: II. Characterization of UF-Membranes and Comparison between the Captive Bubble and Sessile Drop as Methods to obtain Water Contact Angles », *Desalination*, vol. 72, n° 3, p. 263-273, 1989.

[35] L. Benavente *et al.*, « FTIR mapping as a simple and powerful approach to study membrane coating and fouling », *Journal of Membrane Science*, vol. 520, p. 477-489, 2016.

[36] A. Venault, Y. Chang, H.-S. Yang, P.-Y. Lin, Y.-J. Shih, et A. Higuchi, « Surface self-assembled zwitterionization of poly(vinylidene fluoride) microfiltration membranes via hydrophobic-driven coating for improved blood compatibility », *Journal of Membrane Science*, vol. 454, p. 253-263, 2014.

[37] N. Welsch, Y. Lu, J. Dzubiella, et M. Ballauff, « Adsorption of proteins to functional polymeric nanoparticles », *Polymer*, vol. 54, n° 12, p. 2835-2849, 2013.

[38] S. Yu *et al.*, « Interaction of human serum albumin with short polyelectrolytes: a study by calorimetry and computer simulations », *Soft Matter*, vol. 11, n° 23, p. 4630-4639, 2015.

[39] S. Tripathi, Y. V. B. V. Kumar, A. Prabhakar, S. S. Joshi, et A. Agrawal, « Passive blood plasma separation at the microscale: a review of design principles and microdevices », *J. Micromech. Microeng.*, vol. 25, n° 8, p. 083001, 2015.

[40] V. Salunkhe, P. F. van der Meer, D. de Korte, J. Seghatchian, et L. Gutiérrez, « Development of blood transfusion product pathogen reduction treatments: A review of methods, current applications and demands », *Transfusion and Apheresis Science*, vol. 52, n° 1, p. 19-34, 2015.

[41] G. Liumbruno, F. Bennardello, A. Lattanzio, P. Piccoli, et G. Rossetti, « Recommendations for the transfusion of red blood cells », *Blood Transfus*, vol. 7, nº 1, p. 49-64, 2009.

[42] H. Hume, « Red blood cell transfusions for preterm infants: The role of evidence-based medicine », *Seminars in Perinatology*, vol. 21, nº 1, p. 8-19, 1997.

[43] V. R. Muzykantov, « Drug delivery by red blood cells: vascular carriers designed by mother nature », *Expert Opinion on Drug Delivery*, vol. 7, nº 4, p. 403-427, 2010.

[44] H. Wandt, K. Schäfer-Eckart, et A. Greinacher, « Platelet Transfusion in Hematology, Oncology and Surgery », *Dtsch Arztebl Int*, vol. 111, nº 48, p. 809-815, 2014.

[45] A. Lubkowska, B. Dolegowska, et G. Banfi, « Growth factor content in PRP and their applicability in medicine », *J Biol Regul Homeost Agents*, vol. 26, nº 2, p. 3S-22S, 2012.

[46] J. Hardwick, « Blood processing », *ISBT Science Series*, vol. 3, nº 2, p. 148-176, 2008.

[47] G. Lippi, P. Avanzini, et G. Cervellin, « Prevention of hemolysis in blood samples collected from intravenous catheters », *Clinical Biochemistry*, vol. 46, nº 7, p. 561-564, 2013.

[48] W. R. Clark, R. J. Hamburger, et M. J. Lysaght, « Effect of membrane composition and structure on solute removal and biocompatibility in hemodialysis », *Kidney International*, vol. 56, nº 6, p. 2005-2015, 1999.

[49] A. Venault, M. R. B. Ballad, Y.-H. Liu, P. Aimar, et Y. Chang, « Hemocompatibility of PVDF/PS-b-PEGMA membranes prepared by LIPS process », *Journal of Membrane Science*, vol. 477, p. 101-114, 2015.

[50] K. Ishihara, K. Fukumoto, Y. Iwasaki, et N. Nakabayashi, « Modification of polysulfone with phospholipid polymer for improvement of the blood compatibility. Part 2. Protein adsorption and platelet adhesion », *Biomaterials*, vol. 20, nº 17, p. 1553-1559, 1999.

[51] L. Ying, E. T. Kang, et K. G. Neoh, « Synthesis and Characterization of Poly(N-isopropylacrylamide)-graft-Poly(vinylidene fluoride) Copolymers and Temperature-Sensitive Membranes », *Langmuir*, vol. 18, nº 16, p. 6416-6423, 2002.

[52] A. Mollahosseini, A. Abdelrasoul, et A. Shoker, « Latest advances in zwitterionic structures modified dialysis membranes », *Materials Today Chemistry*, vol. 15, p. 100227, 2020.

[53] Z. An, Y. Li, R. Xu, F. Dai, Y. Zhao, et L. Chen, « New insights in poly(vinylidene fluoride) (PVDF) membrane hemocompatibility: Synergistic effect of PVDF-g-(acryloyl morpholine) and PVDF-g-(poly(acrylic acid)-argatroban) copolymers », *Applied Surface Science*, vol. 457, p. 170-178, 2018.

[54] L. Yan, Y. S. Li, et C. B. Xiang, « Preparation of poly(vinylidene fluoride)(pvdf) ultrafiltration membrane modified by nano-sized alumina (Al_2O_3) and its antifouling research », *Polymer*, vol. 46, n° 18, p. 7701-7706, 2005.

[55] Y. Chang, Y.-J. Shih, C.-Y. Ko, J.-F. Jhong, Y.-L. Liu, et T.-C. Wei, « Hemocompatibility of Poly(vinylidene fluoride) Membrane Grafted with Network-Like and Brush-Like Antifouling Layer Controlled via Plasma-Induced Surface PEGylation », *Langmuir*, vol. 27, n° 9, p. 5445-5455, 2011.

[56] J. Yuan, J. Meng, Y. Kang, Q. Du, et Y. Zhang, « Facile surface glycosylation of PVDF microporous membrane via direct surface-initiated AGET ATRP and improvement of antifouling property and biocompatibility », *Applied Surface Science*, vol. 258, n° 7, p. 2856-2863, 2012.

[57] Y.-C. Chiag, Y. Chang, W.-Y. Chen, et R. Ruaan, « Biofouling Resistance of Ultrafiltration Membranes Controlled by Surface Self-Assembled Coating with PEGylated Copolymers », *Langmuir*, vol. 28, n° 2, p. 1399-1407, 2012.

[58] A. Venault *et al.*, « Stimuli-Responsive and Hemocompatible Pseudozwitterionic Interfaces », *Langmuir*, vol. 31, n° 9, p. 2861-2869, 2015.

[59] C. Zhang, J. Jin, J. Zhao, W. Jiang, et J. Yin, « Functionalized polypropylene non-woven fabric membrane with bovine serum albumin and its hemocompatibility enhancement », *Colloids and Surfaces B: Biointerfaces*, vol. 102, p. 45-52, 2013.

[60] S. Takeoka, Y. Teramura, Y. Okamura, M. Handa, Y. Ikeda, et E. Tsuchida, « Fibrinogen-Conjugated Albumin Polymers and Their Interaction with Platelets under Flow Conditions », *Biomacromolecules*, vol. 2, n° 4, p. 1192-1197, 2001.

[61] H. N. Antoniades, C. D. SCHERt, et C. D. Stiles, « Purification of human platelet-derived growth factor », *Proc. Natl. Acad. Sci. USA*, p. 5, 1979.

[62] O. Coskun, « Separation techniques: Chromatography », *North Clin Istanb*, vol. 3, n° 2, p. 156-160, 2016.

Chapter II.

Study of blood proteins-polymers interactions in solution

1. Introduction

As stated in the previous chapter, the development and surface modification of biomaterials used for blood purification requires the understanding and the control of interaction between blood proteins and the modifying polymers [1], [2]. Wherefore, this chapter presents an explicit study of the interaction in solution between some abundant proteins in human plasma (HSA and IgG) and some polymers chosen for surface modification later such as poly acrylic acid (PAA) and polyethylene glycol (PEG).

In addition to biomaterials and medical devices, interactions between proteins and polymeric materials are involved in many other processes in several fields [3], [4]. Thus, the study of these interactions could be relevant for versatile application, as protein separation [5], [6], drugs delivery [7], [8], enzyme immobilization [9], among many other applications in chemistry and biology [10].

In this study, tailored membranes are proposed for blood cells screening and the concentration of growth factors as we report in the previous chapter. For that, the architecture of membrane biointerface at the nanoscale will be customized by coating on it some functional groups such as PAA and PEG. PAA is a negatively charged bioactive polyelectrolyte in aqueous medium suggested to promote platelets adhesion, especially when it is conjugated to proteins such as fibrinogen. But it can also be used to prevent platelets adhesion when it is conjugated to albumin [11]. Thus, nonspecific interactions between other blood components and polymers used for interface modification could hamper the capture of platelets. PEG which is an electrically neutral polymer known for its antifouling properties is often used to reduce these nonspecific interactions [12], [13]. Among those blood components able to interfere, HSA is the most abundant plasma protein ([HSA]≈42 $mg.mL^{-1}$ in blood [14]) that maintains the blood pH and osmotic pressure and transports some molecules in the blood. This protein is able to decrease platelet adhesion and activation on a solid surface by being adsorbed onto that particular surface [11]. Therefore, the control of these nonspecific interactions that could take place between the modifying polymer and blood proteins is required.

According to the literature, a number of protein-polyelectrolyte complexes have been studied in a variety of physicochemical conditions via several analytical techniques [15], [16]. Concerning complexes of serum albumin and polymers, the interaction of bovine serum albumin (BSA) with spherical polyelectrolyte brushes in solution was evidenced using Small Angle X-ray and neutron scattering (SAXS and SANS) [17], [18]. Interactions between BSA

and planar synthetized poly(acrylic acid) were also the object of a dedicated work [19]. Furthermore, binding of HSA with small polyelectrolyte brushes of PAA (with 25 repeating units only) [20], and with dendritic polyglycerol sulfate [21], has also been discussed by isothermal calorimetry (ITC). In fact, it has been proved that only one HSA is bound per chain of PAA 1.8 kDa. Then, for a pH maintained at 7.2, a study on the effect of salt concentration revealed that this binding was dominated by an attractive electrostatic potential between the two solutes [20]. Using Total Internal Reflection Fluorescence (TIRF) spectroscopy, it also has been proven that negatively charged BSA is strongly adsorbed on planar PAA (278 AA units ≈20 kDa) at low ionic strength and pH > 5 due to electrostatic interactions [22]. However, the current knowledge does not permit to give the exact stoichiometry of the polyelectrolyte-protein complexes for larger polymer, and if it is correlated to the size of the polyelectrolyte.

In the present study, we used SAXS combined to chromatography to assess the affinity of HSA to bind to a larger PAA (100 kDa) to check out the formation of multiprotein-polymer complexes compared to the 1HSA-1PAA binding reported in the literature using smaller polyelectrolyte [20]. First, as a starting point for further experiment with polymers, the structure of native HSA is examined in phosphate buffer solution. Then, the HSA/PAA interaction is studied in media with different ionic strengths or pH in order to determine the conditions that could lead to an attractive interaction (section 4.3). After that, a detailed study modeling the Porod volume is conducted to determine the stoichiometry of the (nHSA-PAA) complex found to be formed. For this purpose, the influence of the HSA/PAA molar ratio on the complex size (radius of gyration and Porod volume) is appraised (section 4.4). Eventually, a modelling study is conducted to investigate the protein and complex structures. Thus, a compatible model is calculated using BUNCH program [23] to fit the HSA-PAA complex scattering data. It allowed us to propose an all atoms pearl necklace model that can describe the structure of complex (section 4.5.3). Subsequently, this complexation was investigated using different sizes of PAA at the different physicochemical conditions outlined in the preceding sections and the stoichiometry was assessed (section 4.6). After that, these interactions were studied with another blood protein less abundant than HSA but larger, which is human γ-globulin (IgG). In the end, the interaction of both proteins (HSA and IgG) were tested with PEG instead of PAA.

Many results obtained from the studies reported above have been the subject of a scientific article published in Soft Matter [24], and they have also been discussed in different national and international conferences listed in **Appendix D.**

2. Materials and samples preparation

Human serum albumin (HSA, lyophilized powder, ≥96% agarose gel electrophoresis), and human γ-globulin (IgG, ≥99% electrophoresis), with a molecular weight of 66.5 kDa and of around 155 kDa respectively, were purchased from Sigma Aldrich and used as received. The poly acrylic acid (PAA) of molecular weight around 100 kDa (35 wt. % in H_2O), the poly ethylene glycol (PEG) with a molecular weight of 8 kDa (40wt. % in H_2O), and the PEG methyl ether methacrylate of 2 kDa (50wt. % in H_2O) were bought from Sigma Aldrich.

The other sizes of PAA (5, 30 and 50 kDa), and the PEG with a molecular weight of 20 kDa, were purchased from Biovalley.

Protein powder was dissolved in PBS 1X (0.012M phosphate buffer solution at pH 7.4, ionic strength 0.137 M) to obtain a stock solution of 50 $g \cdot L^{-1}$ (750 µM) for HSA and 30 $g \cdot L^{-1}$ (200µM) for IgG, from which samples of lower concentration were prepared. The same way, the polymer solutions were prepared by dilution in PBS 1X buffer from a stock PBS solution of 100 $g \cdot L^{-1}$ PAA (1 mM).

For the investigation of native HSA structure in solution and HSA-PAA interaction, the concentration of HSA was set at 5 $g \cdot L^{-1}$ to avoid repulsion between particles which can distort the measured intensity in small angles. The pH effect was studied using different buffer solutions at 0.1 M (TRIS base pH 8, HEPES pH 7, MES pH 6, mixture of sodium citrate di-hydrate and citric acid at pH 4-5). To study the ionic strength influence, the salts concentration was adjusted by adding the needed amounts of 4 M NaCl solution.

Then, all samples, whether protein free, polymer free or a mixture of both, were stirred using a Thermo Scientific mini centrifuge (mySPIN 12) at 10 000 rpm for 2 minutes at least, to ensure good dissolution of the solutes, before being pipetted into the samples holder for the SAXS measurement. Out of use, the samples were stored at 4°C in a refrigerator.

3. Methods

3.1. Chromatography

The chromatography unit used consisted of an Agilent 1260 infinity system connected to a UV-visible detector set at a wavelength of 280 nm. Analyses were performed using an Agilent Bio Sec-3 (3µm, 4.6x300 mm, 300 Å) size exclusion column at room temperature. In a typical analytical run, 50 µL of the protein solution were injected, and PBS 1X was used as mobile phase for protein structure investigation at a flow rate of 0.4 ml·min^{-1}. The mobile phase was changed depending on the studied parameter (pH, ionic strength …), but also on the composition of the sample. For instance, depending on the desired pH, PBS was replaced by another buffer from those listed in the materials section. For the study of protein-polymer complexation, solutions containing both solutes were injected and the mobile phase was a buffer solution (chosen depending on the desired pH) containing the polymer. These experiments can help to know if the complexation is reversible or if, at opposite, it leads to stable (irreversible) complex (Figure 2. 1). Indeed, if complexes have been formed initially between the protein and the polymer, they would not be then dissociated due to the absence of polymer in the mobile phase. In the latter case, the equilibrium may move in the opposite direction of complexation, which is dissociation as illustrated in Figure 2. 1.

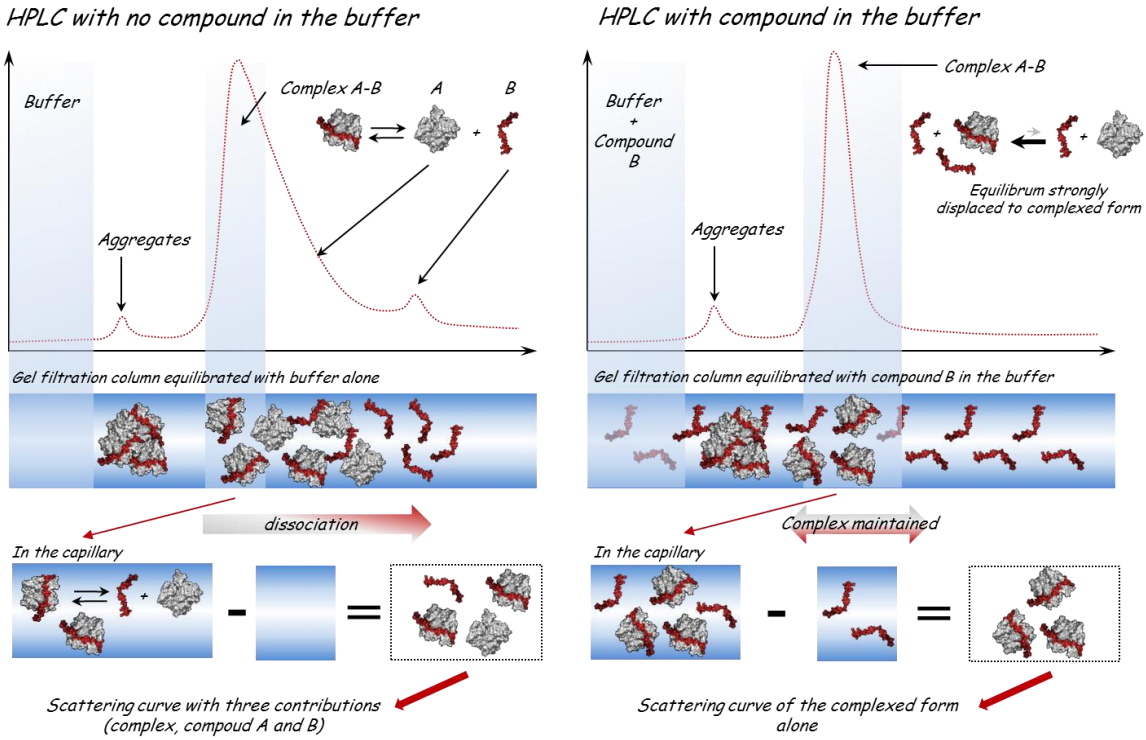

Figure 2. 1. Illustration of the chromatography response according to the stability of complexes and to the composition of the mobile phase. Courtesy of Dr. Pierre Roblin.

The chromatography was also used for the estimation of the molecular mass of complexes that could have been formed. Wherefore, a calibration curve plotting the log of molecular weight versus the retention time was established (Figure 2. 2). For that, some proteins with known molecular weights were used: Ovalbumin (43 kDa), Conalbumin (75 kDa), IgG (150 kDa), Thyroglobulin (660 kDa), Thyroglobulin dimer (1220 kDa).

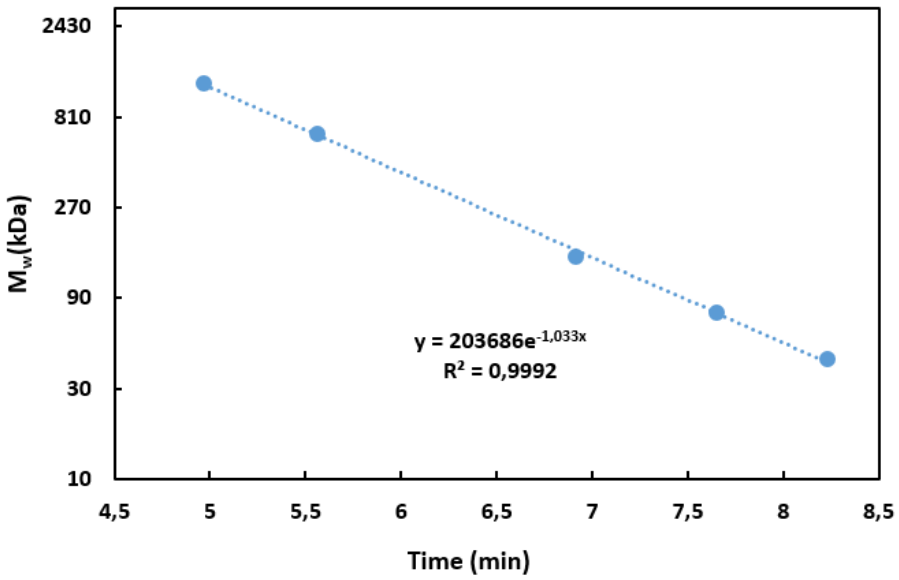

Figure 2. 2. Calibration curve of the molecular weight as a function of the retention time.

Thus, the molecular weight (M_w in kDa) could be expressed as function of the retention time (R_t in min) according to the following equation: $M_w = 203.7 \times 10^3 \times e^{-1,03 \times R_t}$.

3.2. Small angle X-ray scattering (SAXS) measurement

SAXS is a powerful analytical tool for structural analysis, that has become very popular in the biological community with many substantial advancements made over the last few decades, particularly in data collection and analysis [25]. The major advantage of this method is its ability to obtain structural information from macromolecules in solution. It provides detailed structural analysis and physical information by characterizing the sizes and shapes of proteins and complexes in a broad range of molecular sizes from a few kDa to GDa [26]. SAXS also allows to study the behaviour in solution of native particles in conditions close to their physiological environment, and to evaluate the structural variations linked to a modification of the external conditions. Advances in SAXS instrumentation allowed not only to determine a few simple geometric parameters of flexible ensembles, but also to assess their probable configurations in solution [23].

In a SAXS experiment, the sample is exposed to X-rays of a specific wavelength, and the intensity of the scattered X-rays is recorded by a two-dimensional X-ray detector (Figure 2. 3). As the macromolecules are randomly oriented, the resulting scattering intensity folds into a one-dimensional signal varying with the modulus (q in A^{-1}) of the scattering vector calculated as follows [26]:

$$q = \frac{4\pi\ sin(\theta)}{\lambda} \tag{2.1}$$

where λ is the X-rays wavelength, and 2θ denotes the scattering angle.

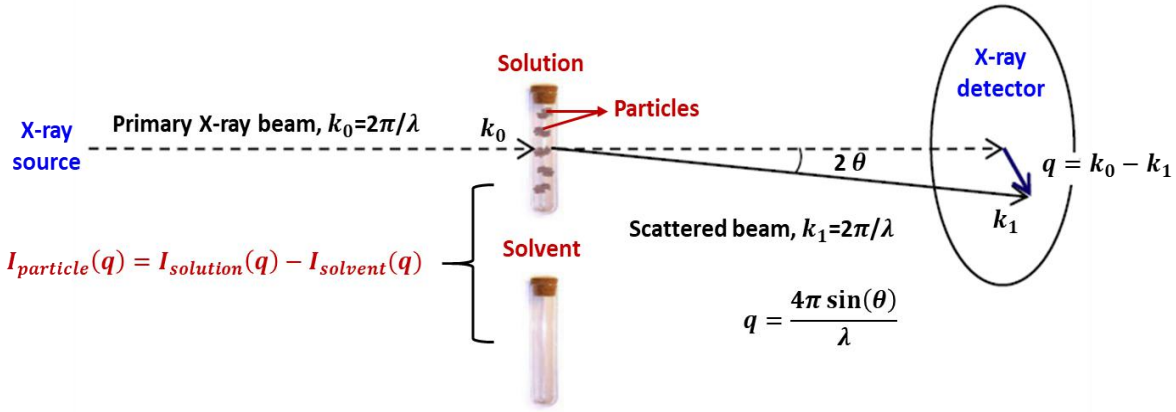

Figure 2. 3. Schematic representation of a SAXS experiment, and illustration of the final scattering intensity calculation by subtracting the solvent contribution from the scattering pattern of the solution. Adopted from [26] and modified.

The scattering pattern of the buffer is carefully collected as well by an independent measurement in the same measuring cell, and subtracted from the sample solution scattering leaving only the signal from the particles of interest. The final curve denoted *I(q)* is the averaged contribution of the structures from all the macromolecules contained in the sample as illustrated in Figure 2. 3. This latter is based on the crystal particles present in the sample, and it is related to the overall shape and size of these particles under investigation. However, it could be altered by various parameters such as contrast (electron density), sample to detector distance, resolution, and beam collimation [27].

The final intensity distribution provides significant information regarding the size, shape, and general structure of the sample. Indeed, several parameters of the investigated sample can be extracted from the experimental scattering pattern including molecular weight, excluded particle volume, maximum dimension D_{max} and the radius of gyration R_g. These parameters directly reflect the overall characteristics of the particles.

In the case of non-ideal (i.e. real) solutions representing the interacting systems, the scattering is proportional to the namely concentration dependent structure factor *S(q)* of the solution that takes into account the interactions between solute particles [28]. The structure factor can readily be obtained from the ratio of the experimental intensity that obtained by extrapolation to infinite dilution were all correlations between particles have vanished [29]. Thus, at infinite dilution *S(q)*=1 and it is thereby advisable to extrapolate scattering patterns collected at several concentrations to zero concentration to obtain an undistorted pattern in the low angle region.

3.2.1. Information provided by SAXS

It is important to mention that a SAXS profile has distinct regions from which the information may be extracted: Guinier, Fourier, and Porod [27]. Figure 2. 4 displays what information could be obtained from a SAXS scattering pattern.

In the Guinier region, the classical and the most known parameter directly extracted from the SAXS data, R_g may be evaluated using the following Guinier approximation:

$$\lim_{q \to 0} I = I_0 \, exp\left(-\frac{1}{3} \, q^2 \, R_g^2\right) \tag{2.2}$$

In principle, the extrapolated forward scattering *I(0)* and R_g can be extracted from the y-axis intercept and the slope of the linear fit of the Guinier plot which is equivalent of a linear variation of *Ln I(q) vs* q^2. The R_g is the average root-mean- square distance to the center of density in the molecule weighted by the scattering length density, and it provides a measure of the overall size of the macromolecule. It is greatly affected by aggregation of particles, polydispersity, and improper subtraction of the background or buffer. As for the determination of *I(0)*, it is particularly interesting because this value allows to calculate the molecular mass. This is based on knowledge of the forward scattering intensities and concentrations of both the macromolecule of interest and a standard such as bovine serum albumin (BSA) [30].

It should be noted that Guinier's law is only valid at small angles and that a deviation from linearity may reflect a non-ideality of the solution (presence of attractive or repulsive interactions). In fact, attractive interactions between particles and nonspecific aggregation result in overestimation of both R_g and *I(0)*, whereas repulsive interactions lead to an underestimation of R_g and *I(0)* [26].

The information deduced from the analysis at small angles remains rather limited (size, molecular mass, interactions...). If one considers the information contained at the larger angles (higher resolution), it is then possible to get more information on the studied system, by measuring the *I(q)* function over a wider range of angles.

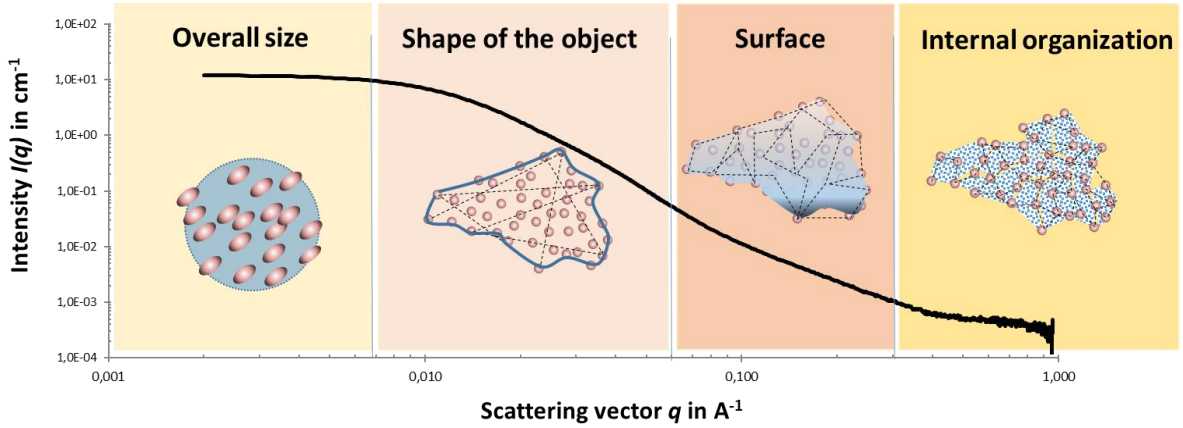

Figure 2. 4 . Information extracted from different regions of the experimental scattering intensity.

In the Fourier region, the pair distribution function *p(r)*, which is a histogram of distances between all possible pairs of atoms within a particle, may be determined by an indirect Fourier transformation of the experimental scattering pattern using the following equation [30]:

$$p(r) = \frac{r^2}{2\pi^2} \int_0^\infty q^2\, I(q)\, \frac{\sin(qr)}{qr}\, dq \qquad (2.3)$$

In some cases, it is more intuitive to interpret the structural properties analyzing the *p(r)* rather than the scattering data itself. The radius of gyration can be calculated from the *p(r)* function which often yields a more reliable estimate compared to the Guinier approximation, in particular for unstructured systems, and that by using the following equation [26]:

$$R_g^2 = \frac{\int_0^{d_{max}} r^2\, p(r)\, d(r)}{2\int_0^{d_{max}} p(r)\, d(r)} \qquad (2.4)$$

This autocorrelation function *p(r)* is a real space representation of the scattering data and allows one to graphically display the peculiarities of the particle shape [29].

Figure 2. 5 presents typical scattering patterns and distance distribution functions of geometrical bodies with the same maximum size. Globular particles (red curve) display bell-shaped *p(r)* functions with a maximum at about $D_{max}/2$. While, flattened particles display a

rather broad maximum (yellow curve), shifted to distances smaller than $D_{max}/2$. As for elongated particles such as long rod, they have skewed distributions with a clear maximum at small distances corresponding to the radius of the cross-section (pink curve). A maximum shifted towards distances larger than $D_{max}/2$ is usually indicative of a hollow particle (purple curve). Whereas, multiple maxima point out the presence of particles consisting of well-separated subunits.

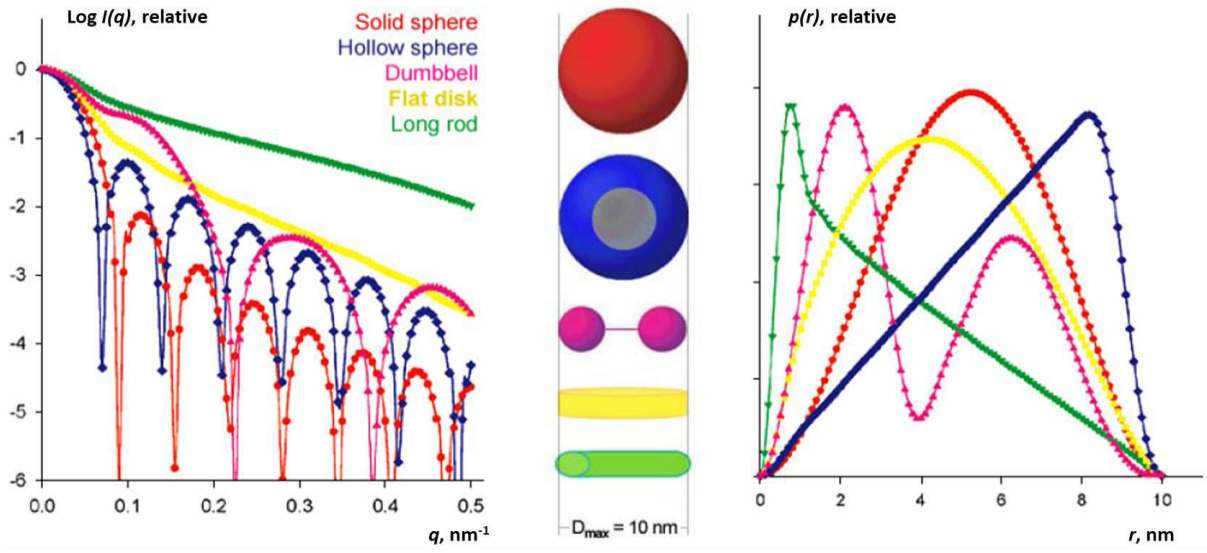

Figure 2. 5. Scattering intensities and distance distribution functions of geometrical bodies. Adopted from Svergun & Koch [29].

All information listed above are obtained at small and medium angles, while at high angle is found the third region of a SAXS profile which is the Porod region, and that provides other information than those extracted from the Guinier and the Fourier regions. For instance, the Porod invariant Q may be determined, providing information on surface, volume and the internal organization of the studied particles. In fact, from the Porod invariant Q it is possible to obtain the Porod volume of an object which is nominally the excluded volume of the macromolecule in solution [31] :

$$V_p = \frac{2\pi^2 I(0)}{Q} * \frac{1-\phi}{S(0)} \qquad (2.5)$$

When the dispersion is diluted the volume fraction $\phi \rightarrow 0$, $S(0) \rightarrow 1$ and the Porod volume can be determined by knowing the zero angle intensity $I(0)$ and Q.

Q is called the Porod invariant because its value does not depend on the structure but on the volume fraction and the contrast between two phases $\Delta\rho$:

$$Q = \int_0^\infty q^2(I(q) - K)dq = 2\pi^2\,\phi\,(1-\phi)\,r_e^2\,(\Delta\rho)^2 \qquad (2.6)$$

Where *K* is a constant defined to ensure the asymptotical intensity decay proportional to q^{-4} at higher angles [32].

The value of *Q* can be roughly obtained from the integration of the Kratky plot (classically with a limited integration boundary at *q*=0.25) by considering *K*=0:

$$Q = \int_0^{0.25} q^2\,I(q)\,dq \qquad (2.7)$$

When the intensity decreases too slowly at large *q* (less than q^{-3}) as for polymeric systems [33], it is well more accurate to integrate the original equation after determining the constant *K*. Whereby the constant *K* is calculated from the Porod asymptote *I(q)*. q^4 versus q^4 at higher angles.

In this Chapter, the asymptote has been always determined for the same range of *q* between 0.3 and 0.445 with a homemade Python code to keep the control of the calculation. The code is given with the plots that show the determination of *K* in **Appendix B**, as well as the corrected dimensionless Kratky plot obtained by subtracting *K* from *I(q)*. An example that illustrates the invariant *Q* calculation and the estimation of the constant *K* is shown in Figure 2. 6. It can be seen that the subtraction of the asymptote *K* leads to a curve that tends to zero for high *q* that then permit a good integration of the invariant *Q* (right-bottom subfigure in Figure 2. 6).

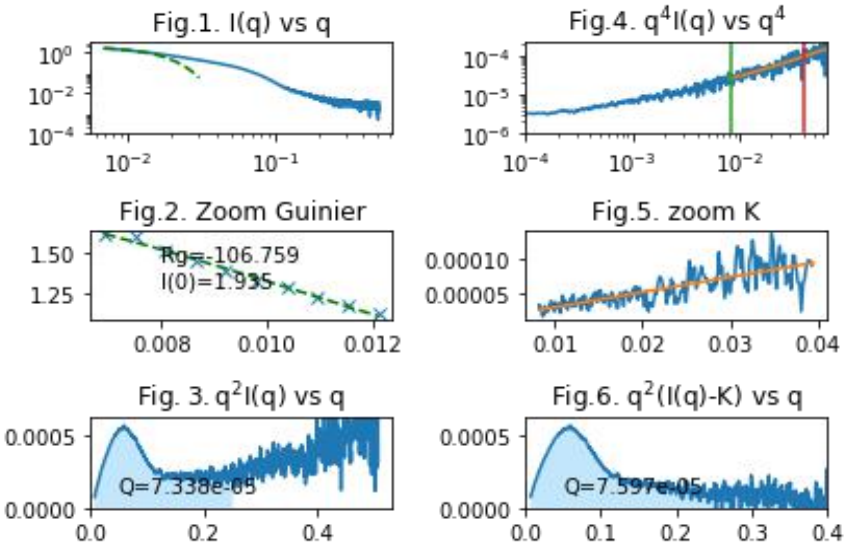

Figure 2. 6. Example of calculation of the Porod invariant *Q* using the constant *K* with the homemade Python code.

3.2.2. Instrumentation and data processing

SAXS measurements were performed at Laboratoire de Genie Chimique, Toulouse, on the XEUSS 2.0 unit[1] (Figure 2. 7.A) provided by the French SAXS manufacturer Xenocs. It is equipped with a copper internal source (Genix3D) that produces an X-ray beam with an energy of 8 keV and a flow of 30.10^6 ph mm^{-2} s^{-1} with a beam sized at 1.5x1.5 mm. The beam size can be changed with a set of low diffusion slits, ranging from 2x2mm (40.10^6 ph mm^{-2} s^{-1}), up to 0.25x0.25mm (5.10^6 ph mm^{-2} s^{-1}). This instrument is managed by **Dr. Pierre Roblin** who helped us with the experiments and the interpretation of the results.

The SAXS bench is equipped with an HPLC online (Agilent 1260 infinity) connected upstream to the SAXS cell allowing to add a purification step by size exclusion chromatography (SEC) as shown Figure 2. 7.B. In fact, the presence of a substantial amount of aggregate readily produces an observable upstroke in very low *q* region. This results in an increase of the measured radius of gyration and extrapolated *I(0)*, that may go unnoticed but necessarily leads to a wrong interpretation in terms of structures. Therefore, a fine SAXS sampling of the HPLC elution peak provides an independent warranty that the resulting experimental data arise from a freshly produced monodispersed sample.

In direct injection mode, that is, without size exclusion chromatography step, 50 µL of sample are pipetted from the samples holder maintained at a constant temperature (20 °C) using a circulating water bath, and are injected to the measurement cell placed under vacuum to limit air absorption. Data were collected on a 150x150 mm area DECTRIS detector (Pilatus 1M) with a sample to detector distance of 1216 mm. The detector is highly sensitive, making it ideal for detecting low scattering samples, and can be shifted along the beam, which increases the angular range of measurement (objects with dimensions between 0.5 and 15nm).

The experimental scattering intensity *I(q)* is expressed as a function of the scattering vector *q* ($Å^{-1}$). Each scattering curve reported in this manuscript is an average of at least 6 measurements on the same sample, and each SAXS measure corresponds to a data collection time of 1800s. Scattering curves were recorded within the range $0.005 < q < 0.5$ $Å^{-1}$. Finally, actual solutes scattering intensity *I(q)* was obtained by subtracting the buffer solution contribution from the total SAXS signal.

[1] An instrument funded by the FERMAT federation (https://www.federation-fermat.fr/) and operated on a shared time basis.

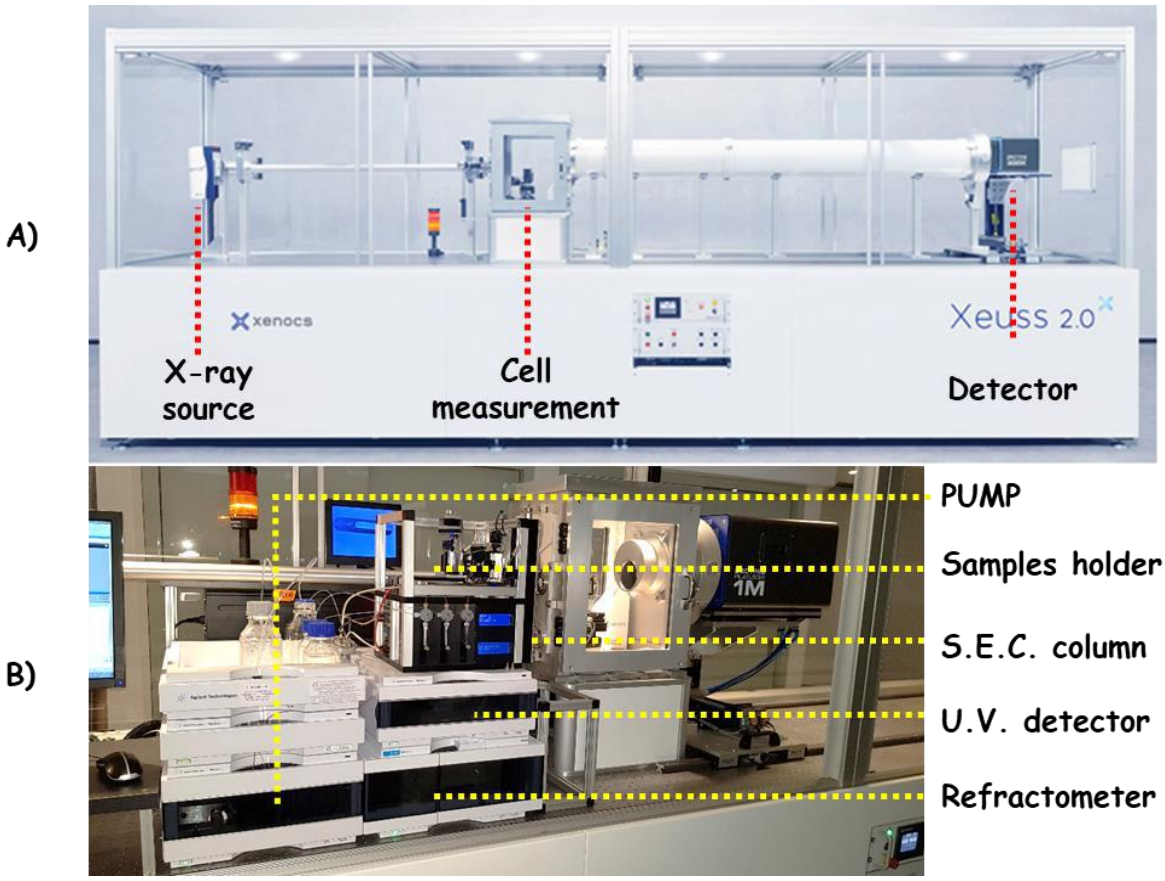

Figure 2. 7. Illustration of A/ the XEUSS 2.0 SAXS bench of Laboratoire de Genie Chimique, Toulouse, and B/ the chromatographic equipment connected upstream to the SAXS cell.

For a given protein, several concentration ranges must be tested. Low concentrations limit the aggregation phenomena observed at small angles, but the signal is very noisy at high angles. The information at high angles can be improved by increasing the concentration of the sample, thus favoring the aggregation phenomena and the loss of information at small angles [30]. It is possible then to group all the high and low concentration data on the same diffusion curve in order to limit the problems of background and aggregation. To do this, the curves must have sufficient overlap, as this type of data manipulation can introduce a significant bias that will affect the envelope and structure calculations.

3.2.3. SAXS-SEC combination

It has been reported in the literature that combining SAXS to the size exclusion chromatography (SEC) could be a very promising and interesting technique to optimize data acquisition [25]. Thus, it allows to improve the information that could be extracted from the scattering pattern.

In fact, data obtained from the SAXS measurement of the elution peaks are combined to those obtained from direct measurement on the same samples without going through chromatography before. In fact, chromatography allows to eliminate aggregates since acquisitions are done on the elution peaks representing the main fraction of the studied particles only. Meanwhile, a direct injection mode permits to improve information at high angles by minimizing the noise at this *q*-range. Thus, scattering data at small angles obtained from acquisitions on the elution peaks are merged with those at high angles obtained from direct injection mode provided that the two curves overlap sufficiently. Figure 2. 8 illustrates a merge performed on experimental SAXS scattering data of HSA obtained through chromatography and in direct injection mode.

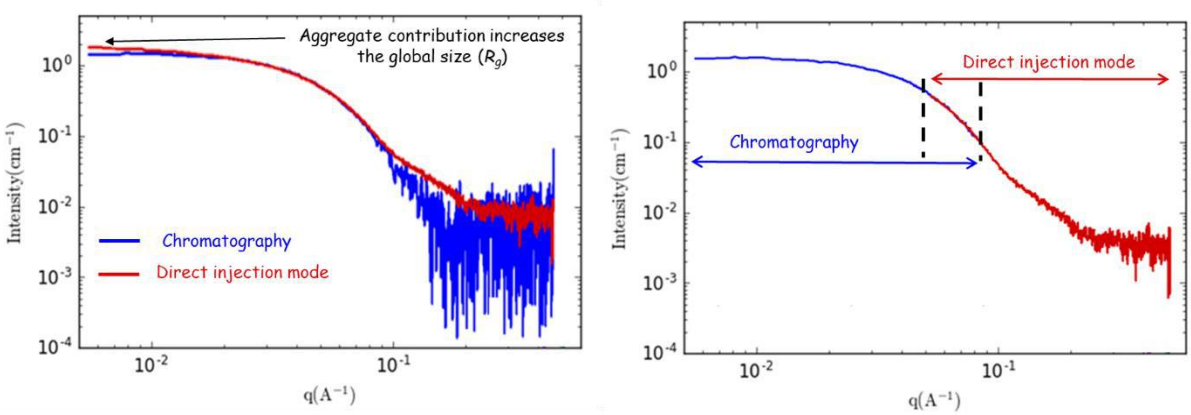

Figure 2. 8. Illustration of the merge of experimental scattering data of HSA.

All data processing operations concerning buffer subtraction, averaging of diffusion curves and other processing (scaling, subtraction or division by constants) are done using Foxtrot software [34], or the graphical interface Primus [31]. Once the data have been processed, it is possible to calculate the *p(r)* with the program GNOM [35].

3.2.4. Computation of scattering from molecular model

Calculation of scattering curves from atomic models, and the comparison of these predicted curves with the experimentally determined SAXS profiles is a method for rapid characterization of proteins and complexes if high-resolution structures or homology models are known. In fact, the availability of a fast, robust and easy-to-use software to compute scattering patterns from atomic coordinates revolutionized the field by providing the link between SAXS data and atomic scale molecular structures [30]. Given a model, the theoretical scattering curve can be computed and fitted to the measured data, and the model that provides a good fit to the data is

considered a valid description of the structure under the solution conditions used for the measurement.

From a molecular model and its atomic coordinates, the CRYSOL code [36] calculates the radius of gyration and an X-ray scattering curve either in vacuum or in a contrasting solvent. From the atomic coordinates, CRYSOL generates an electron density map, which, by Fourier transform, will allow to calculate the scattered intensity. The theoretical scattering curve is obtained by spherical averaging of the intensities.

The experimental scattering curves are obtained by subtracting the scattering of the solvent from that of the solution containing the molecule as illustrated in Figure 2. 9 . However, solvated molecules are characterized by a boundary where the scattering density differs from that of disordered solvent [28]. Therefore, to calculate the diffusion curve from a structure, two additional contributions to the diffusion must be taken into account. The first one is linked to the volume excluded by the particle, and that by considering this volume filled with solvent with a constant diffusion density. The second contribution is related to the hydration layer, i.e. a layer of solvent molecules interacting with the surface of the molecule immobilized on its surface. In this very particular layer the diffusion density is considered constant but with a different value.

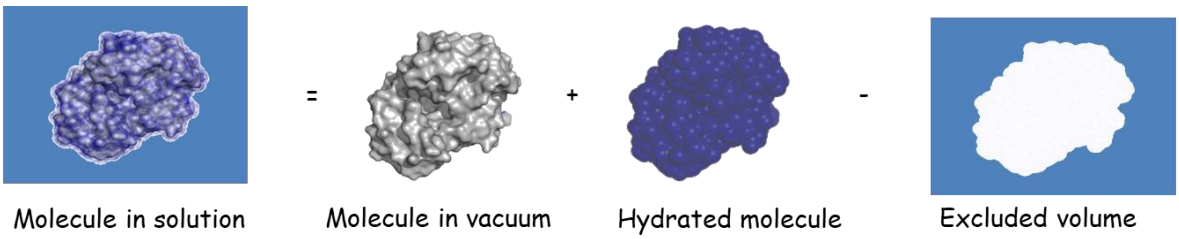

Figure 2. 9. Illustration of the different contributions taken into account in the calculation of the theoretical scattering intensity with GRYSOL program.

CRYSOL employs a Gaussian sphere approximation for the calculation of the excluded volume and uses spherical harmonics to calculate an envelope at the surface of the atomic model to approximate the hydration layer.

3.2.5. Modelling in simple geometrical bodies using Sasview

According to the form of the experimentally determined SAXS pattern, it is sometimes possible to find simple geometrical bodies that can describe the investigated macromolecules. In fact, the theoretical scattering intensities of many known geometrical bodies have been

already defined (Figure 2. 10). These constitute then models to which data obtained for particles with unknown geometry can be compared. Thus, a wide variety of models have been implemented in various software packages that allow to fit the experimental data to existing theoretical models. The diversity of the available models, and the possibility that multiple models having very different physical bases can fit the data equally well, can make the process of data analysis challenging.

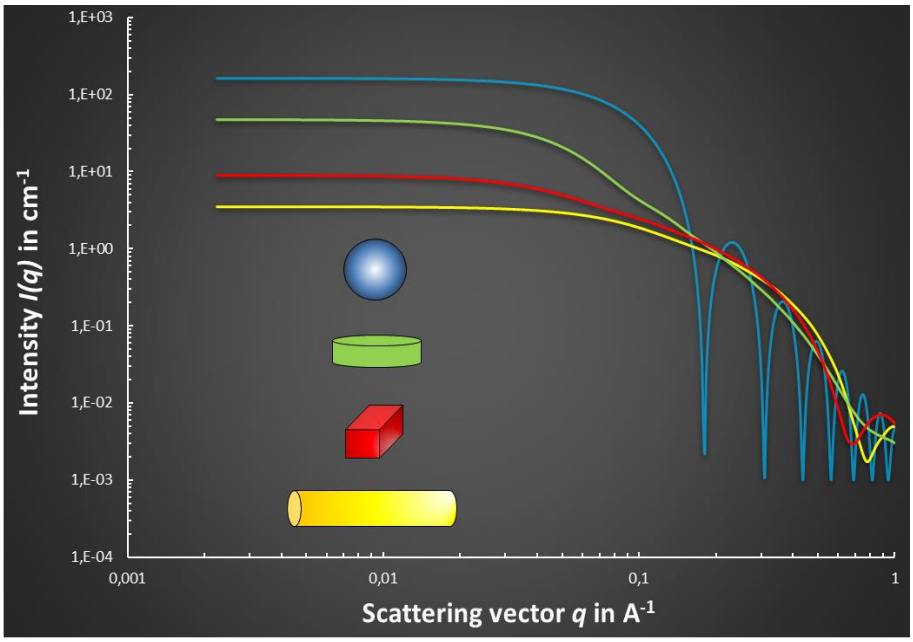

Figure 2. 10. The theoretical SAXS scattering patterns of some simple geometrical bodies. Courtesy of Dr. Pierre Roblin.

Sasview is a free software [37] among those that can perform the fitting process of the SAXS data to a suitable model, which can provide information about the structures present in a sample. It also allows to keep control on the parameters of the used model. In fact, this is done by selecting every time a viable model with which to fit the data and then attempt to get a good fit. If a good fit can't be achieved, another model is selected and attempted to be fitted to. If this fails, the same models can be attempted but the polydispersity of different parameters can be varied. It is important to undertake this time-consuming and thorough approach to ensure the data is fitted as well as possible.

However, to get a good fit in Sasview data should be attempted to be fitted to as few parameters as possible. Using more complex models with fewer parameters runs the risk of over-fitting the data, in which the obtained values lose meaning. Besides, just because a data

set has been fitted to a structural model it doesn't necessarily mean the structure is exactly the dimensions that your fit suggests.

In addition, with Sasview a data set may be sufficiently fitted to two or more different models. In this instance, either both are presented or there may be reason to suggest one is favoured over the other (such as a slightly lower fitting error).

3.2.6. Rigid body modeling from SAXS profile

While *I(q)* can be recreated rapidly from the structural models of the macromolecules or complexes present in the sample, the reverse problem consisting on deducing the possible structure(s) from a scattering profile is harder to do. In fact, it is possible to infer a possible structure for a macromolecule and for the assembly of macromolecular complexes through direct refinement against the scattering data. However, this is possible only with strong external constraints which vary according to the amount of available structural information [30].

In approaches where a shape for the macromolecule is tentatively extracted from the experimental curve and usually represented by bead models [38], very general constraints of connectivity or looseness are used. As for the macromolecular complexes, they are difficult to study because of their large size, internal flexibility and transient nature. However, a large number of individual components structures have been produced [25], so the challenge is to rebuild the macromolecular complexes that these different subunits form. A number of approaches have been developed using SAXS to determine the positions and orientations of subunits within macromolecular complexes [23], [39]. In the rigid-body fitting approach, the integrity of the domains with known atomic structures is maintained, while their position and orientation is varied. Indeed, starting from an arbitrary positioning of subunits, random rigid body movements and rotations (Figure 2. 11.A) are conducted to search for a best fit of the computed complex scattering to the experimental data. The sequence and specific connectivity of the missing residues constitute the additional constraints [25]. In addition, the use of symmetry, inter-residue contacts and inter-subunit distances are fully supported [30].

The automated program BUNCH [40] is among the tools that allow to conduct rigid body modeling. It uses dummy residues to model missing regions in both protein complexes and multi-domain proteins connected by flexible linkers (Figure 2. 11.B). Besides a simulated annealing (SA) minimization process is used to locate a best fitting arrangement of the rigid bodies and also the optimal local conformation of dummy residues. The SA process consist on

decreasing the energy of the system by searching for the most suitable conformation but occasionally allows an increase in energy to explore a larger conformational space.

Initially the missing parts are materialized as chains structured in 'zig-zag' linking the domains together. Then, the domains are moved relative to each other with minimal modifications at the hinge regions, and as the domains stabilize in certain orientations, the loops are progressively rearranged to best mimic the experimental data. BUNCH can also handle multiple diffusion curves corresponding to partial structures of the protein simultaneously.

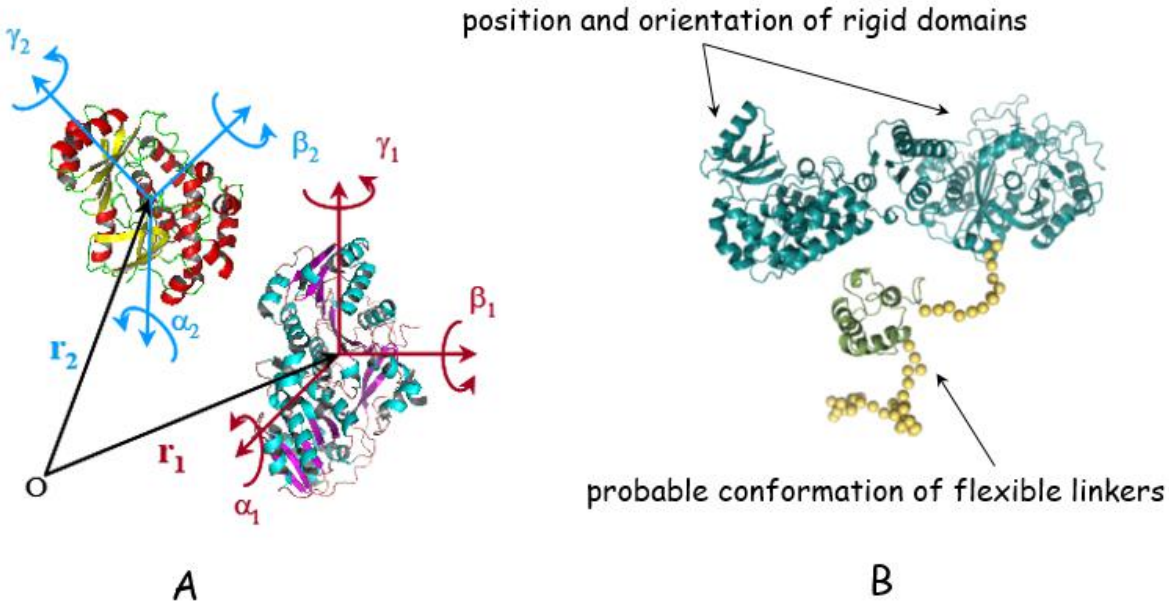

Figure 2. 11. Principle of rigid body modelling showing A/ translational movement along r axis and rotational movement along 3 axes α, β and γ that can undergo the subunits and B/ how rigid domains can be connected with flexible linkers [41].

4. Results and discussion

4.1. Study of single HSA

The structure of native HSA was first examined in a 0.012 M phosphate buffer solution at pH 7.4, and the obtained SAXS scattering intensities were compared to those calculated from the crystal data of HSA on the Protein Data Bank (6EZQ). The *I(q)* corresponding to the crystal structure of HSA was calculated using CRYSOL as explained in the methods sections. In order to guarantee the absence of aggregates in the investigated samples, an Agilent chromatographic system is coupled upstream of the SAXS.

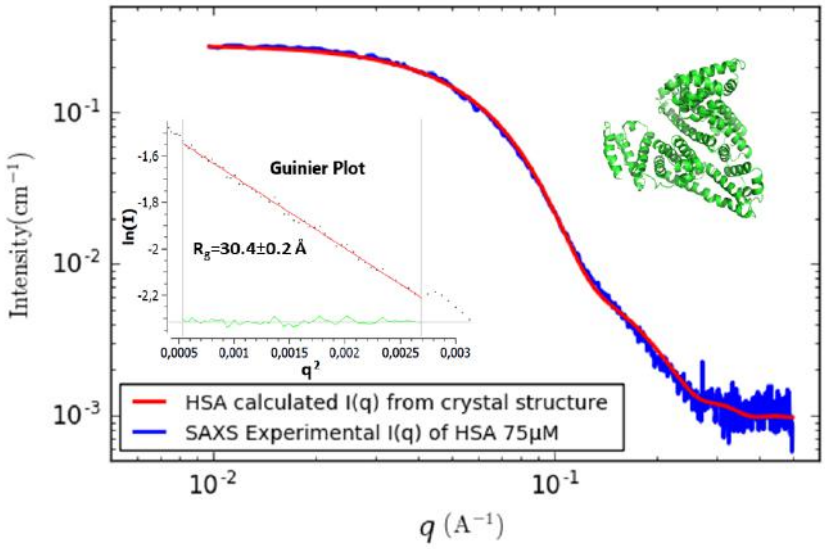

Figure 2. 12. Experimental SAXS scattering intensity *I(q)* of HSA 75 µM (blue line) compared to the SAXS intensity calculated with CRYSOL from HSA crystal structure 6EZQ (red curve). The inset represents the Guinier plot (*Ln I(q) vs* q^2 in red line) with the residual (green curve) that allow to determine the radius gyration using Primus. The HSA 3D structure shown in cartoon representation using PyMOL software.

Figure 2. 12 shows that the experimental SAXS spectrum from purified commercial HSA (blue line) matches very well the calculated intensity from the crystal structure (red line), evidencing that the HSA used for this study is correctly folded at 75 µM in the PBS buffer condition. These preliminary results validate the use of HSA as a template to study protein polymer interaction. In these conditions we can expect that the SAXS will be sensitive enough to sense an interaction between HSA and PAA. The HSA radius of gyration R_g was then evaluated by fits using Foxtrot or Primus. Both software consider the Guinier approximation based on equation 2.2. It allows to determine R_g from the slope of the linear fit at low *q* of *I(q)*

vs q^2 (Figure 2. 12), as it gives the forward scattering intensity *I(0)* from the intercept. The result yields approximately 30 Å (30.4 ± 0.2 Å), which is almost what was found with R_g (30.2 ± 0.4 Å) in a SAXS study for HSA with the same purity >96% [14].

Likewise, the Porod volume and molecular weight were estimated using Primus that consider the Porod law based on the calculation of the Porod invariant *Q* as explained in the methods section. Thus, V_p and M_w were found to be around 100,000 Å ^{3} and 64.5 kDa respectively. These results seem to be consistent with the molecular weight of HSA (66.5 kDa), which validates the use of Primus to evaluate such parameters in further experiments.

It is also important to point out that if the HSA molecule is assimilated to a sphere with the radius being R_g obtained previously, we obtain a volume around 115,000 Å ^{3} which is close to of the HSA Porod volume estimated above using Primus.

4.2. Study of HSA-PAA interaction

4.2.1. Variation of PAA concentration

The characterization of single protein was then followed by assessing the interactions between HSA and the polyelectrolyte chains using direct SAXS measurement. For that, we first studied the effect of an increase in PAA concentration on the SAXS scattering intensity for an HSA/PAA molar ratio ranging from 0 (protein alone as a reference) to a molar ratio of 3/2.

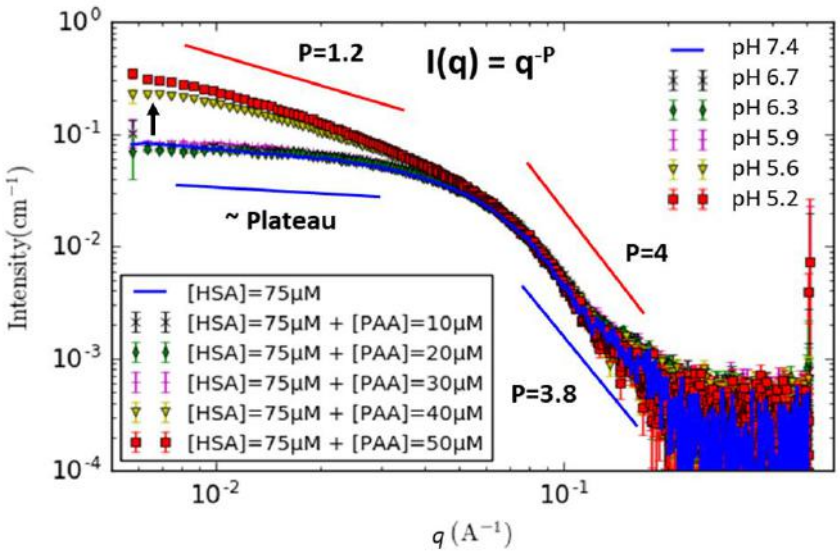

Figure 2. 13. Scattering intensities of HSA-PAA mixture and pH evolution for [HSA]=75 µM as a function of PAA concentration ([PAA]=0 to 50 µM). Evolution of the slope of the power law $I(q) = q^{-P}$ corresponding to small and intermediate angles.

As shown in Figure 2. 13, starting from 40 µM of PAA with 75 µM HSA, a strong change in the signal at small angles is observed, which could be due to the formation of an HSA-PAA complex. While in the intermediate and high *q*-range the SAXS curves remain almost unchanged by the complexation. Indeed, the evolution of the slope *P* of the corresponding power law $I(q) = q^{-P}$ shows that at intermediate angles (0.1 to 0.2 $Å^{-1}$), *P* slightly varies from 3.8 for single HSA and the mixture of HSA+10, 20 and 30 µM of PAA, to 4 when increasing the PAA concentration to 40 and 50 µM (Figure 2. 13). These results indicate a same type of surface despite the big change in the general shape shown by an increase in the slope at small angles (0.005 to 0.05 $Å^{-1}$). In fact, the difference is more obvious, where the slope is going from almost a plateau (*P*=0.3) for single HSA, to a slope of 1.2 when adding 50 µM PAA, which corresponds to the slope of an elongated object [28].

Figure 2. 13 also reveals that despite being in PBS buffer, PAA strongly influences the pH of the solution. Thus, we can suppose that the change in the SAXS curve could be correlated to a pH variation rather than to an effect of the concentration of PAA (explicitly discussed later in this chapter).

In order to confirm that the change in the SAXS signal at small angles is due to the formation of a new object being an HSA-PAA complex, we compared the SAXS curves from the HSA alone at 75 µM (blue line), the PAA alone at 60 µM (green line), the mixture of both kipping the same initial concentrations (yellow line) and the sum (red line) of the SAXS signals of HSA at 75 µM and PAA at 60 µM (Figure 2. 14.A).

For the first three curves, the data were processed with GNOM to determine biophysical parameters such as the radius of gyration R_g, the maximal distance D_{max} using the autocorrelation function *p(r)*. This function was calculated by an indirect Fourier transformation applied to the scattering intensity *I(q)* using the equation (2.3). The pair distribution function refers to the distribution of electrons averaged over a radius *r*. Thus, as stated in the materials section, it entirely depends on the shape and the size of the particle and vanishes at their maximum electron pair distance (D_{max}). The radius of gyration was then derived from *p(r)* using the equation (2.4).

This alternative estimate of R_g makes use of the whole scattering curve, and is much less sensitive to interactions or to the presence of a small fraction of oligomers. The results of the radius of gyration (29.7 Å for HSA and 110.3 Å for the complex) extracted from the *p(r)* were almost the same compared to those obtained by fits from the Guinier plot (30.4 Å for HSA and

108.9 Å for the complex). The Porod volumes (V_p) for the HSA and the complex were also evaluated. For a flexible system such as polymer chains in solution it is difficult to evaluate the exact V_p. All parameters are reported in the table attached to Figure 2. 14.A. Although the curves are calibrated in cm^{-1}, it is impossible to directly determine the mass concentration of the hetero-complex from the *I(0)* because we do neither know the association stoichiometry nor precisely the experimental specific volume and contrast of the PAA.

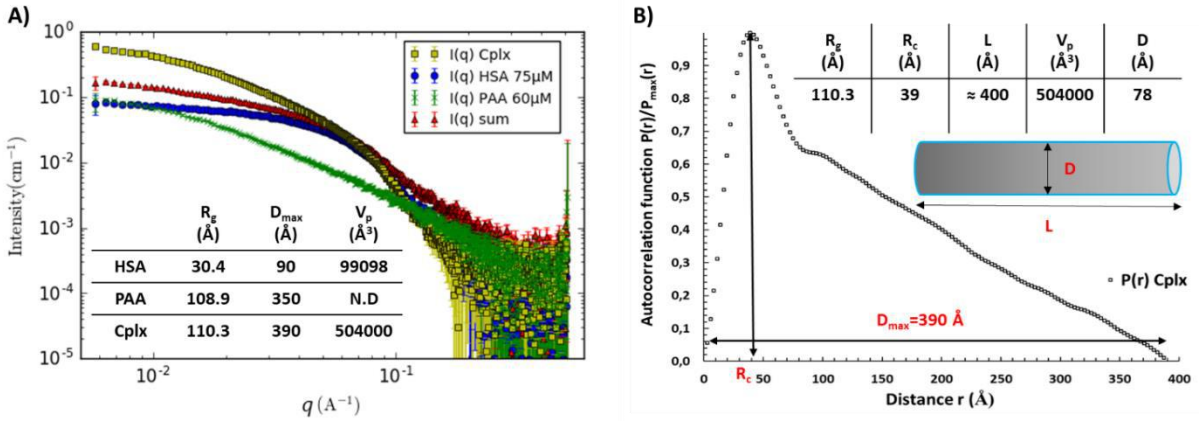

Figure 2. 14. A) Scattering intensities of [HSA]=75 µM (blue curve), [PAA]= 60 µM (green curve), the mixture of HSA and PAA at same concentrations (yellow curve) and the sum of both contributions without interaction (red curve). Table summarizing the radius of gyration, the maximal distance and the Porod volume of HSA, PAA and the complex. B) Autocorrelation function determined with GNOM of the complex and table summarizing the biophysical parameters extracted from the complexes' SAXS data.

As observed in Figure 2. 14.A, the SAXS curve of HSA is consistent with a 3D object with a large plateau at small angles and a typical decrease at intermediate angles, whereas PAA exhibits a behavior of a flexible polymer in solution (large decrease following a power law $I(q) = q^{-P}$ with P close to 1.7 which corresponds to polymers with local rigidity) [42]. The SAXS curve obtained for the complex presents a combination of properties of HSA and PAA. It shows a constant decrease at small angles and the same signal of HSA starting from 0.05 $Å^{-1}$. The direct comparison with a linear combination of HSA and PAA SAXS curves (sum curve in Figure 2. 14.A) in the same conditions of concentration reflecting the case without interactions between both partners, discloses clearly that the SAXS curve observed corresponds to the creation a new object resulting from interactions between HSA and PAA.

The evaluation of R_g and V_p shows that the complex is five times larger than HSA alone but the difficulty to evaluate correctly the Porod volume of PAA (in the complex) or its contribution in the measured *I(0)* does not allow to give directly the numbers of HSA and PAA forming the complex. The form of the autocorrelation function (Figure 2. 14.B) corresponding to the complex shows a skewed distribution with a clear maximum at small distances corresponding to the radius of the cross-section R_c (R_c=39 Å from *p(r)* Figure 2. 14.B). This distribution is typical of elongated objects such as cylinders, rather than corresponding to amorphous aggregates [29]. With these considerations, the length *L* of this cylinder can be calculated using the following relationship $L=(12\ R_g^2 \cdot R_c^2)^{0.5}$. The diameter of the cylinder and the calculated length *L* and all evaluated parameters are summarized in the table attached to Figure 2. 14.B. The value of the calculated length (404 Å) is consistent with the maximal distance (390 Å) determined with *p(r)* calculation. One can assume that the complex of HSA-$PAA_{100\ kDa}$ exhibits a behaviour in solution equivalent to the one of a solid cylinder measuring around 400 Å in length and 78 Å in diameter.

To validate this hypothesis predicting a formation of a defined object instead of amorphous aggregates, solutions of HSA-PAA were flowed in various mobile phases through a size exclusion chromatography column. The chromatographic profiles were then compared to that of the single HSA detected mainly at 7.74 min and as classically with a small amount of dimers at 6.9 min (Figure 2. 15).

In fact, in a PBS mobile phase (without PAA) at pH 7.4, a peak at 7.7 min of retention time was obtained, corresponding to the molecular weight of HSA alone. This experiment shows that the complex can be dissociated in a medium not containing PAA, illustrating the reversibility of the complex formation. On the other hand, if 50 µM of PAA is added to the mobile phase, the pH decreases to 5.2 and the elution profile is modified with a strong shift of the elution peak towards high molecular weights (Figure 2. 15). This observation proves that the protein is no longer single in the solution but bound to the PAA chains. The Gaussian shape of the peak eluted at 5.8 min corresponds to a profile of unique object in solution and not to a continuous distribution of mass such as in aggregates.

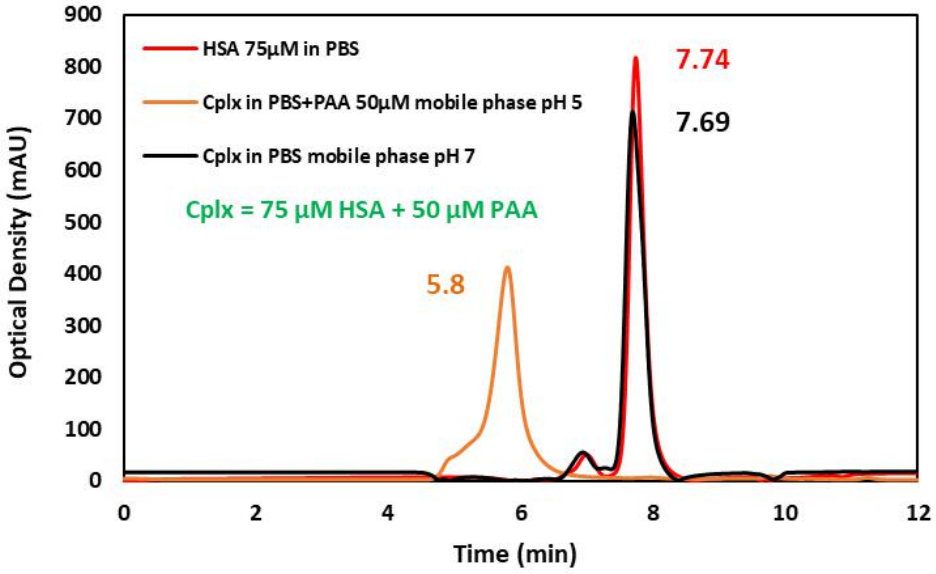

Figure 2. 15. Comparison of chromatographic patterns for HSA 75 µM in PBS 1X mobile phase (red peak), for (75 µM-50 µM) HSA-PAA mixture in PBS 1X (black line) at pH 7, and in 50 µM PAA solution mobile phase at pH 5 (orange peak).

These experiments were run at PBS ionic strength (0.137 M) and at pH controlled by the PAA concentration, ranging from 5.2 to 7.4 as mentioned above (Figure 2. 13). Since the pH remains higher than the HSA isoelectric point (4.7) and knowing that PAA exhibits a pKa of 4.5, we expect repulsive forces that keep them away from each other. It is because they both theoretically bear negative charges. Yet, the adsorption of HSA molecules on PAA chains is found to happen. Attractive interactions between a polyelectrolyte and a protein having the same net charge were reported by several authors [16], [43]–[45]. Since the proteins can carry both positive and negative charges, this binding found to occur in our study could be due to the attractive electrostatic potential between the positive charged patches on the surface of HSA and the negatively charged chains of PAA, which should be the operative force that overcome the repulsion forces. A detailed ITC study performed on the binding between HSA with negative overall charge and a negatively charged PAA [20], shows the same behaviour between the two solutes, where each HSA molecule has found to bind to one PAA chain causing an increase in the system entropy. It has been explained by the action of the HSA surface positive charges as a multivalent counter ion for the polyelectrolyte as illustrated in Figure 2. 16.

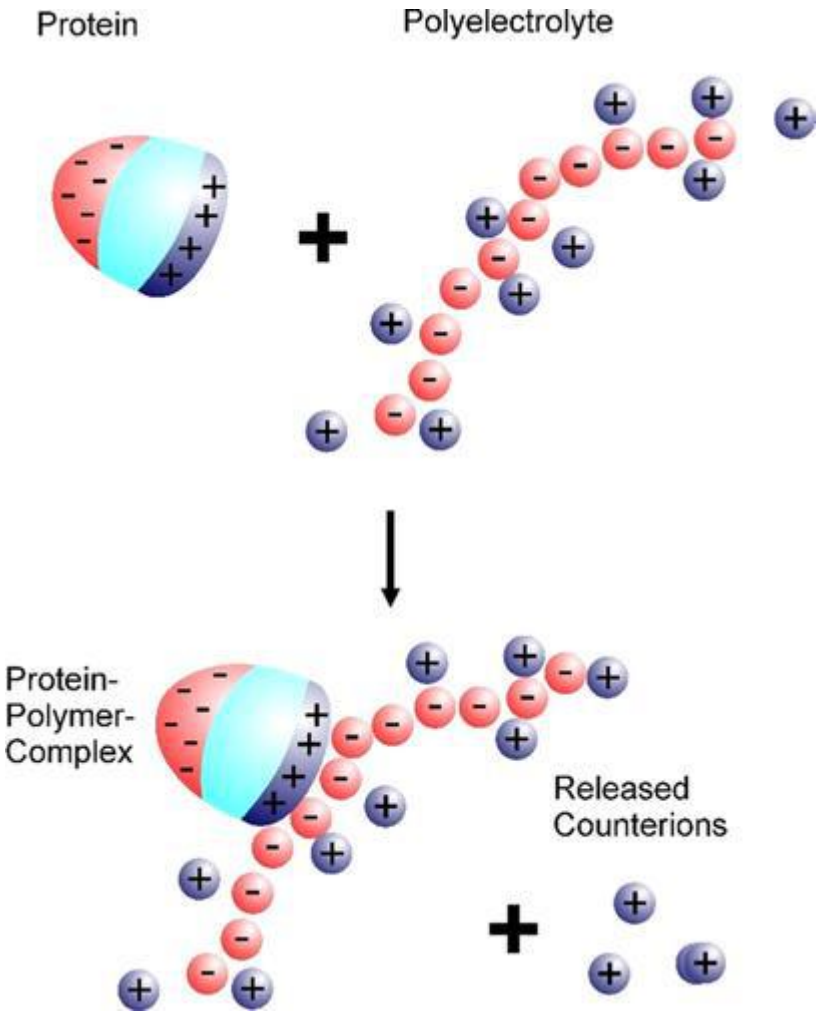

Figure 2. 16. Illustration of the protein-polyelectrolyte electrostatic interaction driven by the counterion release [46].

Other works doing experiments and dynamics computer simulations have addressed more deeply such phenomenon between proteins and polyelectrolytes [47]–[49]. They showed a large binding affinity between charged patchy proteins and like-charged polyelectrolyte brushes despite having the same net charge. It has been shown that the strongest attraction of typical proteins at the brush surface is driven by multipolarity, Born energy (self-energy), and counterion-release contributions, which dominate locally over the monopolar and steric repulsions.

4.2.2. Variation of HSA concentration

In order to check if the concentration of protein also plays a key role in the HSA-PAA interactions, it was varied from 75 to 600 µM for a polymer concentration ranging from 10 to 50 µM.

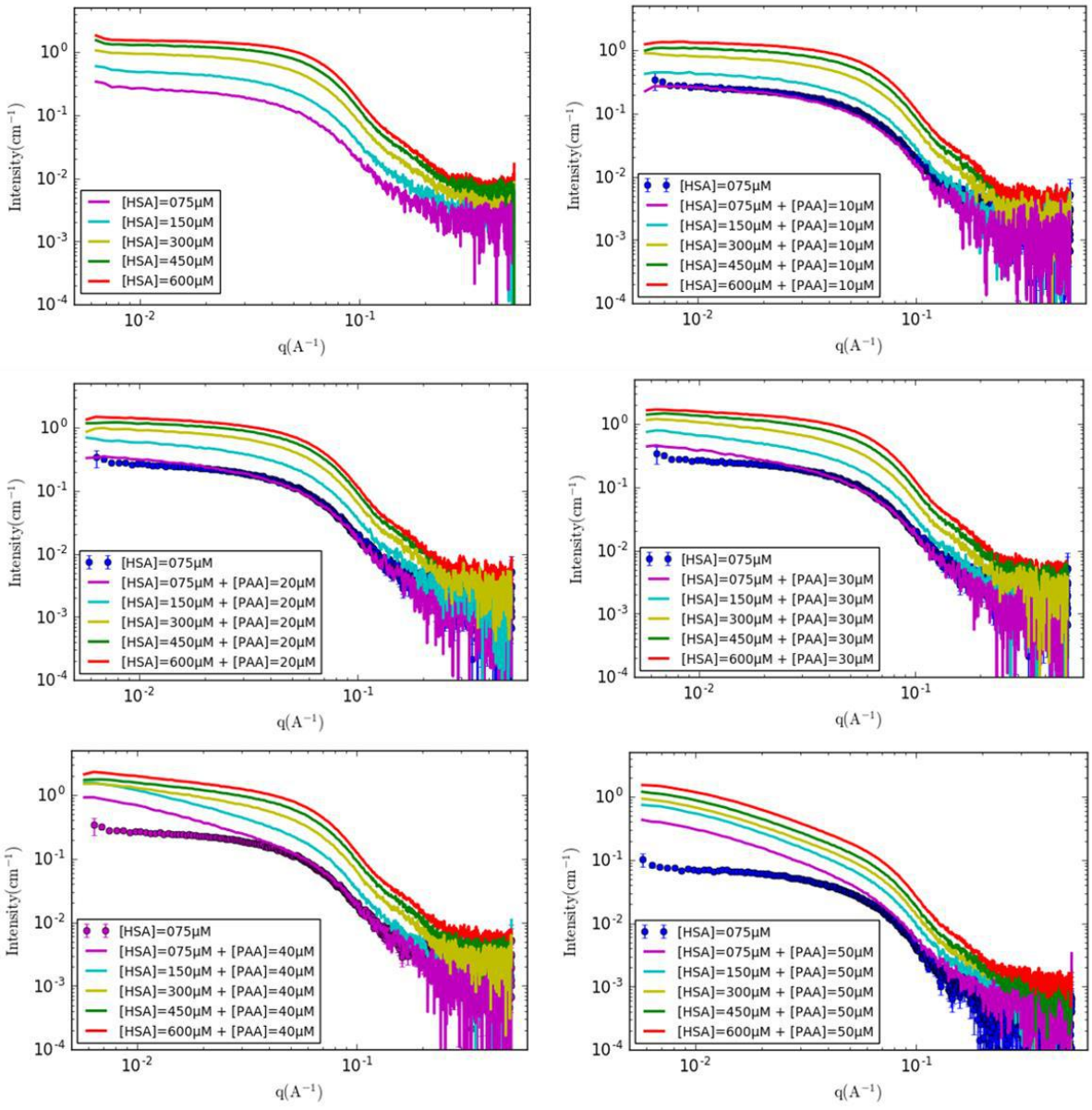

Figure 2. 17. SAXS scattering intensities *I(q)* of the HSA-PAA mixture as a function of HSA and PAA concentrations ([HSA]=75-600 µM and [PAA]=10-50 µM).

Results exposed in Figure 2. 17 have revealed that HSA amount does not play a substantial role in the HSA-PAA complexation as it did the PAA concentration. In fact, the HSA concentration increase has spawned only curves translation among y axis without changing the

slope. This translation is necessarily due to the increase of the protein amount, which could be observed in Figure 2. 17 when single HSA concentration was increased (without PAA).

The SAXS scattering data (Figure 2. 17) corroborate also the fact that when increasing the amount of added polymer to HSA solution, the measured intensity starts to raise suddenly at small angles from a PAA concentration of 40 µM. Indeed, it can be noticed that from 10 to 30 µM of PAA and for 75 µM of HSA, the curves almost overlap with the one representing single protein. Then, SAXS pattern are translated when protein concentration increases without any change in the form factor. That confirms what has been noticed previously, the complexation phenomenon takes place only from a certain critical polymer concentration happened to be around 40 µM of PAA.

In order to support these observations, the scattering profiles were drawn as diagram representing the radius of gyration evolution as function of both HSA and PAA concentrations (Figure 2. 18). R_g values were obtained by fits of the scattering intensities at small angles using Foxtrot software, and they are quoted in Table 2. 1.

Table 2. 1. R_g values (in Å) as a function of both HSA and PAA concentrations obtained by fits of the scattering intensities at small angles using Foxtrot software ([HSA]=0-600µM and [PAA]=0-50µM).

[PAA] µM / **[HSA] µM**	**0**	**10**	**20**	**30**	**40**	**50**
0	0	116	114.3	105.4	103.2	106.1
75	30.4	35.7	41.4	44.3	102.8	101.7
150	29.6	34.6	37	40.8	101.6	102.3
300	28.8	31.4	32.6	37.6	79.7	100
450	27.9	30	29.5	34.1	84	96.4
600	25.2	27.2	30	30.2	77.5	90.2

For a free polymer solution, R_g has found to decrease with the increase of PAA concentration as it can be noticed in Table 2. 1. This could be arising out the compaction of the flexible chains of polymer due to electrostatic repulsion of the PAA chains having the same charge.

The same was observed for single proteins, where greater R_g was obtained for smaller HSA concentrations. In fact, at high HSA concentration, molecules are closer to each other leading to intermolecular interactions and electrostatic repulsions. That distorts the *I(q)* at small angles and so the structure factor which results in a decrease in the radius of gyration.

Then, for each polymer concentration from 10 to 30 µM, R_g decreases when the protein concentration increases from 75 to 600 µM until reaching a value around 30 Å, which is almost the size of single HSA in solution. This finding is reflected by the diagram in Figure 2. 18.

The same way, if we look at this for a fixed protein concentration this time and an increasing polymer concentration from 10 to 30 µM, we notice an increase of R_g remains more or less significant at greater HSA concentration. Indeed, for 75 µM of HSA and going from 2 to 30 µM of PAA, the radius of gyration passes from 30.4 to 44.3 Å, while for 600 µM of HSA, the R_g still around 30 Å, because the protein molar concentration is at least 20 times greater than that of the polymer. Since the radius of gyration obtained here by fitting is an average of the R_g of HSA that yields 30 Å, and the one of PAA that happened to be around 110 Å, it makes sense that the average will be proportional to the amount of each solute.

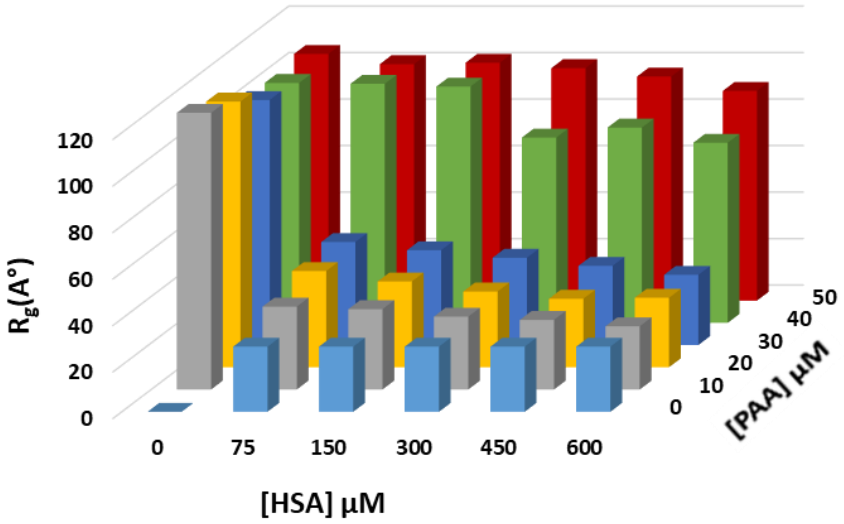

Figure 2. 18. Radius of gyration evolution as a function of both HSA and PAA concentrations showing the threshold PAA concentration needed for complexation phenomenon to occur ([HSA]=0-600 µM and [PAA]=0-50 µM).

The same behaviour was observed for a polymer concentration of 40 or 50 µM, but this time the average radius increases significantly to reach almost the size of PAA single (around 100 Å) for low protein concentration. Further increase in HSA concentration leads to lower the radius of gyration because its contribution become higher.

Previously, we stated that the adsorption of protein on polyelectrolyte was substantiated by an electrostatic attraction between positive charges carried on the HSA surface and the negative PAA chains. This finding make it obvious that this attraction could not be the only operative force that overcome the strong repulsion forces inducted by the fact that both solutes have the same overall charge. Indeed, these last results disclose either a steric hindrance effect involved in the HSA-PAA binding phenomenon. This means that increasing the polymer concentration allows the PAA chains to be close enough to HSA molecules to initiate the attractive electrostatic force between protein positive patches and the polyelectrolyte negatively charged. Or, it could be correlated to the pH of the medium found to be reduced with the increase of PAA amount. Thus, the overall negative charge of the protein is reduced which weakens the repulsive forces between HSA and PAA, and allow the electrostatic attraction to overcome.

4.3. Ionic strength and pH effect on HSA/PAA complexation

In the previous section, we suggested that HSA-PAA complexation was due to electrostatic interactions and that it was potentially correlated to the pH of the medium. Hence, the influence of the ionic strength and pH was investigated in this section.

For the ionic strength study, the [HSA] was set at 75 µM and the [PAA] at 50 µM (pH ~ 5 remains controlled by the polymer concentration), where the complexation was observed, while the ionic strength was varied from 0.137 M to 1 M by adding a needed amount of a 4 M NaCl solution.

Data obtained and reported below (Figure 2. 19.A) reveal a decrease in scattering intensity with the increase in ionic strength. Obviously curves are moving down especially at medium and small angles (0.005 to 0.1 $Å^{-1}$), changing the slope, to collapse for an ionic strength of 0.75 M and 1 M with the theoretical sum (plotted as red line) of two independent signals without interaction (signal of HSA 75 µM+ signal of PAA 50 µM) obtained at I=0.137 M. This finding confirms the previous assumption and bears out the fact that the binding of HSA-PAA is due to electrostatic interactions.

Afterwards, salts concentration was set at 0.15 M and pH was changed from 8 to 4.6 using the different buffer solutions listed in section 39. As shown in Figure 2. 19.B, the decrease in pH down to 5 promotes the formation of the complex whereas at pH > 5 the complex is dissociated giving the same SAXS signal as a mix of two independent contributions.

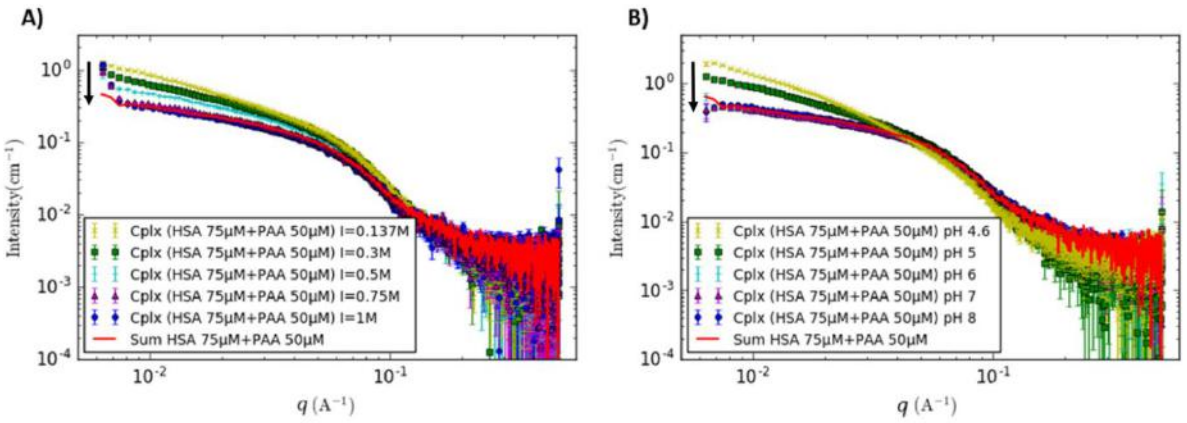

Figure 2. 19. Scattering intensities of HSA-PAA mixture for [HSA]=75 µM and [PAA]=50 µM, (A) as a function of ionic strength (I=0.137 to 1 M) for pH≈5, and (B) as a function of pH (pH=4.6 to 8) for I=0.137 M.

These experiments show the key roles of the pH and the ionic strength on complex formation correlated to the charge distribution of amino acid forming the binding pocket of HSA and to the charge density of the PAA. The decrease in pH allows to reduce the repulsive forces until the initiation of the attractive potential between the positive charges carried on HSA and the negative polyelectrolyte chains. However, at pH lower than 5 (pH 4.6), the obtained SAXS signal (Figure 2. 19.B) is significantly different (slope P=1.5) from the one of a macromolecular complex (slope P=1.2). Since the drop of pH to 4.6 cannot sufficiently alter the net charge of the protein (isoelectric point of HSA 4.7) to create phase separation, one can consider that HSA starts being unfolded and form aggregates, because it undergoes form transition between pH 5.0 and 3.5 [50].

To ensure the stability of the protein structure in the studied range of pH (5 to 8), SAXS measurement were performed on 75 µM of single HSA at pH 5, 6, 7 and 8. Afterwards, the scattering pattern of HSA at pH 5 was compared to the theoretical one calculated from the crystal structure as we did in the study on single HSA in PBS previously. The experimentally obtained SAXS intensities did not exhibit changes on the size neither the form of the protein (Figure 2. 20.A), which confirms the structural stability of HSA in this range of pH. This also corroborates that the increase in intensity at pH 5 after the addition of the polymer was

effectively due to HSA-PAA complexation and not to the aggregation of HSA. Indeed, the theoretical curve has been found to match very well the experimental *I(q)* of HSA at pH 5, which means that HSA is correctly folded in these conditions (Figure 2. 20.B).

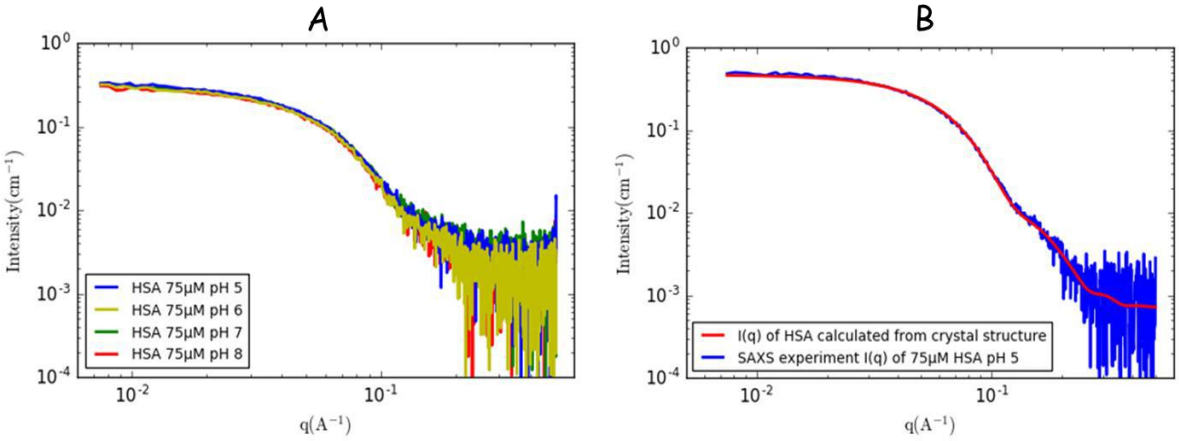

Figure 2. 20. A/ Scattering intensities of 75 µM HSA at different pH (5, 6, 7 and 8). B/ Scattering pattern of 75µM HSA at pH 5 compared to theoretical pattern calculated from the crystal structure.

Subsequently, SAXS measurements on the HSA-PAA mixture for a matrix of conditions were performed where the ionic strength was varied from 0.05 to 0.75 M for each pH 5, 6 and 7, in order to determine the best conditions of complex formation. As the major effects are observable at small angles due to the increase in size when the complex appears, we decided to probe the changes by evaluating the radius of gyration determined from Guinier law for each condition. Although the PAA and the complex have close R_g values ($R_g \approx 110$ Å), the average value of R_g was found around ≈ 50 Å when the HSA and the PAA do not interact, which is much lower than that of the complex. The data are plotted in Figure 2. 21. One can notice that the radius of gyration of free PAA or of single HSA found to be around 110 Å and 30 Å respectively, do not depend on the pH. Besides, pH in the range 6-7 does not affect the radius of gyration of the mixture HSA+PAA, found to be approximately 50 Å for all salt concentrations investigated. This observation highlights the fact that HSA-PAA binding does not take place in these conditions. As stated previously, the radius of gyration obtained here by fits is an average of the R_g of HSA and of the one of PAA, which makes sense to obtain an average proportional to the amount of each solute in the mixture (protein/polymer ratio of 3/2). A different behaviour is observed at pH 5. In fact, increasing the ionic strength from 0.05 to 0.75 M has led to decrease the R_g from 110 Å, (which is almost the polymer radius of gyration), to 69.8 Å. This is due to the fact that beyond 0.15 M of ionic strength the HSA-PAA complex

particles begin to dissociate into free HSA molecules and free PAA chains. This dissociation is not complete at 0.75 M and some complex particles are still in there since the obtained R_g (69.8 Å) is still higher than the average value (≈50 Å) found when the HSA and PAA do not interact. This outcome sustains the previous results (Figure 2. 19.A) suggesting that complete dissociation of the complex is taking place between 0.75 M and 1 M.

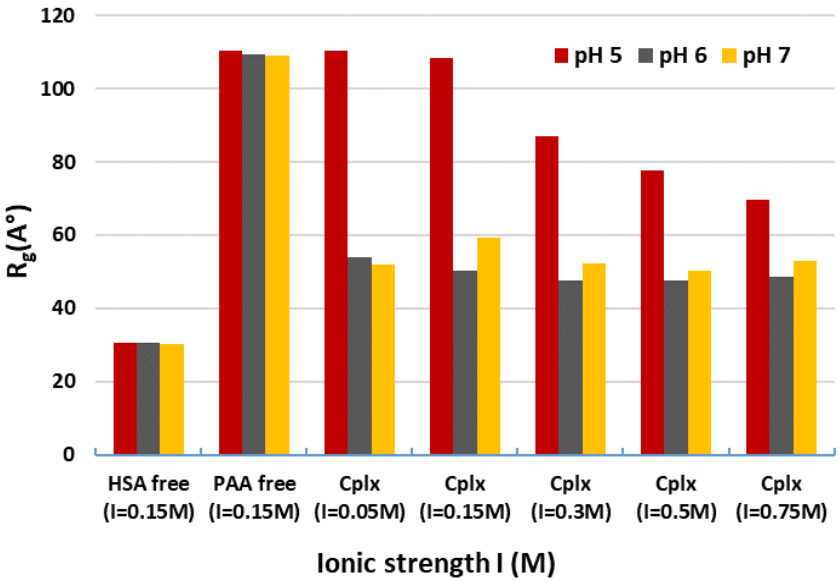

Figure 2. 21. Radius of gyration evolution as a function of both pH and ionic strength showing the threshold needed for complexation phenomenon to occur ([HSA]=75 µM ; [PAA]=50 µM ; pH=5 to 7 and I=0.05 to 0.75 M).

It can be concluded from this study that the complex is stable at pH ≈ 5 and a salt concentration below 0.15 M. This is partially inconsistent with what has been reported in the literature where the HSA has been reported to form complexes with short PAA (2 kDa) at pH of 7 [20]. This could be due to the fact that PAA in our study is much larger, and so it bears higher negative charge which leads to stronger electrostatic repulsions with the protein. Thus, the decrease in pH allowed to reduce the negative charge of PAA until it initiate the electrostatic attraction with the positive charges on HSA surface.

We henceforth know the conditions that lead to the assembly of HSA-PAA complexes in bulk. Therefore, we can imagine that this study constitutes a first knowledge brick to tune these reversible interactions between long PAA grafted on a membrane surface and HSA. Controlling the ionic strength and the pH should enable to regulate these interactions, promoting or preventing their happening. Thus, the effect of the pH and the ionic strength will be again

investigated latter in chapter 3 for the adsorption of HSA on PAA deposited on membrane surface. In fact, we can imagine that to enhance the platelets capture on PAA, pH > 5 should be favoured to prevent the adsorption of HSA on PAA. Now that the conditions of complex formation are controlled, the stoichiometry of complexation can be investigated.

4.4. Determination of the complex stoichiometry (PAA-nHSA)

In order to determine the number of proteins that could bind to each polymer chain, SAXS experiments were performed by setting the concentration of PAA at 50 µM and varying the HSA concentration between 75 and 600 µM. In other words, the [HSA]/[PAA] molar ratio ranged from 1.5 to 12. The experiments were performed at pH 5 and an ionic strength I = 0.15 M to ensure complexation.

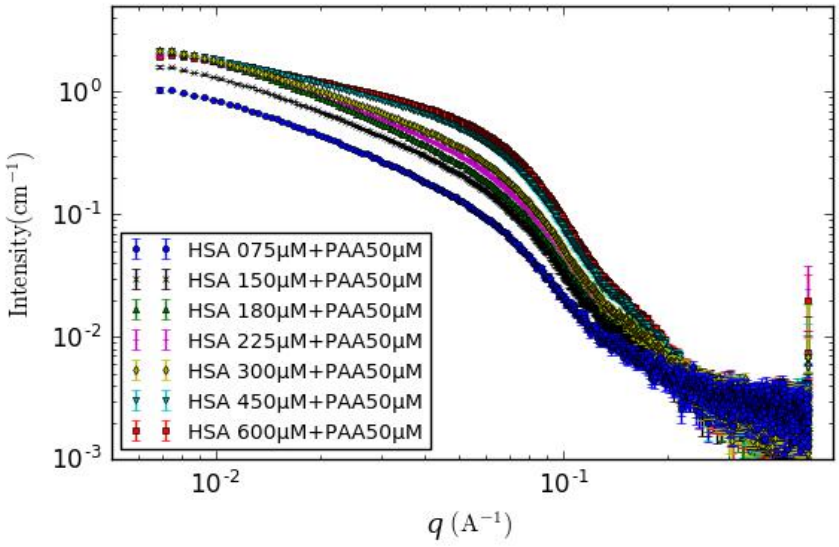

Figure 2. 22. Scattering profiles of HSA-PAA mixture as a function of HSA amount ([HSA]=75 to 600 µM; [PAA]=50 µM; pH=5 and I=0.15 M).

For an HSA concentration lower than 225 µM, the SAXS curve shifts up without a significant change of slope at small and middle angles (0.005 to 0.1 $Å^{-1}$ Figure 2. 22). This shift of the curves corresponds to an increase in concentration of complex, considering that the contribution of PAA is negligible, compared to the one of the complex (cf. Figure 2. 14.A). Given the ratio of Porod volumes between HSA and the complex of R = 1:5, it is expected to have several HSA molecules per chain of PAA. Such behaviour in solution would suggest that the HSA binding mechanism to PAA is cooperative, without intermediates depending on HSA concentration.

When HSA concentration is close to 225 µM, the signal does not increase any more with the concentration. Beyond 225 µM, the signal changes at small angles, with a decrease in R_g and *I(0)* values. At large angles, one observes a change in the SAXS profile. This change is due to an accumulation of free HSA in the medium and eventually the measured signal is a combination of the one of all PAA molecules involved in the complexes and of the un-bound HSA. Table 2. 2 summarizes the values of R_g and the calculated Porod volumes for each ratio of HSA/PAA.

Table 2. 2. The evolution of radius of gyration as well as the Porod volume for the HSA-PAA mixture as a function of the molar ratio ([PAA]=50 µM; [HSA]=75-600 µM).

[HSA] µM	**75**	**75**	**150**	**180**	**225**	**300**	**450**	**600**
nHSA/PAA	Free HSA	1.5	3	3.6	4.5	6	9	12
R_g (± 3 Å)	30.4	108.3	107	110.1	108.6	90.6	81	74.1
V_p .10^3 (Å^3)	99.1	428	502	500	491	400	305	239

From the values of R_g reported in Table 2. 2, it can be concluded that the attachment of proteins to the polymer chains has taken place on all the polyelectrolyte chains available for HSA/PAA molar ratio ranging between 3.6 and 4.5.

To support this hypothesis, the Porod volume was evaluated for the different HSA/PAA molar ratios. As stated in the materials section, from SAXS experiments it is possible to obtain the Porod volume of an object from the Porod invariant *Q*. (Plots given in section 2 of the **Appendix B**).

The calculated Porod volumes (reported in Table 2. 2) exhibit the same behaviour as that of the radius of gyration. For a HSA/PAA molar ratio of 3.6, the Porod volume is found to be around 500.10^3 Å^3, which represents the complex Porod volume (Figure 2. 14). Then, we notice that increasing the HSA concentration reduces the volume to 239.10^3 Å^3 for a molar ratio of 12. That makes sense because after saturation of all PAA chains, the excess of HSA contributes to the average of the Porod volume.

On the other hand, a complexation model has been developed to describe the evolution of the Porod volume for the same range of HSA/PAA molar ratio, making the assumption of the following complexation equilibrium:

$$n\,HSA\ +\ 1\,PAA\ \rightleftarrows\ 1\,complex(PAA-nHSA)$$

Where n is the number of HSA in each complex particle.

Thus, for a given initial $[HSA]_0/[PAA]_0$ molar ratio, it is possible to define [HSA], [PAA] and [c] as the molar concentrations in the mixture during the complexation progress of HSA, PAA and the complex, respectively. Thus, these concentrations can be calculated as follows:

$$[PAA] = [PAA]_0 - [c] \quad (2.8)$$

$$[HSA] = [HSA]_0 - (n \times [c]) \quad (2.9)$$

If the PAA is on excess ($[HSA]_0 < n[PAA]_0$), the composition in the mixture is:

$$[c] = \frac{[HSA]_0}{n} \quad (2.10)$$

$$[PAA] = [PAA]_0 - \frac{[HSA]_0}{n} \quad (2.11)$$

If HSA is on excess ($[HSA]_0 > n[PAA]_0$), the composition in the mixture is:

$$[c] = [PAA]_0 \quad (2.12)$$

$$[HSA] = [HSA]_0 - (n \times [PAA]_0) \quad (2.13)$$

For known $[HSA]_0/[PAA]_0$ molar ratio, it is then possible to determine the relative volume fraction of each solute *i* in the mixture as follows:

$$\varphi_i = \frac{N_{Avo} \cdot [i] \cdot V_i}{\phi} \quad (2.14)$$

Where ϕ is the volume fraction of the mixture of solutes in solution and it is expressed as:

$$\phi = N_{Avo}\ ([c] \cdot V_c + [HSA] \cdot V_{HSA} + [PAA] \cdot V_{PAA}) \quad (2.15)$$

Where V_c, V_{HSA}, V_{PAA} are the volume of a molecule of the complex, HSA and PAA respectively. These volumes were estimated using Primus from SAXS spectra of single solutes and found to be: 500.10^3, 100.10^3 and 50.10^3 Å^3 for the complex, HSA and PAA, respectively. Therefore, assuming a stoichiometry of complexation can allow to evaluate the relative volume fraction of HSA, PAA and the complex using the complexation equilibrium suggested previously (Figure 2. 23).

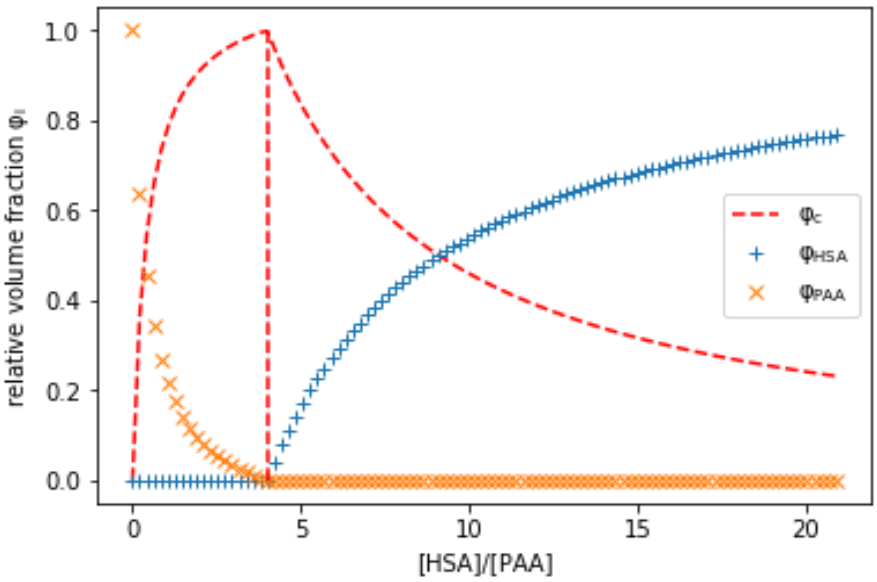

Figure 2. 23. The relative volume fraction of HSA, PAA and the complex as a function of [HSA]/[PAA] molar ratio calculated with the complexation model for a stoichiometry coefficient n=4

Accordingly, the Porod volume could be estimated using a theoretical model. According to the literature when the dispersion is made of n kinds of particles of volume V_i and number N_i, for a dilute dispersion S (0) =1, the average volume can be written as follows (O. Spalla eq. 54) [33]:

$$V_M = \frac{\sum_i^n N_i \cdot V_i^2}{\sum_i^n N_i \cdot V_i} \tag{2.16}$$

The Porod volume of the mixture can be written then as a function of the relative volume fraction of solute, φ_i

$$V_M = \frac{\sum_i^n \varphi_i \cdot V_i}{\sum_i^n \varphi_i} = \sum_i^n \varphi_i \cdot V_i \tag{2.17}$$

$$V_M = \varphi_c \cdot V_c + \varphi_{HSA} \cdot V_{HSA} + \varphi_{PAA} \cdot V_{PAA} \tag{2.18}$$

Porod volume calculations whether from SAXS experiments or from the theoretical model as well as the relative volume fraction were performed using a code written in Python (given in **Appendix B**).

Knowing V_c, V_{HSA}, V_{PAA} estimated previously using Primus, the equilibrium suggested previously can be then used to evaluate the Porod volume by assuming a stoichiometry, n, of complexation.

Figure 2. 24 displays the Porod volume calculation for 3, 4 and 5 HSA molecules bounded to each PAA chain, where the symbols represent the estimated V_p (reported in Table 2. 2) from the SAXS experimental data. The comparison of these experimental data to the theoretical model suggests a stoichiometry of saturation for an [HSA]/[PAA] molar ratio around 4. Indeed, the results show that a complex model containing 4 HSA with 1 PAA gives a better fit than those run assuming 3 or 5 HSA per PAA (Figure 2. 24).

As a matter of fact, when the initial $[HSA]_0/[PAA]_0$ ratio is below 4, the mixture is composed of PAA and of the HSA-PAA complex. The Porod volume is then rising up quickly when increasing the HSA ratio, from the one of PAA to the one of the complex. For a $[HSA]_0/[PAA]_0$ ratio of 4, one can consider that there is only the complex (PAA-4HSA) in the mixture and that the SAXS data gives access to the Porod volume of the complex. When the $[HSA]_0/[PAA]_0$ is larger than 4, the mixture is composed of the complex plus some free HSA.

The complexation model proposed previously in this section can then explain the decrease in the mean Porod volume due to the presence of non-associated HSA in addition to the HSA-PAA complex.

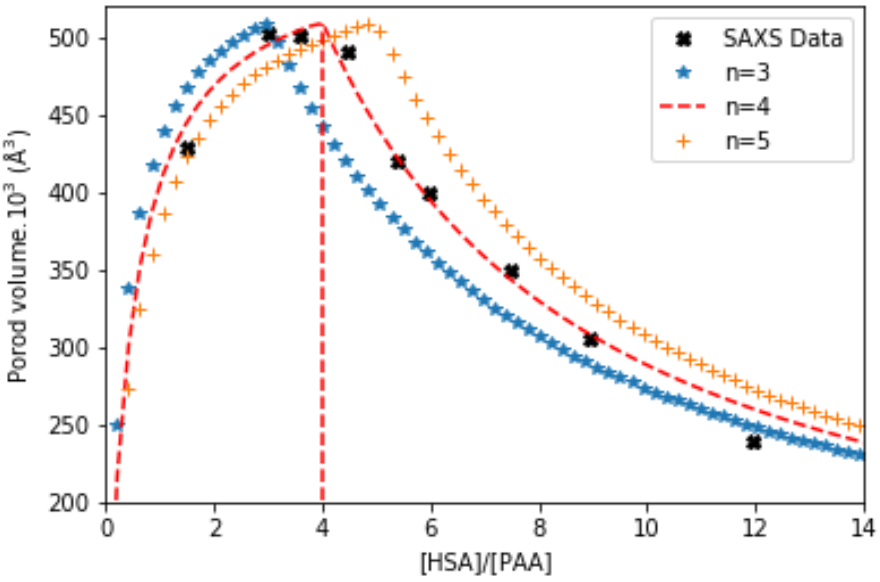

Figure 2. 24. The Porod volume evolution as function of the initial [HSA/[PAA] ratio, using experimental SAXS data and calculation from the complexation model for different stoichiometry coefficient n.

4.5. SAXS Modelling studies

4.5.1. HSA structure investigation

In order to facilitate data processing in further modelling of the structure of HSA-PAA complex, that of native HSA was first investigated to find a simple geometrical model that can describe this structure. For that, simple geometrical bodies were tested using the program Sasview [37]. As exposed in Figure 2. 25, the best fitting curve (plotted as a red line) to the experimental *I(q)* (plotted as blue line), corresponds to a cylinder (Disk) model with a radius of 37 Å and a length of 31 Å. It is important to note that using these dimensions a volume of cylinder that yields 133.10^3 Å^3 is obtained, which is higher than the Porod volume of HSA found to be around 100.10^3 Å^3. This could mean that the HSA does not completely fill the cylinder as it could be seen in Figure 2. 25.

Figure 2. 25 exposes also the HSA 3D structure as shown in cartoon using PyMOL software, and it illustrates how the protein can be represented by a disk model (diameter=74 Å , length=31 Å) from different angles.

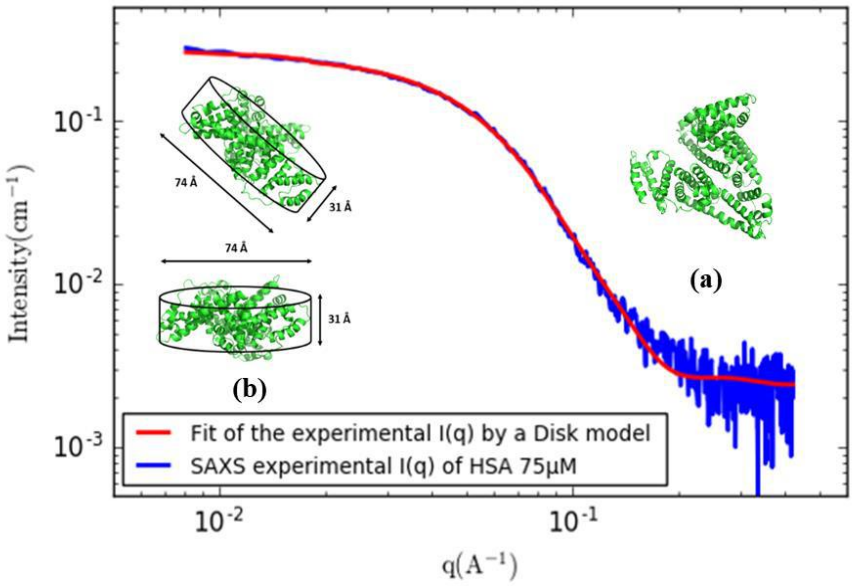

Figure 2. 25. Experimental SAXS scattering intensity *I(q)* of HSA 75µM (blue line) and the optimal fit obtained with a cylinder (disk) model (red line) using Sasview. (a) The HSA crystallographic 3D structure shown using PyMOL software and (b) its representation by disk model as seen from different angles.

4.5.2. HSA-PAA complex structure investigation

Based on what has been done for the protein alone and the stoichiometry proposed for number of HSA molecules that could be bound on each PAA 100 kDa, geometric models were also tested to describe the HSA-PAA complex by fitting the experimental *I(q)* using Sasview program.

The first suitable shape found to fit well the SAXS experimental data corresponds to a cylinder (Radius=22 Å; Length=380 Å) plotted as yellow line in Figure 2. 26. This is consistent with the primary analyses of the *p(r)* function done previously and given in Figure 2. 14.B. Indeed, this latter has revealed that the HSA-PAA complex exhibits a cylindrical form of a length around 400 Å but with a radius that yields 40 Å.

It can be noticed that the obtained radius is also smaller compared to that found for the protein. This could be due to the fact that HSA molecules are only linked to certain areas of the polymer chain, while for the remaining parts of the chain the radius has been evaluated to be 8 Å, so the average radius was around 22 Å.

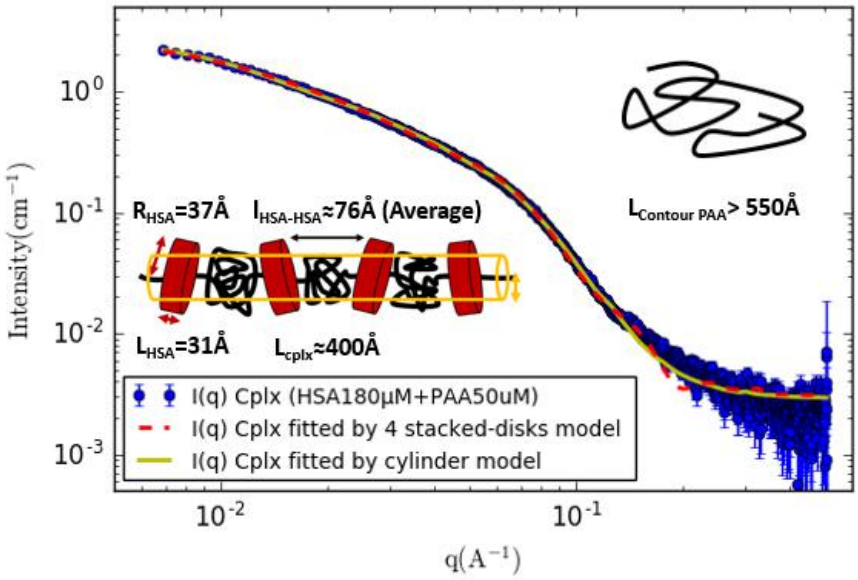

Figure 2. 26. The SAXS scattering intensity for HSA-PAA complex as dotted thick blue line, fitted by cylinder model (Radius=22 Å ; Length=380 Å) as yellow line, and by 4 stacked-disks model (Radius=22 Å ; Length=392 Å) as dashed red line, with the shape of the two patterns how they can be illustrated.

The second shape found to correlate well the experimental data is a 4 stacked-disks model plotted as dashed red line (Figure 2. 26), where every disk represents an HSA molecule bound

to the PAA chain. This model results in a succession of patterns (layer/core/layer), where the core length was found to be the same as the HSA one (31 Å) and the layer length was around 38 Å, thus the average distance between two HSA molecules is 2×layer (76 Å). Thereby a complex of HSA/PAA is a set of 8 layers and 4 cores, so that the length of this ensemble is 392 Å which is almost what was obtained for the first model. Then regarding the radius, it was evaluated to be 22 Å also, and that because this model considers the core and the layer to have the same radius.

As stated previously, for such geometrical bodies the length is theoretically expressed as follows: $\frac{L^2}{12} = R_g^2 + R_c^2$. Thus, knowing that R_g was found to be around 110 Å and the cross-section radius R_c, is estimated to be 22 Å, it can be then concluded that both shapes are consistent with the theoretical model.

The same way the structure of PAA was investigated by fits using Sasview and found to be like a flexible cylinder with radius of 8 Å and a contour length of around 570 Å. Taking this under consideration, the polymer and the complex could be designed as illustrated above (Figure 2. 26).

4.5.3. Modelling of all-atoms structure of HSA-PAA complex

As stated previously, the analysis of the autocorrelation function *p(r)* has revealed that we can fit the data at small and medium *q* (less than 0.2 $Å^{-1}$) using a cylinder of axial length close to 400 Å and diameter equal to 78 Å. Thus, the cylinder body was tested to fit the HSA-PAA complex experimental *I(q)* using Sasview and found to do it well as shown in the previous section. This model can provide information on the global shape of the complex, but provides no structural information on the internal organization of the complex.

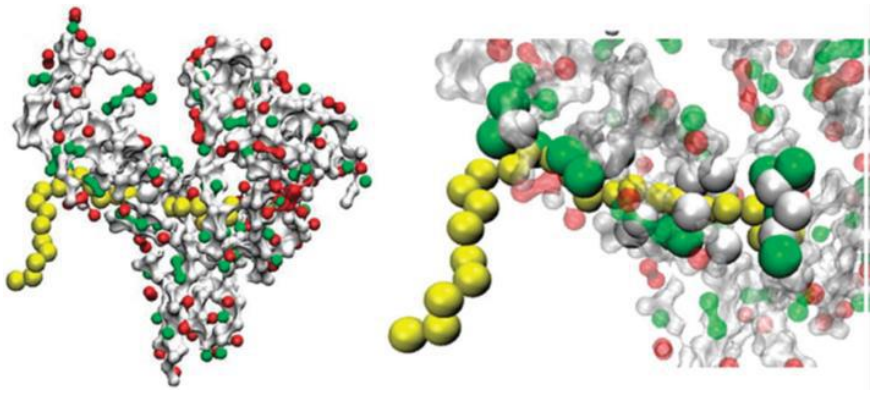

Figure 2. 27. Representative computer simulation snapshot of the HSA-PAA complexation performed with a short PAA (2 kDa) by Ballauff and al [20].

To propose a model that could be compatible with the SAXS data, we used an approach based on rigid bodies molecular modelling, completing the missing parts with dummies residues (BUNCH). The atomic structure of HSA can be used as a template for rigid bodies and the PAA polymer forms the missing part. As shown by Ballauff and al [20], PAA can interact with HSA in a pocket charged positively, giving a starting point to lock a portion of PAA at the surface of HSA as illustrated in Figure 2. 27. In the case of larger PAA these portions of HSA-PAA complex are connected each other as a pearl necklace. The rest of PAA is flexible and the conformation can be modified by the program BUNCH which is working directly with residues of protein rather than with different types of polymer. However, the chemical structure of PAA is close to a peptide residue and the PAA polymer can be transformed into poly-glycine chain. As both chains present a difference of mass (Δ=1.26), the individual form factor of the dummies residues is increased in BUNCH program to compensate this default of mass. In total, the 100 kDa PAA chain can be modelled with a poly glycine chain containing 1389 residues.

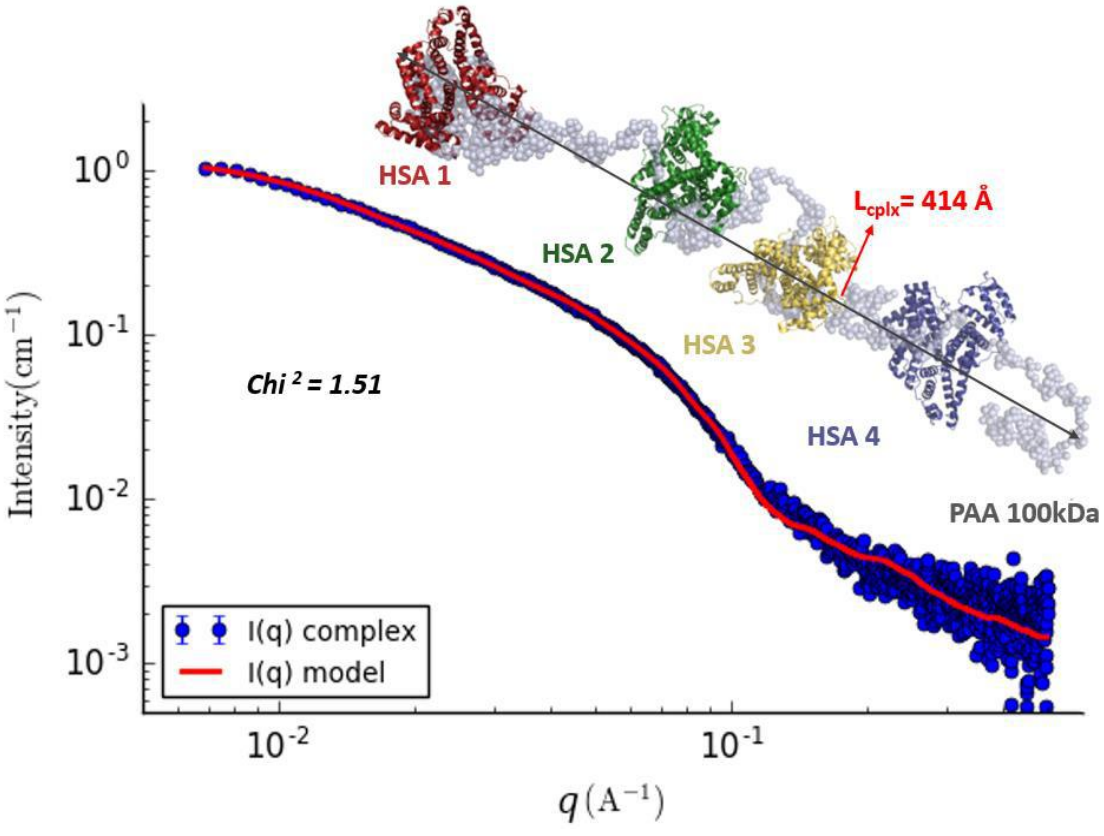

Figure 2. 28. Superimposition of the experimental SAXS data (dotted thick blue circle) of the HSA-PAA complex and those of the compatible model (red line) calculated with the program BUNCH.

During the molecular modelling process against SAXS data, the position and the orientation of individual HSA is free and the conformation of polymer chain is modified in order to describe the space occupied by the PAA. The result obtained is an all atoms model compatible with SAXS data reflecting a possible organization of the complex in solution (Figure 2. 28). Interestingly, the complex forms an elongated structure as a cylinder with a non-specific orientation of the HSA. The absence of correlation peak in the data suggests that HSA does not present a periodic or partially aligned structure in the complex. This model proposes a globally flexible organization in alternative layers composed of HSA and unfold PAA without frozen structures. Many tests have been performed with different templates and all converge to the same organization with some variations in the position or orientation of HSA. However, the distance between two monomers of HSA always ranges between 80 and 100 Å. Besides, the distance between the extremities of the complex remains constant, found to be 414 Å as shown in Figure 2. 28.

4.6. Influence of PAA size on HSA-PAA complexation

In this section, we report investigation of the binding phenomenon between HSA and shorter PAA than that used previously, namely 50, 30 and 5 kDa. For that, the HSA/PAA molar ratio was first studied at pH 5 and I = 0.15 M to estimate the stoichiometry of complexation for each PAA size. That was done by setting the PAA concentration at 50 µM and varying that of HSA from 50 to 300 µM. After that, the radius of gyration for all the obtained scattering intensities was evaluated using Primus program. R_g evolution as a function of the HSA/PAA molar ratio is shown Figure 2. 29 that also shows the obtained SAXS experimental intensities.

For PAA 5 kDa, results show that R_g starts decreasing when [HSA] > 50 µM, which is probably due to greater contribution of the free added HSA. This suggests that all chains of PAA 5 kDa have been already saturated for an HSA/PAA molar ratio of 1. For PAA 30 kDa, results display an R_g almost stable until a molar ratio of 3, which suggests that the saturation of the PAA chains could be achieved in the range from 1 to 3 of HSA/PAA molar ratio. As for PAA 50 kDa, the maximum of R_g was clearly reached at a molar ratio of 3, and then it started decreasing for higher ratios.

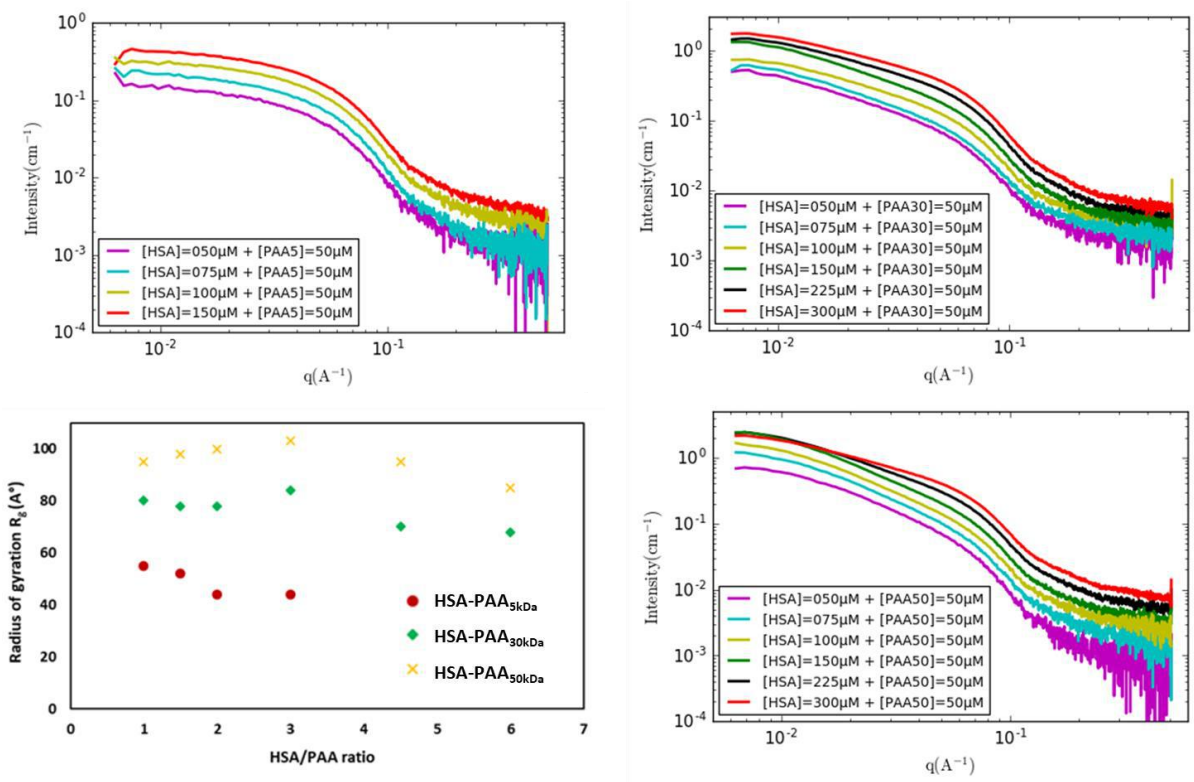

Figure 2. 29. SAXS scattering intensities *I(q)* of the HSA-PAA mixture as a function of HSA concentration and for different PAA sizes ([HSA]=50-300 µM and [PAA]= 50 µM). Table summarizing R_g values as evaluated by Primus program.

These primary results gave us an idea about the potential stoichiometry of HSA-PAA complexation with every size of PAA.

After that, size exclusion chromatography was used to investigate this complexation that has been revealed to be correlated to the PAA size. In fact, for every PAA size, HSA-PAA complex solution was flowed in a mobile phase having the same concentration of the studied PAA that has been used to prepare the complex sample. These experiments were performed by setting HSA concentration at 225 µM to avoid depletion of complex solution from HSA due to the dilution once in the column. The concentration of PAA was then chosen for every size of this latter by respecting the stoichiometry of complexation revealed previously.

The peaks of elution obtained with the different PAA sizes were then compared to each other and to the peak of single HSA illustrated in Figure 2. 30. Results disclosed a shifted peak of elution to higher molecular weights when increasing the size of PAA. This suggests that the size of the formed complex is bigger when the PAA is larger, which confirms that the complexation stoichiometry is effectively related to the PAA size.

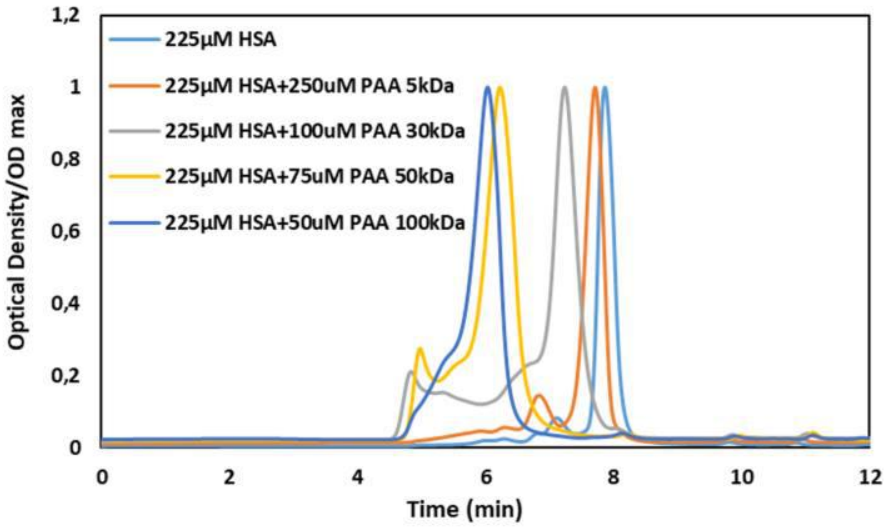

Figure 2. 30. Comparison of chromatographic pattern of HSA 225 µM and those of HSA-PAA mixtures using different PAA sizes.

Afterwards, a SAXS samplings of the chromatography elution peaks were performed to obtain the scattering intensity *I(q)* of the complex fraction only, and to remove the contribution of aggregates. However, since the signal are very noisy at high angles, acquisitions on the same samples with the same concentrations were performed in direct injection mode without passing through the chromatography to improve the information at high angles.

Eventually, in order to make sure good information can be extracted at small and high angles, data obtained from these experiments were merged with those obtained from the SAXS sampling of the elution peaks as explained in the methods section. Results exposed an increase of *I(q)* at small angles, while it remains almost unchanged in the intermediate and high angles range (Figure 2. 31). This indicates that all HSA-PAAs complexes exhibit the same type of surface with an increase in the global size.

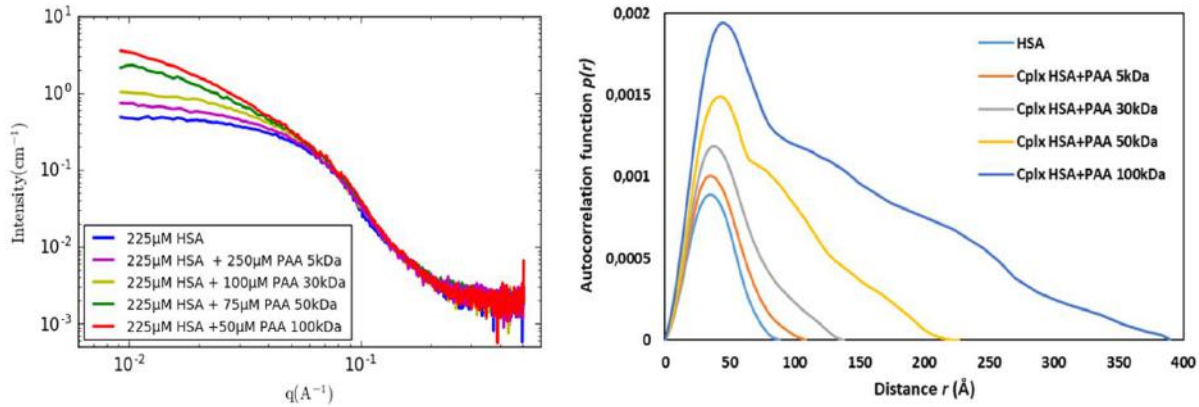

Figure 2. 31. Scattering intensities of HSA-PAA complexes obtained using different sizes of PAA, and the corresponding autocorrelation function calculated from each *I(q)* using Primus.

Subsequently, the autocorrelation function corresponding to every scattering pattern was calculated using Primus program, and it is shown in Figure 2. 31. The primary analysis of *p(r)* displays an increasingly skewed distribution with the PAA size increase, and with a clear maximum at small distances corresponding to the radius of the cross-section R_c. This supports the hypothesis of the formation of more elongated HSA-PAA complex when the PAA is larger. Various parameters were then extracted from these SAXS data (whether *I(q)* or *p(r)*) such as R_g, V_p, R_c and D_{max}, and they are summarized in Table 2. 3.

First, it can be noticed that R_g values estimated from these data are lower than those obtained previously. This confirms that going through chromatography before SAXS measurement allows effectively to eliminate the aggregates contribution, which gives more reliable information at small angles. Despite that, R_g is still increasing with the size of PAA which affirms that the HSA-PAA complex is bigger with larger PAA. The evolution of the Porod volume (V_p) and the maximum distance (D_{max}) came then to sustain all what has been said above. Indeed, they are both increasing with the size of PAA to reach a V_p around 500.10^3 Å^3 and a D_{max} that yields ≈ 400 Å with PAA 100 kDa, which is consistent with the values of these same parameters reported early in this chapter (Figure 2. 14).

As for the radius of the cross-section R_c, it did not vary too much compared to the D_{max}, which indicates that the complex is only becoming more elongated with the increase in PAA size without big changes in size of the section.

Table 2. 3 : Various physical parameters of the HSA-PAA complex that can be formed with every PAA size.

Parameter / Complex	R_g (Å)	$V_p \times 10^3$ (Å^3)	M_w (kDa) SAXS	Retention time (Rt)	M_w (kDa) HPLC	R_c (Å)	D_{max} (Å)
HSA	29.2 ± 0.3	100	65.7	7.8	64.5	36	89
HSA+PAA 5kDa	35.2 ± 0.6	130	85.2	7.7	71.5	36	105
HSA+PAA 30kDa	62.5 ± 1.6	210	125.3	7.24	115	38	138
HSA+PAA 50kDa	81.7 ± 2.4	380	304.9	6.25	320	41	227
HSA+PAA 100kDa	97.7 ± 3.4	520	433.6	6.02	401.6	42	390

After that, the molecular weights of the HSA-PAAs complexes were evaluated from the chromatography data using the calibration curve given in Figure 2. 2. The calculated M_w were then compared to those estimated from SAXS data using Primus program. The obtained results (quoted in Table 2. 3) disclosed the same trend of evolution with both methods with some differences between the two as exposed in Figure 2. 32.

Knowing the M_w of HSA-PAAs complexes and the theoretical M_w of both protein (≈ 67 kDa) and PAAs, it was then possible to estimate the number of HSA molecules that could be bound to the chains of every PAA size. For instance, the evaluated M_w of HSA-PAA_{5kDa} complex suggests that only one HSA molecule is bound to the PAA 5 kDa, while for HSA-PAA_{30kDa} complex, the M_w suggests that one to two HSA molecules could be attached to every chain of PAA 30 kDa as illustrated in Figure 2. 32. This is consistent with the stoichiometry of complexation proposed previously based on the analysis of the other parameters.

As for the HSA-PAA_{50kDa} complex, the estimated M_w supposes that every complex particle contains 3 to 4 HSA molecules and one chain of PAA 50 kDa. Finally, the M_w of the complex HSA-PAA_{100kDa} assumes that this latter could be formed from 4 to 5 HSA molecules with every chain of PAA 100 kDa. Thus, the stoichiometry that we can obtain from the M_w assessment for these two polymers (PAA 50 and 100 kDa), is a bit different compared to that suggested previously. In fact, it has been assumed that a maximum of 3 and 4 HSA molecules could be bound to the chains of PAA 50 and 100 kDa respectively. This outcome could indicate that these stoichiometries are just an average, and that not all the complexes contain the same number of HSA molecules. This could be due to the polydipersity of the polymer, which means that from the beginning not all polymers chains exhibit the same size, which can explain deviation on the stoichiometry of complexation. However, it is not possible to conclude on this because we do not have information on the polydipersity of polymers.

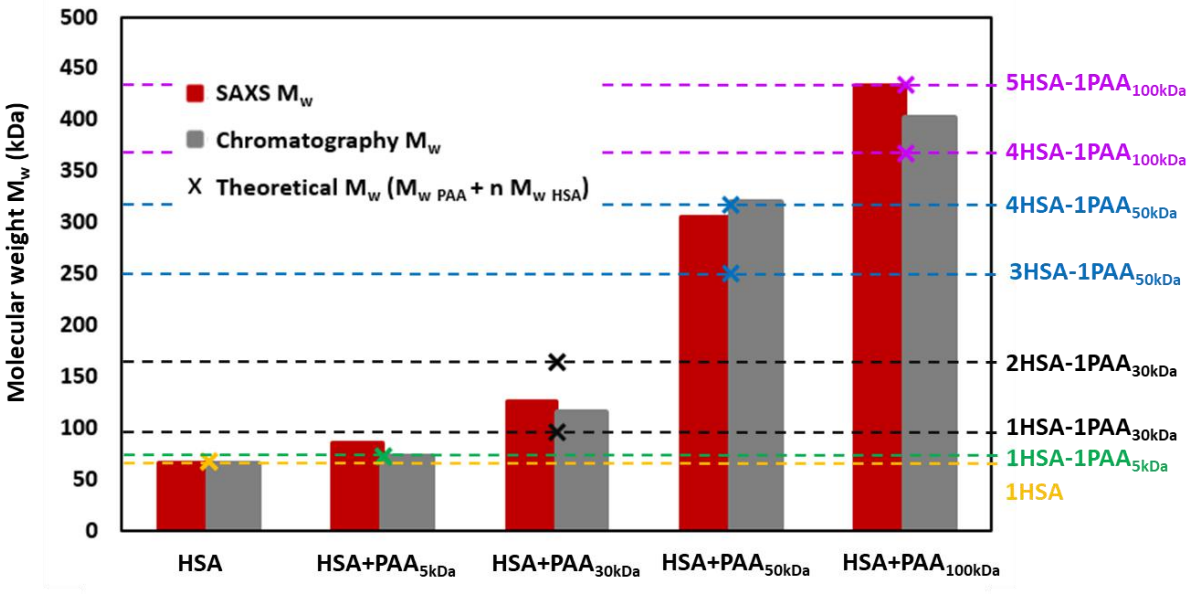

Figure 2. 32. Comparison on the HSA-PAA complex molecular weight estimated from SAXS data and from chromatography data to the theoretical M_w calculate from the stoichiometry of complexation (PAA-nHSA) for each size of PAA.

From these results, it can be also noticed that the stoichiometry of complexation was not proportional to the PAA size. This could be arising out of the electrostatic interactions that could take place between two HSA molecules, and between HSA and PAA. In fact, HSA-PAA binding is supposed to be due to the attractive potential between positives patches carried on the surface of HSA and the negatively charged PAA. At the same time, two protein molecules will repel each other because of their global negative charge. This suggests that a minimal

distance is needed between two HSA molecules attached to the same PAA chain, so that the HSA-PAA attractive potential can overcome the HSA-HSA repulsion.

4.7. Study of HSA-PAAs complexation reversibility

It has been revealed previously in this chapter (section 4.2.1) using chromatography that the HSA-PAA_{100kDa} complex tend to dissociate in medium with pH higher than 5. In this section, the reversibility of HSA-PAA complexation was investigated for different sizes of PAA in mobile phases with pH maintained at 7. In order to assess the role of PAA presence on keeping the stability of complex, this study was also performed in mobile phases at pH 5 either containing PAA or without PAA.

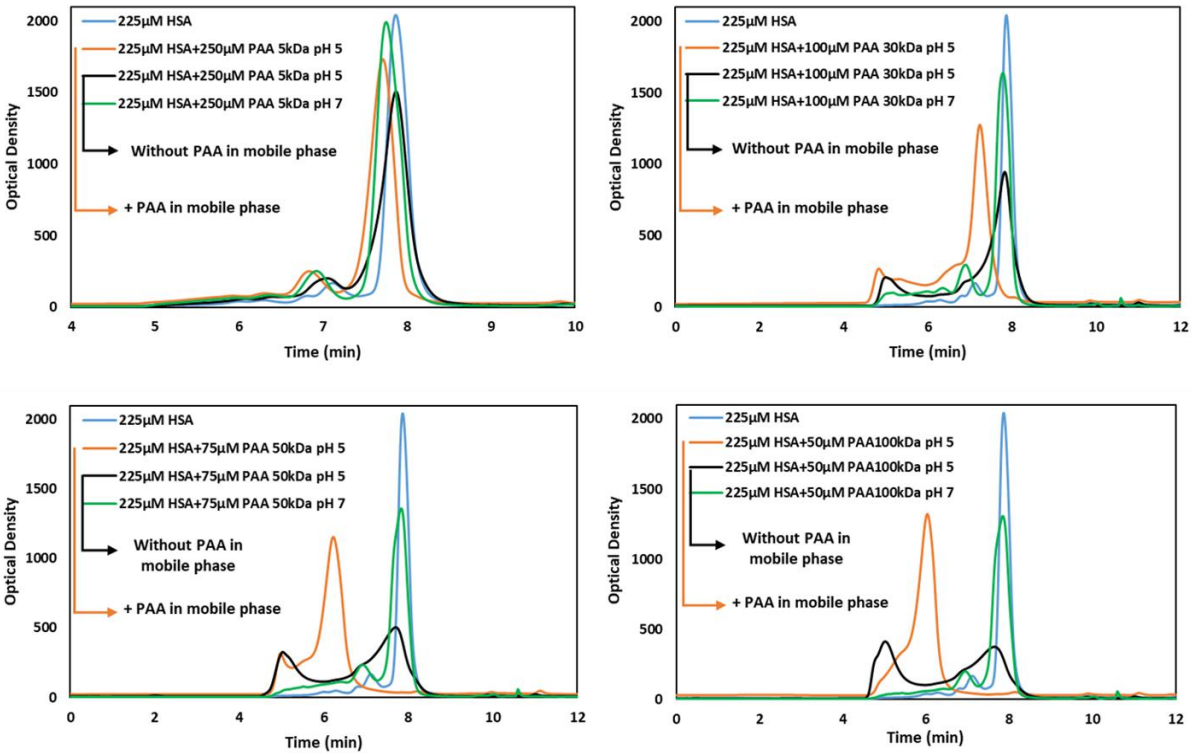

Figure 2. 33. Chromatographic patterns of HSA-PAA mixture as studied in various mobile phases (with PAA in the mobile phase at pH 5 -orange line- and at pH 7 -green line-, and without PAA in the mobile phase at pH 5 -black line-) and compared to the pattern of single HSA in blue.

Results shown in Figure 2. 33 reveal different behaviours of HSA-PAA complex depending on the mobile phase and on the PAA size. First, it can be noticed that at pH 5 and in presence of PAA in the mobile phase, the shift of HSA-PAA_{5kDa} complex peak (orange peak) is not that remarkable, which is understandable as the chains of PAA 5 kDa are supposed to be bound to only one protein. Despite of that, it was possible to see that the peaks are shifted back to that of

single protein in the absence of PAA from the mobile phase (black peak) or when its pH was maintained at 7 (green peak). This indicates that the complex has been dissociated and that the protein is no longer bound to the PAA in these conditions.

When it comes to the other sizes of PAA (30, 50 and 100 kDa), the shift of HSA-PAA complex peaks (orange peaks) is more obvious, which is necessarily due to the higher stoichiometry of complexation. Then, it is possible to notice the reversibility of complexation (dissociation of the complex) even in the presence of PAA in the mobile phase when the pH is maintained at 7 (green peaks) with all PAA sizes. This dissociation of the HSA-PAA complex can also be seen in a mobile phase with pH 5, but not containing PAA (black peaks). However, in this case the dissociation seems to be not complete and various distributions of size could be observed from Figure 2. 33 (black peaks). Indeed, the black peaks are broader showing that a large part of aggregates are still in there, with a part of complex and the detached single HSA, which could be illustrated by Figure 2. 1. In addition, the dissociation seems to be harder in these conditions when the PAA is larger, where less protein is detached which is reflected by smaller peak of single HSA every time the PAA is larger.

4.8. Study of interaction between PAA and IgG

In the previous sections, the HSA-PAA complexation has been proved to take place using several methods. This binding was revealed to be correlated to the pH of the medium and the stoichiometry of complex was proved to be related to the PAA size. In order to check if the HSA-PAA binding was specific of these two solutes, or it can be reproducible with another protein, the interaction of IgG with the same polyelectrolyte was investigated in this section. For that, the experiments were performed using two sizes of PAA (30 and 100 kDa) at I = 0.15 M and pH ranging from 5 to 8. First, to ensure no changes on the global size, shape or the structure of the protein happened because of the change of pH, SAXS measurements were conducted on single IgG at pH 5, 7 and 8. Then, SAXS acquisitions were executed on the mixture of 65 µM IgG + 50 µM $PAA_{30 \text{ or } 100 \text{ kDa}}$ to assess the interactions between IgG and PAA in the same range of pH mentioned above. The obtained SAXS scattering intensities shown in Figure 2. 34 did not display changes on the size or the form of IgG with the pH change, and the evaluation of the radius of gyration found to be around 68 Å has confirmed that. The evaluated R_g for single IgG and for the IgG-PAA mixture at different pH are summarized in the table attached to Figure 2. 34.

It can also be seen from the obtained SAXS patterns that *I(q)* has been found to increase when 50 µM of PAA 30 kDa were added to the protein at pH 5 and 7. Indeed, the radius of gyration of the mixture was found to be around 80 and 75 Å respectively. The same thing was noticed when adding 50 µM of PAA 100 kDa at pH 5 and 7, but the increase of the intensity was a bit higher. However, the curves of *I(q)* did not display a difference at pH 5 or 7 as it was the case with PAA 30 kDa, which was reflected by a values of R_g closer found to be around 91 and 89 Å respectively.

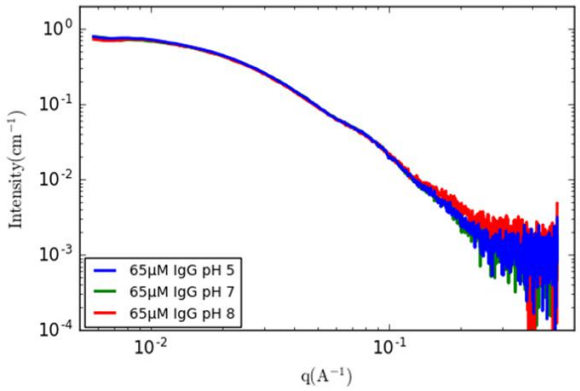

pH / Cplx / IgG +PAA	5	7	8
	Radius of gyration R_g (Å)		
Single IgG	69.8	67.7	68.7
65 µM IgG + 50 µM PAA30 kDa	80.3	74.6	65.6
65 µM IgG + 50 µM PAA 100 kDa	91.3	88.9	66.5

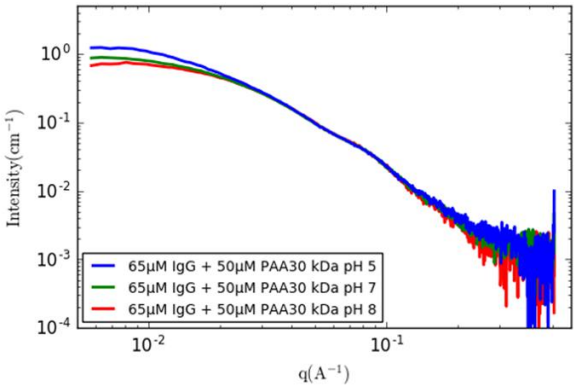

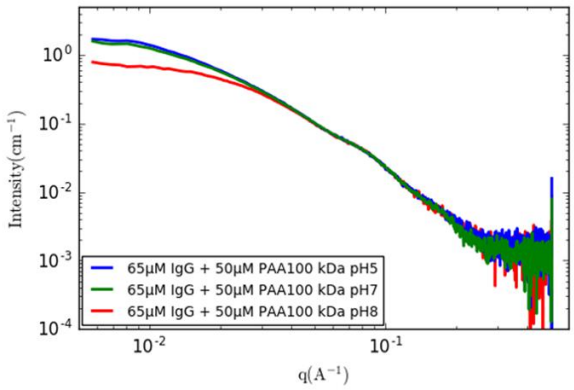

Figure 2. 34. SAXS scattering intensities *I(q)* of the IgG-PAA mixture with different PAA sizes (30 and 100 kDa) and at different pH (5, 7 and 8). ([IgG]=65µM and [PAA]= 50µM). Table summarizing R_g values as evaluated by Primus program.

Since IgG has an isoelectric point around 7.2, it bears a positive overall charge at pH lower than 7.2. Thus, we can imagine that at this range of pH, electrostatic attractions could take place between IgG and the negatively charged chains of PAA, leading to the formation of complex which results in increase of *I(q)* at small angles. However, the overall charge of IgG at pH 7 is supposed to be almost neutral, and despite of that an increase in intensity was observed. This outcome indicates that the increase of *I(q)* reflecting an increase of the global size of the investigated macromolecules inside the sample may not be due to binding between IgG and

PAA as it was the case with HSA. It could be rather related to a bigger amount of aggregates which increases their contribution in the estimation of R_g. A previous study has showed that, in 0.1 M NaCl solutions, PAA could have a role on IgG unfolding, association, and aggregation via Coulomb and hydrophobic interaction [51]. While, a stabilization of oligomers with PAA chains leading to slow aggregation rate was suggested in solutions without NaCl.

Since experiments were performed at I = 0.15 M, we can think that IgG unfolding and aggregation hypothesis would rather be more consistent with our study. In fact, at a pH below 7, the overall charge of IgG becomes positive which could result in electrostatic attraction with the PAA chains causing partial unfolding of IgG as suggested in the study mentioned above [51]. But this could also bring the protein molecules closer to each other, which could lead to their intermolecular interaction, and so aggregation via Coulomb and hydrophobic interaction.

In order to validate that, chromatographic runs were conducted, where samples of IgG-PAA mixture were flowed in mobile phases with pH maintained at 5, 7 and 8 and containing the studied PAA as explained previously. The chromatographic pattern of IgG at different pH were drawn together, and then for each pH the patterns for the mixture with PAA 30 and 100 kDa were compared to that of IgG.

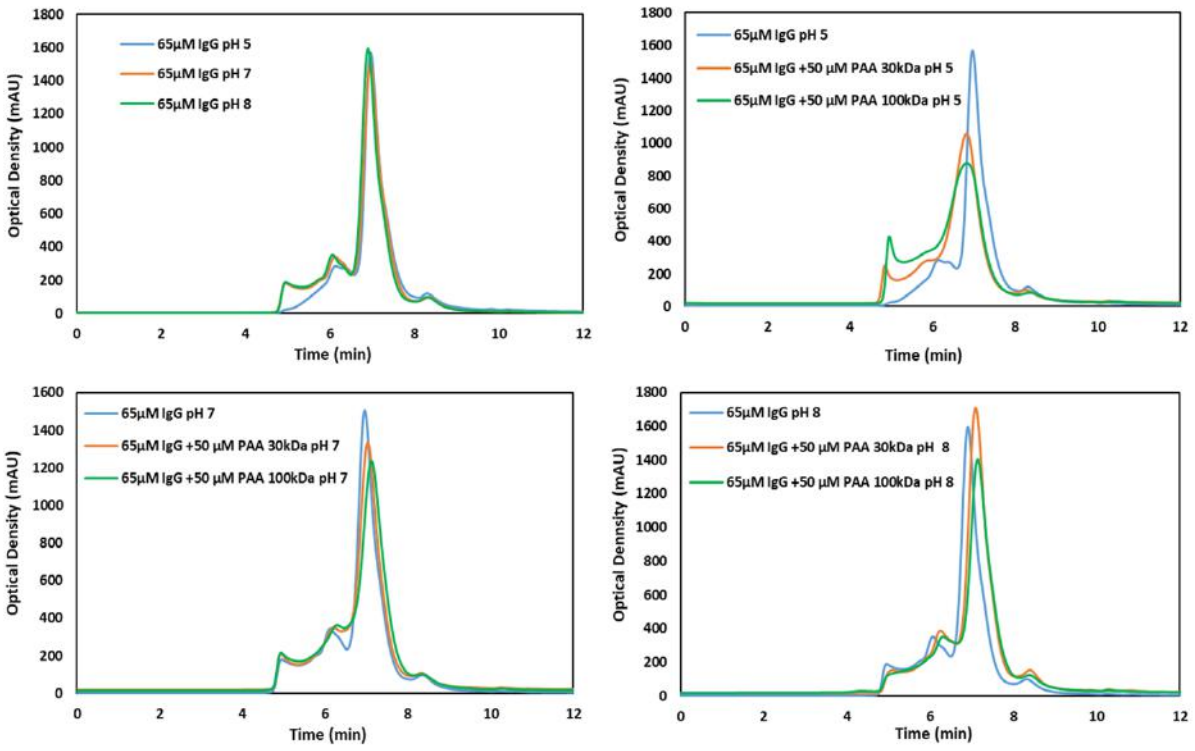

Figure 2. 35. Chromatographic profiles of IgG-$PAA_{30\ kDA}$ and IgG-$PAA_{100\ kDa}$ compared to that of IgG at different pH (5, 7 and 8). [IgG]=65µM and [PAA]=50µM.

The obtained results exposed in Figure 2. 35 confirm first that actually single IgG does not exhibit structural changes due to pH change. Indeed, it can be noticed that the elution peaks of the protein at different pH are perfectly superimposed. However, from these profiles it seems that IgG has more aggregates than HSA did.

After that, different behaviours were observed depending on the pH of the mobile phase when PAA was added to the protein. In fact, no clear shift was observed at pH 7 and 8 after the addition of PAA 30 kDa or PAA 100 kDa, although the SAXS results showed an increase in intensity at small angles at pH 7. This could be due to a greater contribution of aggregates that seems to be somewhat larger after the addition of PAA. As for pH 5, a shift of the elution peak towards higher molecular weights with a greater amount of aggregates is clearly observed. This shift in the elution peak was found to be the same with both PAA 30 and 100 kDa, but the rate of aggregates was higher with the PAA 100 kDa. In addition, the peaks are less resolute, where aggregates are not well separated from the main peak of the protein, which explains the increase of R_g. This upshot supports the hypothesis suggested previously and assuming that a partial aggregation of IgG is taking place after the addition of PAA.

4.9. Study of interaction between PEG and blood protein (HSA and IgG)

In has been revealed in the previous sections that HSA and IgG blood proteins exhibit different behaviours towards a negatively charged polyelectrolyte namely PAA. In fact, this bioactive polymer suggested for the capture of platelets has been found to form complexes with the most abundant protein in plasma (HSA) in some specific conditions of pH an ionic strength. Meanwhile, it did not display a specific interaction with the IgG in these same physicochemical conditions, except for a partial aggregation of this latter.

In this section, the interactions of these blood proteins (HSA and IgG) with a neutral polymer namely PEG known for its resistance to proteins adsorption was investigated. For that, SAXS measurements were performed on the mixture of 10 $g \cdot L^{-1}$ of protein (which makes 150 µM for HSA and 65 µM for IgG) + 500 µM PEG. The experiments were conducted using three sizes of PEG (2, 8 and 20 kDa) with an ionic strength maintained at I = 0.15 M and pH of 5, 7 and 8.

The experimental scattering patterns of proteins at different pH were drawn together as reference to show the stability of the proteins structures with the pH change. Then for every pH we displayed *I(q)* of the protein-PEG mixtures with different PEG sizes compared to that of single protein.

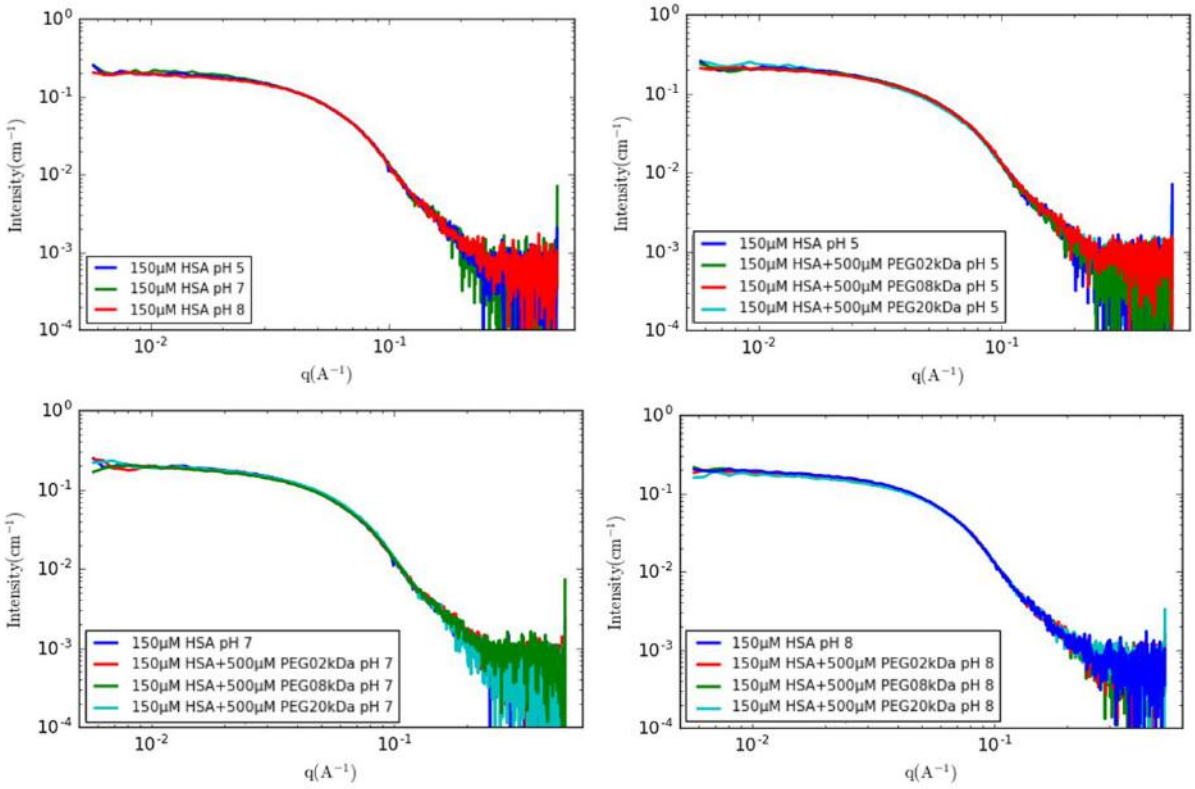

Figure 2. 36. SAXS scattering intensities *I(q)* of HSA-PEG mixture with different PEG sizes (2, 8 and 20 kDa) and at different pH (5, 7 and 8). ([HSA]=150µM and [PEG]= 500µM).

Results shown in Figure 2. 36 and Figure 2. 37 did not show any change in the scattering intensities. Indeed, for both proteins (HSA and IgG) and with the different sizes of PEG, the experimental SAXS spectra remain unchanged in the studied range of pH. This indicates that both HSA and IgG do not undergo through interaction with PEG in these conditions as it was the case with PAA. This could be arising out of the hydrophilicity of PEG which prevents its interaction with proteins through hydrophobic interactions. Besides, PEG is not ionised nor polar in solution and it does not bear neither positive or negative charges, which means that it cannot have electrostatic interactions with the charged proteins.

Some previous studies have attributed the resistance of PEG to protein interaction to its flexibility and to the hydrophilicity of its end group (-OH) [52]. However, other studies reveal that PEG could eventually exhibit weak hydrophobic interactions with proteins in aqueous solutions [53]. Indeed, it has been shown that the hydrophobic CH_2–CH_2 groups of PEG 20kDa could interact with the hydrophobic sites of BSA. It has been stated that such interactions increase with PEG concentration is due to the increased hydrophobicity of the longer PEG chain, and so multiple and steady contact points with proteins [53].

However, nothing of that has been observed in our study even though we used a PEG 2 kDa (PEG methyl ether methacrylate) that has a CH_2=CH-CH_3 hydrophobic end group, which could be due to its small size. But even with the same PEG used in the study mentioned above (PEG 20 kDa), no changes in the scattering intensities was noticed. This indicates that either interactions between PEG and proteins are so week that it is not possible to sense them using SAXS, or no interactions are taking place at all.

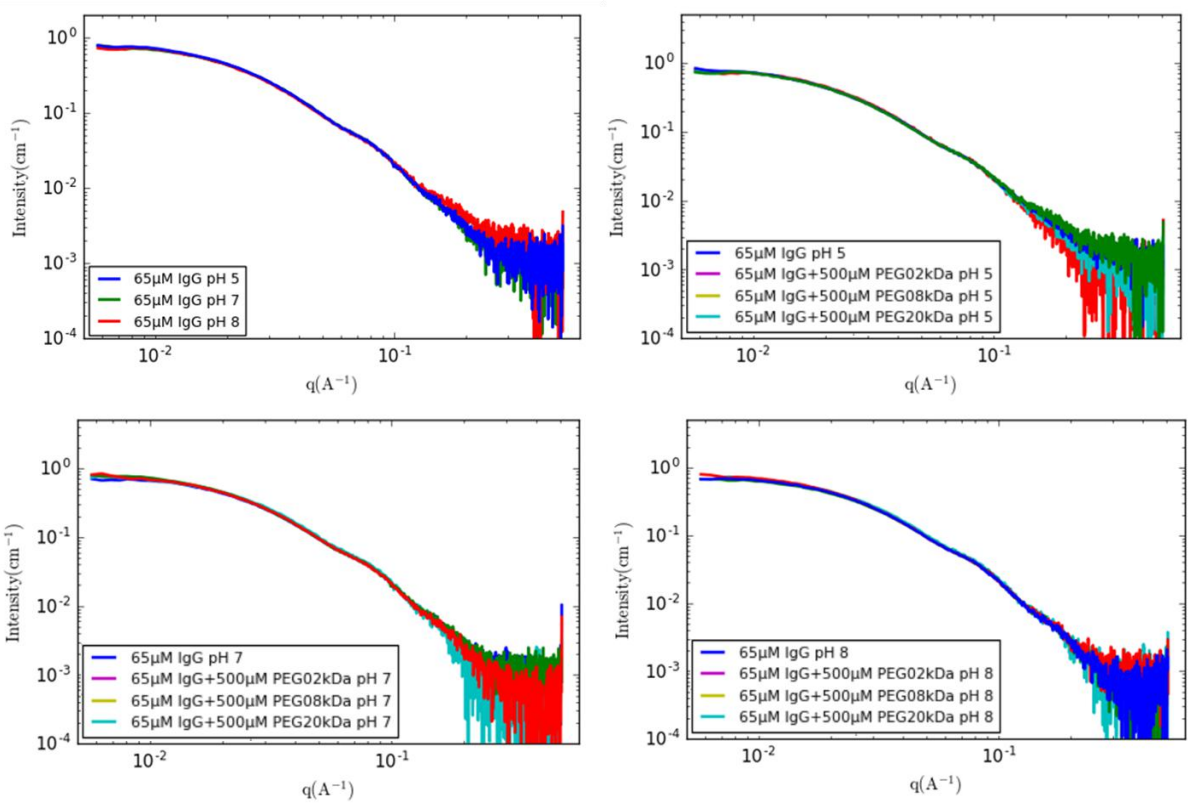

Figure 2. 37. SAXS scattering intensities *I(q)* of IgG-PEG mixture with different PEG sizes (2, 8 and 20 kDa) and at different pH (5, 7 and 8). ([IgG]=65µM and [PEG]= 500µM).

5. Conclusions

SAXS combined to chromatography has been revealed to be a promising tool to probe not only protein behaviour and structure, but even proteins-polymers complexes and interactions.

The study of the HSA-PAA_{100kDa} interactions revealed a complexation phenomenon of protein molecules with the polymer chains. Tests on the effect of the ionic strength showed that this HSA-PAA binding is chiefly an electrostatic interaction, where attractive and repulsive interactions compete. Decreasing the pH to 5 allowed the negative overall charge of the protein to be reduced until the electrostatic attraction between the PAA chains and the positive patches on the protein dominated. The evaluation of the complex size suggests the attachment of several proteins to each polymer chain. Thus, the effect of the ratio of the protein concentration to the polymer concentration was also explored, which revealed that 4 HSA molecules could potentially be bound to each PAA_{100kDa} chain. The complexation model that we proposed, allowed us then to describe the Porod volume of the mixture for different HSA/PAA ratios, which corroborates the stoichiometry of complexation assumed previously.

Besides, this complexation was found to be reversible where the HSA–PAA complex tended to dissociate once put in a diluted medium (without PAA) or at a pH greater than 5. That known, we can imagine that it is now possible to control the interactions between HSA and PAA at the membrane interface by changing the physicochemical conditions (pH, ionic strength).

The SAXS modelling study conducted using Sasview and aimed at describing the complex structure disclosed that the cylinder body ($L \approx 400$ Å) fits well the experimental SAXS data giving an idea of the global shape of the complex, but without providing any structural information. Then, an all-atom model that can describe the final structure of the complex was sought using BUNCH program. Interestingly, the all-atom model found was consistent with that suggested using Sasview. In fact, the complex has been revealed to form an elongated pearl-necklace structure as a cylinder of around 400 Å of length with polymer pellets between the HSA molecules and a non-specific orientation of the HSA.

The HSA-PAA binding as well as the dissociation were found to be reproducible with smaller PAA sizes (5, 30 and 50 kDa) at the same physicochemical conditions of pH and ionic strength outlined previously. However, the complexation stoichiometry has been found to be related to the size of PAA. Indeed, a maximum of 3 HSA molecules has been assumed to be bound to each chains of PAA_{50kDa}, 2 with each chain of PAA_{30kDa}, while 1 HSA was the maximum to bind with PAA_{5kDa} chains.

The formation of the complex seems to be specific to the HSA and PAA solutes. Whether SAXS or chromatography measurements, they do not reveal any specific interaction between IgG and PAA or between neither HSA or IgG and PEG. In fact, IgG has been revealed to be partially unfolded and aggregated via Coulomb and hydrophobic interaction, while both proteins (HSA and IgG) did no display any interaction with PEG.

6. References

[1] A. E. Nel *et al.*, 'Understanding biophysicochemical interactions at the nano-bio interface', *Nat Mater*, vol. 8, no. 7, pp. 543–557, 2009.

[2] Q. Wei *et al.*, 'Protein Interactions with Polymer Coatings and Biomaterials', *Angewandte Chemie International Edition*, vol. 53, no. 31, pp. 8004–8031, 2014.

[3] W. Senaratne, L. Andruzzi, and C. K. Ober, 'Self-Assembled Monolayers and Polymer Brushes in Biotechnology: Current Applications and Future Perspectives', *Biomacromolecules*, vol. 6, no. 5, pp. 2427–2448. 2005.

[4] W. M. de Vos, P. M. Biesheuvel, A. de Keizer, J. M. Kleijn, and M. A. Cohen Stuart, 'Adsorption of the Protein Bovine Serum Albumin in a Planar Poly(acrylic acid) Brush Layer As Measured by Optical Reflectometry', *Langmuir*, vol. 24, no. 13, pp. 6575–6584, 2008.

[5] S. Wang *et al.*, 'Protein immobilization and separation using anionic/cationic spherical polyelectrolyte brushes based on charge anisotropy', *Soft Matter*, vol. 9, no. 47, pp. 11276–11287, 2013.

[6] K. W. Mattison, I. J. Brittain, and P. L. Dubin, 'Protein-Polyelectrolyte Phase Boundaries', *Biotechnol. Prog.*, vol. 11, no. 6, pp. 632–637, 1995.

[7] A. Pourjavadi and Z. M. Tehrani, 'Mesoporous silica nanoparticles with bilayer coating of poly(acrylic acid-co-itaconic acid) and human serum albumin (HSA): A pH-sensitive carrier for gemcitabine delivery', *Materials Science and Engineering: C*, vol. 61, pp. 782–790, 2016.

[8] M. Das, S. Mardyani, W. C. W. Chan, and E. Kumacheva, 'Biofunctionalized pH-Responsive Microgels for Cancer Cell Targeting: Rational Design', *Advanced Materials*, vol. 18, no. 1, pp. 80–83, 2006.

[9] H. Chen and Y.-L. Hsieh, 'Enzyme immobilization on ultrafine cellulose fibers via poly(acrylic acid) electrolyte grafts', *Biotechnology and Bioengineering*, vol. 90, no. 4, pp. 405–413, 2005.

[10] P. Dubin, J. Bock, R. Davis, D. N. Schulz, and C. Thies, *Macromolecular Complexes in Chemistry and Biology*. Springer Science & Business Media, 2012.

[11] C. Zhang, J. Jin, J. Zhao, W. Jiang, and J. Yin, 'Functionalized polypropylene non-woven fabric membrane with bovine serum albumin and its hemocompatibility enhancement', *Colloids and Surfaces B: Biointerfaces*, vol. 102, pp. 45–52, 2013.

[12] Y.-C. Chiag, Y. Chang, W.-Y. Chen, and R. Ruaan, 'Biofouling Resistance of Ultrafiltration Membranes Controlled by Surface Self-Assembled Coating with PEGylated Copolymers', *Langmuir*, vol. 28, no. 2, pp. 1399–1407, 2012.

[13] P. A. George, B. C. Donose, and J. J. Cooper-White, 'Self-assembling polystyrene-block-poly(ethylene oxide) copolymer surface coatings: Resistance to protein and cell adhesion', *Biomaterials*, vol. 30, no. 13, pp. 2449–2456, 2009.

[14] C. Leggio, L. Galantini, and N. Viorel Pavel, 'About the albumin structure in solution: cigar Expanded form versus heart Normal shape', *Physical Chemistry Chemical Physics*, vol. 10, no. 45, pp. 6741–6750, 2008.

[15] C. L. Cooper, P. L. Dubin, A. B. Kayitmazer, and S. Turksen, 'Polyelectrolyte–protein complexes', *Current Opinion in Colloid & Interface Science*, vol. 10, no. 1, pp. 52–78, 2005.

[16] A. Basak Kayitmazer, D. Seeman, B. Baykal Minsky, P. L. Dubin, and Y. Xu, 'Protein – polyelectrolyte interactions', *Soft Matter*, vol. 9, no. 9, pp. 2553–2583, 2013.

[17] S. Rosenfeldt, A. Wittemann, M. Ballauff, E. Breininger, J. Bolze, and N. Dingenouts, 'Interaction of proteins with spherical polyelectrolyte brushes in solution as studied by small-angle x-ray scattering', *Physical Review E*, vol. 70, no. 6, 2004.

[18] W. Wang *et al.*, 'Protein Immobilization onto Cationic Spherical Polyelectrolyte Brushes Studied by Small Angle X-ray Scattering', *Biomacromolecules*, vol. 18, no. 5, pp. 1574–1581, 2017.

[19] M. Topuzoğulları, N. S. Çimen, Z. Mustafaeva, and M. Mustafaev, 'Molecular-weight distribution and structural transformation in water-soluble complexes of poly(acrylic acid) and bovine serum albumin', *European Polymer Journal*, vol. 43, no. 7, pp. 2935–2946, 2007.

[20] S. Yu *et al.*, 'Interaction of human serum albumin with short polyelectrolytes: a study by calorimetry and computer simulations', *Soft Matter*, vol. 11, no. 23, pp. 4630–4639, 2015.

[21] Q. Ran *et al.*, 'Interaction of human serum albumin with dendritic polyglycerol sulfate: Rationalizing the thermodynamics of binding', *The Journal of Chemical Physics*, vol. 149, no. 16, p. 163324, 2018.

[22] O. Hollmann and C. Czeslik, ‘Characterization of a Planar Poly(acrylic acid) Brush as a Materials Coating for Controlled Protein Immobilization’, *Langmuir*, vol. 22, no. 7, pp. 3300–3305, 2006.

[23] M. V. Petoukhov and D. I. Svergun, ‘Global Rigid Body Modeling of Macromolecular Complexes against Small-Angle Scattering Data’, *Biophysical Journal*, vol. 89, no. 2, pp. 1237–1250, 2005.

[24] C. E. Merzougui *et al.*, ‘Pearl-necklace assembly of human serum albumin with the poly(acrylic acid) polyelectrolyte investigated using small angle X-ray scattering (SAXS)’, *Soft Matter*, vol. 16, no. 43, pp. 9964–9974, 2020.

[25] J. Pérez and Y. Nishino, ‘Advances in X-ray scattering: from solution SAXS to achievements with coherent beams’, *Current Opinion in Structural Biology*, vol. 22, no. 5, pp. 670–678, 2012.

[26] A. G. Kikhney and D. I. Svergun, ‘A practical guide to small angle X-ray scattering (SAXS) of flexible and intrinsically disordered proteins’, *FEBS Letters*, vol. 589, no. 19, Part A, pp. 2570–2577, 2015.

[27] L. Boldon, F. Laliberte, and L. Liu, ‘Review of the fundamental theories behind small angle X-ray scattering, molecular dynamics simulations, and relevant integrated application’, *Nano Reviews*, vol. 6, no. 1, p. 25661, 2015.

[28] M. H. J. Koch, P. Vachette, and D. I. Svergun, ‘Small-angle scattering: a view on the properties, structures and structural changes of biological macromolecules in solution’, *Quarterly Reviews of Biophysics*, vol. 36, no. 2, pp. 147–227, 2003.

[29] D. I. Svergun and M. H. J. Koch, ‘Small-angle scattering studies of biological macromolecules in solution’, *Rep. Prog. Phys.*, vol. 66, no. 10, pp. 1735–1782, 2003.

[30] H. D. T. Mertens and D. I. Svergun, ‘Structural characterization of proteins and complexes using small-angle X-ray solution scattering’, *Journal of Structural Biology*, vol. 172, no. 1, pp. 128–141, 2010.

[31] P. V. Konarev, V. V. Volkov, A. V. Sokolova, M. H. J. Koch, and D. I. Svergun, ‘PRIMUS: a Windows PC-based system for small-angle scattering data analysis’, *J Appl Cryst*, vol. 36, no. 5, pp. 1277–1282, 2003.

[32] M. V. Petoukhov, P. V. Konarev, A. G. Kikhney, and D. I. Svergun, ‘ATSAS 2.1 – towards automated and web-supported small-angle scattering data analysis’, *J Appl Cryst*, vol. 40, no. s1, pp. s223–s228, 2007.

[33] *Neutron, X-rays and Light. Scattering Methods Applied to Soft Condensed Matter*, New edition edition. Amsterdam; Boston: North Holland, 2002.

[34] R. Girardot, G. Viguier, J. Pérez, and M. Ounsy, 'FOXTROT: A JAVA-BASED APPLICATION TO REDUCE AND ANALYSE SAXS AND WAXS PILES OF 2D DATA AT SYNCHROTRON SOLEIL', p. 1.

[35] D. I. Svergun, 'Determination of the regularization parameter in indirect-transform methods using perceptual criteria', *J Appl Cryst*, vol. 25, no. 4, pp. 495–503, 1992.

[36] D. Svergun, C. Barberato, and M. H. J. Koch, 'CRYSOL – a Program to Evaluate X-ray Solution Scattering of Biological Macromolecules from Atomic Coordinates', *J Appl Cryst*, vol. 28, no. 6, pp. 768–773, 1995.

[37] SasView, 'Publications'. https://sasview.github.io/publications/.

[38] M. V. Petoukhov and D. I. Svergun, 'Analysis of X-ray and neutron scattering from biomacromolecular solutions', *Current Opinion in Structural Biology*, vol. 17, no. 5, pp. 562–571, 2007

[39] P. Bernadó, E. Mylonas, M. V. Petoukhov, M. Blackledge, and D. I. Svergun, 'Structural Characterization of Flexible Proteins Using Small-Angle X-ray Scattering', *Journal of the American Chemical Society*, vol. 129, no. 17, pp. 5656–5664, 2007.

[40] P. V. Konarev, M. V. Petoukhov, V. V. Volkov, and D. I. Svergun, 'ATSAS 2.1, a program package for small-angle scattering data analysis', *J Appl Cryst*, vol. 39, no. 2, pp. 277–286, 2006.

[41] P. Roblin, 'Caractérisation structurale de la polykétide synthase pks13 de mycobactérium tuberculosis : étude structurale des composés S et F de la gamma-hémolysine de staphylococcus aureus sous forme d'hétérodimère covalent', PhD thesis, Toulouse 3, 2007.

[42] B. Chu and B. S. Hsiao, 'Small-Angle X-ray Scattering of Polymers', *Chem. Rev.*, vol. 101, no. 6, pp. 1727–1762, 2001.

[43] X. Xu, S. Angioletti-Uberti, Y. Lu, J. Dzubiella, and M. Ballauff, 'Interaction of Proteins with Polyelectrolytes: Comparison of Theory to Experiment', *Langmuir*, vol. 35, no. 16, pp. 5373–5391, 2019.

[44] E. Seyrek, P. L. Dubin, C. Tribet, and E. A. Gamble, 'Ionic Strength Dependence of Protein-Polyelectrolyte Interactions', *Biomacromolecules*, vol. 4, no. 2, pp. 273–282, 2003.

[45] Y. Xu, M. Mazzawi, K. Chen, L. Sun, and P. L. Dubin, 'Protein Purification by Polyelectrolyte Coacervation: Influence of Protein Charge Anisotropy on Selectivity', *Biomacromolecules*, vol. 12, no. 5, pp. 1512–1522, 2011.

[46] K. Achazi *et al.*, 'Understanding the Interaction of Polyelectrolyte Architectures with Proteins and Biosystems', *Angewandte Chemie International Edition*, vol. 60, no. 8, pp. 3882–3904, 2021.

[47] C. Yigit, J. Heyda, M. Ballauff, and J. Dzubiella, 'Like-charged protein-polyelectrolyte complexation driven by charge patches', *J. Chem. Phys.*, vol. 143, no. 6, p. 064905. 2015.

[48] C. Yigit, J. Heyda, and J. Dzubiella, 'Charged patchy particle models in explicit salt: Ion distributions, electrostatic potentials, and effective interactions', *J. Chem. Phys.*, vol. 143, no. 6, p. 064904, 2015.

[49] C. Yigit, M. Kanduč, M. Ballauff, and J. Dzubiella, 'Interaction of Charged Patchy Protein Models with Like-Charged Polyelectrolyte Brushes', *Langmuir*, vol. 33, no. 1, pp. 417–427, 2017.

[50] M. Dockal, D. C. Carter, and F. Rüker, 'Conformational Transitions of the Three Recombinant Domains of Human Serum Albumin Depending on pH', *J. Biol. Chem.*, vol. 275, no. 5, pp. 3042–3050, 2000.

[51] N. Martin, D. Ma, A. Herbet, D. Boquet, F. M. Winnik, and C. Tribet, 'Prevention of Thermally Induced Aggregation of IgG Antibodies by Noncovalent Interaction with Poly(acrylate) Derivatives', *Biomacromolecules*, vol. 15, no. 8, pp. 2952–2962, 2014.

[52] R. S. Kane, P. Deschatelets, and G. M. Whitesides, 'Kosmotropes Form the Basis of Protein-Resistant Surfaces', *Langmuir*, vol. 19, no. 6, pp. 2388–2391, 2003.

[53] J. Wu *et al.*, 'Probing the weak interaction of proteins with neutral and zwitterionic antifouling polymers', *Acta Biomaterialia*, vol. 10, no. 2, pp. 751–760, 2014.

Chapter III.

Membrane surface modification and investigation of blood proteins adsorption onto

1. Introduction

It has been shown in the previous chapter that in some specific physicochemical conditions, the polymers suggested for the membrane functionalization such as PAA exhibit a specific interaction or not in solution with some blood proteins such as HSA and IgG. However, this does not mean that the interactions between these proteins and the same polymer fixed at the interface of a membrane would be similar to those revealed in solution. Thus, the reproducibility of these interactions on a functionalized membrane surface was investigated in this chapter, but since the modification of the membrane surface is an essential step, it was first explicitly explored.

Many studies have investigated surface modification of polymeric membranes in order to capitalize on their usefulness in filtration processes [1], [2]. Depending on the application, some physical, chemical or biological characteristics are incorporated into the surface to enhance a specific affinity with a target solute or prevent an unwanted phenomenon. Wherefore, the appropriate modification technique to use among many others is often explored to achieve excellent hydrophilicity and biocompatibility of the membrane. Overall, the modification technique can be either physical or chemical depending on whether or not a chemical reaction takes place during the modification process [3]. Although chemical methods allow to control better the deposition of the modifying layer, the physical modification is simpler, cost effective, and environmentally friendly [1]. One of the most common techniques based on physical processes is coating via physisorption. It is a simple method wherein a material is deposited on the membrane to form a thin layer and non-covalently adheres to the surface mainly because of van der Waals attractive interactions [4].

In this chapter, the functionalization of hydrophobic PVDF membranes surfaces is studied using coating by immersion, which involves the physical adsorption, an interesting membrane surface modification technique due to its simplicity and scalability. It only involves two steps: 1) immersion of the membrane in the coating bath (copolymer solution) for a specific time followed by 2) drying to remove residual solvent for the characterization of the membrane. The coating is performed using different copolymers as surface modifiers such as polystyrene-block-poly(acrylic acid) (PS-b-PAA) and polystyrene-block-poly(ethylene oxide) (PS-b-PEO).

Since coating via physisorption relies on non-covalent interactions between the coating layer and the membrane surface, the coating amount depends on the extent of interaction between the two. That can be influenced by the nature of the coating copolymer (polymer chain length,

hydrophobic/hydrophilic block ratio, configuration), of the substrate and process conditions. Thus, to get the best yield of this modification, the optimization of the process was conducted at room temperature by tuning different operating conditions (coating time, copolymer concentration, hydrophobic/hydrophilic chain length …etc), and it is discussed later in this chapter.

After that, the adsorption of blood proteins (HSA mostly and IgG) on the modified PVDF membranes was investigated using mainly Fourier-transform infrared spectroscopy (FTIR). As stated earlier, it allows to compare the interactions that could take place on a modified interface to those revealed in the previous chapter to happen in solution between blood proteins (HSA and IgG) and polymers (PAA and PEG) at some specific physicochemical conditions of pH and ionic strength. Thus, the effect of these conditions (pH and ionic strength) found to be decisive on the happening or not of the protein-polymer interactions was assessed.

As stated in chapter one, a training on the copolymers synthesis and membrane surface modification was carried out during a 6-weeks stay in the Research and Development Center for Membrane Technology (Chung Yuan Christian University, ChungLi, Taiwan). In addition, the adsorption of platelets on polystyrene well plates modified with some PS-PAA and PS-PEG copolymers was tested, and results are given in **Appendix A**.

It is important to note that two master students (Abigail Rosales and Sharath Jayakumar) hired to work on the project for 6-months each one have contributed to conduct some experiments reported in this chapter.

2. Literature review on parameters affecting coating

2.1. Effect of coating time

Optimization of coating time is rarely discussed in the literature related to membrane coating. Researchers usually specify coating time without further explanation as to why that time was used. Intuitively, an increase in coating time should lead to more coating since the copolymers are given enough time to assemble on the surface. This was confirmed in the literature when PVDF membranes were coated with PS-PEGMA copolymers [5]. Besides, a study investigating the variation of the coating time from 2 to 12h showed an increase in deposition degree of tannic acid and tetraethylenepentamine on PVDF membranes until it reached a plateau at 7h [6]. Similarly, an increasing trend with plateau was also observed when PVDF membrane was coated with polystyrene-poly(sulfobetaine methacrylate) (PS-r-PSBMA) [7]. These studies suggest that the adsorption process reaches a saturation point at longer coating time. That's because after certain time of coating the copolymers in the solution need to overcome the barrier created by the already attached copolymers. Consequently, coating becomes less and less favorable as coating time increases. Thus, optimum coating time depends on the studied copolymer/substrate system and should be established for every system.

The results obtained from these studies display some adsorption kinetics that could be described by the adsorption models reported in section 4.1 of chapter I such as Langmuir model that assumes the monolayer adsorption. However as stated in this same section, deviations from the model could be observed in the case of copolymer adsorption related to the copolymer specific properties such as, configuration, size, hydrophobic/hydrophilic ratio, etc.

2.2. Effect of copolymer concentration

Copolymer concentration is a parameter to be considered in optimizing the coating process. Studies have shown that coating density increases with the copolymer concentration until it reaches a plateau regardless of the copolymer configuration [5], [8], which could be described as stated above by the well-known adsorption models such as Langmuir isotherm. However, as stated in next paragraph, the hydrophobic/hydrophilic segment ratio also plays a significant role in coating concentration efficiency [9], which leads to deviation from the adsorption model.

According to the literature, varying the concentration of poly(styrene-r-4-vinylpyridine) coated on PVDF membranes showed an increase in coating density with copolymer concentration [10]. Results exhibit a plateau reached at larger concentrations (10 $mg \cdot mL^{-1}$) which could be an indication of the saturation of the interface.

Many other studies have investigated the effect of copolymer concentration on the coating density. For instance, it has been assessed in the case of PS-r-PSBMA deposited on PVDF membrane surface [7]. Results revealed a decrease of the water contact angle and fibrinogen adsorption when increasing the copolymer concentration in solution until the protein adsorption reached a plateau implying the potential increase of coating on the surface until it reached saturation. As shown in Figure 3. *1*, similar trend was obtained when the coating density increased with the copolymer concentration and eventually reaches a plateau in the case of PVDF membranes coated with poly(propylene oxide)-block-poly(sulfobetaine methacrylate) PPO-b-PSBMA [11].

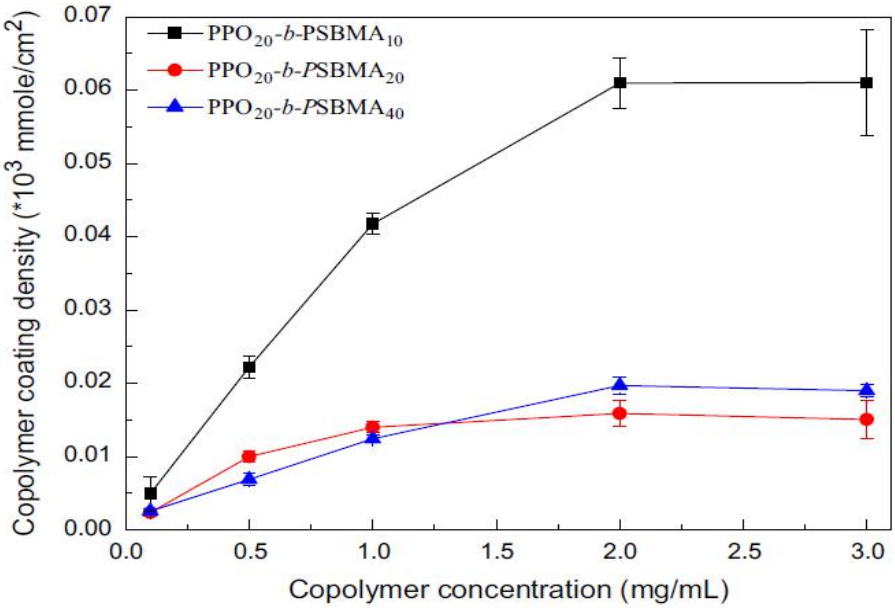

Figure 3. 1. Effect of varying concentration of poly(propylene oxide)-block-poly (sulfobetaine methacrylate) copolymer in solution and PPO/PSBMA ratio on copolymer coating density [11].

The results of these studies suggest that the occurrence of plateau or saturation is common. This is because at higher concentration, the surface may be fully covered, and the copolymers already attached to the surface may prevent the copolymers in the solution to reach the surface and be attached to it. Thus, copolymer concentration should be optimized when designing a coating process to avoid the excess use of coating material.

2.3. Effect of Hydrophobic/hydrophilic chain length

The adsorption of a copolymer on a membrane surface can be optimized by controlling the copolymer hydrophobic/hydrophilic block ratio and the block molecular size or chain length.

Studies of PS-PEGMA coating on hydrophobic PVDF membranes have shown that increasing the chain length of the hydrophilic PEGMA blocks reduces the copolymer adhesion [9], [12]. An increase in chain length of PEGMA while keeping the chain length of PS anchoring block constant (also decrease in PS/PEGMA ratio) decreased the adsorbed coating and required higher copolymer concentration to reach the plateau (Figure 3. 2) [9]. This means that larger PEGMA moieties introduced increased steric hindrance blocking the access of PS moieties to the PVDF surface.

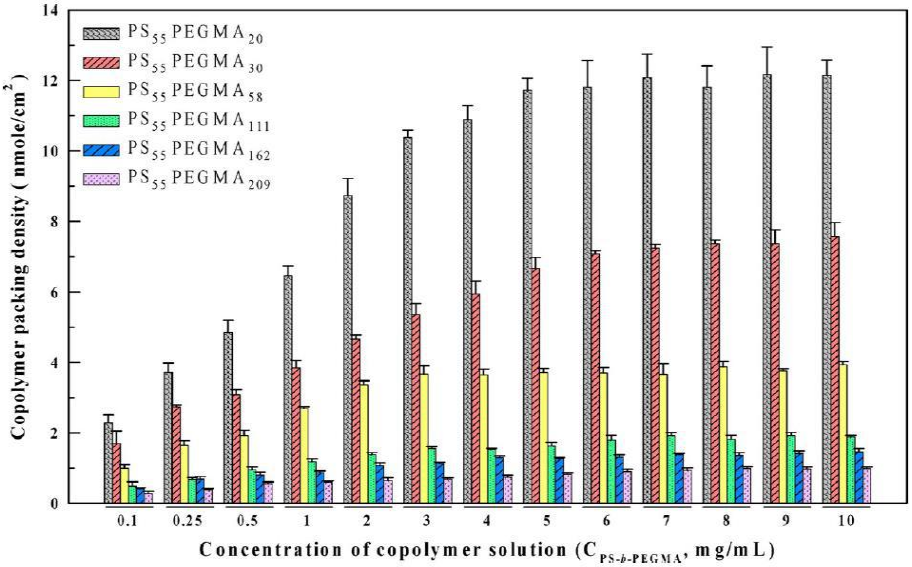

Figure 3. 2. PS-b-PEGMA coating density on PVDF membrane vs concentration of copolymer solution used as coating bath for different PS/PEGMA ratio [9].

The same behaviour is reported in a study aiming at improving the biocompatibility of PVDF membranes by coating them with PPO-b-PSBMA [11]. PPO was used as an anchoring block since it has a high tendency to establish hydrophobic interactions with any hydrophobic membrane material. PPO block length was kept constant while PSBMA chain length was varied. The highest coating density was obtained at the lowest PSBMA/PPO ratio (0.5) where PSBMA had the shortest length (Figure 3. 1), which was attributed to two factors. First, when the PSBMA segment is relatively short, hydrophobic interactions between the PVDF membrane and PS dominate over hydrophilic interactions between the solvent and the PSBMA segment. Conversely, when the PSBMA segment is long (PSBMA/PPO ratio=1 and 2), hydrophilic interactions become stronger since more PSBMA is available. As a result, it diminishes the coating efficiency driven by hydrophobic interactions. Second, similar to the previous study, longer hydrophilic PSBMA chains length increase steric hindrance. In addition, it can be observed that the effect of PSBMA chain length on coating density is not linear (Figure 3. 1).

Another example of the hydrophobic/hydrophilic chain length effect is shown in a study mentioned before, where PVDF membrane surface was modified with a random copolymer of PS and PSBMA (PS-r-PSBMA) [7]. In this study, the adsorption of fibrinogen was found to be higher for bigger hydrophilic block amounts (70 % wt. PSBMA). This could mean that there was an insufficient coating amount due to larger PSBMA segment implying that it was difficult to establish hydrophobic interactions between the PS block and PVDF surface. These studies show that an increase in the hydrophilic blocks size does not improve the coating density. Thus, to achieve good coating coverage, the hydrophilic interactions between the solvent and copolymer, and steric hindrance caused by hydrophilic block must be minimized.

2.4. Effect of copolymer configuration

Copolymer configuration also plays a role in coating adhesion. This was proved in a previous study that investigated the effect of varying PS-PEGMA copolymer configuration (diblock, triblock, random) with similar copolymer molecular weights and hydrophilic/hydrophobic block (PS/PEGMA) ratio on coating density [8]. The random copolymer has the highest coating density, followed by diblock, then triblock. This was attributed to the random arrangement of the styrene units in the random copolymer as illustrated in Figure 3. 3. The latter provided the most anchoring configurations to the PS surface than diblock and triblock copolymers assuming there are no chain repulsion and minor steric hindrance (Figure 3. 3).

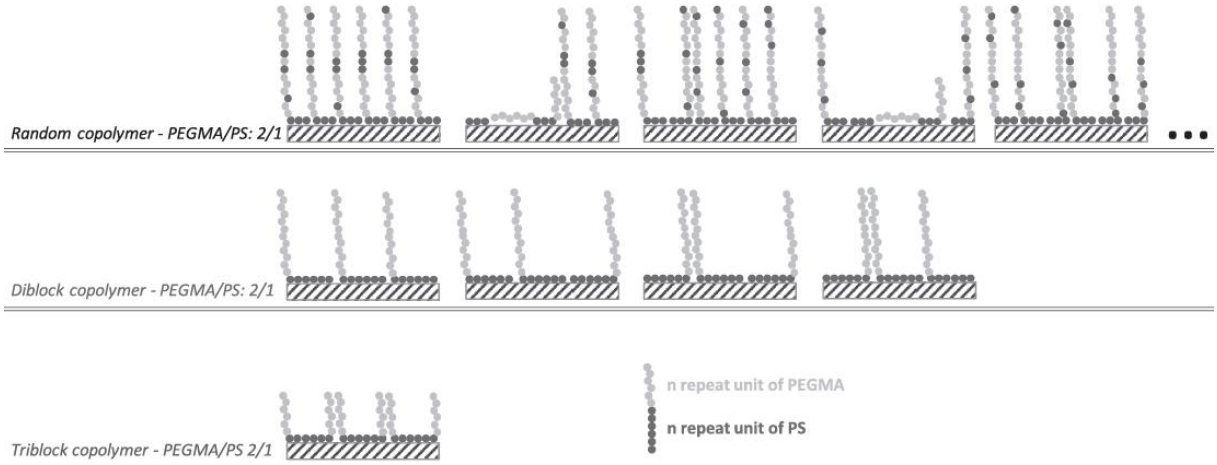

Figure 3. 3. Proposed assembly combinations of random, diblock and triblock PS-PEGMA copolymers on PS surfaces [8].

Also, it is possible to have multilayer coating with random copolymers since the hydrophobic blocks are not completely in contact with the PS surface. In fact, the available PS blocks can have intermolecular interactions leading to multilayer coating [8].

A similar trend in coating density was found when various PS-PEGMA copolymer configurations were used to coat PVDF membranes [12]. The random copolymer has a higher coating density than di-block copolymer whether it has a higher or a lower molecular weight (Figure 3. 4).

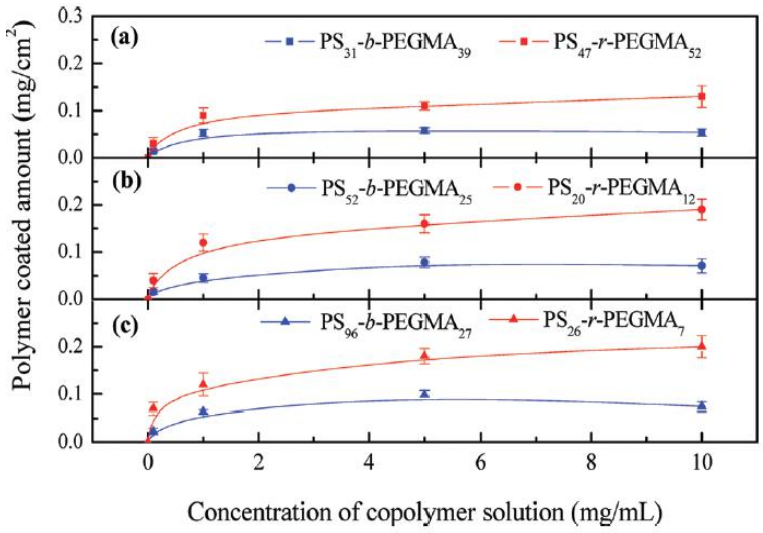

Figure 3. 4. Block and random PS-PEGMA coating density on PVDF membrane vs concentration of copolymer solution for a) PS/PEGMA ratio = 0.8-0.9, b) PS/PEGMA ratio = 1.7-2.1, and c) PS/PEGMA ratio = 3.7-3.9 [12].

Another study using FTIR mapping to identify PS-PEGMA coating presence and to analyze its heterogeneity on PVDF membranes showed a different trend than the previous studies [5]. Results showed that the diblock copolymer had a better coating coverage level than the random copolymer at lower copolymer concentrations (1 and 5 mg·mL^{-1}) but similar at a higher concentration (10 mg·mL^{-1}). In addition, the diblock copolymer had slightly better anti-adsorption properties towards BSA protein than the random one at lower concentration (1 mg·mL^{-1}) but similar at 5 and 10 mg·mL^{-1}. The difference in the trend from the first study could be due to different surfaces used. The first study used PS surfaces, which have stronger interaction with the copolymer than PVDF surfaces due to hydrophobic interactions between two groups of the same chemical nature. The second study used PEGMA blocks that were shorter or almost similar chain length with PS blocks (Figure 3. 4) while the last one used a PEGMA block twice longer than the PS block (PS_{53}-b-$PEGMA_{124}$ and PS_{61}-r-$PEGMA_{121}$). As mentioned earlier, long PEGMA brushes could introduce steric hindrance minimizing its coating efficiency.

2.5. Summary of different parameters effect on coating

The table below (Table 3. 1) summarizes the main trends that can be observed regarding the effect of the different parameters reported in this section on coating density evolution, as well as the deviations from Langmuir adsorption model related to each parameter.

Table 3. 1. Effects of the different parameters reported in this section on the coating density evolution, as well as the deviations from Langmuir adsorption model related to each parameter.

Parameter	**Effect on coating density**	**Comparison to Langmuir adsorption model**
Coating time	The coating density increases with coating time increase until it reaches a plateau.	Matches with the adsorption kinetic described by the model theory.
Copolymer concentration	The coating density increases with the increase of copolymer concentration in solution until it reaches a plateau.	Matches with the adsorption kinetic described by the model theory.
Hydrophobic/hydrophilic blocks ratio	Larger hydrophilic segment decreases the coating density while it increases with larger hydrophobic blocks.	It could exhibit some deviations from the model theory due to the size of the copolymer segments.
Copolymer configuration	Random copolymers exhibit the highest coating density followed by diblock, then triblock copolymers.	The deviations would be more observed with the random copolymer because of the multilayer adsorption.

3. Materials and methods

3.1. Materials

Commercial polyvinylidene fluoride (PVDF) microporous membranes (VVHP, Millipore Co.) with an average pore size of 0.1 µm and a thickness of 125 µm were used as-received for the whole study. The specific properties of this membrane are summarized in Table 3. 2 below.

Table 3. 2. Specific properties of the commercial PVDF membrane used in this study as provided by Millipore.

Parameter	**Data given by Millipore**
Pores size	0.1 µm
Thickness	125 µm
Porosity	70 %
Water flux	> 0.33 $mL \cdot min^{-1} \cdot cm^{-2}$
Air flux	3 $L \cdot min^{-1} \cdot cm^{-2}$
Protein adsorption	150 $\mu g \cdot cm^{-2}$
Refraction index	1.42
Wettability	Hydrophobic
Bubble point à 23°C	≥ 4.8 bar
Maximal temperature of use	85 °C

The copolymers set used in this study were purchased from Sigma Aldrich for PS_{30}-b-PAA_2, PS_{30}-b-PAA_5 and PS_{30}-b-PAA_8, and from Polymer Source (Montreal, Canada) for the other copolymers: PS_{13}-b-PAA_{22}, PS_{26}-b-PAA_{76}, PS_{100}-b-PAA_{107}, PS_{28}-b-PEO_{13}, PS_{16}-b-PEO_{72} and PS_{12}-b-PEO_{30}. They all have a Polydispersity Index (PDI) ≤ 1.3, implying minor heterogeneities on the distribution of the molecular mass. The PDI of a polymer is calculated as follows:

$$PDI = \frac{M_w}{M_n} \tag{3.1}$$

Where M_w is the weight average molecular weight and M_n is the number average molecular weight. The size of the copolymers used in this study has been evaluated using dynamic light scattering (DLS). After that, the evaluated hydrodynamic diameter (D_h) was used to estimate the copolymers radius of gyration using the following equation [13]:

$$R_h = 0{,}665 \times R_g \quad (3.2)$$

Where $R_h = D_h/2$ is the hydrodynamic radius and R_g is the radius of gyration.

All the copolymers used in the study with their average molecular weight, PDI, molecular structure and the evaluated hydrodynamic diameter and radius of gyration are summarized in the Table 3. 3.

Absolute ethanol ($EtOH_{abs}$) and tetrahydrofuran (THF) used to solubilize the copolymer were purchased from VWR Chemicals Avantor® and Acros Organics, respectively. As for phosphate buffered saline (PBS) solution 10X (BP399, Fisher BioReagents), it was diluted to PBS 1X (pH=7.4; I=137mM) using ultrapure water before use. Ultrapure water was purified using ELGA PURELAB Prima purification system with an ELGA PURELAB Classic water purification system (final minimum resistivity of 18 MΩcm).

As for blood proteins used for the proteins adsorption study, ɣ-globulins from human blood (G4386), and albumin from human serum (A1653) were purchased from Sigma-Aldrich.

Table 3. 3. List of copolymers used for surface modification with their properties.

Formula	M_n (kDa)° 1Da=1g.mol^{-1}	PDI° M_w/M_n	D_h* (nm)	R_g* (nm)	Molecular structure
PS_{30}-b-PAA_2	PS ≈ 27-31 PAA ≈ 1-2 $M_{n\ average}$ ≈ 28-33	≤ 1.1	4.6	3.5	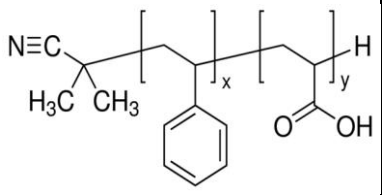
PS_{30}-b-PAA_5	PS ≈ 27-31 PAA ≈ 4-6 $M_{n\ average}$ ≈ 31-37	≤ 1.3	5.1	3.8	
PS_{30}-b-PAA_8	PS ≈ 27-33 PAA ≈ 7-9 $M_{n\ average}$ ≈ 34-42	≤ 1.3	5.9	4.4	
PS_{13}-b-PAA_{22}	PS ≈ 13 PAA ≈ 22 $M_{n\ average}$ ≈ 35	≤ 1.3	5.4	4.1	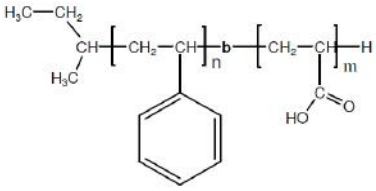
PS_{26}-b-PAA_{76}	PS ≈ 26 PAA ≈ 76 $M_{n\ average}$ ≈ 102	≤ 1.2	8.3	6.2	
PS_{100}-b-PAA_{107}	PS ≈ 100 PAA ≈ 107 $M_{n\ average}$ ≈ 207	≤ 1.1	12.9	9.7	
PS_{28}-b-PEO_{13}	PS ≈ 28 PAA ≈ 13 $M_{n\ average}$ ≈ 41	≤ 1.08	4.8	3.6	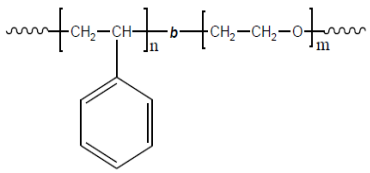
PS_{16}-b-PEO_{72}	PS ≈ 16 PAA ≈ 72 $M_{n\ average}$ ≈ 88	≤ 1.08	7.5	5.6	
PS_{12}-b-PEO_{30}	PS ≈ 12 PAA ≈ 30 $M_{n\ average}$ ≈ 42	≤ 1.1	4.8	3.6	

* Data obtained by DLS measurement performed in this study.

° Data provided by the furnishers of the copolymers.

3.2. Methods for experiments

3.2.1. Coating of PVDF membranes

Operating process, coating time, copolymer concentration, and the hydrophobic/hydrophilic chain length were investigated to optimize the coating procedure using the different copolymers mentioned in the materials paragraph as surface modifiers. The experiments were performed at an average room temperature measured to be around 22 ± 3 °C.

The copolymer solutions were prepared by dissolving the desired weight of copolymer in 50% (v/v) $EtOH_{abs}$-THF solvent. An area of 0.5 cm^2 of PVDF membrane was then immersed in 1 mL of the copolymer solution at the desired concentration and for the required time. For each set of experiments, a pristine membrane was taken as blank and was treated the same way as the coated ones but using the $EtOH_{abs}$-THF solvent instead of copolymer solution.

For the change in process conditions, two operating processes were tested (Figure 3. 5) with the following order of procedure: 1) Immersion - Washing - Drying (IWD) and 2) Immersion - Drying - Washing (IDW). It is important to note that in the second case the membrane was drained and left to air for one minute before it was put in a Petri dish and placed in the oven to dry. In order to check the stability of coating when washing before and after drying, these two procedures were compared to a third one consisting of two steps only, Immersion and Drying (ID). For all experiments in this part drying time was 2h at 40°C while washing was done three time using PBS 1X solution to remove the non-adsorbed copolymer.

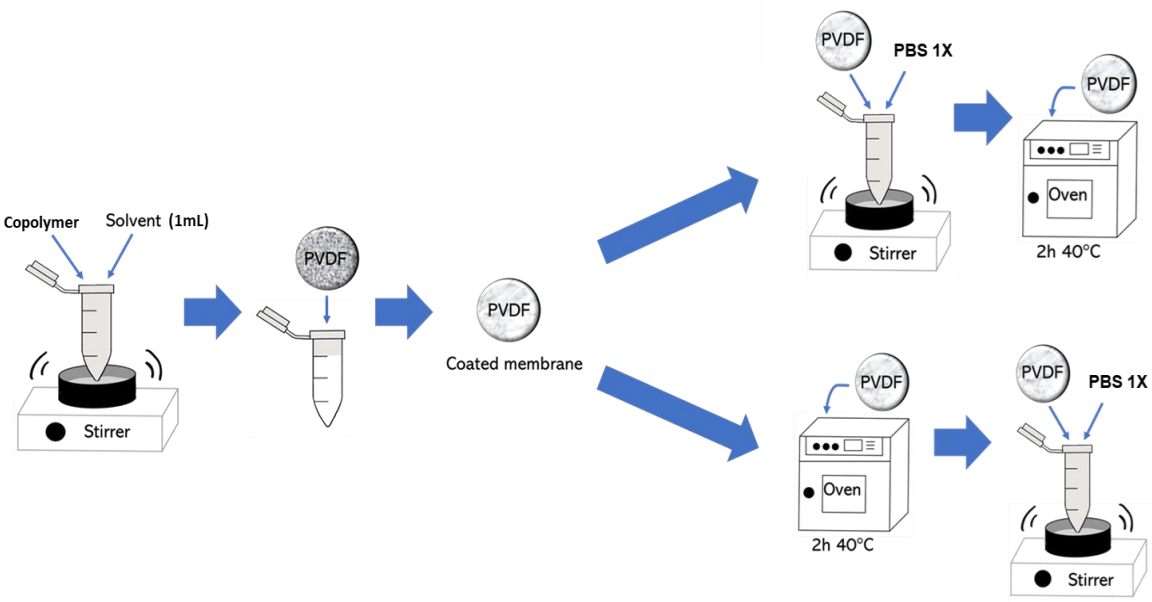

Figure 3. 5. Illustration of the studied coating procedures of PVDF membranes.

As for the optimization of coating time, PVDF membranes have been immersed for 1h, 2h, 4h, and 6 h using 5 mg·mL^{-1} copolymer solution. These experiments have been conducted using two copolymers, PS_{30}-b-PAA_5 and PS_{30}-b-PAA_8, and followed with only one variable changing for the other copolymers. That variable is the copolymer concentration in solution, which was varied from 1 to 10 mg·mL^{-1} while fixing the coating time at 2 hours.

The other optimization condition was to check the copolymer hydrophobic/hydrophilic chain length effect on the coating ability of the copolymer over the membrane surface. Thus, to assess first the hydrophilic part effect, the length of the hydrophobic group was fixed using three copolymers with the same PS size and different PAA sizes. Then, the size of the hydrophobic block was also varied by changing the length of PS using both PS-b-PAA and PS-b-PEO. The experiments were conducted using a copolymer concentration of 5 mg·mL^{-1} and a coating time of 2 hours.

3.2.2. Static adsorption of blood proteins

The protein solutions were prepared by dissolving 1 mg of the desired protein (HSA or IgG) in 1 mL of PBS 1X. They were prepared the day before the adsorption experiment and kept refrigerated. The membrane was modified according to the optimum conditions fixed as mentioned previously. It was then immersed in 1 mL of PBS 1X overnight to hydrate the copolymer structure. Afterwards, PBS was replaced by 1 mg·mL^{-1} of protein solution for 2h at room temperature. Then, it was rinsed three times with PBS to remove the non-adsorbed proteins, and finally the membrane was dried in the oven for 2h at 35°C for further characterization. Figure 3. 6 illustrates the procedure of the protein adsorption on PVDF coated membrane. For each set of experiments, the adsorption of protein on the pristine membrane was performed as reference to compare it to its adsorption on the modified one.

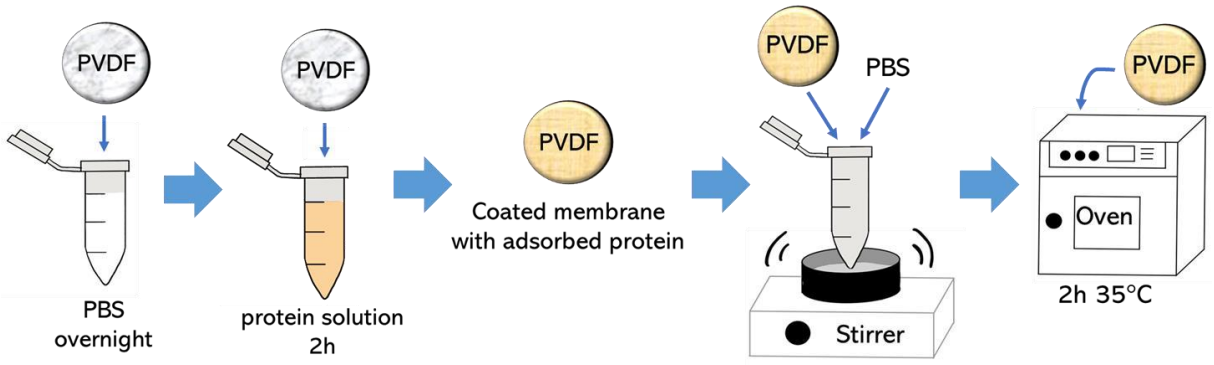

Figure 3. 6. Illustration of the procedure of protein adsorption on the coated membrane.

Most of the experiments were conducted using the HSA because it was the one that showed specific affinity with PAA as discussed in the previous chapter. IgG was used to compare its affinity to that of HSA regarding PAA.

3.3. Methods for characterization of coating and proteins adsorption

3.3.1. UV Visible spectroscopy

As stated in section 4.3.3.2 of chapter I, UV-visible spectroscopy could be used to evaluate the coating density and the amount of the proteins adsorbed onto the membrane surface by analysing the solute concentration before and after the adsorption. Since the absorbance is proportional to the concentration according to Beer-Lambert's Law (equation 3.3), the final concentration of the copolymer inside the coating bath can be calculated by measuring its absorbance.

$$A = \varepsilon \cdot c \cdot l \tag{3.3}$$

Where ε is absorptivity ($M^{-1}\,cm^{-1}$), c is concentration (M), and l is optical path length (cm).

For that, the absorbance of different standard solutions with known concentration of copolymer should be measured first to establish a calibration curve of the absorbance versus the concentration of the copolymer. That was done for all the copolymers used for surface modification as well as the proteins (HSA and IgG) used for the proteins adsorption study. Whether for the copolymers or the proteins, the calibration curves were obtained using concentrations ranging between 0 and 2 $mg \cdot mL^{-1}$, and results are given in section 1 of **Appendix C**. After that, since the initial concentrations are already known, the quantity of the coated copolymer or the adsorbed protein can be calculated by difference of mass using the equation below:

$$m_{ads} = C_i \cdot V - C_{eq} \cdot V \tag{3.4}$$

Where, m_{ads} is the adsorbed mass of the copolymer or the protein, C_i and C_{eq} are the initial concentration and that at the equilibrium respectively of the concerned solutes (copolymer or protein), and V is the volume.

Samples for coating are prepared the same way as mentioned previously depending on the studied parameter. 1 mL of the initial copolymer solution is prepared in addition to check the exactitude of the concentration and to avoid possible fluctuation in the UV apparatus response. Once the modification has been performed, the final solutions from which the membranes have

been removed are analysed with the help of a UV-visible spectrometer Lambda 365, PERKIN ELMER. The same procedure is implemented for the protein adsorption study. Some solutions of copolymer whether before or after coating have been diluted 4 to 5 times depending on the initial concentrations before the measurement because of the absorbance limit of the spectrometer according to which the calibration curves were also established.

The spectrometer used in this study is fitted with a beam splitter that allows dividing the coming beams in two (Figure 3. 7), one going through the reference cuvette when the other one is going through the sample cuvette. Therefore, for each measurement two quartz cells are used, one filled with 3 mL of solvent as reference, and the second one is filled with the same volume but of copolymer solution. The scans were carried out each time in a wavelength λ interval between 1000-100 nm, and the absorbance value was taken at 261 nm for the copolymer and at 280 nm for the proteins, where their peaks appear respectively.

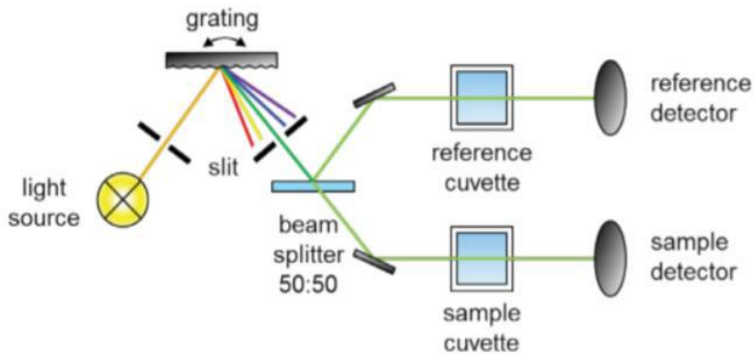

Figure 3. 7. Working principle of the Lambda 365, PERKIN ELMER UV visible spectrometer.

3.3.2. Attenuated Total Reflectance Spectroscopy (ATR)

ATR is one of the most common sampling techniques in Fourier transform infrared (FTIR) spectroscopy. It is based on total internal reflection where infrared (IR) light and sample interact only at the point where IR light is reflected. ATR allows samples to be analysed without complex sample preparation.

In ATR sampling, an infrared beam is directed onto an optically dense crystal with a high refractive index. The infrared beam reflects from the internal surface of the crystal and creates the so-called evanescent wave that is projected towards the sample, which is in contact with the crystal (Figure 3. 8). Some energy from the wave is adsorbed by the sample and the rest is transferred to the detector [14]. In regions of the infrared spectrum where the sample absorbs energy, the evanescent wave will be attenuated or altered. The attenuated energy from each evanescent wave is passed back to the IR beam, which then exits the opposite end of the crystal and is passed to the detector in the IR spectrometer. The system then generates an infrared spectrum. The detection and quantification of certain functional groups can be done by combining FTIR with ATR and it was found to be a high quality analysis tool for determining the chemical groups of complex samples [15].

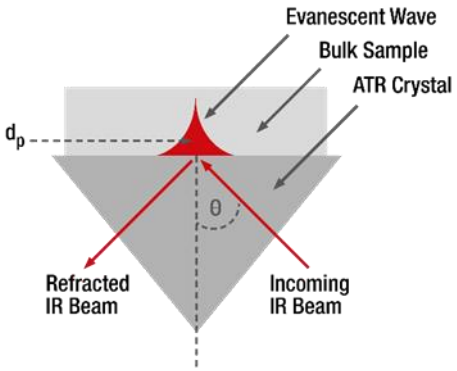

Figure 3. 8. Working principle of Attenuated Total Reflectance Spectroscopy (ATR) [16].

Attenuated Total Reflectance (ATR) spectroscopy (Nicolet 6700, Thermo Scientific) with diamond crystal, 45° incident angle, 16 scans, and 4 cm^{-1} spectral resolution was used to obtain spectra and verify the presence of the coating and the proteins on the membranes surface. Initially the sample holder was cleaned with ethanol and the background spectrum was collected using air to ensure there was no disturbance in the spectra due to the presence of impurities. The membrane was then placed over the sample holder and was tightened to the point where it was in contact with the diamond crystal, and the sample spectrum was collected. All spectra

were recorded over the wavenumber range from 4000 to 400 cm^{-1}, and they were unprocessed except for baseline alignment to qualitatively compare absorbance peak heights. Beer-Lambert Law (equation 3.3) states that absorbance is proportional to concentration. Thus, when comparing similar material, a higher absorbance peak means higher concentration on the surface.

3.3.3. Fourier transform infrared spectroscopy (FTIR)

FTIR is a technique that is used to obtain an infrared spectrum of absorption or emission of a solid, liquid and gas. It can be used for microscopy and imaging to characterize interfacial modifications. The instrument that determines the absorption spectrum for a compound is called a spectrophotometer, which is schematically illustrated in Figure 3. 9.

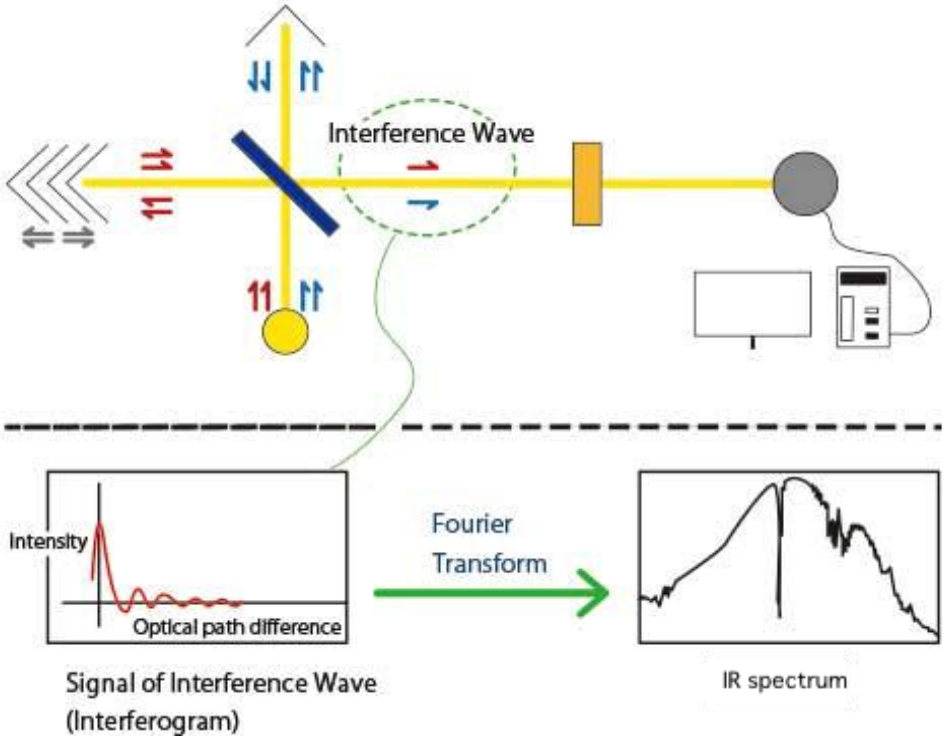

Figure 3. 9. Illustration of operating steps of the FTIR spectrometer to get to the sample spectrum.

FTIR spectrophotometer produces a beam of IR irradiation, which passes through into the interferometer where the spectral encoding takes place and which allows to create an interferogram. Subsequently, the beam goes to the sample compartment and the sample absorbs specific frequencies of energy, which are uniquely characteristic of the sample from the interferogram. The special interferogram is measured then in energy for all frequencies simultaneously by the detector. In the meantime, a beam is superimposed to provide a reference

(background) spectrum, which is subtracted from the sample spectrum by Fourier transformation computer software to get finally the desirable spectrum [17].

FTIR spectroscopy is one of the most powerful tools for the determination of functional groups in a membrane together with possible molecular bonds between chemical compounds of membrane. Understanding of positions of IR absorption bands in the spectrum as wave numbers could be used for identification of the various chemical components (e.g., aromatic, amides). Basically, transition energies corresponding to changes in vibrational energy state for many functional groups are located in the mid-IR region (4000 - 400 cm^{-1}). Hence, the appearance of an absorption band in this region can be used to determine whether specific functional groups exist within the molecule [17]. Typically, a single bond such as O-H, C-H, and N-H is detectable in higher wavenumber (2500-4000 cm^{-1}). Whereas, the triple bond and double bond are detectable in the middle wavenumber region 2000-2500 cm^{-1} and 1500-2000 cm^{-1} respectively. Additionally, the vibration of the molecule as a whole gives rise to a complex pattern of vibrations at low wavenumber region 650-1500 cm^{-1} that are characteristic of the molecule as a whole and hence can be used for the identification.

In FTIR, the absorption intensity relies on the molecule's change in dipole moment as a result of the absorption. Consequently, functional groups containing polar bonds, such as O-H, C=O, and N-H, are detected easily with FTIR, while detection of nonpolar groups can be difficult [18]. However, membrane samples should be analysed in its dry state since the OH group absorbs strongly in the infrared region and could obscure other interesting bands.

FTIR can be combined with attenuated total reflectance (ATR) technique, which is useful for surface characterization due to its access to the surface vibrational frequencies. In this mode, the sample is placed in contact with a crystal made from high refractive index transparent material as stated in the previous paragraph. The incident infrared light is focused on one end of the crystal at a certain angle and it undergoes several total internal reflections in the crystal until it reaches the detector (Figure 3. 10).

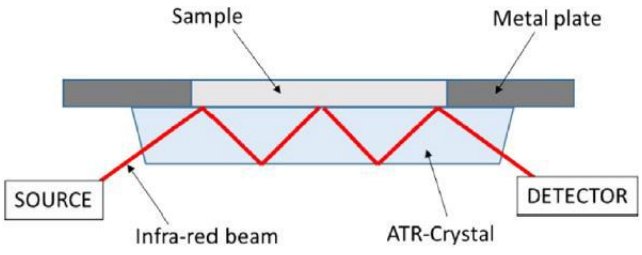

Figure 3. 10. Schematic representation of FTIR-ATR operation [15].

The incident beam penetrates slightly onto the sample at each reflection, which results in a spectrum describing the surface chemical composition of the sample. However, the use of rough and highly porous membranes decreases the contact between the membrane and the crystal which could disturb the measurements [18].

FTIR is used in this study due to its ease of operation and simplicity. The membrane surfaces were scanned with an infrared spectrometer (IN10MX Thermo Scientific) under ATR mode using a germanium crystal with 25° incident angle. The spectrometer is equipped with a detector MCT-A cooled with liquid nitrogen, and a KBr beam splitter. The spectral resolution is 8 cm^{-1}, and 16 scans are acquired on each measurement point. 50x50 points were measured (with step size of 100 µm between 2 points), which makes a total area of 25 mm^2 that was used for surface chemical mapping to determine the coverage of the coating and the protein adsorption. The sample was prepared by fixing the dried membranes to the glass slide with an adhesive tape and ensured that the surface was flat to obtain proper results. The glass slide was fixed to the sample holder. The focus was adjusted such that the light falls on the center point of the membrane. The sample was set at the required position and the ATR tip was fixed to the microscope to perform mapping after being cleaned to ensure there was no impurities.

Files obtained from the FTIR analysis were first processed with the OMNIC Software Suite (OMNIC Atlµs v.9.2, Thermo Fisher Scientific) which allowed the scanned maps to be opened.

To generate the chemical maps, peaks of interest that confirm the presence of the coating and proteins were first identified using ATR. Peaks with the highest absorbance and unique to the material of interest are chosen for the chemical mapping. Then, the peak area was measured to generate the chemical maps, which are color-coded according to absorption peak intensity from blue (lowest intensity) to red (highest intensity). A higher peak intensity indicates more coating or protein presence on the surface. All maps generated are unprocessed except for the atmospheric and the baseline corrections.

It is important to note that experiments of membrane coating with copolymer and protein adsorption on the membrane were repeated from 2 to 3 times, and so the mapping to confirm the reproducibility of the results.

4. Methodology for the analysis of ATR-FTIR results

4.1. Determination of copolymers and proteins characteristic peaks

Since FTIR mapping is the major technique used to characterize the modified membrane in this part, the spectra of the PVDF pristine membrane and the pure copolymers were determined first using ATR. These spectra were then compared to differentiate the peaks representing the chemical structure of the copolymer that are used after that to generate the chemical color-coded maps. The obtained ATR spectra of PVDF pristine membrane and the pure PS-b-PAA copolymers are shown in Figure 3. 11.

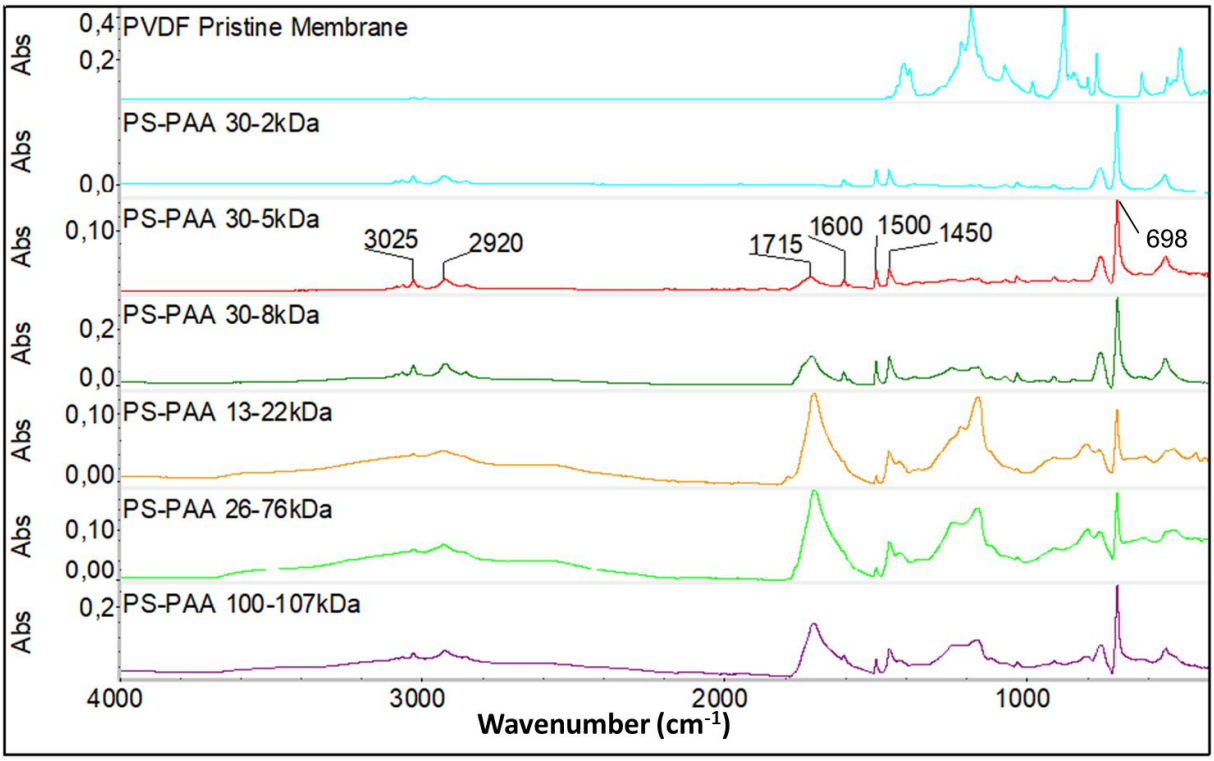

Figure 3. 11. ATR spectra of PVDF pristine membrane and the pure PS-b-PAA copolymers.

Based on the molecular structure of the copolymer given in Table 3. 3, and the ATR spectra shown in Figure 3. 11 it can be noticed that the PS group and the copolymer backbone can be easily seen for all PS-b-PAA copolymers. In fact, whether C-H deformation and C=C stretching of the aromatic in PS, =C-H stretching in PS, or -C-H stretching in the copolymer backbone, they are all observable in the ATR spectra and their peaks are summarized in Table 3. 4**.** As for the hydrophilic group, ideally, the spectrum of carboxylic acid in PAA should have strong absorption for O-H stretching at 3300-2500 cm^{-1} (broad peak), and for C=O stretching at 1700 cm^{-1}. However, not all the peaks are observable for all the PS-b-PAA copolymers. As a matter of fact, C=O stretching is seen for all of them except for PS_{30}-b-PAA_2, which could be due to

the small length of PAA (copolymer is only 10 wt.% of PAA). As for the O-H stretching, it starts being seen in the spectra when the PAA molecular weight is higher than 20 kDa.

Table 3. 4. Absorption bands of functional groups in PS-b-PAA copolymers and those in proteins (HSA and IgG).

Absorption (cm^{-1})	**Functional groups of PS-b-PAA**
3300-2500	O-H stretching in PAA
3105-3000	=C-H stretching in PS
3000-2850	-C-H stretching in the polymer backbone
1720-1706	C=O stretching in PAA
1600, 1500, 1450	C=C stretching of the aromatic in PS
700	C-H deformation of monosubstituted aromatic in PS
Absorption (cm^{-1})	**Functional groups of proteins**
3500-3070	N-H stretching in the amide
1680-1630	C=O stretching in the amide

Table 3. 4 summarizes the peaks of interest representing the chemical structure of PS-b-PAA and that of proteins (HSA and IgG) with the corresponding functional groups of each one, as well as their wavenumbers of absorption.

The same procedure has been done for the PS-b-PEO to determine the peaks representing its chemical structure. From the ATR spectra given in section 2 of the **Appendix C**, it can be noticed that the PS group and the copolymer backbone are easy to observe as it was for the PS-b-PAA. Whereas, the absorbance of C-O stretching in PEO could be seen at 1150-1085 cm^{-1}, but it overlaps a bit with peaks of the PVDF membrane.

Therefore, for most of FTIR mapping results, absorption peak at 700 cm^{-1} was chosen to analyse the presence of copolymer over the membrane surface as it had strong absorbance and it did not overlap with the peaks of the membrane material (PVDF).

As for the human blood proteins (HSA and IgG), ATR spectra of their powder form were also obtained and are given in **Appendix C**. Their general structure is intricate, but it is known that they are made of amino acids connected by peptide bonds (amide) [19]. Therefore, notable peaks are observed in their spectra at 3500-3070 cm^{-1} attributed to the amide N-H stretching vibration, and at 1680-1630 cm^{-1} due to the amide C=O stretching as shown in Table 3. 4.

4.2. FTIR maps processing

The areas of the characteristic peaks of the copolymers and those of the proteins determined using ATR were then measured using OMNIC Software Suite (OMNIC Atlμs v.9.2, Thermo Fisher Scientific) to generate the color-coded maps from FTIR mapping. The obtained maps display the qualitative distribution of the copolymer or the protein (depending of the chosen peak of interest) over the membrane surface. However, FTIR mapping was used to assess the variation of different conditions (coating time, concentration, etc), which results in different intensity colour scales (rainbow scales) for the maps obtained under different conditions, and thereby these maps cannot be compared.

For that, the color-coded maps with different rainbow scales (using the full scale value given by the OMNIC software) were converted to maps coded with the same grey scale from black (lowest intensity) to white (highest intensity) using a Python code given in section 3 of the **Appendix C**. The code allows then to evaluate the grey value all over the analysed area to calculate an intensity average value for the area of the peak of interest (that should be correlated to the adsorbed quantity). Besides, the code evaluates the standard deviation around the average value that could estimate the heterogeneity of coating or that of the protein distribution.

Below in Figure 3. 12 is shown an example of conversion of a color-coded map generated for the peak at 700 cm^{-1} for the coating at different concentrations of PS_{30}-b-PAA_2 as compared to a pristine membrane (PM), to a map coded with a grey scale. Thus all the maps latter in this chapter were converted using this same grey scale, so they can be compared.

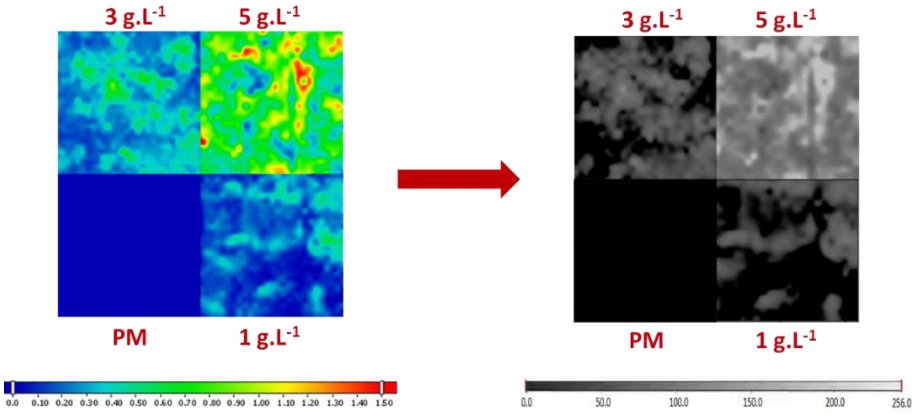

Figure 3. 12. Example of the conversion of a color-coded map generated for the peak at 700 cm^{-1} for the coating of PS_{30}-b-PAA_2 at different concentrations in solution as compared to a pristine membrane (PM), to a map coded with a grey scale.

5. Results and discussions

In this section we will be discussing the results we obtained as part of the coating procedure optimization of PVDF membranes with the different copolymers. Besides, the adsorption of blood proteins on PS-b-PAA coated membrane is explored under different conditions to investigate the selectivity of PAA towards HSA revealed in the previous chapter in solution. The adsorption of HSA on membrane coated with PS-b-PEO is also studied to test the efficiency of PEO on improving the resistance of PVDF membranes to fouling.

5.1. Variation of the coating operating process

In this part of the optimization study, the influence of the coating procedure (illustrated in Figure 3. 5) on the coating of PS_{30}-b-PAA_5 and PS_{30}-b-PAA_8 is investigated. The best coating procedure determined from this study will be used for the coating of the other copolymers. A copolymer concentration of 5 mg·mL^{-1} and a coating time of 2 hours are used in this study. The influence of these two parameters on the coating density will be analysed latter in this chapter (section 5.2 and 5.4).

As stated previously, the PS segment is the anchoring block to the PVDF membrane surface as a result of their hydrophobic/hydrophobic interactions, while the PAA block forms a hydrophilic layer. That implies that the stability of coating depends on the strength of the interactions between the PS segment and the membrane surface. Thus, the main reason for checking the various operating processes is to analyse the effect of washing on the stability of the copolymer coated over the membrane surface before and after the membrane is dried. Wherefore, the coating was performed by either Immersion - Washing - Drying (IWD) and Immersion - Drying - Washing (IDW), and the results are compared to a procedure consisting only on Immersion and Drying (ID). The three samples are dried at 40°C before being then compared with the pristine PVDF membrane (PM) as reference using FTIR mapping. The FTIR maps were generated in this section using three peaks (2920 cm^{-1}, 1715 cm^{-1} and 700 cm^{-1}) assessing respectively the presence of the copolymer backbone, the PAA chains and the PS block. It was done by measuring the area of each peak alone to see qualitatively the distribution of the corresponding functional group over the membrane surface as shown in Figure 3. 13 and Figure 3. 14 for the coating of PS_{30}-b-PAA_5 and PS_{30}-b-PAA_8 respectively.

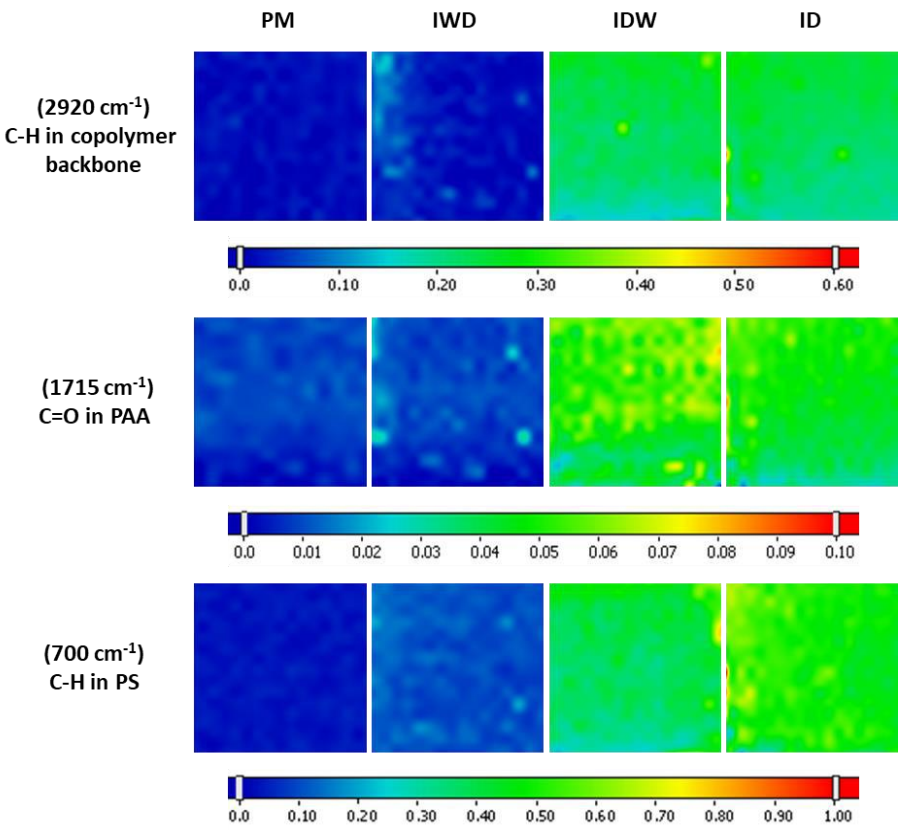

Figure 3. 13. FTIR maps obtained for three functional groups of the PS_{30}-b-PAA_5 coated on PVDF membranes using different processes (IWD, IDW and ID), 2 hours of coating time and a copolymer concentration of 5 mg·mL^{-1}.

First, differences in the intensity of absorbance of the different peaks are noticeable from the obtained maps. In fact, for the 700 cm^{-1} and the 2920 cm^{-1} peaks, the intensity of absorbance is higher than that of the peak at 1715 cm^{-1}, which makes it easier to assess the presence of the PS and the copolymers backbone than the PAA. That confirms what has been figured out previously from the ATR spectra. Despite of that, the maps show that both copolymers adhered to the membrane surface, and almost the same trend of coating is observed for both of them using the three peaks. Indeed, more copolymer presence is observed with ID and IDW than IWD as it can be seen from Figure 3. 13 and Figure 3. 14. This suggests that washing after drying results in better copolymer deposition than washing immediately after immersion. The latter involves the presence of both the solvent used for coating and the PBS used for washing in the environment. This could mean that the interactions between the copolymer and the surrounding medium is slightly stronger than the hydrophobic interactions between the copolymer and the membrane resulting in partial removal of the coating. Otherwise, this could be owing to the fact that some copolymer chains were deposited but not adsorbed onto the

membrane surface and they were then removed during rinsing step. Meanwhile, when washing was done after drying, the solvent had already dried out in between the copolymer brushes before washing. This could ensure stronger hydrophobic interactions leading to better copolymer adhesion, and so higher copolymer amount over the membrane surface. Besides, this could increase the deposition of the copolymer chains not initially adsorbed onto the membrane surface.

From the FTIR maps, it is also possible to observe that the distribution of the copolymer over the membrane surface was not always homogeneous, and especially with PS_{30}-b-PAA_8. This could be due to heterogeneities of the membrane morphology and on the distribution of the membrane pores.

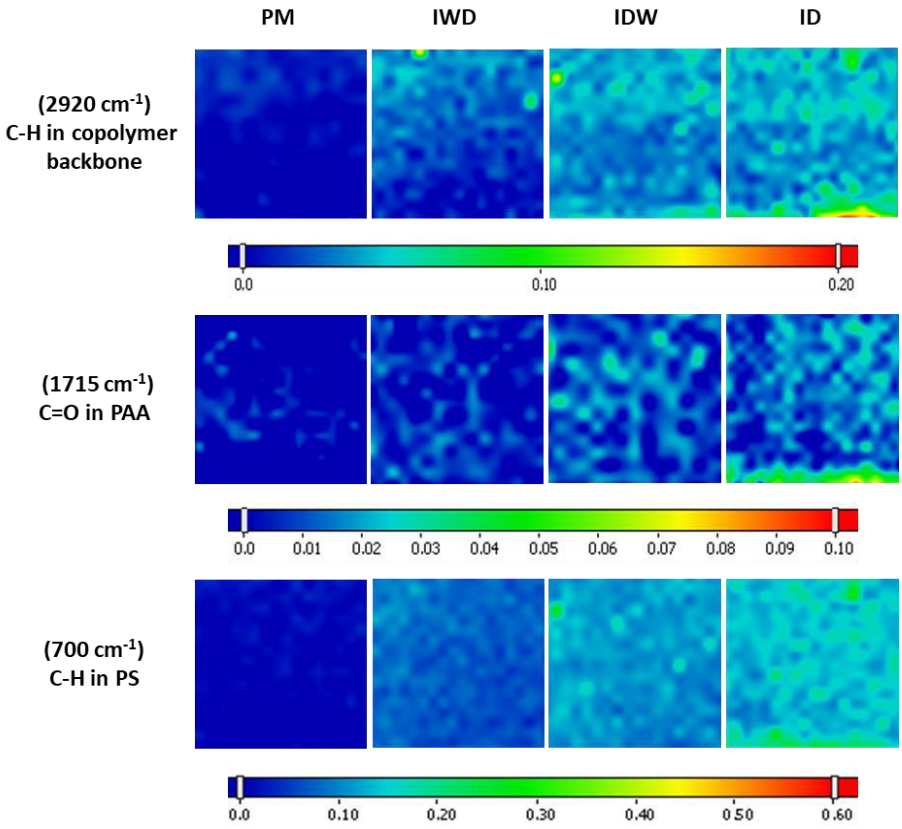

Figure 3. 14. FTIR maps obtained for three functional groups of the PS_{30}-b-PAA_8 coated on PVDF membranes using different processes (IWD, IDW and ID), 2 hours of coating time and a copolymer concentration of 5 $mg \cdot mL^{-1}$.

A visual comparison between the maps obtained for the coating of PS_{30}-b-PAA_5 copolymer (Figure 3. 13) and that of the PS_{30}-b-PAA_8 (Figure 3. 14) shows a wider coverage of the surface with the first copolymer than the second one, with higher peaks absorbance. That suggests a better adhesion of PS_{30}-b-PAA_5 to the membrane surface even if both copolymers have the same

length of PS block supposed to ensure the hydrophobic interactions with the PVDF hydrophobic membrane. However, this is still an observation and not a conclusion at this stage that needs to be studied with different sizes of copolymer, which is discussed explicitly later in this chapter (section 5.3).

Now, if the difference between IWD and IDW processes was clear enough by a simple visual analysis of the maps, the comparison between IDW and ID processes is harder this way. For that, the color-coded maps with different rainbow scales were converted to maps with the same grey scale as explained in section 4.2. Since the C-H stretching in PS showed the highest intensity of absorbance at 700 cm^{-1}, the map generated for this peak area was chosen to conduct these processing. From the converted maps in the grey scale exposed in Figure 3. 15, we can notice that the coating is more heterogeneous for IWD than IDW and ID, which is the same thing that has been previously observed from the color-coded FTIR maps. This is consistent with the fact that less copolymer is present on the surface for the IWD process after the non-homogeneous removal of the adsorbed copolymer during washing step.

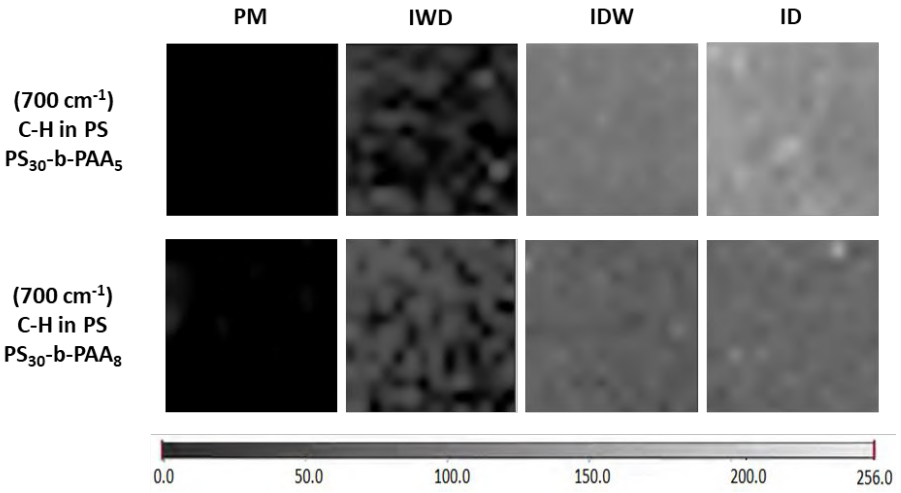

Figure 3. 15. FTIR maps generated for the peak area at 700 cm^{-1} and converted in the same grey scale for both copolymers.

From these image analyses, the average intensity of the peak area and the standard deviation (represented by error bars) are quantitatively evaluated for each copolymer and for the different operating conditions as shown in Figure 3. 16. Eventually, the mean value of the peak area for the ID process is a bit higher than that of the IDW for the coating of both copolymers as shown in Figure 3. 16. Despite the difference in intensity is not that great, these results suggest that washing is still removing a small part of coating even after drying. This could mean that the PS/PVDF hydrophobic interactions of this removed part of the copolymer are weaker than the

interactions with the PBS used for washing. Otherwise, it could mean that the removed part was only deposited and not adsorbed, and even after the membrane was dried this part was not attached to the surface. The results display also a higher standard deviation for the IWD process implying bigger heterogeneity, which confirms what has been noticed previously from FTIR maps and the converted maps.

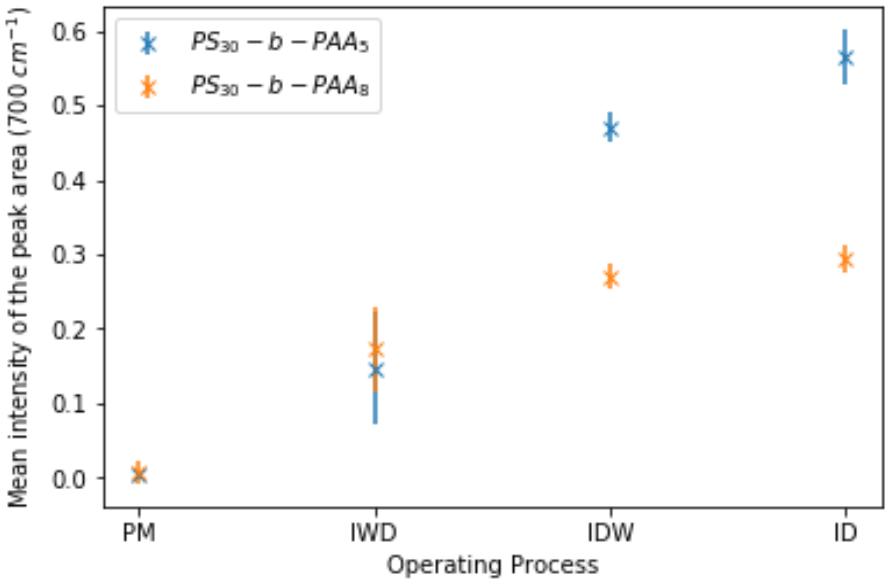

Figure 3. 16. Intensity average of the peak area (symbols) and the standard deviation (error bars) at 700 cm^{-1} as function of the operating process for the coating of PS_{30}-b-PAA_5 and PS_{30}-b-PAA_8 with a concentration of 5 mg·mL^{-1} and coating time of 2 hours.

The obtained mean intensities plotted in Figure 3. 16 confirm also the observation made previously from the FTIR maps regarding the comparison of the copolymer adhesion to the membrane surface. In fact, a higher intensity was obtained for the coating of PS_{30}-b-PAA_5 than that of PS_{30}-b-PAA_8 involving a bigger amount of the first copolymer attached to the membrane surface.

At this stage, the optimization study aims to covering the membrane surface with the copolymer in order to investigate then the copolymer interactions with the human blood proteins. Therefore, the ID process was chosen to conduct the experiments on the other parameters explored later in this chapter.

5.2. Variation of coating time

As stated in the literature review of this chapter, not much attention has been drawn to the fact that the coating density may be dependent on the time that the membrane has been left in contact with the copolymer solution. Therefore, the effect of the coating time on the coating density is evaluated in this section. For that, the membranes were immersed for 1, 2, 4 and 6 hours in a 5 mg·mL^{-1} copolymer solution (PS_{30}-b-PAA_5 and PS_{30}-b-PAA_8) at room temperature (22 ± 3 °C). The samples were then prepared for FTIR mapping as explained previously, and the maps were generated for the peak at 700 cm^{-1}.

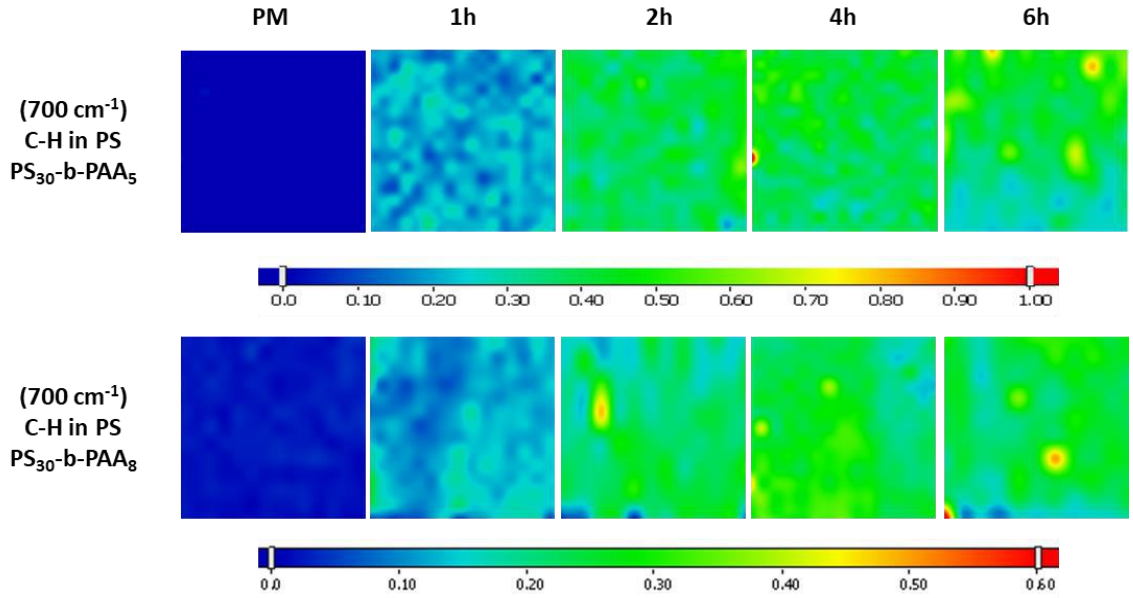

Figure 3. 17. FTIR maps for membranes modified with the PS_{30}-b-PAA_5 and PS_{30}-b-PAA_8 using different coating times (1, 2, 4 and 6 hours) while keeping the copolymer concentration at 5 mg·mL^{-1}.

The obtained results exposed in Figure 3. 17 display clearly an increase in the copolymer presence, so of the coating density when the coating time increases. However, this increase was quickly not that notable after 2 hours of immersion. In fact, the maps at 2, 4 and 6 hours evince the presence of the copolymer all over the analysed area, which could involve almost a complete coverage of the membrane with the copolymer. Eventually, this could mean that the copolymers were already given enough time to adsorb on the surface until a plateau is reached indicating saturation of the surface. The same trend is obtained with both copolymers but with higher intensities of absorption for PS_{30}-b-PAA_5 than PS_{30}-b-PAA_8 suggesting again a better adhesion of the first copolymer than the second one. That confirms what has been noticed in the previous

section during the variation of the operating process, where PS_{30}-b-PAA_5 exhibited a higher adsorption intensity than PS_{30}-b-PAA_8 (Figure 3. 16).

In order to compare quantitatively the maps, we proceeded to apply a similar images analysis as previously to determine the mean intensity of the peak area. Wherefore, the maps were converted using the same grey scale, and the calculated mean intensity was drawn versus the coating time for the two copolymers (Figure 3. 18).

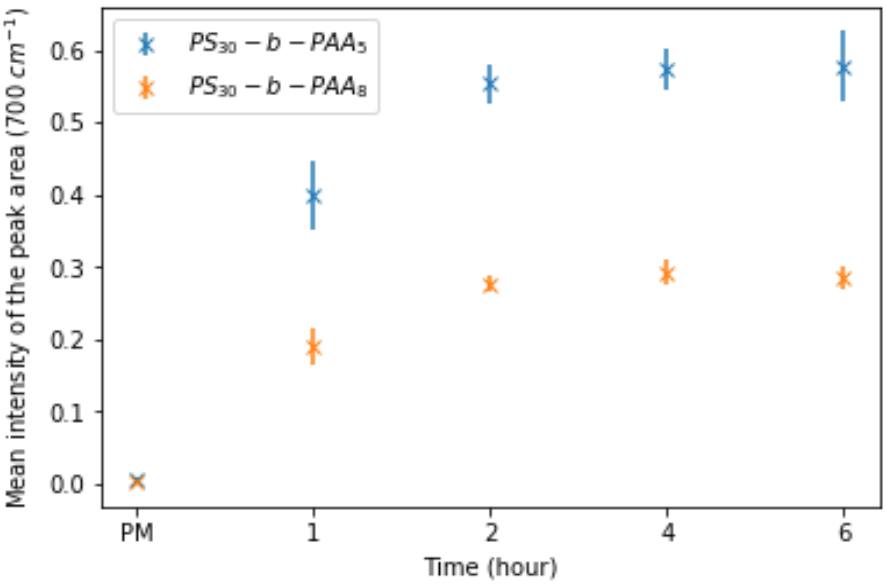

Figure 3. 18. The intensity average of the peak area at 700 cm^{-1} as function of coating time for the coating of PS_{30}-b-PAA_5 and PS_{30}-b-PAA_8.

The obtained results confirm what has been observed on the FTIR maps, and that 2 hours of immersion was enough to achieve almost the maximum of intensity. Indeed, the mean intensity of the peak area was found to be 0.55 after 2 hours of immersion in PS_{30}-b-PAA_5 solution, against 0.57 and 0.58 after 4 and 6 hours respectively, which makes a variation of 5% in the mean intensity. As for the PS_{30}-b-PAA_8 copolymer, the mean intensity was 0.28 for 2 hours against 0.29 for 4 and 6 hours, which makes a variation of 3 %. This also sustains the fact that a greater amount of PS_{30}-b-PAA_5 copolymer has been attached to the PVDF membrane surface than that of PS_{30}-b-PAA_8 using the same operating conditions. The mean intensities for the peak area are given in Table 3. 5 with the standard deviation to the average value.

To validate these outcomes, we proceeded to the evaluation of the coating density as a function of the coating time. That was done by measuring the difference of the copolymer mass inside the coating bath before and after immersion using the UV-visible spectroscopy as

explained in section 3.3.1. The experiments have been repeated at least three times to calculate the standard deviation to the obtained average coating density. Even known, the initial concentrations have been checked to consider the deviations to the calibration curve that could be due to the solutions preparation and the dilutions done before each measurement. As a matter of fact, the measured initial concentrations have been found to be 5.06 and 5.2 mg·mL^{-1} for PS_{30}-b-PAA_5 and PS_{30}-b-PAA_8 respectively, which is higher than 5 mg·mL^{-1}. As exposed in Table 3. 5, this deviation is not negligible compared to the final concentration obtained after immersion and needs to be considered. Thus, the measured concentrations were used to calculate the difference of mass instead of 5 mg·mL^{-1}, since after immersion the same solutions are used for the UV-visible spectroscopy measurement.

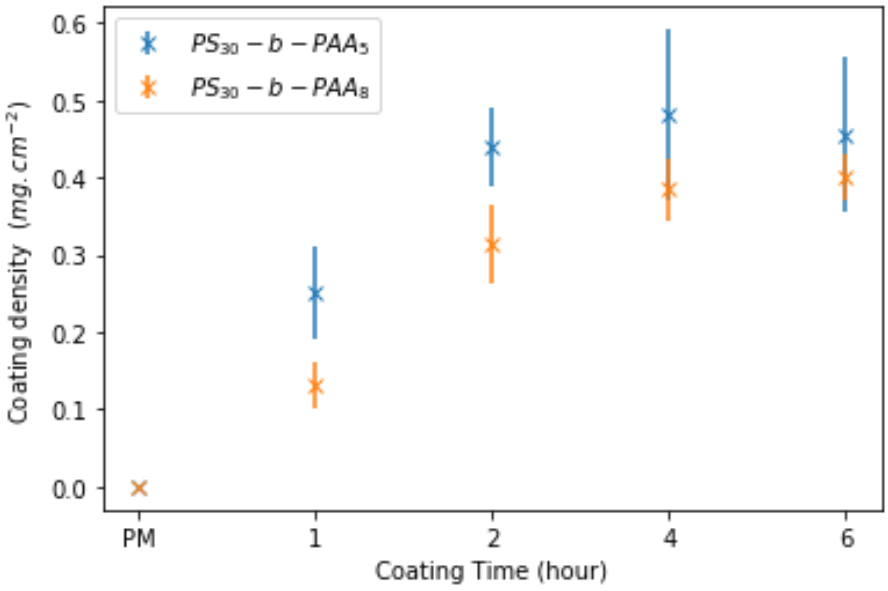

Figure 3. 19. Coating density calculated as function of the immersion time (1, 2, 4 and 6 hours) for the coating of PVDF membranes with a PS_{30}-b-PAA_5 and PS_{30}-b-PAA_8 solutions with a concentration of 5 mg·mL^{-1}.

It has to be mentioned that since the coating was performed by immersion, the calculated coating density corresponds to the attachment of copolymer on both sides of the membranes, each one has an area of 0.5 cm^2, which makes a total area of 1 cm^2. In addition, the adsorbed amount estimated this way includes the copolymer that penetrated into the pores during coating and about which we do not have any clear information. Despite of that, the obtained results exhibited almost the same trend whether shown by the FTIR maps or by the calculation of the mean intensity of the peak area. Indeed, the coating density has been found to increase when the immersion time increases. Even after 2 hours a slight increase is observed where the coating

density of the PS_{30}-b-PAA_5 copolymer is raised from 0.44 mg·cm^{-2} at 2 hours to 0.48 mg·cm^{-2} at 4 hours, then 0.46 mg·cm^{-2} at 6 hours. This increase is greater in the case of PS_{30}-b-PAA_8, where the coating density raised from 0.31 mg·cm^{-2} at 2 hours to 0.38 mg·cm^{-2} and then 0.4 mg·cm^{-2} at 4 and 6 hours respectively. This could suggest that the copolymer is still able to adhere to some areas of the membranes not visible on the mapping since the analysed area is very small (25 mm^2 for each sample) compared to the total coated one (0.5 cm^2). It could also be due to the fact that the copolymer is still diffusing inside the pores of the membranes even after the saturation of the surface, which is not possible to see with FTIR mapping or the calculation of the intensity because both techniques are related to the surface only. Indeed, DLS measurement proved that all the copolymers exhibit a very small size as shown in Table 3. 3 compared to the average pore size (0.1 µm) of the membrane.

Table 3. 5. The calculated coating density and the measured mean intensity of the peak area (700 cm^{-1}) with their standard deviations for different coating times.

PS_{30}-b-PAA_5						
Coating Time (hour)	**$[PS_{30}$-b-$PAA_5]_0$ (mg·mL^{-1})**	**$[PS_{30}$-b-$PAA_5]_f$ (mg·mL^{-1})**	**Coating density (mg·cm^{-2})**	**Standard deviation (mg·cm^{-2})**	**Mean intensity**	**Standard deviation**
0	0	0	0	0	0.005	0
1	5.06	4.81	0.25	0.06 (24%)	0.4	0,048 (12%)
2	5.06	4.62	0.44	0.05 (11%)	0.55	0,026 (5%)
4	5.06	4.58	0.48	0.11 (23%)	0.57	0,028 (5%)
6	5.06	4.61	0.46	0.1 (22%)	0.58	0,048 (8%)
PS_{30}-b-PAA_8						
Coating Time (hour)	**$[PS_{30}$-b-$PAA_8]_0$ (mg·mL^{-1})**	**$[PS_{30}$-b-$PAA_8]_f$ (mg·mL^{-1})**	**Coating density (mg·cm^{-2})**	**Standard deviation (mg·cm^{-2})**	**Mean intensity**	**standard deviation**
0	0	0	0	0	0.003	0
1	5.2	5.07	0.13	0.03 (23%)	0.19	0.026 (14%)
2	5.2	4.88	0.31	0.05 (16%)	0.28	0.011 (4%)
4	5.2	4.81	0.38	0.04 (10%)	0.29	0.018 (6%)
6	5.2	4.8	0.4	0.03 (8%)	0.29	0.015 (5%)

Now, considering the relatively high standard deviations to the average of the calculated coating density shown in Table 3. 5, it is difficult to conclude on the differences between 2, 4 and 6 hours. However, at this stage the study aims at covering the membrane surface with the copolymer layer, so it will be possible then to investigate the interactions with human blood proteins. Therefore, we estimated that 2 hours of immersion was enough to do that and is faster to perform experiments, thus it was chosen as the optimum coating time for further experiments.

5.3. Variation of hydrophobic/hydrophilic chain length

The copolymer hydrophobic/hydrophilic block ratio and the chain length have a substantial role in the adsorption of the copolymers onto the membrane surface. In fact, the primary results obtained in the previous sections show different abilities of adhesion to the surface by two copolymers having the same hydrophobic group and a different hydrophilic chain length. In order to corroborate this outcome, coating has been conducted this time with six different sizes of PS-b-PAA copolymer and three of PS-b-PEO using ID process, 2 hours of immersion and a copolymer concentration of 5 $mg \cdot mL^{-1}$. Since we can put four samples at most for each mapping, one of which is the pristine membrane (PM) as reference, two mapping have been done to analyze all the coated samples with the six PS-b-PAA copolymers and one mapping for PS-b-PEO. The first mapping was to confirm what has been noticed on the effect of the hydrophilic chain length, as the copolymers used are PS_{30}-b-PAA_2, PS_{30}-b-PAA_5 and PS_{30}-b-PAA_8. As for the second and the third mapping, it was done to assess the effect of both hydrophobic/hydrophilic chain lengths on the attachment of the copolymer on the membrane surface. One of them was for the coating of PS_{13}-b-PAA_{22}, PS_{26}-b-PAA_{76} and PS_{100}-b-PAA_{107}, while the second one assesses the coating of PS_{28}-b-PEO_{13}, PS_{12}b-PEO_{30} and PS_{16}-b-PEO_{72}.

Results from the first mapping (Figure 3. 20) sustain what has been noticed in the previous sections. In fact, for a same hydrophobic chain length, the copolymer with the shortest hydrophilic block adheres better to the membrane surface. This means that hydrophobic interactions between the PVDF membrane and PS block are diminished by stronger hydrophilic interactions between the solvent and PAA segment due to the increase of PAA size. The decrease in adhesion propensity could be also due to the fact that larger PAA moieties introduced increased steric hindrance blocking the access of PS moieties to the PVDF surface. This outcome is consistent with what has been reported in the literature [9], [11] and stated in the review section of this chapter (section 2.3).

From the second mapping it can be noticed that the higher coating is obtained for the copolymer PS_{100}-b-PAA_{107} (PAA/PS ratio ≈ 1), which makes sense because the two other copolymers are of a PAA/PS ratio around 2 and 3. This suggests that copolymers with smaller hydrophilic/hydrophobic blocks ratio can be deposited better onto the membrane surface due to stronger hydrophobic interactions with the PVDF membrane. However, PS_{26}-b-PAA_{76} (PAA/PS ratio ≈ 3) has been found to adhere more to the membrane surface than PS_{13}-b-PAA_{22} (PAA/PS ratio ≈ 2) although the first copolymer has higher hydrophilic/hydrophobic ratio. This means that the block's ratio is not the only parameter involved in the coating of the copolymer, a minimum of PS length is also required to have sufficient hydrophobic interactions with the PVDF membrane. As a matter of fact, the presence of PS_{13}-b-PAA_{22} is almost not seen in the map shown in Figure 3. 20, which is probably due to the small size of PS, and so weaker hydrophobic interactions with the membrane.

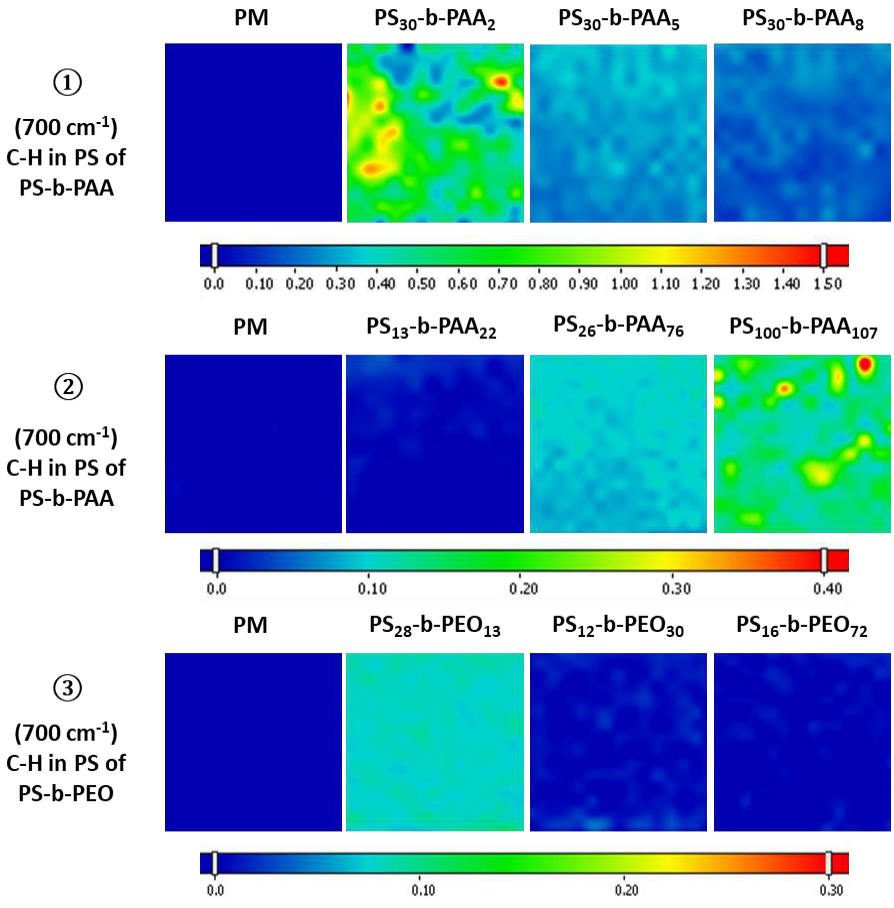

Figure 3. 20. FTIR maps for the coating of different sizes of PS-b-PAA and PS-b-PEO using ID process, 2 hours of immersion and a copolymer concentration of 5 mg·mL^{-1}.

The same thing has been observed in the third mapping for the coating by PS_{12}-b-PEO_{30} and PS_{16}-b-PEO_{72}, where their presence is not that remarkable, while the coating by PS_{28}-b-PEO_{13}

is clearly seen from the map (Figure 3. 20). This result affirms that smaller PS length implies weaker hydrophobic interactions which results in very weak adhesion of the copolymer to the membrane surface. It also suggests that the minimum of PS size required to have the coated layer onto the PVDF membrane surface is more than 20 kDa in our study. However, this threshold of hydrophobic block length could be different (smaller or higher) depending on the hydrophilic block size and the blocks ratio.

Since the three mapping are shown for different full-scale values (rainbow scales), the generated maps were converted then using the same grey scale, and the mean intensity was evaluated for further comparison. The evaluated intensities for the coating of each copolymer are given in Figure 3. 21.A, and are plotted as a function of the hydrophilic/hydrophobic ratio in Figure 3. 21.B.

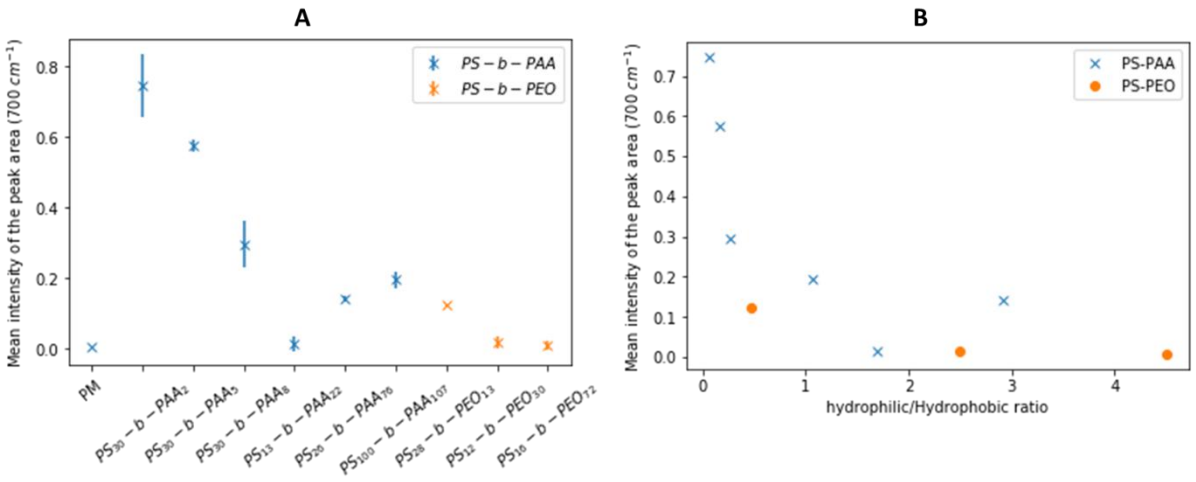

Figure 3. 21. The intensity average of the peak area at 700 cm^{-1} as shown A/ for the coating of different PS-b-PAA and PS-b-PEO using ID process, 2 hours of immersion time and a copolymer concentration of 5 $mg \cdot mL^{-1}$ and B/ the intensity as a function of the hydrophilic/hydrophobic ratio.

These results came first to sustain what has been noticed from the FTIR maps, but it also allows to compare the coating ability of all copolymers. In fact, it confirms that copolymers with PS block size less than 20 kDa show a very weak propensity to deposit compared to the other copolymers. However, the most remarkable thing from Figure 3. 21 is that the difference of intensity is more obvious when the hydrophilic chain is small as can be seen for a PAA segment of 2, 5 and 8 kDa with a PS block of 30 kDa. When the hydrophilic chain is larger (PAA of 76 kDa), the difference is lower even though the PS block size (26 kDa) is close to that of the previous copolymers. Then, increasing the PS block size from around 30 to 100 kDa,

the increase in intensity is not that big compared to the increase in size, which is maybe due to the steric hindrance introduced by the size of PAA. This suggests that from a certain length of hydrophilic segment, the steric hindrance dominates over the hydrophobic interactions of PS block with the PVDF membrane. However, since we are looking for the peak at 700 cm^{-1} representing the PS group, the latter could be hidden by the largest PAA segments which form the top layer, whereas the PS is attached to the membrane. This depends on how the copolymer chains are arranged on the membrane surface, something that we do not know in this case.

From Figure 3. 21, it can also be observed that PS_{26}-b-PAA_{76} copolymer has higher intensity than PS_{28}-b-PEO_{13}, even though the former has a larger hydrophilic chain. This means that the strength of interactions between the hydrophilic block and the solvent depends on the hydrophilic segment nature. The latter could also have a role on how the copolymer is attached to the membrane, which affects the ability to see the PS group using FTIR mapping.

5.4. Variation of the copolymer concentration

5.4.1. Effect of PS-b-PAA concentration on HSA adsorption

One of the parameters usually explored in membrane surface modification study is the concentration of the modifier substance. Classically, in coating studies using copolymers as surface modifiers, the coated amount is evaluated as a function of the copolymer concentration in the coating bath by calculating coating densities [9], [12]. In this section, the effect of this latter on the coverage of the membrane surface is first investigated by evaluating the mean intensities from FTIR maps as explained previously (section 4.2). The coating was performed with PS_{30}-b-PAA_5, PS_{30}-b-PAA_8, PS_{26}-b-PAA_{76} and PS_{100}-b-PAA_{107}, and that by using ID process, 2 hours of immersion and a copolymers concentration of 5 $mg{\cdot}mL^{-1}$. The FTIR maps were generated this time for the peak at 700 cm^{-1} representing the PS group, and the one at 1715 cm^{-1} representing the PAA segment. That was done to check what has been discussed in the previous section about the ability of seeing the PS block using FTIR mapping depending on the hydrophilic and the hydrophobic blocks lengths. It also allowed to show the presence of both PS and PAA over the membrane surface, and to have an idea about the deposition way of the copolymer onto.

Subsequently, the effect of the copolymer concentration on the adsorption of HSA, the most abundant protein in human plasma, is discussed using FTIR mapping. The adsorption of HSA on the coated membranes was conducted using a protein concentration of 1 $mg{\cdot}mL^{-1}$ at a pH around 7. The FTIR maps were generated for the peak at 1660 cm^{-1} to check the presence of

HSA over the modified membrane. It has to be mentioned that the maps showing the presence of PS block, PAA segment and HSA protein, were all generated from the same membrane sample.

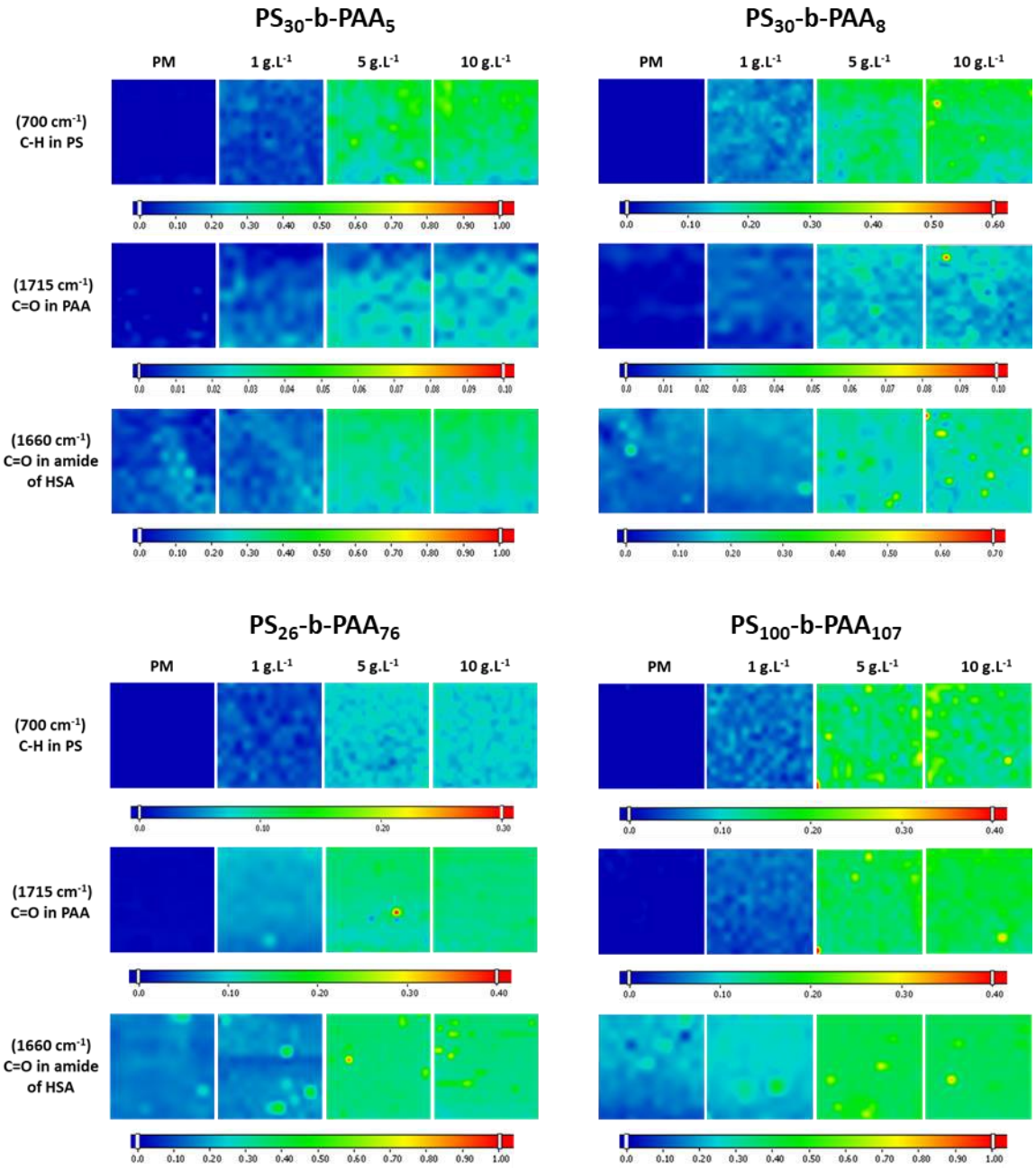

Figure 3. 22. FTIR maps for the coating of PVDF membranes with various PS-b-PAA copolymers using ID process, 2 hours of immersion and different copolymer concentrations, and the adsorption of HSA on these same modified membranes; [HSA] = 1 mg·mL^{-1}; pH ≈ 7.

FTIR results exposed in Figure 3. 22 have all displayed the same trend of coating with the four PS-b-PAA copolymers. Indeed, whether for the presence of PS, PAA or HSA, an increase in intensity is observed by increasing the copolymers concentration until 5 mg·mL^{-1}. Beyond

this concentration, the maps do not show clear visual differences. In fact, almost the same coverage of the surface by the copolymers is observed at 5 and 10 mg·mL^{-1} implying a saturation of the membrane surface at 5 mg·mL^{-1}. In contrast, what has been clearly visible from the maps is that the PAA is not necessarily visible in the same locations over the membrane surface as the PS block.

Subsequently, the effect of the copolymer concentration on the adsorption of HSA, is discussed using FTIR mapping. The adsorption of HSA on the coated membranes was conducted using a protein concentration of 1 mg·mL^{-1} at a pH solution around 7. The FTIR maps were generated for the peak at 1660 cm^{-1} to check the presence of HSA over the modified membrane. It has to be mentioned that the maps showing the presence of PS block, PAA segment and HSA protein, were all generated from the same sample.

This excludes the theoretical scheme of vertical deposition of the copolymer brushes on the membrane proposed in the presentation of the project in the general introduction (section 6.3 of chapter I). It would be more logical to imagine a horizontal deposition of the hydrophobic part (PS block) due to the hydrophobic interactions with the PVDF membrane and maybe a, stretched orientation perpendicular to the membrane surface of the hydrophilic chains (PAA segment). This configuration of coating has been suggested in a study aimed at coating PS surfaces with different PS-b-PEGMA copolymers (Figure 3. 3) [7].

These results support also what has been noticed in the previous section. In fact, the copolymers do not exhibit all the same ability of adhesion onto the membrane surface by having different intensities of absorbance. But the scale of intensity has been found to be also correlated to each part (hydrophilic or hydrophobic) and its size. This means that larger hydrophilic chains either introduce higher steric hindrance preventing the access of PS moieties, or they hide certain parts of PS that we can no longer see with the FTIR. These are maybe the reasons of a weaker presence of the PS in the case of PS_{26}-b-PAA_{76} and PS_{100}-b-PAA_{107}, despite of having almost the same size of PS block or higher than PS_{30}-b-PAA_5 and PS_{30}-b-PAA_8.

The mean intensities (Figure 3. 23) of the peaks area (at 700 cm^{-1} and 1715 cm^{-1}) evaluated from the converted maps using the same grey scale, illustrate better what has been said above.

Logically, the presence of PAA was found to be greater with PS_{100}-b-PAA_{107}, PS_{26}-b-PAA_{76}, and then PS_{30}-b-PAA_8 and PS_{30}-b-PAA_5 where no big differences are displayed. As for the PS presence, the biggest intensity was obtained for PS_{30}-b-PAA_5 followed by PS_{30}-b-PAA_8, and

then PS_{100}-b-PAA_{107} and PS_{26}-b-PAA_{76}, which confirms what was previously suggested regarding the effect of hydrophilic segment size on the PS presence or visibility.

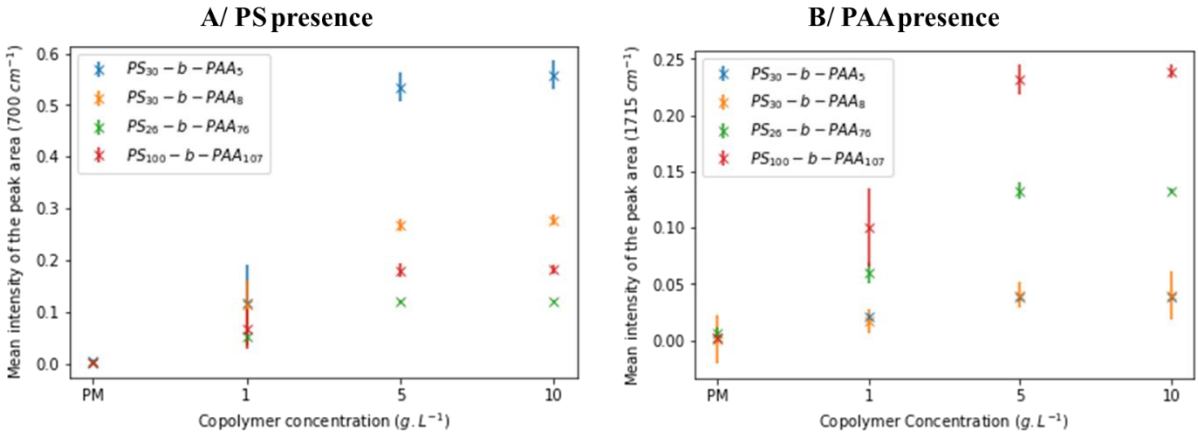

Figure 3. 23. The intensity average of the peaks area at 700 cm^{-1} and 1715 cm^{-1} for the coating of different PS-b-PAA copolymers as function of copolymer concentration using ID process, 2 hours of immersion time.

In addition, the evaluated intensities validate that a copolymer concentration of 5 $mg{\cdot}mL^{-1}$ sufficiently covers the membrane surface and using higher concentration would be excessive.

From the FTIR maps, it can also be seen that the HSA presence increased with the concentration of copolymer until 5 $mg{\cdot}mL^{-1}$. But, it seems that this increase is not correlated to the copolymer size since the same scale of intensity was obtained except for PS_{30}-b-PAA_8. The evaluated mean intensities (Figure 3. 24) confirm that the HSA adsorption reached the maximum for a copolymer concentration of 5 $mg{\cdot}mL^{-1}$. Beyond this copolymer concentration, the mean intensities are almost unchanged for all the copolymers, despite some differences of HSA adsorption are disclosed on membranes coated with different copolymers, especially on PS_{30}-b-PAA_8 coated membrane.

These results (Figure 3. 24) expressed first the ability of the PVDF pristine membrane (PM) to adsorb HSA, but the adsorption has been found to vary considerably between the different samples. This adsorption could be due to the hydrophobic interactions between the membrane and the hydrophobic parts of the HSA [20]. However, it has to be noted that the variabilities of HSA adsorption displayed on the PM (first points in Figure 3. 24) could induce some inaccuracies on HSA adsorption on membranes coated the different copolymers.

In addition, results evince that the distribution of the protein was not homogeneous, which is shown in Figure 3. 24 by the standard deviations to the average value of the intensity. This is

probably due to heterogeneities on the morphology of the membrane implying variation of the hydrophobic interactions strength over the membrane surface.

After that, results displayed greater ability of PS-b-PAA coated membrane than the PM to adsorb HSA. Indeed, the HSA adsorption increased with the presence of the copolymer until reaching a plateau at a copolymer concentration of 5 mg·mL^{-1}.

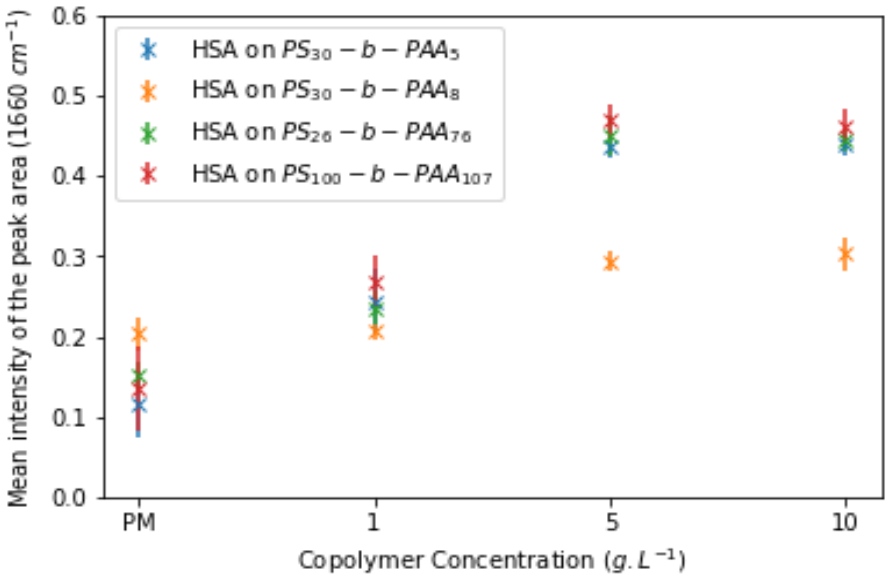

Figure 3. 24. The intensity average of the peak area at 1660 cm^{-1} for the HSA adsorption on PVDF membranes coated with different PS-b-PAA copolymers, [HSA]= 1 mg·mL^{-1}; pH=7.

Since the experiment was carried out at pH 7, this could not be a complexation between PAA and HSA as observed in solution in the previous chapter at pH 5 only and not at 7. Two explanations could be brought to this behaviour. For long PAA chains, the adsorption of HSA on the coated membrane could be due to the steric hindrance that retains the protein in between the brushes of copolymers. For smaller PAA chain, it could also be due to the hydrophobic interactions between the hydrophobic parts of the protein and the accessible PS block on the surface, which is also possible to happen in the case of large PAA chains. As a matter of fact, if the distance between two PAA moieties is large enough, that increases the chances for the HSA molecules to be in contact with the PS segments horizontally attached to the membrane surface regardless of the size of PAA. Thus, the electrostatic repulsions between HSA and PAA will be reduced and the hydrophobic interactions between the protein and the coated membrane will be stronger. This would be consistent with what is reported in the literature regarding the adsorption of HSA on PS surfaces. Indeed, it has been shown using UV spectroscopy that HSA adsorbs strongly onto polystyrene plates and onto polystyrene latex [21]. That could be also the

reason why the presence of HSA on the membrane surface was not correlated to the length of the PAA segment. However, this does not explain the increase of HSA adsorption on coated membranes than on PM if in both cases the adsorption is driven by hydrophobic interactions. Thus, we can imagine that these hydrophobic interactions are stronger between the protein and PS than those between the protein and the pristine PVDF. Otherwise, the adsorption on membrane coated with PS-b-PAA may be driven by the combination of both hydrophobic interactions between HSA and the visible PS blocks, and the electrostatic attractions that could take place between positive patches carried on HSA and the negatively charged PAA.

5.4.2. Effect of PS-b-PEO concentration on HSA adsorption

As a water-soluble and electrically neutral polymer, poly(ethylene oxide) (PEO) is well-known for its excellent resistance to the nonspecific adsorption of proteins [22]. Wherefore, it's sometimes used as copolymer when conjugated to a hydrophobic group such as PS for the modification of biomaterials interfaces to prevent cells adhesion [23]. However, its resistance to the non-specific adsorption of proteins strongly depends on having a good coating layer of PEO onto the material surface. For that, the effect of PS_{30}-b-PEO_{13} concentration on HSA adsorption is investigated in this section using ID process and 2 hours of coating time. The copolymer PS_{30}-b-PEO_{13} was chosen to perform these experiments because it was the one that showed the best ability of adhesion to the membrane surface in the previous section. The maps were generated for the peaks at 700 cm^{-1} (copolymer) and at 1660 cm^{-1} (HSA), and the mean intensities for these peaks areas were evaluated from the converted maps using the grey scale.

Results shown in Figure 3. 25 evince the reaching of a plateau at a copolymer concentration of 5 $mg.mL^{-1}$, implying almost a complete occupation of the available sites for HSA adsorption. As for HSA adsorption, it was found to be reduced with the increase in copolymer concentration, which confirms the antifouling properties of PEO. The exact behaviour has been proven to take place in a previous study, where the rejection of HSA was found to increase with increased grafting density of PEG of molecular weight 5kDa [24].

This resistance to protein adsorption is probably due the strong water affinity of PEO, its large excluded volume and strong coordination capability to water molecules [25]. Many studies have demonstrated that PEO chains physically or chemically fixed on the material surface form a surface hydration layer and thus resist the nonspecific adsorption of foreign substances [26].

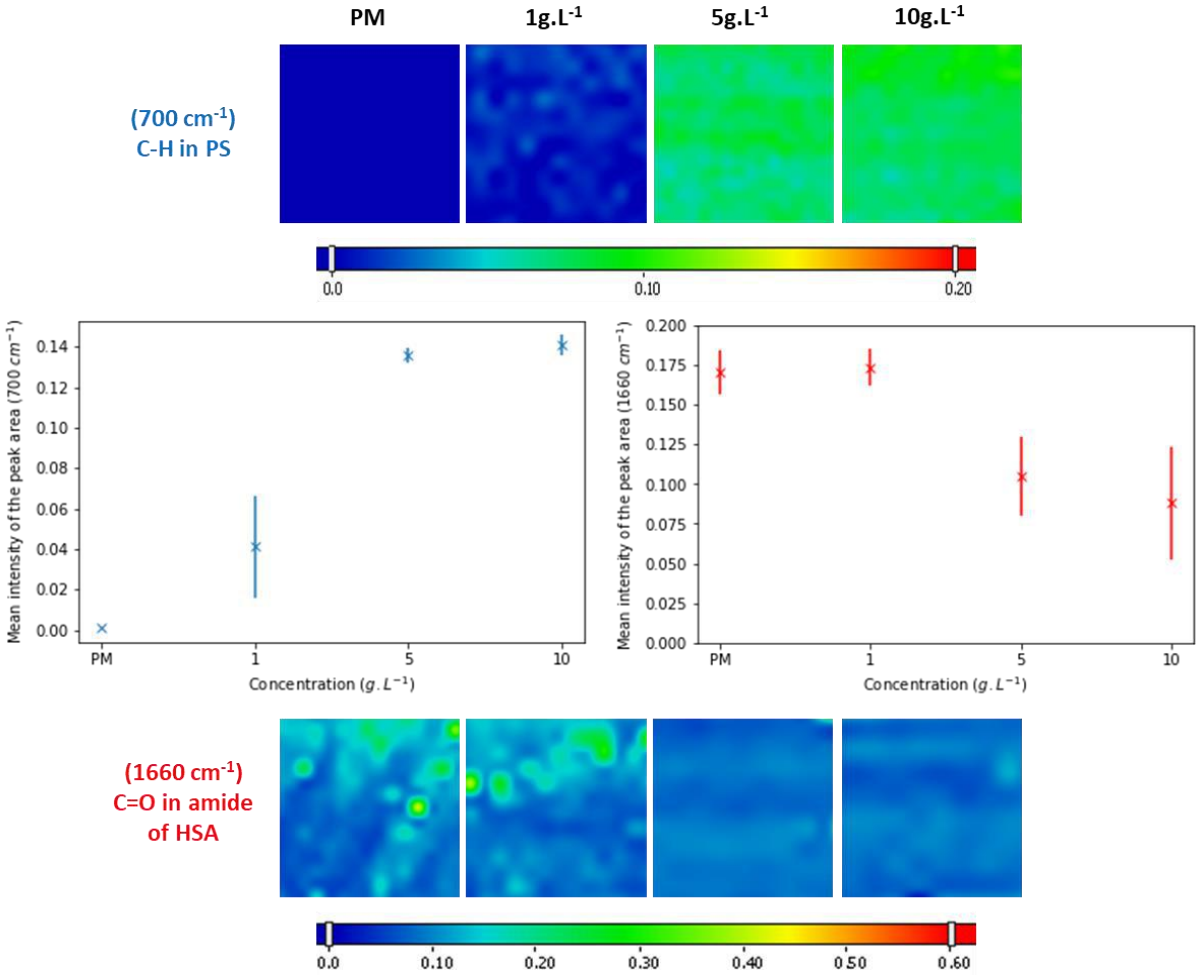

Figure 3. 25. FTIR maps for the adsorption of HSA protein on PVDF membranes coated with different concentrations of PS_{30}-b-PEO_{13} copolymer, as well as the evaluated mean intensities for the peaks area at 700 cm^{-1} and 1660 cm^{-1}; [HSA]= 1 $mg{\cdot}mL^{-1}$.

5.5. HSA adsorption on membrane coated with both PS-b-PAA and PS-b-PEO

The previous results have evinced the adsorption of HSA on PS-b-PAA coated membranes. Meanwhile, the adsorption of the same protein on membrane coated with PS-b-PEO was proved to be reduced. In this section, the adsorption of HSA is tested on PVDF membranes coated with both copolymers at the same time, and it was compared to that on each copolymer alone. The coating was performed using PS_{26}-b-PAA_{76} and PS_{28}-b-PEO_{13}, two copolymers that have shown almost similar abilities of PS adhesion to the membrane surface. The copolymer concentration used for coating was 5 $mg{\cdot}mL^{-1}$ each one alone, and 5 $mg{\cdot}mL^{-1}$ of PS_{26}-b-PAA_{76} + 5 $mg{\cdot}mL^{-1}$ of PS_{28}-b-PEO_{13} in the mixture. Samples were characterized using FTIR mapping and maps were generated for the peaks area at 700 cm^{-1} and 1660 cm^{-1} to check the presence of copolymers and HSA respectively.

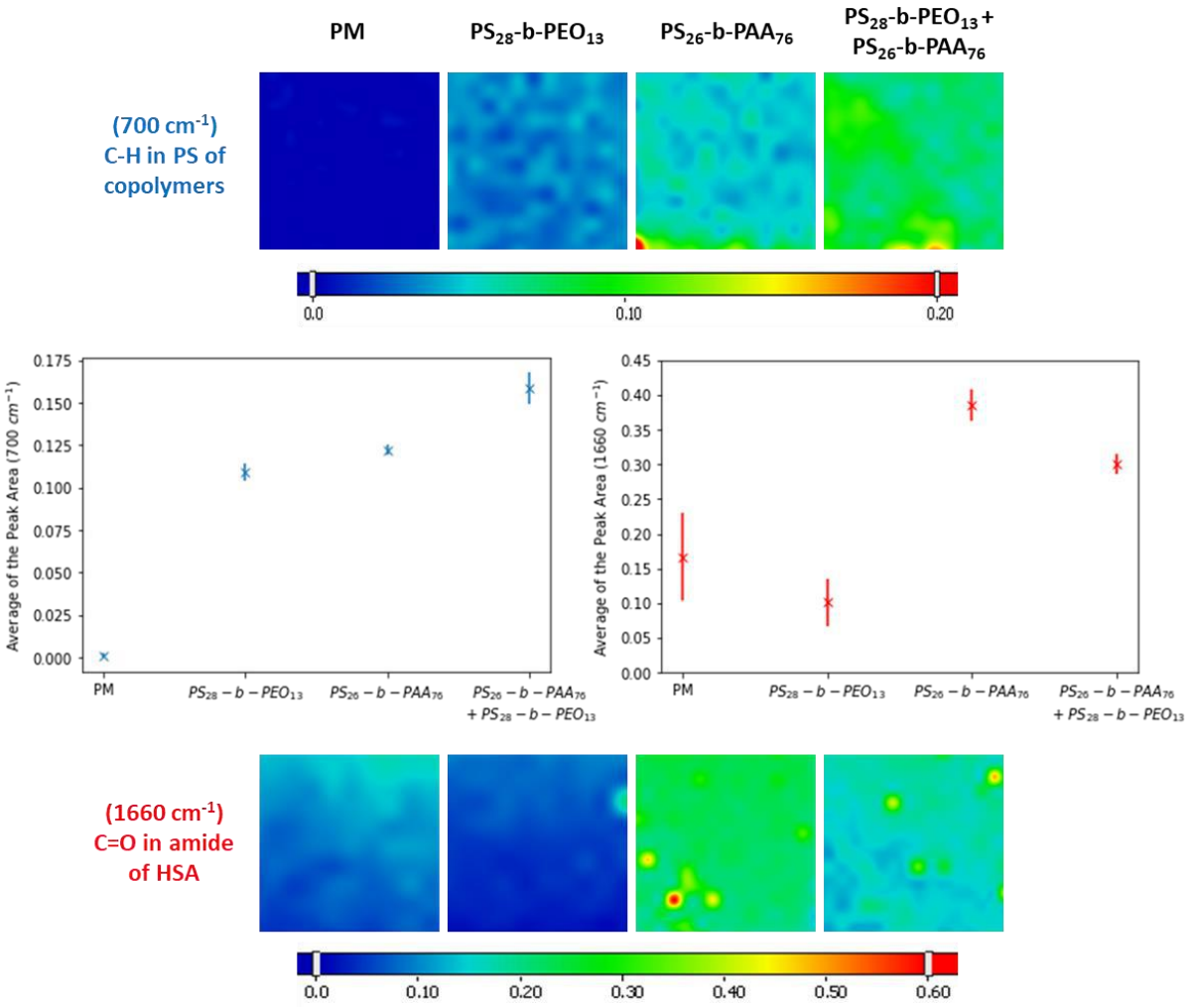

Figure 3. 26. FTIR maps for the adsorption of HSA protein on PVDF membranes coated with PS_{26}-b-PAA_{76} and PS_{28}-b-PEO_{13} as well as the evaluated mean intensities for the peaks area at 700 cm^{-1} and 1660 cm^{-1}; [HSA]= 1 $mg \cdot mL^{-1}$.

FTIR maps and the evaluated mean intensities, shown in Figure 3. 26, confirm the presence of both copolymers on the same surface. Indeed, the coverage of the membrane coated with the mixture of both copolymers was found to be larger than that with each copolymer alone at the same concentration. As for the HSA adsorption, results proved once again that it increased in the presence of PS-b-PAA, and that it was reduced in the presence of PS-b-PEO. When both copolymers are present, the adsorption of HSA seems to be less compared to that on PS-b-PAA alone but higher compared to that on PM and on PS-b-PEO alone. This suggests that the interactions between HSA and the visible segments of PS dominate against those between HSA and PEO. This could probably be due to the random arrangement of the copolymer brushes on the membrane surface, which creates heterogeneity on the distribution of the PEO chains and on the spaces between the copolymer moieties.

5.6. Influence of pH on HSA adsorption onto membrane coated with PS-b-PAA

In the previous section, the adsorption of HSA on PVDF membranes coated with PS-b-PAA was observed at pH 7, which was probably due to its hydrophobic interaction with the PS blocks combined to some electrostatic attractions with the negatively charged PAA. Meanwhile, it has been proven explicitly that at this same pH, the HSA does not show any affinity with PAA chains in solution. In fact, the binding between the two was found to happen only at pH 5 forming HSA-PAA complexes. Moreover, the number of HSA bound to each PAA chain has been proven to be correlated to the PAA chain length. In order to check the reproducibility of these same findings, but with a PAA fixed onto a surface, the adsorption of 1 $mg \cdot mL^{-1}$ of HSA on PVDF membrane coated with PS-b-PAA was studied again in this section. However, the adsorption was carried out this time at different pH (5, 7 and 8) and for the coating of two copolymers (PS_{30}-b-PAA_5 and PS_{100}-b-PAA_{107}), with a short PAA segment and with a larger one. The coating was performed using ID process, 2 hours of coating time and a copolymers concentration of 5 $mg \cdot mL^{-1}$. The pH of HSA solutions used for the immersion of the coated membranes was controlled using different buffer solutions at 0.1 M (TRIS base pH 8, HEPES pH 7, and a mixture of sodium citrate di-hydrate and citric acid at pH 5). While, the ionic strength of these protein solutions was fixed at 0.15 M by adding the required amounts of a 4 M NaCl solution.

The FTIR maps were generated first for the peak area at 700 cm^{-1} to confirm that the copolymer was correctly coated onto the membrane surface and then for the peak area at 1660 cm^{-1} to assess the presence of HSA. The obtained results (Figure 3. 27) confirm that both copolymers were correctly coated and show their presence all over the membrane surface. Indeed, for the coating of both copolymers, the evaluated mean intensities (Figure 3. 28) of the peak area at 700 cm^{-1} were almost the same for the different coated samples. That allowed us to compare then the adsorption of HSA at different pH on these same samples.

The maps evince also the presence of HSA over the whole range of studied pH, but its adsorption has been revealed to be greater for a pH of 5. The evaluation of the mean intensities of the peak area at 1660 cm^{-1} (Figure 3. 28) has affirmed that, where an intensity of 0.58 was obtained at pH 5 against 0.37 at pH 7 and 8 on membranes coated with PS_{30}-b-PAA_5 copolymer. As for membranes coated with PS_{100}-b-PAA_{107} copolymer, the intensity yields 0.64 at pH 5 against 0.41 and 0.40 at pH 7 and 8 respectively.

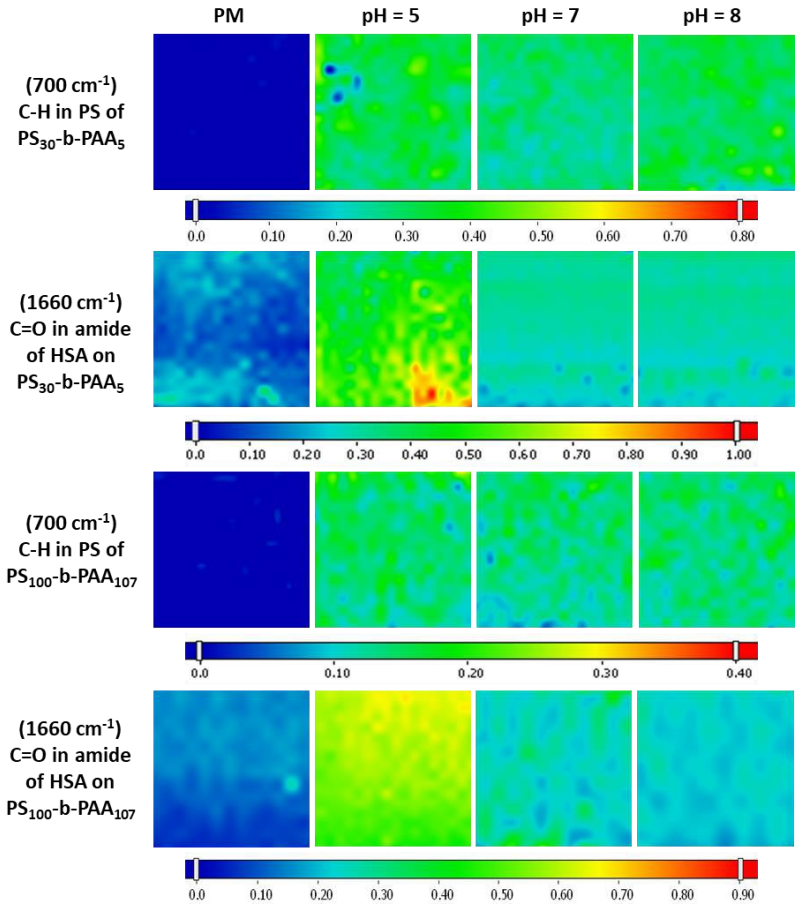

Figure 3. 27. FTIR maps for the adsorption of HSA at different pH (5, 7 and 8) on PVDF membranes coated with PS_{30}-b-PAA_5 and PS_{100}-b-PAA_{107} copolymers using ID process, 2 hours of immersion and a copolymer concentration of 5 mg·mL^{-1}; [HSA]= 1 mg·mL^{-1}.

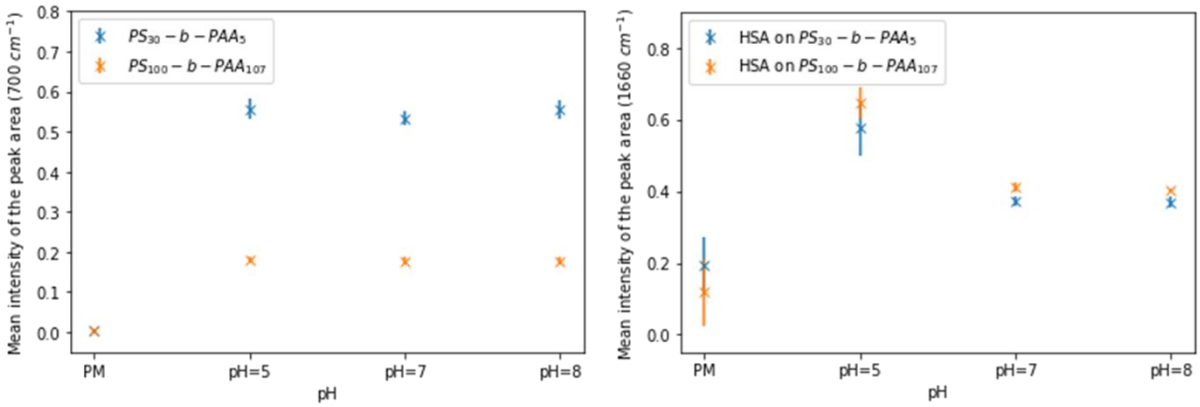

Figure 3. 28. Evaluated mean intensities of the peaks area at 700 cm^{-1} and 1660 cm^{-1} showing respectively the uniformity of coating on different samples and the adsorption of HSA onto these samples at different pH; [HSA]= 1 mg·mL^{-1}.

It is important to remember that the protein and the PAA chains are both negatively charged because the HSA has an isoelectric point around 4.7, and the PAA has a pKa that yields 4.5. However, even though the overall charge of the protein is negative this latter carried positives patches on its surface [27] as shown in Figure 3. 29.

Thus, repulsive electrostatic interactions are supposed to happen because of the negative overall charges that both HSA and PAA bear, whereas the adsorption of HSA was found to take place. As stated previously, this behaviour is probably due to hydrophobic interactions between HSA and the visible PS segments in the spaces between PAA brushes, in addition to electrostatic attractions that could take place between the negatively charged PAA and the positive patches on HSA surface (Figure 3. 29). Thereby, the increase in adsorption at pH 5 could be due to the reduction in the negative overall charge of the protein, which reduces the electrostatic repulsions and allows HSA molecules to get closer to PAA chains. Thus, it could increase the HSA adsorption driven by the attractive electrostatic interactions with PAA, and so increases the total amount of HSA adsorbed onto the membrane surface.

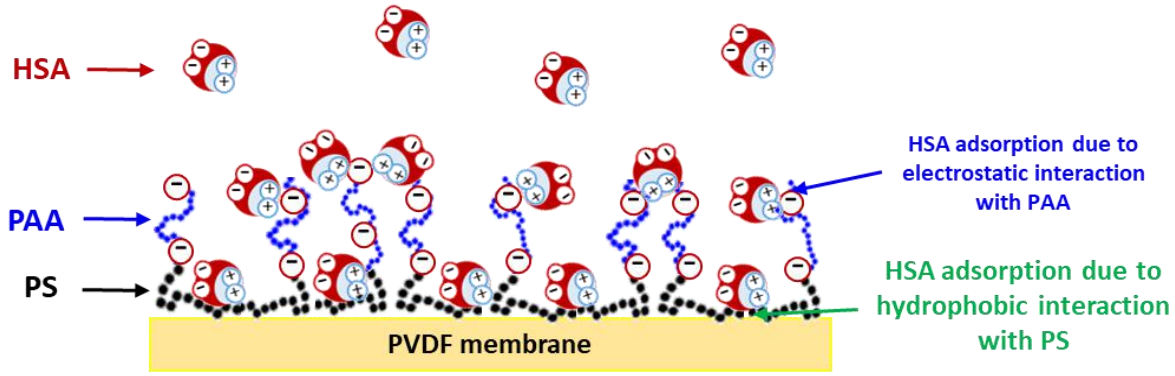

Figure 3. 29. Illustration of the HSA adsorption onto PS-PAA coated membrane due its hydrophobic interactions with the visible PS and electrostatic interactions with PAA brushes.

These results have proved also that the adsorption was not correlated to the PAA size as it was the case in the previous chapter (section 4.6). This could be due to the fact that the protein molecules may not have access to the full length of the PAA chains linked from one end to the PS block which is attached to the membrane in a random way. This suggests that not all the length of the PAA segment is in contact with the protein molecules, which makes it difficult to imagine the same interactions as in solution.

In order to support these findings, the adsorbed amount of HSA has been estimated by difference of mass before and after immersion of the coated membranes in the protein solution

using the UV-visible spectroscopy. As previously explained, the initial concentrations were evaluated also for more reliable measurement. Since the adsorption was carried out by immersion, the adsorbed amount of HSA was calculated by considering the area of both sides of the membrane (1 cm^2). Even though the adsorbed amounts of HSA are estimated for both sides of the membrane, results summarized in Table 3. 6 confirms the adsorption of HSA onto the coated membranes with higher amount at pH 5. This outcome corroborates the hypothesis suggesting that HSA adsorption at pH 5 is controlled by two forces, the hydrophobic interactions with the PS, and an increased electrostatic attraction with the PAA due to the reduction of the negative overall charge of HSA. The HSA-PAA interaction evidenced in solution at pH 5 is here responsible of an increase in adsorbed HSA by c.a. 53%.

Table 3. 6. The amounts of HSA adsorbed onto PVDF membranes coated with PS_{30}-b-PAA_5 and PS_{100}-b-PAA_{107} estimated using UV-visible spectroscopy.

HSA adsorption on PVDF membranes coated with PS_{30}-b-PAA_5				
pH	**Initial concentration ($mg \cdot mL^{-1}$)**	**final concentration ($mg \cdot mL^{-1}$)**	**coating density ($mg \cdot cm^{-2}$)**	**standard deviation ($mg.cm^{-2}$)**
PM (pH=7)	1.15	0.96	0.19	0.06 (32%)
5	1.15	0.63	0.52	0.07 (13%)
7	1.15	0.82	0.33	0.05 (15%)
8	1.15	0.8	0.35	0.05 (14%)
HSA adsorption on PVDF membranes coated with PS_{100}-b-PAA_{107}				
PM (pH=7)	1.15	0.99	0.16	0.05 (31%)
5	1.15	0.57	0.58	0.06 (10%)
7	1.15	0.76	0.39	0.04 (10%)
8	1.15	0.79	0.36	0.06 (17%)

5.7. Ionic strength effect on HSA adsorption onto membrane coated with PS-b-PAA

Since we suggested that the increase in HSA adsorption at pH 5 could be due to the increased attractive electrostatic interactions, we varied in this section the salts concentration by adding the desired amount of NaCl to the protein solutions in order to check that. Therefore, the ionic strength was increased from 0 M of added salts (0.05 M provided by the buffer) to 0.5 M final concentration, and the pH was set at 5 using a mixture of sodium citrate di-hydrate and citric

acid. As previously, the coating was performed for PS_{30}-b-PAA_5 and PS_{100}-b-PAA_{107} using ID process, 2 hours of coating time and a copolymer concentration of 5 mg·mL^{-1}. After that, the modified membranes were immersed in 1 mg·mL^{-1} HSA solution, before being dried and characterized using FTIR mapping. The maps were then treated the same way and the mean intensities of the peaks area at 700 cm^{-1} and 1660 cm^{-1} were evaluated.

Whether from FTIR maps exposed in Figure 3. 30 or from the evaluated mean intensities shown in Figure 3. 31, it can be confirmed that both copolymers have been coated all over the membrane surface. As for the adsorption of HSA, it has been found to decrease with the increase of the ionic strength. Indeed, for membranes coated with PS_{30}-b-PAA_5, the intensity yields 0.53 for an ionic strength (I) of 0.05 M and 0.15 M, against 0.3 for I=0.5 M. As for membranes modified with PS_{100}-b-PAA_{107} the intensity yields 0.51 and 0.58 for a salts concentration of 0.05 M and 0.15 M respectively, against 0.28 for I=0.5 M.

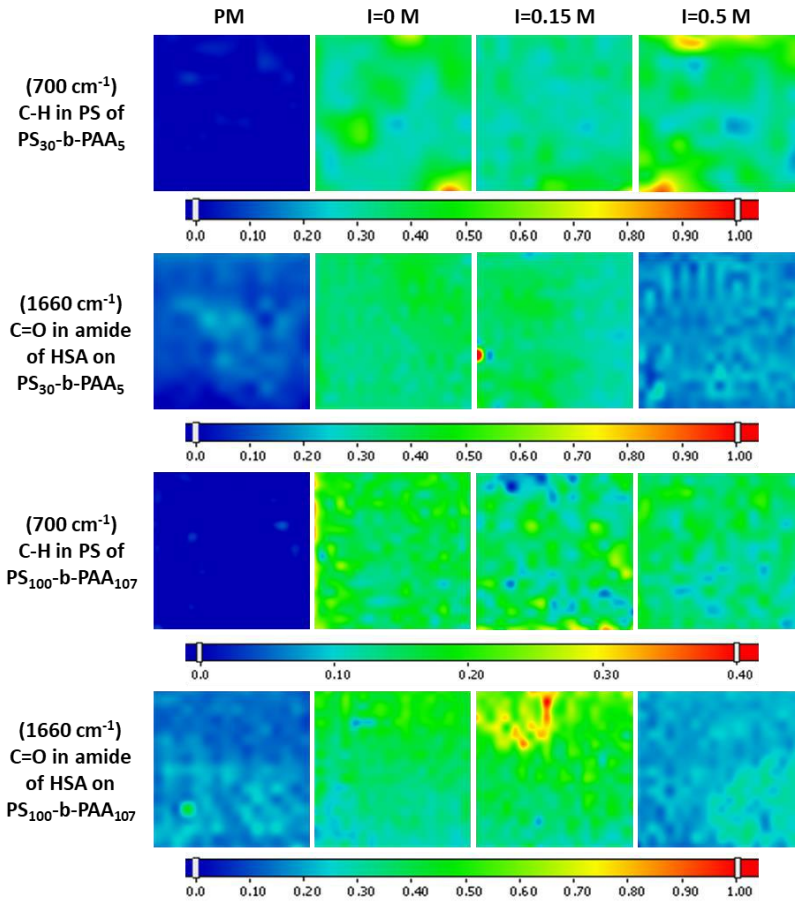

Figure 3. 30. FTIR maps for the adsorption of HSA at different ionic strength on PVDF membranes coated with PS_{30}-b-PAA_5 and PS_{100}-b-PAA_{107} using ID process, 2 hours of immersion and a copolymer concentration of 5 mg·mL^{-1}; [HSA]= 1 mg·mL^{-1}.

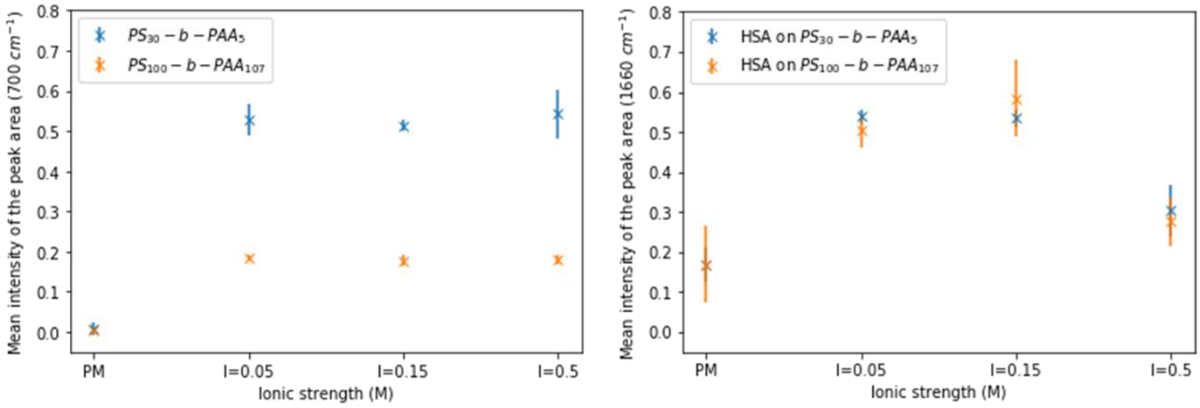

Figure 3. 31. The evaluated mean intensities of the peaks area at 700 cm^{-1} and 1660 cm^{-1} showing respectively the coating on different samples and the adsorption of HSA onto these same samples at different ionic strength; [HSA]= 1 $mg \cdot mL^{-1}$.

This outcome is consistent with what has been proven in the previous chapter (section 4.3), where the interactions between HSA and PAA were found to take place only at ionic strength ≤ 0.15 M. This confirms in some way the attractive electrostatic nature of the interactions between the protein and the PAA layer negatively charged. This could be coherent with the results of a study reported in the literature regarding interactions between HSA and PAA [27]. In this latter, simulations have showed that PAA can bind to some preferential positives patches on HSA because of specific electrostatic interactions.

In fact, in presence of attractive interactions, adding salt leads to screen, and thus to reduce the range of the attractive interactions. Thereby, the attraction between positive patches carried on the HSA surface and the PAA brushes should then be less efficient to induce adsorption. Therefore, the electrostatic repulsion due to negative overall charge of both overcomes the attractive forces and reduces the adsorption (as shown at I=0.5 M in Figure 3. 31). Indeed, the intensity was around 0.3 at I=0.5 M even though the pH was 5, which is lower than the intensity found to be around 0.4 at pH 7 and I=0.15 M. This confirms that the adsorption of HSA at pH 7 on a PVDF membrane coated with PS-b-PAA was not due only to hydrophobic interactions. It proved that electrostatic attraction between PAA and positive patches carried by HSA plays effectively a role even at pH 7 and this role became bigger at pH 5 due to stronger electrostatic attractive forces.

Eventually, these results confirm once again that, unlike interactions in solution with free PAA chains in the medium, those between HSA and a fixed PAA are not correlated to the PAA chain length.

5.8. IgG adsorption on membranes coated with PS_{30}-b-PAA_5 and PS_{100}-b-PAA_{107}

Previous results revealed the adsorption of HSA protein on PS-b-PAA coated membranes. This adsorption was found to be correlated to the pH and the ionic strength of the protein solution as it was also proved in the previous chapter. Indeed, it took place more at low ionic strength (≤ 0.15 M) and a pH of 5, while at higher pH and salts concentration the adsorption was much lower. In this section, the adsorption of IgG protein on membranes coated with two copolymers (PS_{30}-b-PAA_5 and PS_{100}-b-PAA_{107}) was studied at different pH and I=0.15 M.

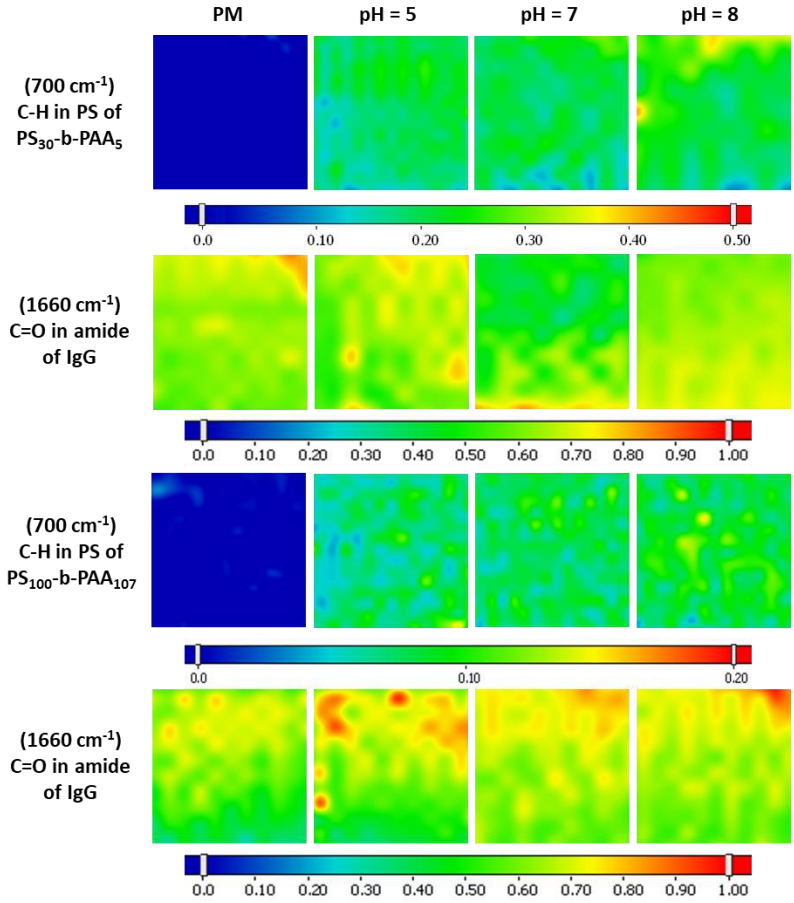

Figure 3. 32. FTIR maps for the adsorption of IgG at different pH (5, 7 and 8) on PVDF membranes coated with PS_{30}-b-PAA_5 and PS_{100}-b-PAA_{107} using ID process, 2 hours of immersion and a copolymer concentration of 5 mg·mL^{-1}; [IgG]= 1 mg·mL^{-1}.

As previously, before checking the presence of the protein over the membrane surface, that of the copolymer is first verified. FTIR mapping results (Figure 3. 32) confirm the presence of the coating layer of both copolymers all over the membrane surface. This made it possible to investigate then the adsorption of IgG found to take place similarly at different pH onto the coated membranes and onto the PVDF PM. That has been supported by the evaluation of the

mean intensities given in Figure 3. 33. However, the intensities for the PS presence have been found to be lower for both copolymers compared to those gotten in the previous sections. In fact, we got 0.25 and 0.1 for the coating of PS_{30}-b-PAA_5 and PS_{100}-b-PAA_{107} respectively, against intensities around 0.55 and 0.18 previously. This could be due to the large size of IgG (~150 kDa), which makes the copolymer less visible after the adsorption of the protein onto the surface. This also suggests that the IgG adsorption is due to the hydrophobic interactions between the PS segments of the copolymer brushes and the hydrophobic parts of the protein. Thereby, a large part of the PS blocks is hidden by the protein presence on it. Therefore, IgG does not exhibit specific interactions with PAA chains as it did for HSA. That could also be the reason why no difference was observed between the adsorption of IgG on coated membranes and on PM. Thus, HSA is much more soluble than IgG in PBS which means that the latter protein has weaker interactions with the solvent which increases its relative affinity for hydrophobic surfaces such as PVDF and PS. This is consistent with the behaviour of IgG already reported in the literature, where it was proved to be adsorbed strongly whether on PVDF [20], [28], or on PS surfaces [29].

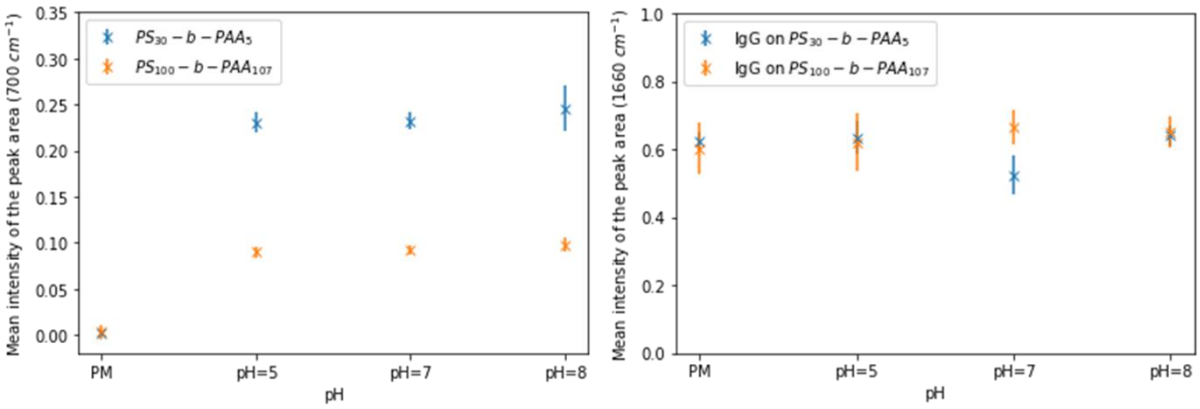

Figure 3. 33. The evaluated mean intensities of the peaks area at 700 cm^{-1} and 1660 cm^{-1} showing respectively the uniformity of coating on different samples and the adsorption of IgG onto these samples at different pH; [IgG]= 1 $mg \cdot mL^{-1}$.

These results proved that IgG can be adsorbed on membranes coated with PS-b-PAA even if the protein has no affinity with the hydrophilic PAA chains, something that has been proved in the previous chapter.

6. Conclusions

FTIR mapping is a powerful tool that allowed to assess the presence of different components with different chemical structure qualitatively on the membrane surface. It permitted us to investigate the distribution of the copolymers and proteins on the same surfaces.

The processing of FTIR maps using the Python code that allowed to evaluate the mean intensities of the peaks absorbance has strengthened the reliability of the mapping results. It gave the quantitative aspect to the analyses of the copolymer attachment and the protein adsorption.

The evaluation of the coating density by mass balance using the UV-visible spectroscopy sustained the FTIR results, despite the high standard deviation to the values and the non-consideration of the copolymer that penetrated into the membrane pores.

Coating via physisorption has been proved to be an effective technique for the modification of PVDF membranes even if it does not allow to control the distribution of the copolymer brushes over the membrane surface. In addition, drying immediately after the immersion was found to strengthen the attachment of the copolymer layer to the membrane surface, and make it difficult to remove with washing. Meanwhile, washing immediately after immersion and before drying removed a big part of this layer.

Two hours of immersion and a copolymer concentration of 5 $mg \cdot mL^{-1}$ were enough to allow copolymers (PS-b-PAA and PS-b-PEO) to adsorb on the membrane surface and to cover it almost completely.

The adsorption of HSA on PS-b-PAA coated membranes has been revealed to be correlated to the pH and the ionic strength as it was the case for the HSA-PAA complexation in solution. That involved the electrostatic attraction role between HSA and PAA on this adsorption, but also the hydrophobic interactions between HSA and PS blocks.

The coating of PS-b-PEO over the membrane surface increased the rejection of HSA and enhanced the resistance of the membrane to the nonspecific adsorption of proteins. The coating of both copolymers (PS-b-PAA and PS-b-PEO) onto the same membrane surface has been found to be possible, where each copolymer has brought its contribution to the HSA adsorption. In fact, the protein adsorption on membrane coated with both copolymers was lower than on PS-b-PAA alone but greater than that on PS-b-PEO alone.

The IgG has shown a different behaviour on the PS-b-PAA coated membrane than that shown by HSA. Indeed, it exhibited the same ability of adsorption whether on a PVDF pristine membrane or on a coated one.

7. References

[1] Y. Fang, Z.-K. Xu, and J. Wu, 'Surface Modification of Membranes', in *Encyclopedia of Membrane Science and Technology*, American Cancer Society, 2013, pp. 1–15.

[2] K. C. Khulbe, C. Feng, and T. Matsuura, 'The art of surface modification of synthetic polymeric membranes', *Journal of Applied Polymer Science*, vol. 115, no. 2, pp. 855–895, 2010.

[3] C. Bellmann, 'Surface Modification by Adsorption of Polymers and Surfactants', in *Polymer Surfaces and Interfaces: Characterization, Modification and Applications*, M. Stamm, Ed. Berlin, Heidelberg: Springer, 2008, pp. 235–259.

[4] L. W. Bruch, M. W. Cole, and E. Zaremba, *Physical Adsorption: Forces and Phenomena*. Courier Dover Publications, 2007.

[5] L. Benavente *et al.*, 'FTIR mapping as a simple and powerful approach to study membrane coating and fouling', *Journal of Membrane Science*, vol. 520, pp. 477–489, 2016.

[6] F. Senusi, M. Shahadat, and S. Ismail, 'Treatment of emulsion oil using tannic acid/tetraethylenepentamine-supported polymeric membrane', *Int. J. Environ. Sci. Technol.*, vol. 16, no. 12, pp. 8255–8266, 2019.

[7] A. Venault *et al.*, 'A combined polymerization and self-assembling process for the fouling mitigation of PVDF membranes', *Journal of Membrane Science*, vol. 547, pp. 134–145, 2018.

[8] C.-C. Yeh *et al.*, 'Universal Bioinert Control of Polystyrene Interfaces via Hydrophobic-Driven Self-Assembled Surface PEGylation with a Well-Defined Block Sequence', *Macromolecular Chemistry and Physics*, vol. 218, no. 19, p. 1700102, 2017.

[9] N.-J. Lin *et al.*, 'Surface Self-Assembled PEGylation of Fluoro-Based PVDF Membranes via Hydrophobic-Driven Copolymer Anchoring for Ultra-Stable Biofouling Resistance', *Langmuir*, vol. 29, no. 32, pp. 10183–10193, 2013.

[10] S.-H. Tang, A. Venault, C. Hsieh, G. V. Dizon, C.-T. Lo, and Y. Chang, 'A bio-inert and thermostable zwitterionic copolymer for the surface modification of PVDF membranes', *Journal of Membrane Science*, vol. 598, p. 117655, 2020.

[11] A. Venault, Y. Chang, H.-S. Yang, P.-Y. Lin, Y.-J. Shih, and A. Higuchi, 'Surface self-assembled zwitterionization of poly(vinylidene fluoride) microfiltration membranes via hydrophobic-driven coating for improved blood compatibility', *Journal of Membrane Science*, vol. 454, pp. 253–263, 2014.

[12] Y.-C. Chiag, Y. Chang, W.-Y. Chen, and R. Ruaan, 'Biofouling Resistance of Ultrafiltration Membranes Controlled by Surface Self-Assembled Coating with PEGylated Copolymers', *Langmuir*, vol. 28, no. 2, pp. 1399–1407, 2012.

[13] H. Bessaies-Bey, 'Polymères et propriétés rhéologiques d'une pâte de ciment: une approche physique générique', p. 267.

[14] L. Barbeş, C. Rădulescu, and C. Stihi, 'ATR-FTIR SPECTROMETRY CHARACTERISATION OF POLYMERIC MATERIALS', p. 13.

[15] D. J. Johnson, D. L. Oatley-Radcliffe, and N. Hilal, 'State of the art review on membrane surface characterisation: Visualisation, verification and quantification of membrane properties', *Desalination*, vol. 434, pp. 12–36, 2018.

[16] P. R. Griffiths and J. A. D. Haseth, *Fourier Transform Infrared Spectrometry*. John Wiley & Sons, 2007.

[17] M. A. Mohamed, J. Jaafar, A. F. Ismail, M. H. D. Othman, and M. A. Rahman, 'Chapter 1 - Fourier Transform Infrared (FTIR) Spectroscopy', in *Membrane Characterization*, N. Hilal, A. F. Ismail, T. Matsuura, and D. Oatley-Radcliffe, Eds. Elsevier, 2017, pp. 3–29.

[18] M. Kallioinen and M. Nyström, 'Membrane Surface Characterization', in *Advanced Membrane Technology and Applications*, John Wiley & Sons, Ltd, 2008, pp. 841–877.

[19] J. Schaller, S. Gerber, U. Kaempfer, S. Lejon, and C. Trachsel, *Human Blood Plasma Proteins: Structure and Function*. John Wiley & Sons, 2008.

[20] A. Venault, M. R. B. Ballad, Y.-H. Liu, P. Aimar, and Y. Chang, 'Hemocompatibility of PVDF/PS-b-PEGMA membranes prepared by LIPS process', *Journal of Membrane Science*, vol. 477, pp. 101–114, 2015.

[21] H. G. W. Lensen, W. Breemhaar, C. A. Smolders, and J. Feijen, 'Competitive adsorption of plasma proteins at solid—liquid interfaces', *Journal of Chromatography B: Biomedical Sciences and Applications*, vol. 376, pp. 191–198, 1986.

[22] H. Yang, L. Guo, Z. Wang, N. Yan, and Y. Wang, 'Nanoporous Films with Superior Resistance to Protein Adsorption by Selective Swelling of Polystyrene-block-poly(ethylene oxide)', *Ind. Eng. Chem. Res.*, vol. 55, no. 29, pp. 8133–8140, 2016.

[23] P. A. George, B. C. Donose, and J. J. Cooper-White, 'Self-assembling polystyrene-block-poly(ethylene oxide) copolymer surface coatings: Resistance to protein and cell adhesion', *Biomaterials*, vol. 30, no. 13, pp. 2449–2456, 2009.

[24] M. Malmsten, K. Emoto, and J. M. Van Alstine, 'Effect of Chain Density on Inhibition of Protein Adsorption by Poly(ethylene glycol) Based Coatings', *Journal of Colloid and Interface Science*, vol. 202, no. 2, pp. 507–517, 1998.

[25] W. R. Gombotz, W. Guanghui, T. A. Horbett, and A. S. Hoffman, 'Protein adsorption to poly(ethylene oxide) surfaces', *Journal of Biomedical Materials Research*, vol. 25, no. 12, pp. 1547–1562, 1991.

[26] H. Yang, Z. Wang, Q. Lan, and Y. Wang, 'Antifouling ultrafiltration membranes by selective swelling of polystyrene/poly(ethylene oxide) block copolymers', *Journal of Membrane Science*, vol. 542, pp. 226–232, 2017.

[27] X. Xu, S. Angioletti-Uberti, Y. Lu, J. Dzubiella, and M. Ballauff, 'Interaction of Proteins with Polyelectrolytes: Comparison of Theory to Experiment', *Langmuir*, vol. 35, no. 16, pp. 5373–5391, 2019.

[28] Y. Chang, Y.-J. Shih, R.-C. Ruaan, A. Higuchi, W.-Y. Chen, and J.-Y. Lai, 'Preparation of poly(vinylidene fluoride) microfiltration membrane with uniform surface-copolymerized poly(ethylene glycol) methacrylate and improvement of blood compatibility', *Journal of Membrane Science*, vol. 309, no. 1, pp. 165–174, 2008.

[29] J. L. Brash and D. J. Lyman, 'Adsorption of plasma proteins in solution to uncharged, hydrophobic polymer surfaces', *Journal of Biomedical Materials Research*, vol. 3, no. 1, pp. 175–189, 1969.

Chapter IV.

Membrane transport properties assessment via dead-end filtration

1. Introduction

As reported in the previous chapter, the modification of PVDF membrane was successfully performed by coating PS-b-PAA and PS-b-PEO onto the surface. Besides, these copolymers were either found to selectively attach to blood proteins in the case of PS-b-PAA or to enhance the resistance to their adsorption in the case of PS-b-PEO. In this chapter, the modification was repeated on larger membrane surfaces, and the dynamic (i.e. in filtration mode) adsorption of HSA was investigated via its dead-end filtration through the modified membrane. This could help analyzing the extent to which blood proteins are adsorbed to the membrane surface in dynamic mode since in long terms our system is meant to capture of platelets when blood is passed as feed through the filtration system.

However, there are certain aspects that need to be considered during the filtration process. Especially during microfiltration, pore narrowing or pore blocking can reduce the membrane permeability and prevent the transmission of certain components of blood cells through the membrane. Pore blocking can be caused by both blood proteins and by the copolymers used for surface modification and that penetrate into the pores. Blood proteins tend to foul the surface whereas the pores are narrowed down by aggregates formed by the protein [1]. The aggregates formation can be due to the pressure, temperature, pumping, stirring and also due to electrostatic forces and hydrophobic interactions [2]. Another important phenomenon that affects the filtration performance is concentration polarization. It is a function of hydrodynamic conditions along the membrane and is independent of the membrane physical properties. It can create in some cases a new phase at the interface such as a protein gel layer, which reduces the permeate flux by offering a hydraulic resistance to the flow of solvent and by causing osmotic back pressure [3]. Moving on to certain important characteristic properties of membrane filtration are pH and ionic strength. It has been reported in the literature that at low pH, there was more selectivity in separating proteins like IgG and BSA, which was attributed to electrostatic interactions [4]. This is something that we also probed in the previous chapters, whether in solution using SAXS [5] or on the membrane surface using FTIR. It is to be noted that electrostatic interactions between the charged groups of the protein and the polymeric groups of the membrane play a major role in the aggregation or deposition [6]. Apart from electrostatic interactions, protein transport performance also depends upon operating conditions of the membrane used for filtration like the pore morphology, and surface physicochemical properties [7].

Hence, the effect of surface modification on the membrane permeability is first assessed in this chapter. Then, the deposition of HSA on PVDF membrane coated with different sizes of PS-b-PAA is explored during dead-end filtration experiments. Besides, the influence of HSA retention on the membrane transport properties is investigated by following the flux evolution during the dead-end filtration of HAS through the membrane. The permeability measurement is also performed on PS-b-PEO coated membrane, and the HSA filtration through was then carried out.

Eventually, the filtration is performed on PS-b-PAA coated membrane at pH 5, at which the adsorption has been revealed to be increased in the previous chapters whether at the interface of a modified membrane in static mode, or in solution.

It is important to note that the experiments presented in this chapter were performed with the help of a master student (Sharath JAYAKUMAR) hired for 6 months to work on this project.

2. Materials

The membranes used in this chapter are the same as those used in chapter III. It is a commercial polyvinylidene fluoride (PVDF) microporous membrane (VVHP, Millipore Co.) with an average pore size of 0.1 µm and a thickness of 125 µm. However, a larger area of membrane (3.8 cm^2) was used here compared to 0.5 cm^2 used previously. The different properties of this membrane are given in Table 3. 2 (section 3.1 of chapter III).

The copolymers used for surface modification are chosen among those which exhibited a good propensity of adhesion to the membrane surface in the previous chapter and that also showed a clear response to blood proteins whether adsorption or rejection. Hence, we used PS_{30}-b-PAA_5, PS_{30}-b-PAA_8, PS_{26}-b-PAA_{76}, PS_{100}-b-PAA_{107} and PS_{28}-b-PEO_{13}.

The filtration experiments were performed with either ultrapure water or solutions of albumin from human serum (A1653) purchased from Sigma-Aldrich, and that by using a pressurized stirred Amicon cell (Series 8010, Merck Millipore).

Copolymers were dissolved in 50% (v/v) absolute ethanol ($EtOH_{abs}$) and tetrahydrofuran (THF) purchased from VWR Chemicals Avantor® and Acros Organics, respectively. While HSA was dissolved in PBS 1X (pH=7.4; I=0.137M) diluted from phosphate buffer saline (PBS) solution 10X (BP399, Fisher BioReagents) using ultrapure water. Ultrapure water was purified was obtained from an ELGA PURELAB Prima purification system combined to an ELGA PURELAB Classic water purification system (final minimum resistivity of 18 MΩcm).

3. Methods

3.1. Permeability measurement and membrane coating

Before the filtration experiments are conducted, precautions should be taken to obtain accurate data. First, the hydrophobicity of the membrane could result in low transport characteristics. To overcome this and to help wetting the membrane, it was first immersed in absolute ethanol for a while before starting its compaction. Membrane compaction was a second step, which is the compression of the membrane due to applied pressure resulting in the unsteady and declining transport properties. The primary reason to perform membrane compaction is to reach steady transport characteristics.

In order to perform compaction, dead-end filtration of ultrapure water was conducted through the membrane placed in the Amicon cell (Series 8010, Merck Millipore). For that, the pressure was increased between 0.2 and 1 bar (by steps of 0.2 bar), and for each pressure the

weight of the permeate was measured every 5 minutes during 20 min to observe the instantaneous flux change and verify its stability. At 1 bar, the flux was noted until it reached almost a steady state.

After that, the pressure was decreased in the same range and the permeability was determined from the slope of the curve plotting flux vs pressure as stated by the following Darcy Law:

$$J_w = \frac{L_p}{\mu} \Delta P \quad (4.1)$$

Where J_w is the water flux ($m^3 \cdot m^{-2} \cdot s^{-1}$), L_p is the permeability (m), μ is the viscosity of the fluid (Pa·s) and ΔP is the transmembrane pressure (Pa).

After the evaluation of the pristine membrane permeability, its coating was performed. For this purpose, the cell was emptied of water without removing or touching the compacted membrane and the copolymer solution was then added. The membrane was left in contact of 4 mL of 5 $mg \cdot mL^{-1}$ copolymer solution during 2 hours. Subsequently, the copolymer solution was removed from the cell and the permeability of the coated membrane was determined the same way as for the pristine membrane. The filtration of ultrapure water through the coated membrane was performed by varying the pressure between 0.2 bar and 1 bar. For each pressure, the weight of the permeate was then collected every 5 min during 20 min, which was sufficient to reach almost a steady flux. The flux J_w was then calculated (in $L \cdot m^{-2} \cdot h^{-1}$) by relating the weighted mass of permeate to the time and the membrane area (3.8 cm^2). It is important to mention that all experiments were performed at a room temperature of 22 ± 3 °C.

3.2. Dead-end filtration of HSA

The dead-end filtration of HSA was performed on membranes coated with the different copolymers mentioned in the previous section and the HSA retention was compared to that of the pristine membrane. This experiment was carried out by filling the Amicon cell with 10 mL of protein solution with a concentration of 1 $mg \cdot mL^{-1}$ that was filtered through the membrane. The pressure was set at 1 bar and the weight of permeate was noted down every minute until almost 3 mL was left in the retentate. The volume reduction factor (*VRF*), that can be calculated using the formula below would be equal to 3.3.

$$VRF = \frac{V_0}{V_R} = \frac{V_0}{V_0 - V_P} \quad (4.2)$$

Where V_0 is the initial volume of HSA solution, while V_P and V_R are the volume of permeate and retentate, respectively. The dead volume that may remain between the membrane and the support and in the permeate pipe was collected with permeate.

The permeate and retentate were then collected and the absorbance of the samples was measured at 280 nm using UV-vis spectroscopy as explained in section 3.3.1 of chapter III. The absorbance value was noted down and the concentrations of the permeate and retentate were then calculated using the calibration curve (given in section 1 of the **Appendix C**) obtained with absorbance of HSA at known concentrations. Then the retention was calculated using the following equation:

$$Retention\ (R) = 1 - \frac{C_P}{C_R} \tag{4.3}$$

Where C_P and C_R are the HSA concentration in permeate and retentate, respectively, at the end of the dead end filtration (i.e for a *VRF*=3.3).

Besides, the concentration factor (*FC*) can be then defined as follows:

$$FC = \frac{C_R}{C_0} \tag{4.4}$$

In order to analyse the extent of membrane fouling during dead-end filtration of protein solution, the flux reduction was calculated using the following formula:

$$Flux\ reduction = \frac{J}{J_w} \tag{4.5}$$

Where J is the final flux at 1 bar during filtration of protein solution and J_w is the flux at 1 bar during water filtration.

Further, mass balance can also be used during filtration of protein solution to calculate the amount of protein adsorbed on the membrane surface using the following mass balance equation:

$$V_i\ C_i = V_P\ \cdot C_P + V_R\ \cdot C_R + m_{ads} \tag{4.6}$$

It is important to mention that all experiments from membrane compaction, to its coating and then dead-end filtration of HSA, were performed at a room temperature of 22 ± 3 °C. Experiments have been repeated at least twice to confirm the obtained results.

3.3. FTIR and ATR analysis

As stated in the previous chapter, FTIR was used to assess qualitatively the presence of the copolymer and the protein over the membrane surface. Thus, the membrane surfaces were scanned with an infrared spectrometer (IN10MX Thermo Scientific) equipped with a detector MCT-A cooled with liquid nitrogen, and a KBr beam splitter. FTIR mapping was performed under ATR mode using a germanium crystal with 25° incident angle where 16 scans are acquired on each measurement point with a spectral resolution of 8 cm^{-1}. A total membrane area of 25 mm^2 was covered during each mapping where 50x50 points were measured (with step size of 100 µm between 2 points). Since the analysed area (0.25 cm^2) is too small compared to that coated initially (3.8 cm^2), simple ATR measurements were carried out on the membrane area not assessed by FTIR mapping. For that, ATR spectra are measured by collecting 16 scans for each point in five different locations of the membranes with a spectral resolution of 4 cm^{-1} using a Nicolet 6700, Thermo Scientific instrument. The five ATR spectra obtained from the five different locations were then averaged to get a spectrum that represents the chemical composition of the membrane surface.

FTIR analysis were processed with the OMNIC Software Suite (OMNIC Atlµs v.9.2, Thermo Fisher Scientific) which allowed the scanned maps to be displayed. The maps were generated at 700 cm^{-1} and 1720 cm^{-1} to evaluate the PS-b-PAA distribution over the membrane surface, and at 1660 cm^{-1} and 3300 cm^{-1} to assess that of HSA.

The average mean intensities from FTIR maps are evaluated as explained in section 4.2 of chapter III to compare qualitatively the presence of HSA over the membrane surface.

It is important to mention that FTIR and ATR analysis were carried out only after finishing all the steps of the filtration experiment, going through membrane compaction, permeability measurement, membrane coating and finally protein filtration. Besides, all samples were dried in the oven at 35 °C during 2 hours before ATR and FTIR measurement.

3.4. Water contact angle

Water contact angle is used to study the wettability of the modified membrane and compare it to that of the pristine one (principle explained in section 4.3.3.2 of chapter I). Since PVDF membranes were coated using copolymers of different hydrophobic/hydrophilic blocks sizes, the contact angle is expected to change by changing the block ratio. That was studied for various copolymers among those mentioned in section 2. Results are discussed later here in this chapter.

Accordingly, contact angle meter was used to determine the hydrophobicity of the membrane before and after coating, and then after HSA dead-end filtration. Initialization of the device was carried out by checking the base level of the contact angle meter to ensure that the sample holder was flat. The method used to determine the contact angle of the sample was by deposit drop method. The microscope attached to the device was tilted downwards between 0° and 1° at a position between 5 and 6 mm. The syringe used for measuring the contact angle was SY20 (28944) that was specifically used for the deposit drop method. The syringe was cleaned with pure water twice to ensure removal of impurities. Then it was pressed gently to remove any air gap. The substance that was used to measure the contact angle was water and the phase environment was set to air. The sample was prepared in such a way that the membrane was fixed tightly to the glass plate with an adhesive tape and ensured that the membrane was flat to prevent errors during measurement of contact angle. Then the glass plate was placed on the sample holder. The light was kept at high intensity to obtain a clear image of the measurement. The magnification of the microscope was set to 2.5X to obtain a precise image of the measurement. The adjustment knobs were used to position the sample at the center of the screen and the baseline was corrected. Then, the measurement was taken by bringing the needle closer to the sample and running the procedure. Once the water droplet (4 µL) falls on the sample, the syringe was moved away, and the measurement was saved. In such a way, five measurements were taken for each sample and the same procedure was followed for different samples. All samples were dried in the oven at 35 °C during 2 hours before contact angle measurement.

4. Results and discussions

4.1. Membrane conditioning and permeability measurement

As explained in section 3.1, the permeability of the PVDF membrane was determined only once the compaction had been achieved. Results shown in Figure 4. 1 show a hysteresis evolution of the flux when changing the pressure. In fact, the flux logically increased with the increase in pressure until 1 bar, before starting decreasing during the compaction of the membrane at this same pressure. Indeed, it decreased from around 280 $L \cdot m^{-2} \cdot h^{-1}$ before compaction to around 86 $L \cdot m^{-2} \cdot h^{-1}$ after compaction. This evinces the importance of the compaction step to avoid unsteady transport properties during filtration experiments. However, this significant decrease in flux is probably not only due to membrane compaction but also to the solvent exchange because the membrane had been soaked in absolute ethanol before water was passed through. Once the flux had reached almost a steady state at 1 bar, its evolution showed a linear correlation with the pressure. Thus, the permeability was obtained from the slope of this linear evolution of the flux versus the pressure according to Darcy's law given by equation 4.1, and it was found to be around 86 $L \cdot m^{-2} \cdot h^{-1} \cdot bar^{-1}$.

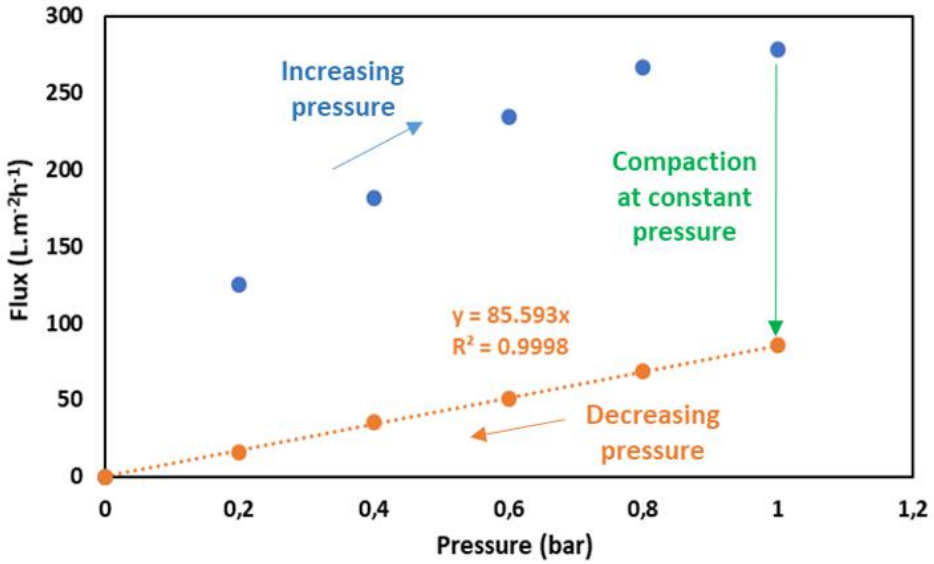

Figure 4. 1. Compaction of pristine membrane and solvent exchange, and the plot of the water flux versus pressure given the permeability of the pristine membrane.

Accordingly, the membrane was every time wet in ethanol and then compacted before the coating by copolymers or HSA filtration was performed. Thus, any further deviation of the transport properties would not be due to the compression of the membrane or to the solvent exchange, but to coating or fouling.

4.2. Effect of the copolymer size on the permeability of coated membranes

Once the compaction had been carried out, the Amicon cell was emptied from water to add then the copolymer solution in order to perform the coating of the compressed membrane (single contact of 4 mL of 5 mg·mL^{-1} copolymer solution during 2 hours). These experiments were conducted using PS_{30}-b-PAA_5, PS_{26}-b-PAA_{76} and PS_{100}-b-PAA_{107} in order to explore the copolymer size influence on the permeability of the membrane. Wherefore, permeability measurements were performed for membranes coated with each copolymer mentioned above. Eventually, membranes were dried and FTIR mapping was performed to check the coating presence and that the copolymer layer had not been removed during the permeability measurement i.e. when the water was passed through. FTIR maps were generated for the peaks at 700 cm^{-1} and 1715 cm^{-1} to assess respectively the presence of PS and that of PAA. For each peak, the maps are taken using the same scale for different copolymers, so that their coating over the membrane surface can be qualitatively compared.

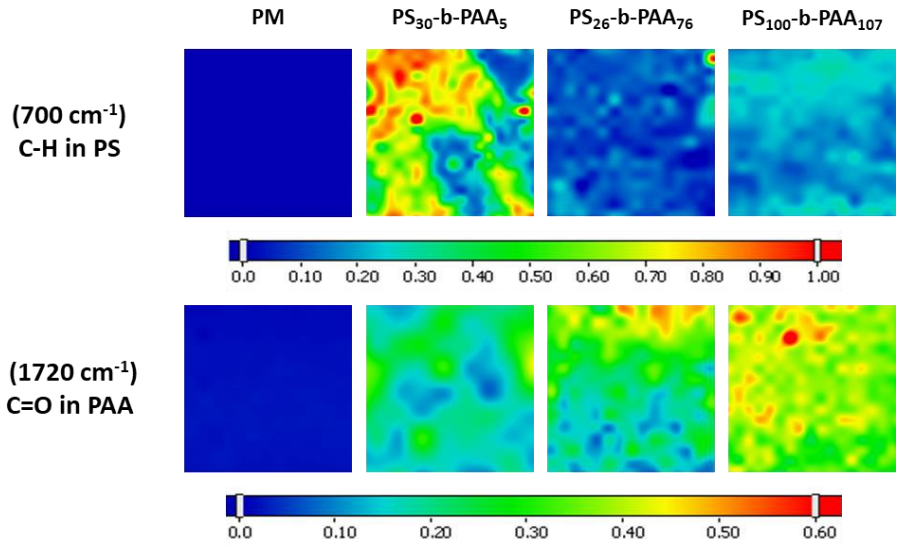

Figure 4. 2. FTIR maps generated at 700 cm^{-1} and 1715 cm^{-1} for the coating of PVDF membranes with different PS-b-PAA copolymers with a concentration of 5 mg·mL^{-1} and during 2 hours of coating time.

Results shown in Figure 4. 2 confirm the presence of both PS blocks and PAA segments, although their distribution over the membrane surface was heterogeneous. This means that physical adsorption of the copolymer onto the membrane surface has taken place and it is stable even if water was passed through the membrane immediately after coating for permeability measurement. This is probably due to the fact that the copolymer is not soluble in aqueous solutions which reduces its interaction with water and favors its stability onto the membrane.

However, it can also be noticed in Figure 4. 2 that the PS seems to be more present for the coating of PS_{30}-b-PAA_5 than for PS_{100}-b-PAA_{107} coating and then PS_{26}-b-PAA_{76} that showed the lowest intensity of coating. This would confirm hypothesis reported in the literature that longer hydrophilic chain could introduce increased steric hindrance blocking the access of PS moieties to the PVDF surface [8]. Besides, larger PAA necessarily have stronger interactions with the solvent [9], which reduce the copolymer adhesion into the membrane surface. However, longer hydrophilic segments could hide some parts of the PS blocks from being visible in FTIR. In fact, PAA seems to be logically more visible for the coating of PS_{100}-b-PAA_{107} than the coating of PS_{26}-b-PAA_{76} and then that of PS_{30}-b-PAA_5. Hence, if larger PAA hide some PS segments from being seen in FTIR maps, it is not possible to say which copolymer is more or less present but it is more accurate to say which part of each one is more visible. This outcome is consistent with what has been stated in the previous chapter (section 5.3) regarding the coating of membrane with different sizes of copolymer, which reinforces the validity of the result and makes it reliable.

Since the membrane samples used in this study were larger than in the previous chapter, contact angle measurements were carried out on the part not analyzed with FTIR. The obtained value of contact angle is an average of five measurements taken in different locations of the membrane because the distribution of copolymer has been shown to be heterogeneous over the surface. The results summarized in Table 4. 1 show a slight decrease in the contact angle from 123° for the PM to 105° after PS_{30}-b-PAA_5 coating to reach 97° and 101° after PS_{26}-b-PAA_{76} and PS_{100}-b-PAA_{107} coating. This is necessarily due to the presence of the hydrophilic PAA moieties over the membrane surface, which increases its hydrophilicity.

Table 4. 1: contact angles of PVDF membranes coated with different PS-b-PAA copolymers compared to that of the pristine membrane.

Sample	**Pristine membrane**	**PS_{30}-b-PAA_5**	**PS_{26}-b-PAA_{76}**	**PS_{100}-b-PAA_{107}**
Contact angle	123 ± 4	105 ± 3	97 ± 3	101 ± 6

Afterwards, the permeability of coated membranes was calculated as explained in section 3.1, and it was compared to that of the pristine membrane to evaluate the deviation of transport properties due to coating. Plots of the flux versus pressure from which the permeability was calculated after coating with each copolymer are shown in Figure 4. 3.

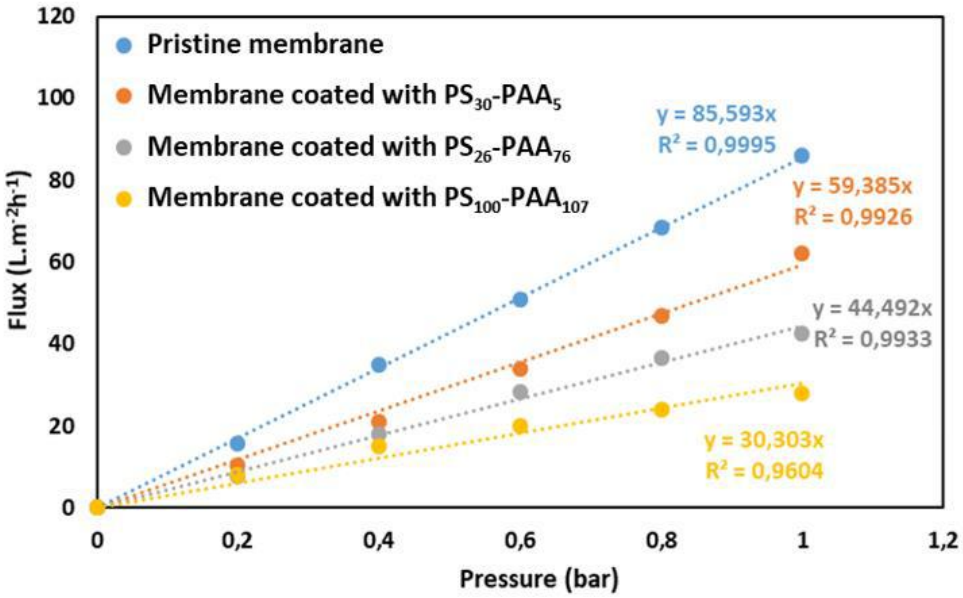

Figure 4. 3. Plots of the water flux vs pressure after coating with each copolymer from which the permeability was calculated.

From Figure 4. 3, it can be noticed that the permeability decreases with the increase in size of the copolymer coated over the membrane surface as evidenced by the permeability decline due to coating (Table 4. 2). Indeed, the permeability was found to be reduced by around 31% after the coating of PS_{30}-b-PAA_5 and by 48 % after that of PS_{26}-b-PAA_{76} whereas the decline was of 65 % after PS_{100}-b-PAA_{107} coating. This could be arising from the fact that larger chains length of the copolymer block the passage of water through the membrane by creating additional resistance to the system thereby reducing its permeability.

Table 4. 2. Permeability of membranes coated with different PS-b-PAA copolymers compared to that of the pristine membrane, as well as the decline percentage caused by coating.

Sample	**Permeability ($L \cdot m^{-2} \cdot h^{-1} \cdot bar^{-1}$)**	**Permeability decline (%)**
Pristine membrane	86	—
Membrane coated with PS_{30}-b-PAA_5	59	31
Membrane coated with PS_{26}-b-PAA_{76}	44	48
Membrane coated with PS_{100}-b-PAA_{107}	30	65

4.3. Dead-end filtration of HSA through membrane coated with PS-b-PAA

4.3.1. Assessment of HSA adsorption onto the membrane during dead-end filtration

Once the coating of compacted membrane had been successfully performed, the dead-end filtration of HSA was carried out in the Amicon cell. For that, the cell was filled with 10 mL of HSA solution and the filtration was performed at 1 bar until around 3 mL are left in the retentate (*VRF* = 3.3). The presence of HSA over the membrane surface was assessed using FTIR as shown in Figure 4. 4.

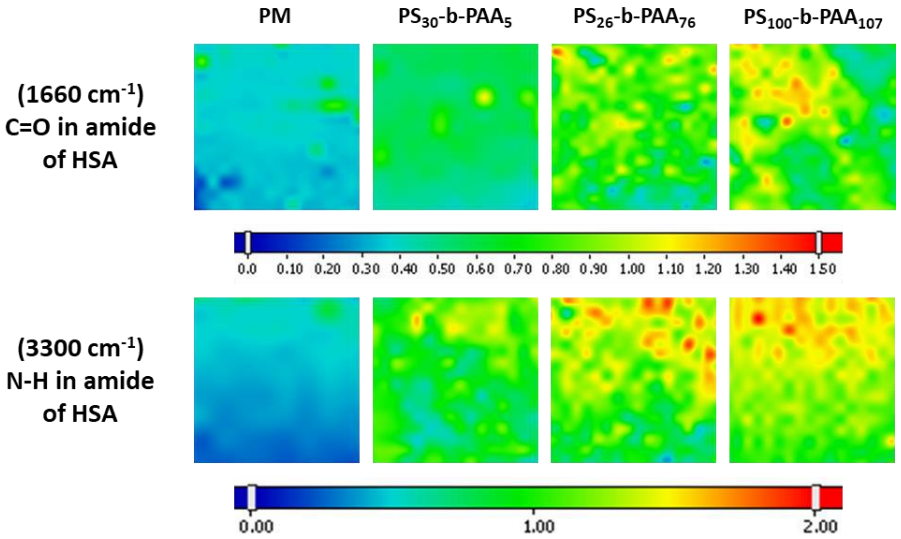

Figure 4. 4. FTIR maps generated at 1660 cm^{-1} and 3300 cm^{-1} for the adsorption of HSA during dead-end filtration on PVDF membranes coated with different PS-b-PAA copolymers. pH ≈ 7 ; [HSA]= 1 $mg \cdot mL^{-1}$; I ≈ 0.15M.

Results evince first the adsorption of HSA on the pristine membrane, which is probably due to hydrophobic interactions between the hydrophobic parts of protein and the PVDF membrane. The deposition of HSA seems to be then greater on coated membrane. Besides, a visual analysis of the FTIR maps discloses that it is slightly increasing with the increase in the copolymer size. However, since the visual difference is slight and the protein distribution over the membrane surface is heterogeneous, it is difficult to conclude on that by saying on which case the HSA deposition would be higher.

It is important to remember that the pH of HSA solution in this case was around 7 (pH of PBS). Thus, the HSA deposition would be due first to the adsorption driven by the combination of the hydrophobic interactions of the protein with the visible PS blocks on the membrane surface and the electrostatic attraction between the positive patches carried on HSA surface and

the negatively charged PAA brushes. This is what has been suggested in the previous chapter (section 5.7) and proved by the investigation of the ionic strength. This could also explain why the HSA adsorption is higher on modified membranes than on pristine membranes (PM) where it is probably caused by only hydrophobic interactions. However, the HSA deposition is taking place during dead-end filtration which is operated under pressure. Thus, the increase of HSA deposition could also be related to the accumulation of HSA once all the sites of adsorption are saturated, which could lead to the formation of a protein gel on the surface.

Otherwise, we can think that the greater adsorption of HSA on coated membrane than on PM could be due to stronger hydrophobic interactions between the protein and PS blocks than between the protein and the PVDF membrane. One can imagine that this could also be due to the fact that proteins are trapped between the polymer brushes in the case of coated membranes. Thereby, their removal when water is passed through the membrane would be easier on a pristine membrane than on a coated one, and it would be difficult when the copolymer brushes are larger.

ATR measurements were also performed on the remaining surface of the membrane, which was not analysed by FTIR. As for the contact angle measurement, ATR spectra were taken in five different locations of the membrane surface, before being averaged then to obtain the final spectrum that can give information about the chemical composition of the membrane surface. The obtained averages representing the chemical composition of the membrane surface after the adsorption of HSA on membrane coated with different PS-b-PAA copolymers are compared to that of HSA adsorption on PM as shown Figure 4. 5.

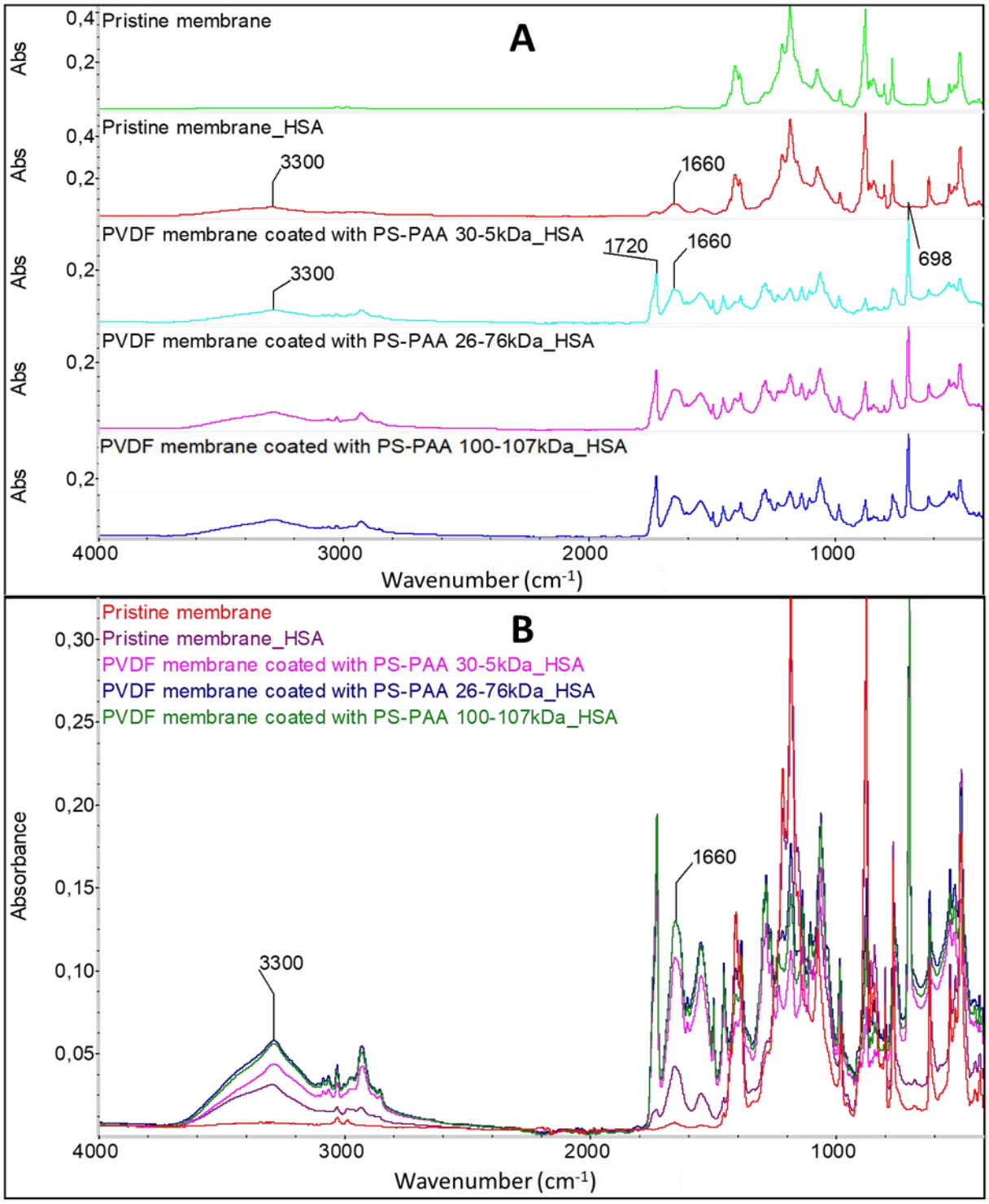

Figure 4. 5. ATR spectra representing the chemical composition of the membrane surface after the adsorption of HSA on membrane coated with different copolymers as compared to that of HSA adsorption on PVDF pristine membrane. B/ superimposition of spectra for the comparison of the peaks high.

First, the characteristic peaks of the copolymer at 700 cm^{-1} for PS and at 1720 cm^{-1} for PAA appear on these spectra (Figure 4. 5.A) which supports the results discussed in the previous section confirming the presence of the copolymer all over the membrane surface. Then, it is also possible to observe on the same spectra the characteristic peaks of HSA at 1660 cm^{-1} and at 3300 cm^{-1}, which affirms its presence too. However, while this outcome with the FTIR maps shown previously confirm the presence of the copolymer and the protein all over the membrane surface, it does not address the issue of their heterogeneous distribution.

For a more quantitative comparison, the spectra were superimposed to compare their peaks height, and so the amount of HSA adsorbed onto the surface. In fact, as stated in the previous chapter (section 3.3.2) and according to the Beer-Lambert law (equation 3.3), a higher absorbance peak means higher concentration on the surface. Therefore, the comparison of the spectra shown in Figure 4. 5.B indicates that more HSA was found on the membrane coated with PS_{30}-b-PAA_5 than on the PM since the characteristic peaks of protein (1660 cm^{-1} and 3300 cm^{-1}) are higher in the first case. Compared to this latter case, these peaks are then even higher for membranes coated with PS_{26}-b-PAA_{76} and PS_{100}-b-PAA_{107}, whereas no difference is shown between these two copolymers, as their peaks whether at 1660 cm^{-1} or 3300 cm^{-1} overlap almost entirely. These results are consistent with what has been observed from FTIR mapping. However, the trend observed here is partially different compared to that obtained in the previous chapter (section 5.4.1), where the adsorption of HSA was found to be not related to the copolymer size. This could be arising out of the fact that the pressure applied during filtration helps to trap more HSA between longer PAA brushes. In addition, it could enhance electrostatic interactions between the proteins and larger PAA chains by pushing HSA in contact with bigger part of PAA brushes. In other words, a longer part of the PAA chains becomes accessible to the HSA molecules to interact with it.

After dead-end filtration of HSA through modified membranes, the contact angle was also measured as previously explained. The obtained average values were compared to that obtained on the pristine membrane and on the modified membranes without HSA on the surface i.e. before the protein filtration is performed (Table 4. 1).

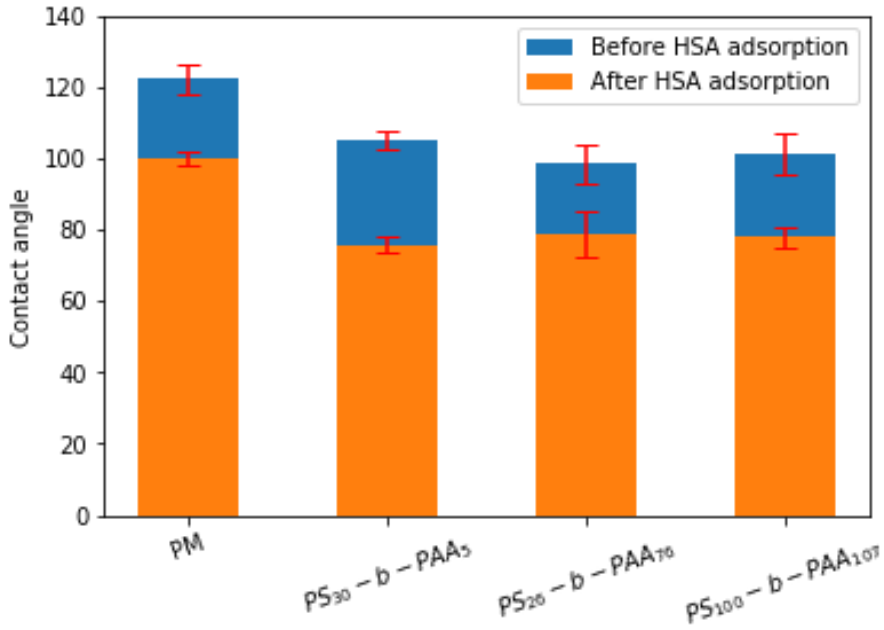

Figure 4. 6. Contact angles on PVDF membranes coated with different PS-b-PAA copolymers before and after filtration of HSA compared to that on the pristine membrane. pH ≈ 7 ; [HSA]= 1 mg·mL^{-1}; I ≈ 0.15M.

The bar graph in Figure 4. 6 represents the contact angle versus different conditions previously discussed. First, it is obvious that the contact angle decreased after the filtration of HSA through the membrane whether modified or not. This indicates that the adsorption of the protein onto the membrane surface increased its hydrophilicity. This makes sense since the HSA is adsorbed on the membrane due to interactions between its hydrophobic pockets and the membrane, which leave the hydrophilic amino acids of the protein more exposed on the surface. However, the contact angle is still higher on the pristine membrane than on coated one even after the adsorption of HSA. This could be indicative that the PM is not completely covered by the protein which would be consistent with what has been noticed from FTIR maps. Because if the coverage of the membrane surface by HSA were the same on PM as on coated membrane, the hydrophilicity would be the same, so we would expect the same contact angle on both membranes.

However, if FTIR and ATR results suggest a relatively higher adsorption on membranes coated with PS_{26}-b-PAA_{76} and PS_{100}-b-PAA_{107}, than on membrane coated with PS_{30}-b-PAA_5, the contact angle results do not exhibit exactly the same trend. Indeed, contact angles of around 76°, 79° and 78° have been obtained on membranes coated with PS_{30}-b-PAA_5, PS_{26}-b-PAA_{76} and PS_{100}-b-PAA_{107} respectively after the deposition of HSA. Thus, the hydrophilicity doesn't

seem to change much. This could mean that the contact angle technique is not that sensitive to slight differences of HSA adsorption previously observed from FTIR and ATR measurements.

4.3.2. HSA retention influence on membrane transport properties

As stated in section 3.2, during dead-end filtration, the permeate mass was noted down every minute until 3 mL are left in the retentate, so that the permeate flux could then be calculated. The flux evolution during HSA filtration on every modified membrane has been plotted versus time and is compared to that obtained on the pristine membrane (Figure 4. 7). From these results we can first notice that for a same volume (≈ 7 mL) that has been passed through the membrane, the filtration lasted less time on the PM than on the modified membranes and that on the latter it lasted longer when the copolymer was larger. Indeed, it lasted 13 min on the pristine membrane, while it lasted 23 min, 33 min and 47 min on membranes coated with PS_{30}-b-PAA_5, PS_{26}-b-PAA_{76} and PS_{100}-b-PAA_{107} respectively. This makes sense since we showed earlier in this chapter (section 4.2) that the permeability of the membrane decreased with the size of the copolymer.

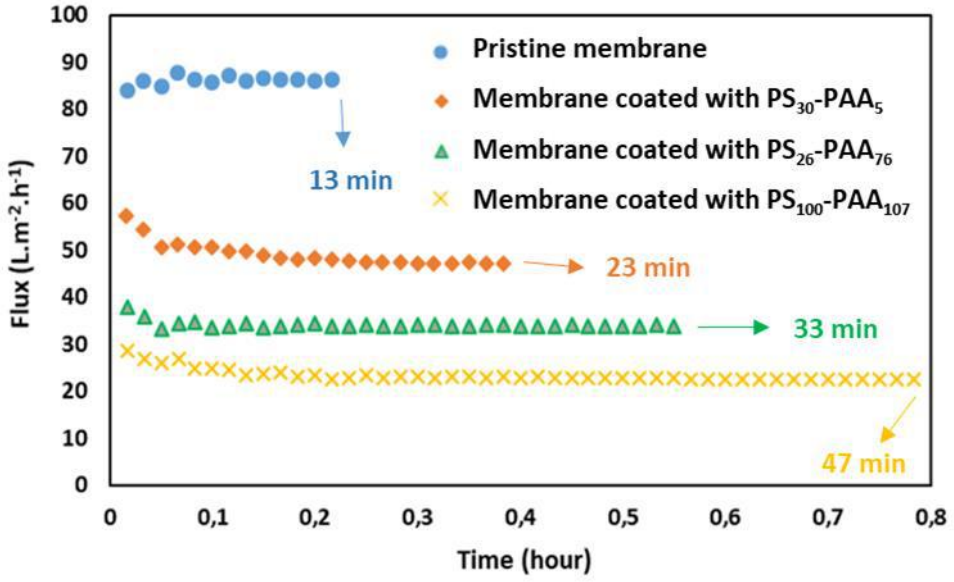

Figure 4. 7. Flux evolution versus time during HSA filtration at 1 bar on pristine and modified membranes with different PS-b-PAA copolymers.

It can also be noticed from Figure 4. 7 that the flux evolution displays almost the same trend on different copolymers where it decreased slightly in the beginning before becoming almost stable. This could be due to the adsorption of HSA on the membrane, which reduces the flux. However, the pristine membrane did not exhibit the same behaviour, where the flux was slightly

fluctuating between 84 and 87 $L \cdot m^2 \cdot h^{-1}$ but it was almost stable. This suggests that the adsorption of HSA on the pristine membrane does not affect its transport properties. In order to assess the effect of HSA adsorption on the membrane transport properties when it is coated with the different copolymers, the flux reduction was calculated using equation (4.5). The flux of water (J_w) was taken each time at 1 bar before HSA filtration was started, while J is the final flux at 1 bar after the filtration of 7 mL of protein solution. The obtained results plotted in Figure 4. 8 confirm first that the permeability of the PM was almost not affected by HSA adsorption, where J/J_w was found to be 0.98. However, deviations of the flux in the case of coated membranes have been displayed. Indeed, the J/J_w ratio has been found to be 0.82, 0.87 and 0.79, after the filtration of HSA on membranes coated with PS_{30}-b-PAA_5, PS_{26}-b-PAA_{76} and PS_{100}-b-PAA_{107} respectively. Meanwhile, the flux reduction does not exhibit much difference between the three copolymers and it does not seem to be related to the copolymer size. Thus, one can consider that the deviations observed could be due to deviations on the measurement during the experiments.

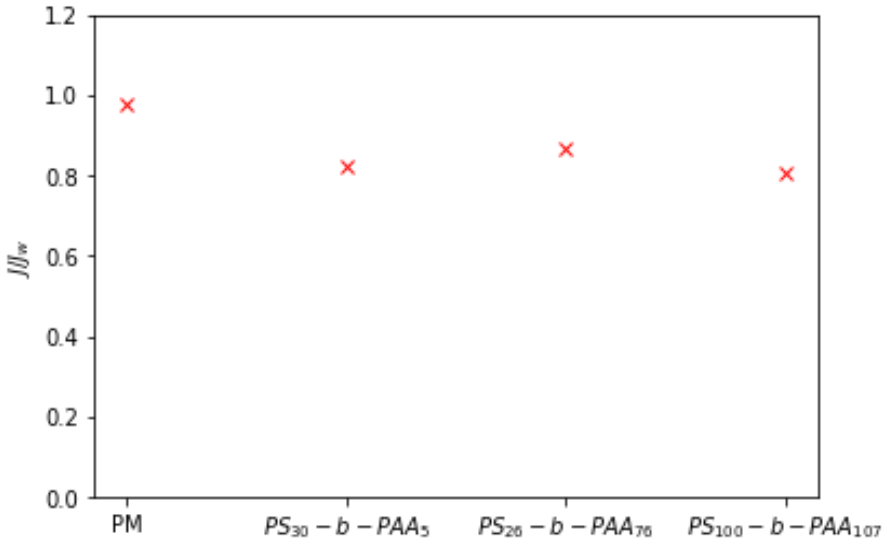

Figure 4. 8. Flux reduction after HSA filtration at 1 bar through pristine and modified membranes with different PS-b-PAA copolymers.

These results mainly evince that the reduction in permeability due to the adsorption of the protein is less substantial than that due to the deposition of the copolymer. This could be illustrated by plotting the flux evolution after surface modification by different PS-b-PAA copolymers, then after HSA filtration through these modified membranes (Figure 4. 9).

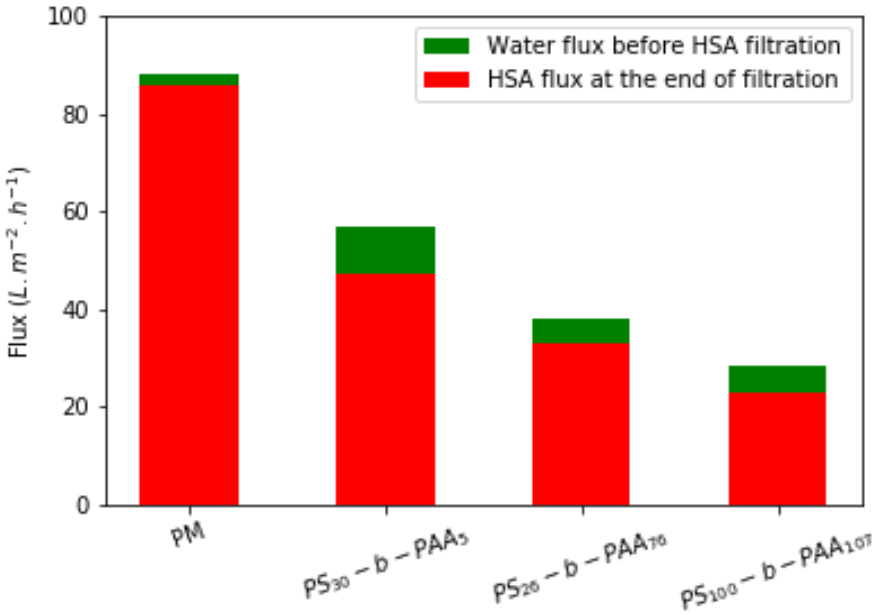

Figure 4. 9. The evolution of water flux J_w after surface modification by different PS-b-PAA copolymers, and the flux of HSA solution J in the end of filtration through these modified membranes.

Subsequently, the concentration of HSA in the permeate and in the retentate collected at the end of filtration was estimated using UV-visible spectroscopy. Thus, the membrane retention of HSA was evaluated using equation (4.3), to deduce the amount of protein adsorbed on the membrane surface by mass balance using equation (4.6). The outcomes of these calculations are summarized in Table 4. 3. One observes a decreasing HSA concentration in the permeate, while it increased in the retentate with the increase in copolymer size, which was then logically reflected by an increased retention rate. This is probably arising out of the fact that larger copolymers block more the pores and make them narrower. This has been shown earlier to decrease the membrane permeability and may also contribute to preventing the HSA passing through. Besides, the adsorption density of HSA onto the membrane surface was found to be around 0.11 mg·cm^{-2}, which is comparable to the protein adsorption density of the commercial membrane reported by the supplier to be 0.15 mg·cm^{-2} as shown in Table 3. 2. Then, the HSA adsorption density has been revealed to increase to 0.39 mg·cm^{-2} on membrane coated with PS_{30}-b-PAA_5, to reach 0.48 mg·cm^{-2} and 0.52 mg·cm^{-2} on that coated with PS_{26}-b-PAA_{76} and PS_{100}-b-PAA_{107} respectively. This is consistent with the FTIR and ATR results. In fact, the HSA adsorption has been shown to be higher on the membrane coated with PS_{30}-b-PAA_5 than on the pristine membrane, and even higher on membranes coated with PS_{26}-b-PAA_{76} and PS_{100}-b-PAA_{107} with not much difference between these two copolymers. As explained earlier, this

could be due to the fact that with the applied pressure, larger part of PAA is accessible to HSA molecules to interact with, which means that larger PAA would adsorb more HSA.

Table 4. 3. Calculations of protein retention by the PM and membranes coated with different PS-b-PAA copolymers as well as the evaluation of the amount of HSA adsorbed on the membrane surface and/or structure by mass balance.

Sample	Concentration of HSA in permeate ($mg \cdot mL^{-1}$)	Concentration of HSA in retentate ($mg \cdot mL^{-1}$)	Retention rate (%)	Mass of HSA adsorbed (mg)	Adsorption density ($mg \cdot cm^{-2}$)
Pristine membrane	0.92	1.05	12.4	0.41	0.11
Membrane coated with PS_{30}-b-PAA_5	0.74	1.11	33.3	1.49	0.39
Membrane coated with PS_{26}-b-PAA_{76}	0.58	1.37	57.7	1.83	0.48
Membrane coated with PS_{100}-b-PAA_{107}	0.49	1.53	68	1.98	0.52

4.4. Dead-end filtration of HSA through membrane coated with PS-b-PEO and with both PS-b-PAA and PS-b-PEO in the mixture

The procedure detailed previously was followed for the membranes coated with PS-b-PEO or with both PS-b-PAA and PS-b-PEO at the same time. Thus, coating of the compacted pristine membrane was performed using a 5 mg·mL^{-1} solution of PS_{28}-b-PEO_{13} copolymer. As for the coating of both copolymers at the same time, a mixture of 5 mg·mL^{-1} of PS_{26}-b-PAA_{76} + 5 mg·mL^{-1} of PS_{28}-b-PEO_{13} was used. The permeability of the membrane was evaluated before and after coating to assess the effect of coating on the membrane transport properties. After that, dead-end filtration of 10 mL HSA solution at 1 mg·mL^{-1} and pH ≈ 7 through the modified membranes was carried out until 3 mL are left in the retentate (*VRF* = 3.3). The flux was also noted down from the beginning to the end of the protein filtration to rate the reduction that could be due to fouling of the membrane with HSA.

Samples were characterized using FTIR mapping and maps were generated for the peaks area at 700 cm^{-1} and 1660 cm^{-1} to check the presence of copolymers and HSA respectively. Thereby, the amount of HSA found after dead-end filtration on membranes coated with both PS_{26}-b-PAA_{76} and PS_{28}-b-PEO_{13} is compared to the amount on the PM and on membrane coated with each copolymer alone.

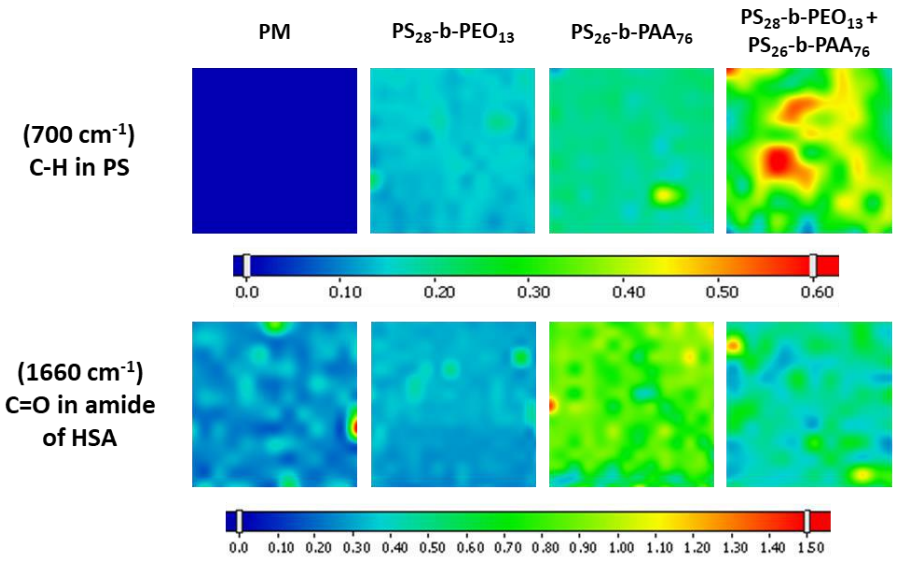

Figure 4. 10. FTIR maps generated at 700 cm^{-1} and 1660 cm^{-1} showing the presence of the coating layer and that of the protein after HSA filtration through modified membrane (pH ≈ 7; [HSA]= 1 mg·mL^{-1}).

FTIR maps shown in Figure 4. 10 confirm first the presence of coating and they show once again that the copolymers distribution over the membrane surface is heterogeneous. Besides, these maps display a higher intensity with the coating of both copolymers than the coating of each one alone, which indicates clearly the presence of both of them on the membrane surface in the first case.

A visual analysis of these maps evinces the presence of HSA on the membrane surface, and confirms once again that this amount is greater on the membrane coated with PS_{26}-b-PAA_{76} than on the PM. In addition, it has been shown to be also greater on membrane coated with copolymers in mixture than on a PM, but lower than that on a membrane coated with PS_{26}-b-PAA_{76}, which is consistent with what has been shown in the previous chapter (section 5.5). This is necessarily due to the presence of PS_{28}-b-PEO_{13}, which reduces the contact of HSA with PS_{26}-b-PAA_{76}. In fact, the PEO is able to create a hydration layer [10], which makes the PAA chains less accessible to the HSA. In addition, this could reduce the hydrophobic interactions of the protein with the visible blocks of PS on the membrane. However, the adsorption of HSA on membrane coated with PS_{28}-b-PEO_{13} seems to be equivalent to that on the PM or even slightly greater. This is not exactly what is reported in the previous chapter (section 5.4.2), where the adsorption of HSA is found to be reduced on membranes modified with this copolymer. This resistance to the protein adsorption was mainly attributed to PEO ability to form a surface hydration layer, its large excluded volume, and strong coordination capability to water molecules [11]. Apparently, this is not valid in this case, and one can assume that the flow through the membrane during filtration overcomes this hydration layer leading to the adsorption of protein molecules on the PS blocks due to hydrophobic interactions.

As explained earlier in this section, the permeability was evaluated after coating and it was logically found to be reduced as shown in Figure 4. 11. Indeed, it declined by around 40 % after the coating of the membrane with PS_{26}-b-PAA_{76} and by around 58 % after the deposition of both PS_{26}-b-PAA_{76} and PS_{28}-b-PEO_{13}. This makes sense because the presence of copolymer creates additional resistance to the passage of water, which reduces the membrane permeability. Thereby, the reduction is higher when the membrane is coated with both copolymers because more copolymers are deposited onto the surface. We noticed here that the permeability of the pristine membrane found to be around 91 $L \cdot m^2 \cdot h^{-1} \cdot bar^{-1}$ is slightly higher than that obtained in the previous section that yields 86 $L \cdot m^2 \cdot h^{-1} \cdot bar^{-1}$. This indicates that two pieces of the same membrane could have different permeability, which is probably due to the heterogeneity of the pores distributions over the same membrane coupon.

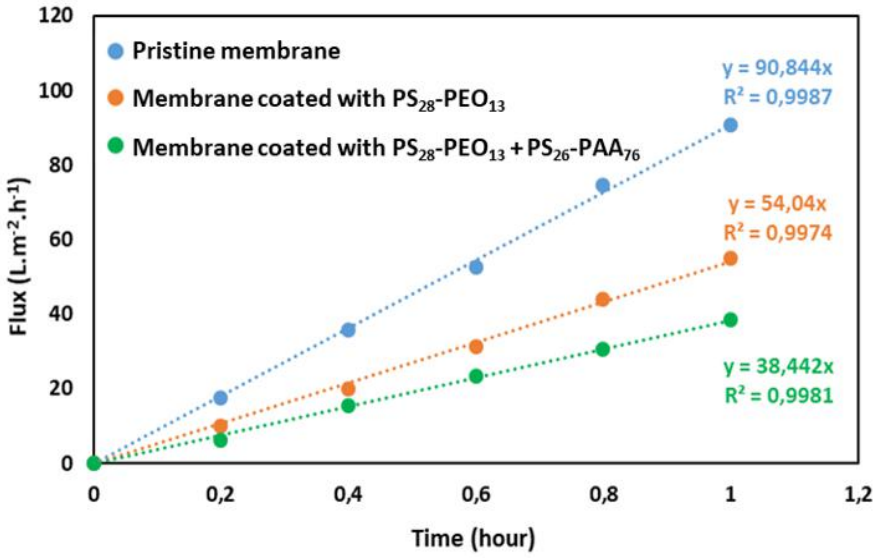

Figure 4. 11. Plots of the water flux J_w vs pressure from which the permeability was calculated for PM and for membranes coated with PS_{28}-b-PEO_{13} and with PS_{28}-b-PEO_{13} + PS_{26}-b-PAA_{76} at the same time.

Afterwards, the dead-end filtration of HSA solution was performed at 1 bar and the flux evolution was monitored as shown in Figure 4. 12. Results show a slight flux decline through the PM from almost 89 $L \cdot m^2 \cdot h^{-1}$ to 85 $L \cdot m^2 \cdot h^{-1}$ at the end of the filtration, which gives a J/J_w ratio of around 96 %. The ratio obtained here is slightly lower than that previously found on PM to be around 98 %, which one can consider negligible. Thereby, this outcome confirms that the adsorption of HSA proved to take place onto the membrane surface using FTIR, does not affect much the transport properties of the membrane. The reduction of the flux was a bit greater (J/J_w ratio yields 90 %) for the membrane coated with PS_{28}-b-PEO_{13}, where the flux decreased from 55 $L \cdot m^2 \cdot h^{-1}$ to 49 $L \cdot m^2 \cdot h^{-1}$. This suggests that the HSA adsorption is effectively taking place more onto this surface than on PM despite the presence of PEO, which sustains what has been noticed from FTIR maps. Besides, it could be owing to higher HSA retention of the coated membrane than the PM since the permeability of the first one has been shown to be reduced. Furthermore, it can be observed in Figure 4. 12 that the decrease in flux lasted longer before the flux became almost constant. This supports the hypothesis we established before assuming that the HSA deposition was maybe forced by the flow through the membrane to overcome the hydration layer created by the presence of PEO. Eventually, the reduction in flux was even higher (J/J_w = 84 %) for membrane coated with both PS_{28}-b-PEO_{13} + PS_{26}-b-PAA_{76} where the flux decreased from 38 $L.m^2.h^{-1}$ to 32 $L \cdot m^2 \cdot h^{-1}$. This is necessarily due to the adsorption of HSA shown to be higher in this case from FTIR maps due to the presence of PS_{26}-b-PAA_{76}.

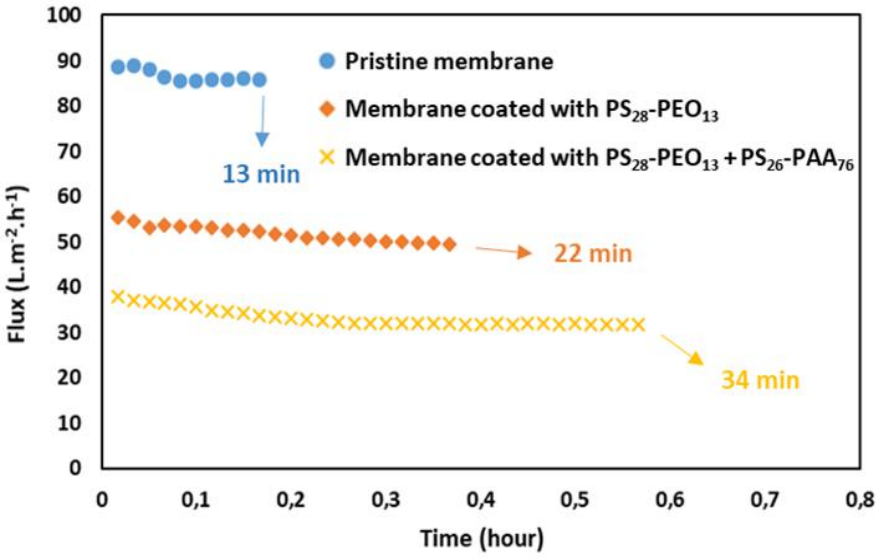

Figure 4. 12. Evolution of flux *J* versus time during HSA filtration at 1 bar on pristine membrane and on membranes coated with PS_{28}-b-PEO_{13} and with PS_{28}-b-PEO_{13} + PS_{26}-b-PAA_{76} at the same time (pH ≈ 7; [HSA]= 1 mg·mL^{-1}).

Subsequently, the retention of HSA was evaluated by measuring the protein concentration in the permeate and in the retentate using UV-visible spectroscopy and by using equation (4.3). Thereby, the amount of protein deposited on the membrane surface was calculated by mass balance using equation (4.6). The results of these calculations are summarized in Table 4. 4.

From these results, it can be first noticed that the membrane coated with PS_{28}-b-PEO_{13} displayed an HSA adsorption density of 0.16 mg·cm^{-2}, which is close (slightly higher) to that obtained on the PM that yields 0.13 mg·cm^{-2}. This validates what has been observed from FTIR maps and supports the hypothesis assuming that the slight increase in flux reduction during HSA filtration through the membrane coated with PS_{28}-b-PEO_{13} than through PM, was probably due to greater HSA deposition onto the surface. The protein adsorption density increased then on the membrane coated with both PS_{28}-b-PEO_{13} and PS_{26}-b-PAA_{76} to reach 0.36 mg·cm^{-2}, which is lower than the density obtained previously on membrane coated with PS_{26}-b-PAA_{76} that yields 0.48 mg·cm^{-2}. This confirms that the presence of PS_{28}-b-PEO_{13} effectively plays a role on reducing the adsorption of HSA. As for calculation of the retention, it was logically found to increase from 17.1 % on PM to 26.1 % and 57.7 % on membrane coated with PS_{28}-b-PEO_{13} and on that coated with both PS_{28}-b-PEO_{13} + PS_{26}-b-PAA_{76} respectively.

Table 4. 4. Calculations of protein retention as well as the amount of HSA adsorbed on the membrane surface in the case of PM and of membranes coated with PS_{28}-b-PEO_{13} and with both PS_{28}-b-PEO_{13} + PS_{26}-b-PAA_{76}.

Sample	Concentration of HSA in permeate ($mg \cdot mL^{-1}$)	Concentration of HSA in retentate ($mg \cdot mL^{-1}$)	Retention (%)	Mass of HSA adsorbed (mg)	Adsorption density ($mg \cdot cm^{-2}$)
Pristine membrane	0.89	1.08	17.1	0.49	0.13
Membrane coated with PS_{28}-b-PEO_{13}	0.85	1.15	26.1	0.6	0.16
Membrane coated with PS_{28}-b-PEO_{13} + PS_{26}-b-PAA_{76}	0.67	1.32	57.7	1.35	0.36

4.5. Dead-end filtration of HSA at pH 5 through membrane coated with PS-b-PAA

In the previous chapters, HSA binding with PAA in solution and its static adsorption on membrane coated with PS-b-PAA have been proved to take place more at pH 5. In this section, dead-end filtration of HSA was repeated but at pH 5 through PVDF membrane coated with PS_{100}-b-PAA_{107} in order to check the effect of pH on HSA adsorption and retention in dynamic mode. The same procedure of compaction, coating and filtration was used as explained previously, except the change in pH of HSA solution during filtration. It is important to note that unlike the other experiments reported previously in this chapter this one was performed only once. The presence of the copolymer and the protein was, as usual, assessed using FTIR mapping. In order to explore the effect of pH, the results obtained here at pH 5 were compared to those obtained earlier at pH 7 on the same copolymer.

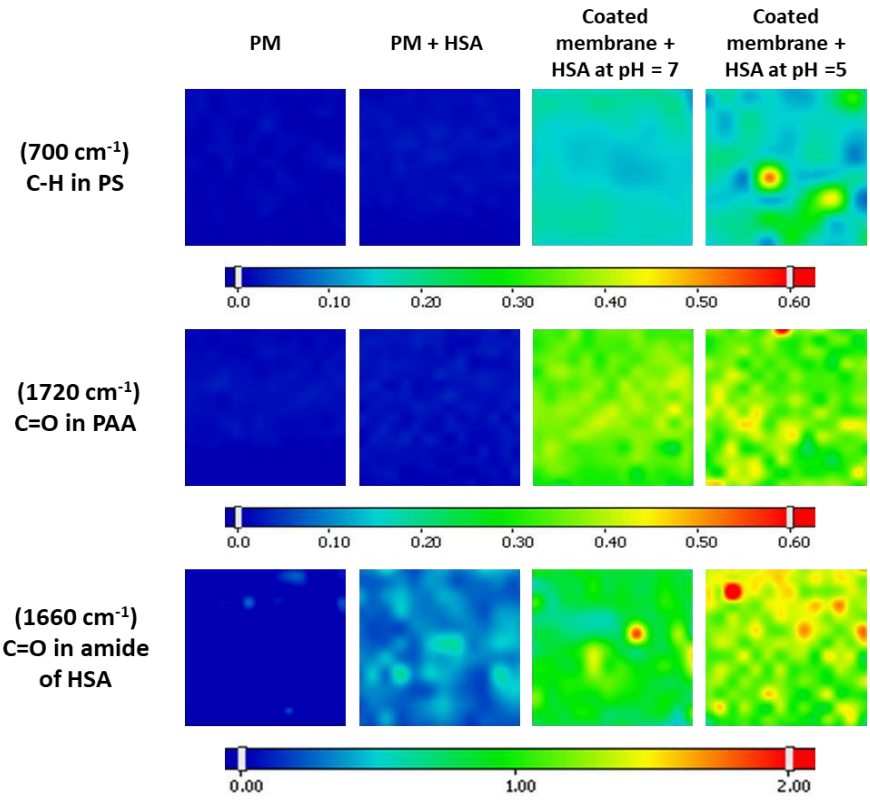

Figure 4. 13. FTIR maps generated at 700 cm^{-1}, 1720 cm^{-1} and 1660 cm^{-1} showing the presence of the coating layer and that of the protein after HSA dead-end filtration through membrane coated with PS_{100}-b-PAA_{107} (pH = 5 and 7; [HSA]= 1 $mg \cdot mL^{-1}$).

FTIR maps shown in Figure 4. 13 confirm first the presence of the copolymer all over the membrane surface, which allows us to discuss the deposition of HSA onto it. In fact, FTIR maps show a greater adsorption of HSA at pH 5, which is the same trend revealed previously

in solution and during static adsorption. This is probably due to the increase of electrostatic attraction between the negatively charged PAA and the positive patches carried on HSA surface after the reduction of its negative overall charge when reducing pH to 5.

In order to validate that, the concentration of HSA in the permeate and in the retentate was estimated by UV-visible spectroscopy and the amount of HSA deposited onto the membrane surface was determined by mass balance.

Table 4. 5. Comparison of HSA retention and deposition on PVDF membrane coated with PS_{100}-b-PAA_{107} during dead-end filtration at different pH (5 and 7).

Sample	Concentration of HSA in permeate ($mg \cdot mL^{-1}$)	Concentration of HSA in retentate ($mg \cdot mL^{-1}$)	Retention rate (%)	Mass of HSA adsorbed (mg)	Adsorption density ($mg \cdot cm^{-2}$)
pH = 7	0.49	1.53	68	1.98	0.52
pH = 5	0.51	1.39	63	2.26	0.59

The results reported in Table 4. 5 show a retention rate of 63 % when the filtration was performed at pH 5, which is close (slightly lower) to that obtained previously at pH 7 that yields 68 %. However, these calculations support what has been noticed from FTIR maps, where HSA deposition onto the membrane surface at pH 5 was revealed slightly higher. Indeed, the adsorption density of HSA was found to be around 0.59 $mg \cdot cm^{-2}$ at pH 5, and 0.52 $mg \cdot cm^{-2}$ at pH 7. On the other hand, this increase (12 %) is not that sufficient to conclude definitively on the increase in protein adsorption at pH 5, especially as the method used (UV-visible) previously showed standard deviations of around 10% or more. The standard deviations are not calculated here because the experiment was performed once as stated earlier. Thus, to confirm HSA adsorption increase, we resorted to calculating the mean intensities from the maps converted into grey scales as explained in section 4.2 of chapter III. The obtained results exposed in Figure 4. 14 were then compared to the mean intensities reported in section 5.6 of chapter III regarding the static adsorption of HSA onto PS_{100}-b-PAA_{107} coated membrane at different pH.

These results evince effectively that the HSA adsorption at pH 5 is greater than that at pH 7, where the mean intensity has been evaluated to be around 0.93 and 0.59 at pH 5 and 7

respectively. It can also be noticed in Figure 4. 14 that the HSA deposition during filtration is clearly greater than its static adsorption. Indeed, the evaluated intensities in static adsorption of HSA yields 0.64 and 0.41 at pH 5 and 7. This outcome sustains the hypothesis we established earlier assuming that HSA deposition during filtration is enhanced by the flow through the membrane. Thus, the HSA observed on the membrane surface would be due to the adsorption and the accumulation of HSA once all the adsorption sites were occupied.

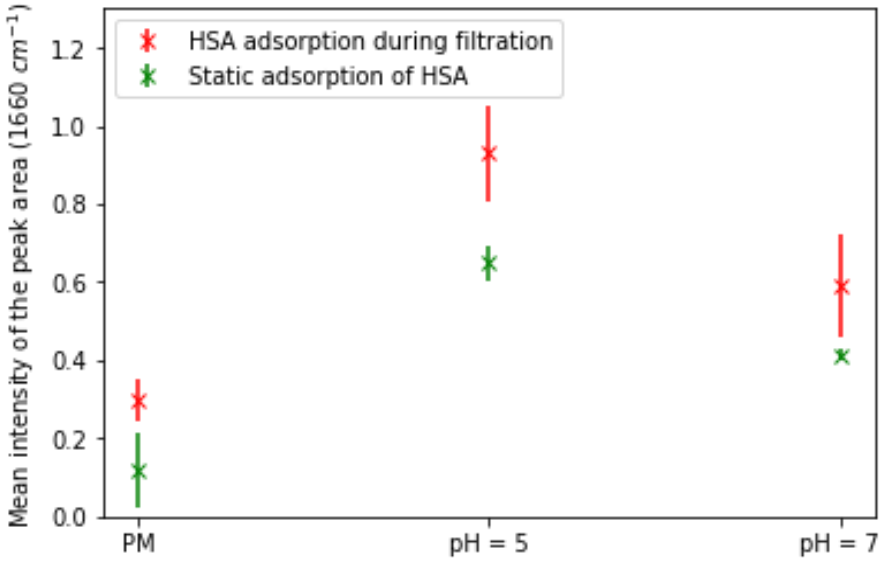

Figure 4. 14. Evaluated mean intensities of the peak area at 1660 cm^{-1} showing the adsorption of HSA onto PS_{100}-b-PAA_{107} coated membrane at pH 5 and 7 during filtration as compared to those obtained for static adsorption of HSA in the same conditions; [HSA]= 1 mg·mL^{-1}.

The membrane transport properties were also investigated before and after dead-end filtration. In fact, permeability measurements were performed after coating and it was found to be around 36 L·m^2·h^{-1}·bar^{-1} (Figure 4. 15), which is higher than that obtained earlier for membrane coated with the same copolymer and that yields around 30 L·m^2·h^{-1}·bar^{-1}. This was also noticed previously in the case of PM and it confirms that two different pieces of membrane prepared in exactly the same conditions could have different permeability, which would be due to the heterogeneity of pores distribution over the membrane surface.

After that, the flux evolution during HSA filtration was followed as shown in Figure 4. 15, and it was found to decrease from almost 36 L·m^2·h^{-1} to 29 L·m^2·h^{-1} after that a volume of 7 mL was passed through the membrane (*VRF* = 3.3). This makes a flux reduction J/J_w of 81 %, which is almost the same (79 %) as that obtained when the filtration was performed at pH 7. This suggests that the flux reduction was not affected more by the additional deposition of HSA

shown at pH 5. Thus, one can consider once again that the small differences in flux reduction could be due to deviations on the measurement during the experiments.

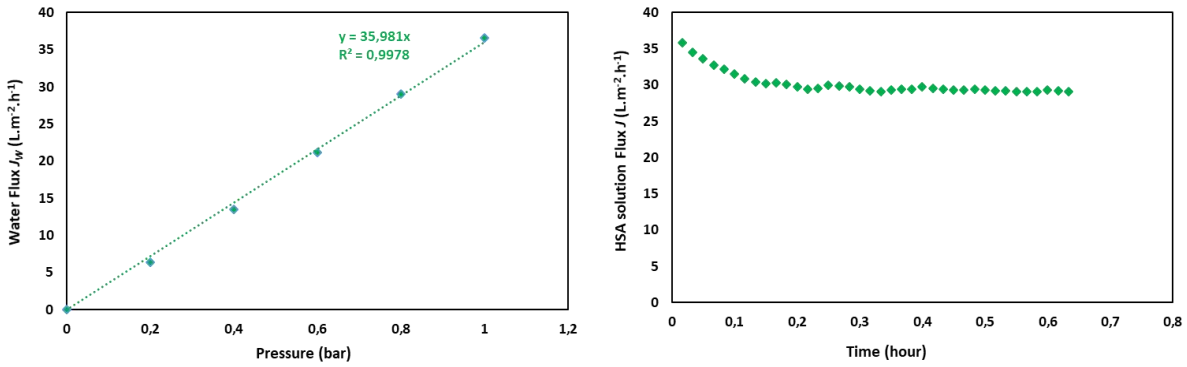

Figure 4. 15. Plot of the water flux versus pressure from which the permeability was calculated for membranes coated with PS_{100}-b-PAA_{107} and evolution of HSA solution flux versus time during HSA filtration (pH=5) through this same membrane.

5. Conclusions

Dead-end filtration is the process that is close to real conditions in which the suggested system in this project can work in long terms. Thus, it was interesting to run experiments in a dynamic mode via dead-end filtration of protein solutions. In fact, it allowed us to investigate the reproducibility of interactions proved to take place in the previous chapters whether in solution or at the interface of a modified membrane in static mode.

Dead-end filtration experiments provide interesting results on the stability of the coating layer deposited by physical adsorption on the membrane. The presence of the copolymer over the membrane surface has been every time confirmed by FTIR, after the filtration, although water and HSA solution were passed through the membrane under pressure after the coating was performed.

The presence of HSA was also investigated using FTIR and as in static mode, it was revealed to be deposited more on PS-b-PAA coated membrane than on pristine membranes. However, it was found to be slightly related to the copolymer size unlike in static mode where it was shown to be almost similar over different copolymer sizes. This suggests that the applied pressure during filtration helps HSA molecules interacting more with larger PAA, as it lead to the accumulation of HSA onto the surface.

In the case of membrane coated with PS-b-PEO, results showed a different trend than that shown in static mode in the same case, where HSA adsorption was found to be mitigated compared to that on PM. In fact, it seems that the pressure applied on HSA solution during filtration helped molecules overcoming the hydration layer created by PEO to be adsorbed onto the membrane surface. While in the case of membrane coated with both PS-b-PAA+PS-b-PEO copolymers, HSA adsorption was reduced compared to that on PS-b-PAA coated membrane.

The deposition of HSA onto membrane coated with PS-b-PAA copolymer increased at pH 5 during dead-end filtration, which is the same thing proved to happen during static adsorption or for complexation in solution.

The membrane transport properties were found to be slightly affected by the deposition of HSA during dead-end filtration where the flux was reduced around 20%. However, they seem considerably affected by the coating and highly related to the copolymer size. Indeed, the membrane permeability was found to be reduced of around 30 % with the shortest copolymer, and the decline reached 65 % with the largest copolymer.

6. References

[1] J. W. Chew, J. Kilduff, and G. Belfort, 'The behavior of suspensions and macromolecular solutions in crossflow microfiltration: An update', *Journal of Membrane Science*, vol. 601, p. 117865, 2020.

[2] S. T. Kelly and A. L. Zydney, 'Protein fouling during microfiltration: Comparative behavior of different model proteins', *Biotechnology and Bioengineering*, vol. 55, no. 1, pp. 91–100, 1997.

[3] Y. Wang, J. A. Howell, R. W. Field, and D. Wu, 'Simulation of cross-flow filtration for baffled tubular channels and pulsatile flow', *Journal of Membrane Science*, vol. 95, no. 3, pp. 243–258, 1994.

[4] A. L. Zydney, 'Protein Separations Using Membrane Filtration: New Opportunities for Whey Fractionation', *International Dairy Journal*, vol. 8, no. 3, pp. 243–250, 1998.

[5] C. E. Merzougui *et al.*, 'Pearl-necklace assembly of human serum albumin with the poly(acrylic acid) polyelectrolyte investigated using small angle X-ray scattering (SAXS)', *Soft Matter*, vol. 16, no. 43, pp. 9964–9974, 2020.

[6] A. L. Zydney, 'Membrane technology for purification of therapeutic proteins', *Biotechnology and Bioengineering*, vol. 103, no. 2, pp. 227–230, 2009.

[7] K. Nakamura and K. Matsumoto, 'Properties of protein adsorption onto pore surface during microfiltration: Effects of solution environment and membrane hydrophobicity', *Journal of Membrane Science*, vol. 280, no. 1, pp. 363–374, 2006.

[8] N.-J. Lin *et al.*, 'Surface Self-Assembled PEGylation of Fluoro-Based PVDF Membranes via Hydrophobic-Driven Copolymer Anchoring for Ultra-Stable Biofouling Resistance', *Langmuir*, vol. 29, no. 32, pp. 10183–10193, 2013.

[9] A. Venault, Y. Chang, H.-S. Yang, P.-Y. Lin, Y.-J. Shih, and A. Higuchi, 'Surface self-assembled zwitterionization of poly(vinylidene fluoride) microfiltration membranes via hydrophobic-driven coating for improved blood compatibility', *Journal of Membrane Science*, vol. 454, pp. 253–263, 2014.

[10] H. Yang, Z. Wang, Q. Lan, and Y. Wang, 'Antifouling ultrafiltration membranes by selective swelling of polystyrene/poly(ethylene oxide) block copolymers', *Journal of Membrane Science*, vol. 542, pp. 226–232, 2017,.

[11] W. R. Gombotz, W. Guanghui, T. A. Horbett, and A. S. Hoffman, 'Protein adsorption to poly(ethylene oxide) surfaces', *Journal of Biomedical Materials Research*, vol. 25, no. 12, pp. 1547–1562, 1991.

Chapter V.

General conclusions and perspectives

1. General conclusions

Overall, the different elements brought by this thesis constitute a fairly important knowledge base on the interactions between some abundant blood proteins and certain polymers used for membrane surface modification. This study allows not only to understand these interactions but also to control them by tuning the operating physicochemical conditions at different level i.e. in solution and at the interface of a modified membrane either in static mode or during dead-end filtration operations.

For instance, the bioactive PAA suggested to capture blood platelets has been found to form complexes in solution with the most abundant protein in plasma namely HSA, whereas another blood protein namely IgG tended to aggregate in the presence of the same polyelectrolyte. Then, neither HSA or IgG exhibited any specific interactions with the neutral PEG assumed to prevent the nonspecific adsorption of proteins.

Deeper investigations using SAXS and chromatography proved that the HSA-PAA complexation takes place at some specific physicochemical conditions of pH and ionic strength disclosing that this phenomenon was driven by electrostatic attractive interactions. In fact, the HSA-PAA binding was found to take place only at pH 5 and an ionic strength ≤ 0.15 M, and it was reversible at higher pH or ionic strength where the complex was shown to be dissociated. The dissociation has been also revealed to occur when the complex is put in a medium not containing PAA. The evaluation of the complexation stoichiometry suggested that 4 HSA molecules could be bound to each PAA_{100kDa} chains as assumed in the equilibrium given below:

$$4\,HSA\ +\ 1\,PAA\ \rightleftarrows\ 1\,complex(PAA-4HSA)$$

Besides, the occurrence and the reversibility of this binding has been shown for different PAA sizes. Moreover, the evaluation of the HSA-PAA complexes size has evinced that the number of HSA bound to each PAA chain was related to the size of the latter.

After that, functionalized PVDF membrane were prepared by coating PS-b-PAA copolymers onto the membrane surface to investigate the interactions stated above. For that, the modification process has been first optimized (procedure of coating, coating time, etc.). Thus, the physical adsorption of copolymers due to hydrophobic interactions of the anchoring PS block with the hydrophobic PVDF membrane has been an effective technique for the membrane surface modification. In fact, the presence of the copolymer layer was confirmed every time using FTIR before the study of proteins adsorption onto the modified membrane.

Subsequently, the adsorption of HSA on PS-b-PAA coated membrane was shown using FTIR to be higher than its deposition onto PVDF pristine membrane (PM). This interaction was disclosed to be once again specific to HSA because IgG exhibited a different behaviour, which adsorbs similarly on PVDF PM as on PS-b-PAA coated membrane. In fact, besides the electrostatic interactions assumed to be the driving force of the HSA-PAA complexation in solution, the hydrophobic interactions were revealed to play also a role on HSA adsorption onto PS-b-PAA coated PVDF membrane. As a matter of fact, the HSA adsorption was shown to take place at pH 7 mostly due to hydrophobic interactions between hydrophobic pockets of HSA and the PS, but also due the electrostatic interactions of HSA with PAA. Then, the adsorption has been evinced to be enhanced at pH 5 owing to increased electrostatic interactions after the reduction of the HSA overall negative charge (isoelectric point ≈ 4.7) to come closer to the negatively charged PAA chains (pKa = 4.5). The ionic strength effect assessment confirmed then the major role of the attractive electrostatic interactions on the HSA adsorption onto the PS-b-PAA coated membrane. In fact, the adsorption was greater at an ionic strength ≤ 0.15 M, and it was mitigated at higher ionic strength. Furthermore, the HSA adsorption was not related to the PAA size as it was the case for HSA-PAA complexation in solution.

As for the adsorption of HSA onto PS-b-PEO coated membrane in static mode, it has been mitigated compared to its adsorption onto PVDF pristine membrane. In fact, the hydration layer that could be formed by PEO has been suggested to be the barrier that prevents the adsorption of proteins. However, this barrier was not sufficient to preclude the HSA deposition onto the same membrane during dead-end filtration operations. Indeed, the HSA deposition was found to increase slightly on PS-b-PEO coated membrane compared to that on PM suggesting that the pressure applied on HSA solution helped overcoming the hydration layer created by PEO. Otherwise, the same trend of HSA adsorption on PS-b-PAA coated membrane obtained in static mode has been observed during dead-end filtration operations. However, the deposition was greater due to the flow of HSA solution which maybe helped the HSA getting more in contact with the membrane surface, and so increase its interactions with the copolymer and raise the deposited amount due to the accumulation of HSA.

Table 5. 1 summarizes the behaviours of blood proteins (HSA and IgG) towards PAA and PEG in solution, and at the interface of PVDF membrane surface modified with PS-b-PAA or with PS-b-PEO, in static mode and during dead-end filtration.

Eventually, the assessment of the membrane transport properties unveiled that the membrane permeability and its selectivity can be tuned with the size of the copolymer used for coating.

Table 5. 1 : Summary of the blood proteins (HSA and IgG) interactions with polymers (PAA and PEG) in solution, and at the interface of a functionalized PVDF membrane in static mode and during dead-end filtration.

Medium / Protein	In solution	
	PAA	**PEG**
HSA	Formation of HSA-PAA complexes only at pH 5 and ionic strength ≤ 0.15 M, which is attributed to electrostatic interactions.	No specific interaction has been shown
IgG	Partial aggregation of IgG	No specific interaction has been shown
Medium / Protein	**At the interface of a modified membrane in static mode**	
	PS-PAA	**PS-PEO**
HSA	- HSA adsorption onto PS-b-PAA PVDF coated membrane at pH 7 due to electrostatic interactions of HSA with PAA, and due to hydrophobic interactions between HSA and the visible PS. - Increase of HSA adsorption on the same membrane at pH 5 due to increased electrostatic interaction of HSA with PAA.	Reduction of HSA adsorption on PS-PEO PVDF coated membrane compared to its adsorption on PVDF pristine membrane, which maybe owing to the hydration layer created by the PEO preventing the adsorption of proteins.
IgG	Adsorption of IgG similarly on PVDF pristine membrane as on PS-b-PAA PVDF coated membrane	Not investigated.
Medium / Protein	**At the interface of a modified membrane during dead-end filtration**	
	PS-PAA	**PS-PEO**
HSA	The same trend of HSA adsorption obtained in static mode has been observed during dead-end filtration but with greater amounts due to the pressure applied on the HSA solution. The role of the pH and ionic strength leading to the complexation is observable but is screened by the role of the filtration rate on the deposit formation.	Slight increase of HSA adsorption on PS-PEO PVDF coated membrane due to the pressure applied on the HSA solution which probably overcome the hydration layer created by the PEO.
IgG	Not investigated.	Not investigated.

At the end, these results summarized in the Table 5. 1 regarding the proteins adsorption on coated membrane with copolymers (PS-b-PAA, PS-b-PEO) sustain those evidenced in solution by SAXS and chromatography concerning the interactions between the same proteins and functional groups such as PAA and PEG.

Overall, going from the understanding of local interactions, functionalization of the membrane and the study of its performance for filtration process, which are the objectives initially outlined for this thesis, one can consider that a good part has been covered in this study.

2. Perspectives

First, it would be interesting to complete some parts already covered in this thesis by bringing more elements to the discussion, and to go also further in experiments by considering other approaches. This will allow to improve even more the contribution of this study to the MOSAIC 3D project aiming at designing a suitable membrane technology for blood cells screening and in particular for platelets capture and separation.

Referring to Table 5. 1 for instance, it would be important to compare the behaviour of IgG to that displayed by HSA on PS-b-PAA coated membrane during dead-end filtration process. Besides, it could be interesting to study the adsorption of IgG on PS-b-PEO coated membrane to confirm the effect of PEO on preventing the non-specific adsorption of proteins either in static mode and during dead-end filtration. The study of HSA deposition at pH 5 on PVDF pristine membrane may provide more clarifications and new elements that would maybe sustain the hypotheses we have already assumed about the difference of HSA adsorption on coated membrane at pH 5 and 7.

Moreover, the study of interactions could be extended to other blood proteins such as the Fibrinogen from human blood. In fact, some experiments conducted by our partners in the Research and Development Center for Membrane Technology (Chung Yuan Christian University, ChungLi, Taiwan) showed that the Fibrinogen conjugated to the PAA could even enhance the platelets capture. Thus, it would be substantial to explore the interaction of Fibrinogen with PAA at different levels as done for the other proteins. Otherwise, it would be perhaps advisable to think to graft the fibrinogen onto the PS-b-PAA modified membrane, and then test the adsorption of other blood proteins.

It would be also of interest to investigate the behaviour of these proteins (HSA, IgG and fibrinogen) towards the thermosensitive NIPAAM suggested to release the platelets after being

activated by tuning the temperature. Thereby, it will be significant to probe the proteins-NIPAAM interactions at different temperatures in solution. Then, as it has been done for the other copolymers, the adsorption of blood proteins onto PS-b-NIPAAM coated membrane either in static mode and during dead-end filtration should be examined using FTIR.

As stated previously, going further in experiments by considering new approaches could also improve significantly this study. For example, the use of other techniques can provide more information and reliability to the types of interactions that can be had in solution and at the interface of modified membrane. For instance, Isothermal Titration Calorimetry (ITC) has been shown to be very sensitive to investigate the interactions between blood proteins and polymers in solutions [1], [2]. While Confocal Microscopy (CM) has been disclosed to be an effective technique for the study of blood proteins adsorptions onto membrane surfaces. Indeed, it was successfully used to evaluate the adsorption of white blood cells (WBC), red blood cells (RBC) and platelets on PVDF membrane modified with PS-r-PSBMA [3], or with PS-r-PAA [4].

It would also be possible to use microscopic methods such as fluorescence microscopy to explore the competitive adsorption of different proteins at the interface of a modified membrane using labelled proteins [5]. This could be tested either in static mode or during dead-end filtration operations. This study should be carried out either on PS-b-PAA, PS-b-PEO and on PS-b-NIPAAM coated membranes. Subsequently, it would be even more significant to perform the adsorption of the blood proteins mixture on PVDF membrane coated with the three copolymers mentioned previously. For that, the functionalization of the membrane surface by the three copolymers should be first performed as it has been done in this study using two of them (PS-b-PAA and PS-b-PEO).

Another approach to explore the adsorption of proteins to polymeric surfaces is to use colloidal core-shell particles with a well-defined polymer shell [6]. In fact, functionalized nanoparticles have been proved to be a good alternative to study these interactions, using SAXS, ITC, FTIR, etc [7]. Thus, it would be interesting to investigate blood proteins (HSA, IgG and fibrinogen) interactions with colloidal core-shell particles with the core being PS and the shell formed of PAA, PEO or NIPAAM, or it could be the three of them.

One of the approaches that also can permit to investigate the interaction in solution is the measurement of the osmotic pressure. In fact, the complexation should drastically decrease the osmotic pressure of the mixture as the number of molecules of the solution changes from 5 molecules (for example 1 PAA and 4 HSA), to 1 molecule of complex (1PAA-4HSA).

A tentative of experimental measurement has been realised in dialysis bag with the help of a master student (Ema Louati), but aggregates of HSA and moisture have been observed on these experiments that need long time to reach the equilibrium. Experiments should be carried out with microfluidic devices using the membranes that are currently developed in the laboratory. Thus, for the same PAA + HSA mixture the measurement of the osmotic pressure should be performed by changing pH in the permeate. It should allow to confirm the stoichiometry (through the change of osmotic pressure) but also to have a quantitative measurement of the complexation reversibility degree.

Finally, it would be more worthwhile to run some experiments using PRP solutions (platelet rich plasma) to assess the interactions of platelets with the polymers stated previously either in solution and at the interface of a modified membrane. Besides, it could be interesting to explore the optimization of the PDGF transmission through the membrane by changing the coated functional groups size evidenced in this study to have a major role on the membrane retention. After that, it will be substantial to consider the use of the real human blood as a feed during dead-end filtration process, and to sought to understand what could happen at the interface of the modified membrane.

3. References

[1] S. Yu *et al.*, 'Interaction of human serum albumin with short polyelectrolytes: a study by calorimetry and computer simulations', *Soft Matter*, vol. 11, no. 23, pp. 4630–4639, 2015.

[2] Q. Ran *et al.*, 'Interaction of human serum albumin with dendritic polyglycerol sulfate: Rationalizing the thermodynamics of binding', *The Journal of Chemical Physics*, vol. 149, no. 16, p. 163324, 2018.

[3] A. Venault *et al.*, 'A combined polymerization and self-assembling process for the fouling mitigation of PVDF membranes', *Journal of Membrane Science*, vol. 547, pp. 134–145, 2018.

[4] A. Venault, Y.-T. Chin, I. Maggay, C.-C. Yeh, and Y. Chang, 'Poly(vinylidene fluoride)/poly(styrene-co-acrylic acid) nanofibers as potential materials for blood separation', *Journal of Membrane Science*, vol. 641, p. 119881, 2022.

[5] M. Weinhart, T. Becherer, N. Schnurbusch, K. Schwibbert, H.-J. Kunte, and R. Haag, 'Linear and Hyperbranched Polyglycerol Derivatives as Excellent Bioinert Glass Coating Materials', *Advanced Engineering Materials*, vol. 13, no. 12, pp. B501–B510, 2011.

[6] S. Rosenfeldt, A. Wittemann, M. Ballauff, E. Breininger, J. Bolze, and N. Dingenouts, 'Interaction of proteins with spherical polyelectrolyte brushes in solution as studied by small-angle x-ray scattering', *Physical Review E*, vol. 70, no. 6, 2004.

[7] N. Welsch, Y. Lu, J. Dzubiella, and M. Ballauff, 'Adsorption of proteins to functional polymeric nanoparticles', *Polymer*, vol. 54, no. 12, pp. 2835–2849, 2013.

Appendices

A. Supporting information on analysis of confocal microscope images

The quantitative analysis of the confocal microscope images is exposed in SI-Table 1 given below. The images are shown in section 6.3 of chapter I, and they were performed to explore the adhesion of platelets on polystyrene well plates modified with triblock PS-PAA and with random PS-PEG copolymers.

SI-Table 1. Quantitative analysis of the confocal microscope images performed using Image J software for the adhesion of the platelets on polystyrene (PS) well plate modified with triblock PS-PAA and with random PS-PEG copolymers.

Parameter / Measure	Count	Total area	Average size	Covered area (%)	Average	Standard deviation (%)
Pristine PS well plate						
1	556	2692	4.84	0.62	**0.49**	**28**
2	309	1560	5.05	0.35		
PAA_{50}-PS_{50}-PAA_{50}						
1	732	5489	7.49	1.13	**0.97**	**17**
2	640	3574	5.58	0.8		
PAA_{50}-PS_{100}-PAA_{50}						
1	1396	8240	5.9	1.77	**1.81**	**2**
2	1266	8239	6.51	1.85		
PS_{132}-PEG_{112}						
1	277	1012	3.65	0.22	**0.25**	**12**
2	218	1246	5.72	0.28		
PS_{235}-PEG_{104}						
1	194	921	4.75	0.2	**0.16**	**29**
2	122	448	3.92	0.11		

B. Supporting information on SAXS data analysis

The SAXS data (*I(q)* being the scattering intensity obtained from SAXS measurement) have been analysed to obtain the main properties of the HSA and the HSA-PAA complex. The Python home code used for different calculations presented in Chapter II of the manuscript is found in the following link:

https://github.com/CharafMerzougui/Supporting-information/blob/master/Porod%20volume%20estimation %20-%20modif%20.ipynb

1. Determination of the radius of gyration and *I(0)*

As stated in section 3.2.1 of chapter II, the radius of gyration R_g is the average root-mean-square distance to the center of density in the molecule weighted by the scattering length density as illustrated in SI-Figure 1.

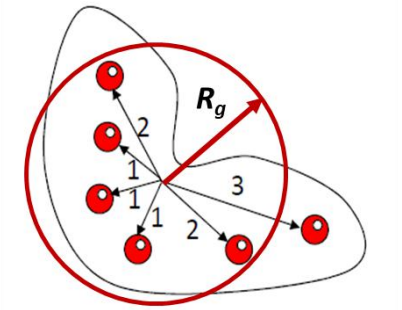

$$R_g^2 = (1^2 + 1^2 + 1^2 + 2^2 + 2^2 + 3^2)$$

SI-Figure 1. Illustration of the radius of gyration meaning

Thus, R_g is obtained by applying the Guinier law given by following equation at small q:

$$\lim_{q \to 0} I = I_0 \; exp\left(-\frac{1}{3} q^2 R_g^2\right)$$

Close to q=0, the scattering intensity of a particle is described by a Gaussian curve. The Guinier law is equivalent of a linear variation of *Ln I(q) vs* q^2 (Guinier plot), providing R_g and *I(0)*. The code given in the link above performs the curve fitting to obtain the values of R_g and *I(0)* for the 10 first values of q. Here q is then less than 0.012 and should then met the criteria $q.R_g < 1.5$ if R_g is less than 125 nm. It is important to note that in the different sections of Chapter II, R_g was evaluated using Foxtrot or Primus program that consider the Guinier approximation given above, and not the Python code.

It can be checked from Fig.1 and Fig.2 that the data fitting is correct: there is no deviation from the straight line indicating no intermolecular interaction or aggregation in this concentration range.

2. Determination of the Porod volume

The calculations of the Porod volume exposed in section 4.4 of chapter II were carried out for all the studied HSA/PAA molar ratio (1.5 to 12) and were performed using the Python code mentioned earlier. The table below summarize the figures that show the estimation of radius of gyration R_g, the constant K as well as the invariant Q, which allow then the evaluation of the Porod volume for the studied range of HSA/PAA molar ratio.

[HSA]/[PAA] =1.5	**[HSA]/[PAA] =3**
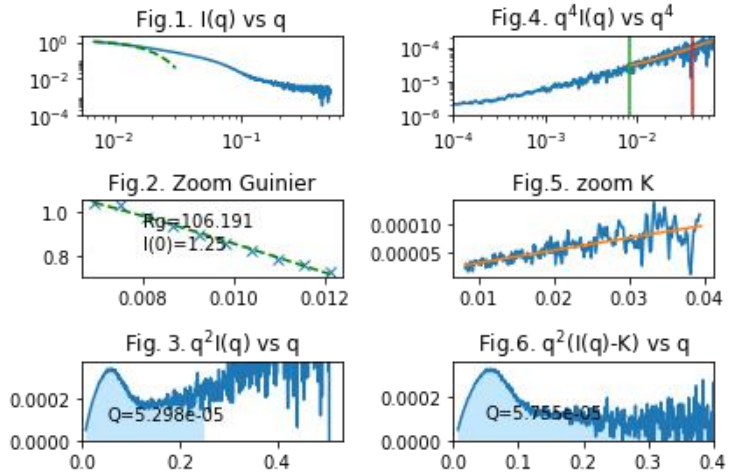	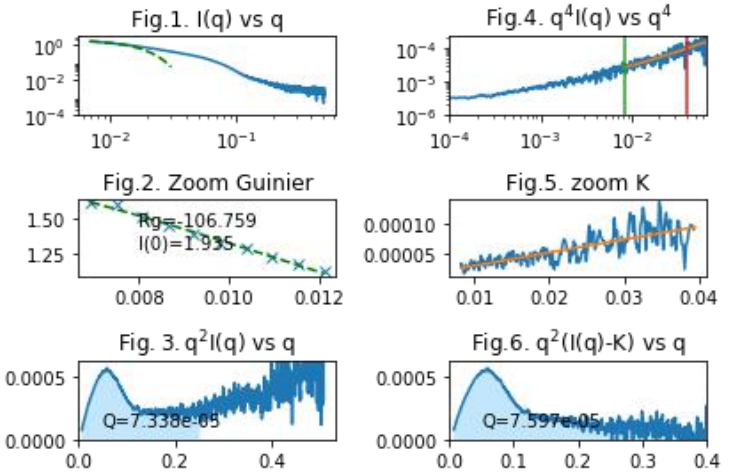
[HSA]/[PAA] =3.6	**[HSA]/[PAA] =4.5**
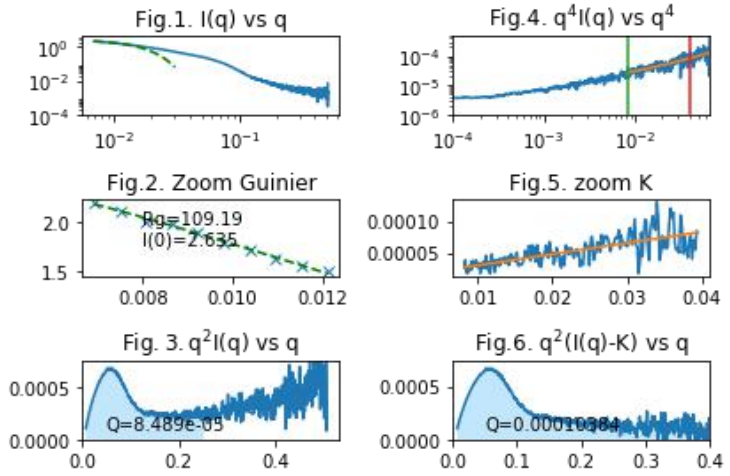	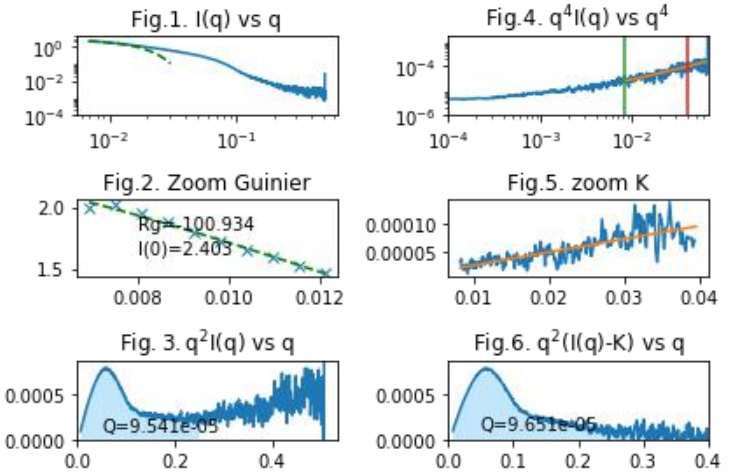

[HSA]/[PAA] =6

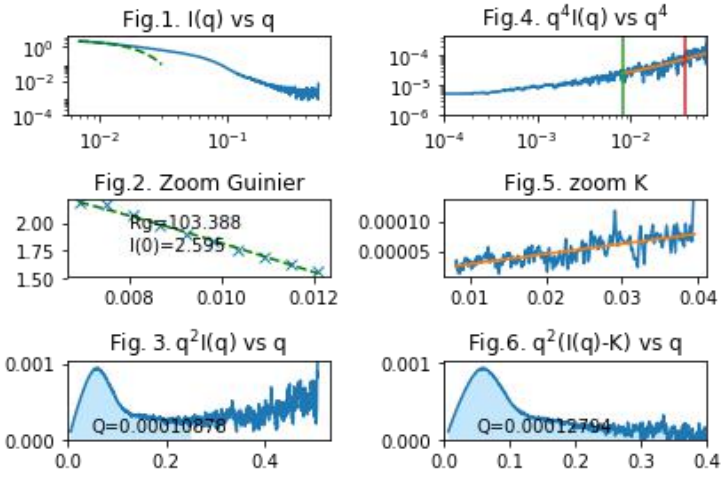

[HSA]/[PAA] =9

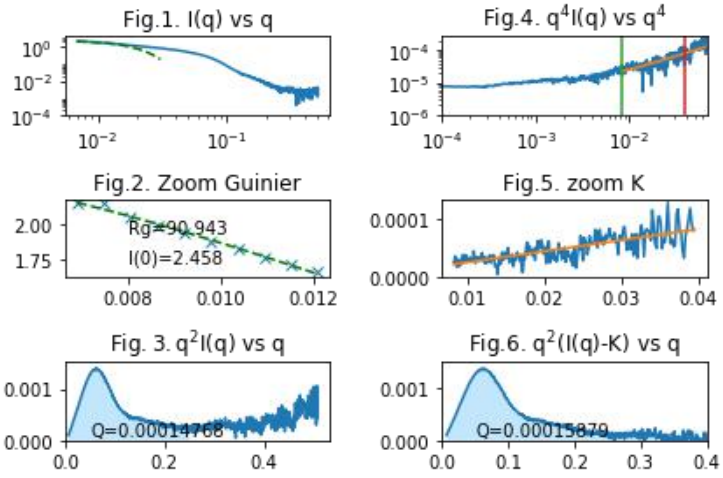

[HSA]/[PAA] =12

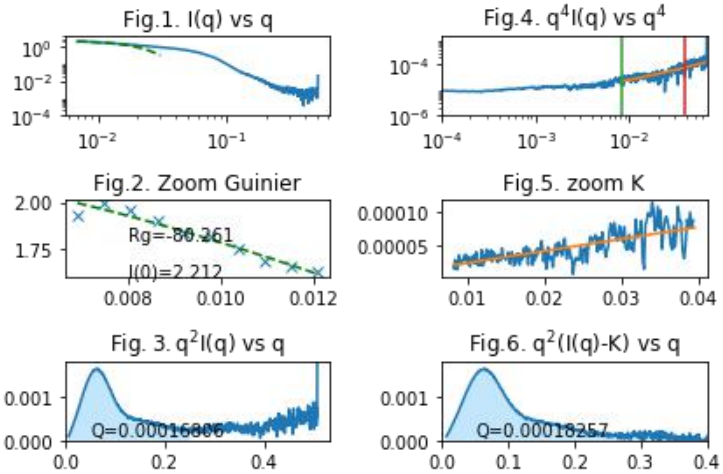

It has to be noted that the value of Q has been plotted as a function of $\phi\ (1-\phi)$ to estimate the value of the contrast between two phases $\Delta\rho$ in the mixture according the equation 2.6 given in section 3.2.1 of Chapter II. The obtained result 1.45. 10^{-6} Å^2 (SI-Figure 2) seems to be consistent with the contrast of proteins found to be around 2. 10^{-6} Å^2 (Svergun et Koch, 2003) and also with what was found for surfactants (Bombelli et al., 2002).

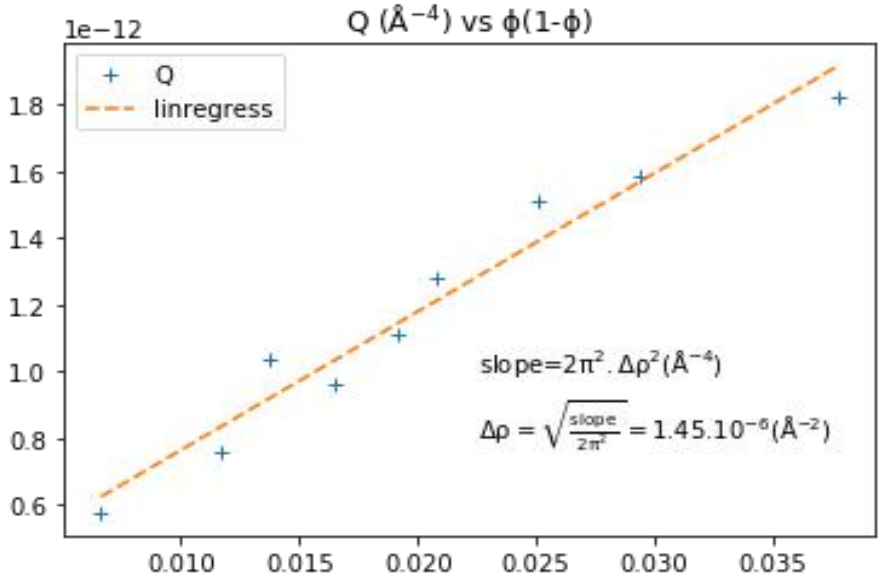

SI-Figure 2. Calculation of the contrast $\Delta\rho$ of the mixture HSA+PAA from the slope of the linear regression of the invariant Q as function of $\phi\ (1-\phi)$ for an HSA/PAA malar ratio ranging from 1.5 to 12.

C. Supporting information on characterization of surface modification and protein adsorption onto the membrane

1. Calibration curves for UV-visible analysis

In order to evaluate the amount of the copolymer attached to the membrane during the modification process, some calibration curves of the absorbance versus the concentration of the copolymer have been established using UV-visible spectroscopy. For that, the absorbance of different standard solutions with known concentration of copolymer were measured. Hence, the concentration of the remain copolymer in the coating bath can be calculated after the membrane is removed. Thus, the mass of the copolymer attached to the membrane surface can be then evaluated as stated in section 3.3.1 of Chapter III by mass balance using the following equation:

$$m_{ads} = C_i \cdot V - C_{eq} \cdot V$$

The same procedure has been used to evaluate the amount of the protein adsorbed onto the membrane surface.

Therefore, below are exposed the calibration curves (SI-Figure 3 and SI-Figure 4) of two copolymers (PS_{30}-b-PAA_5 and PS_{30}-b-PAA_8) for which the attached amount was estimated in section 5.2 of chapter III. Besides, the calibration curve of HSA is shown in SI-Figure 5, the protein for which the adsorbed amount has been calculated in section 5.6 of Chapter III.

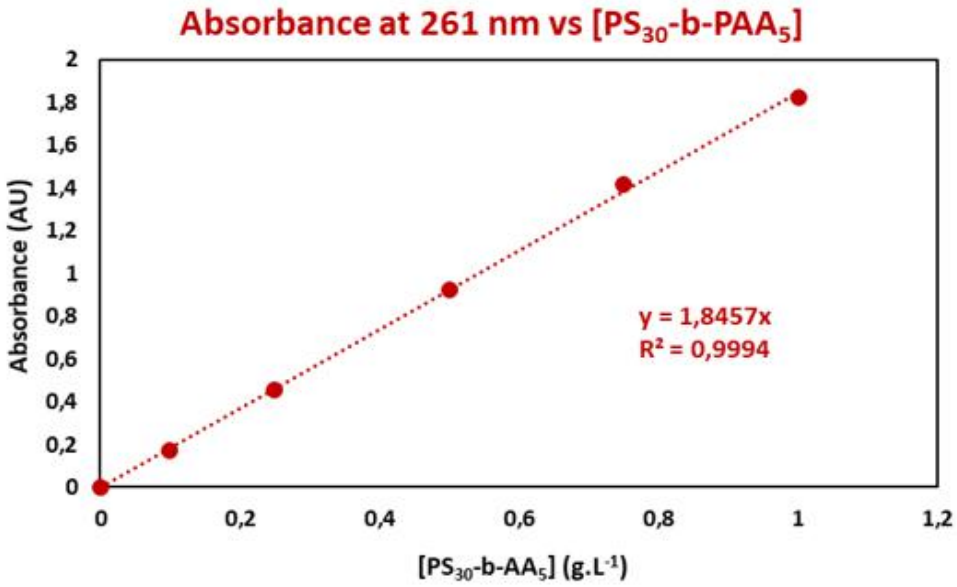

SI-Figure 3. Calibration curve of the absorbance obtained at 261 nm by UV-visible spectroscopy as function of PS_{30}-b-PAA_5 concentration

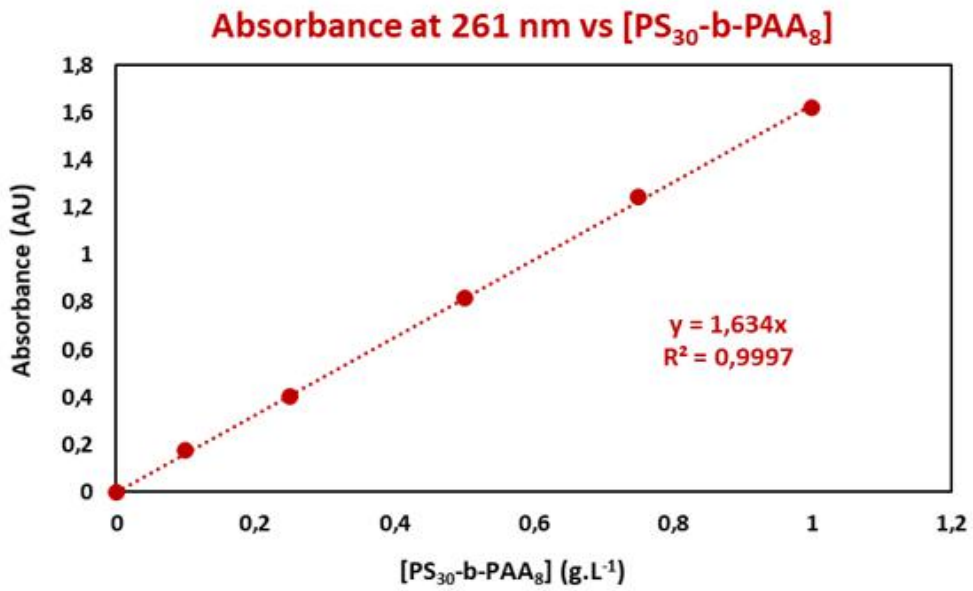

SI-Figure 4. Calibration curve of the absorbance obtained at 261 nm by UV-visible spectroscopy as function of PS_{30}-b-PAA_5 concentration.

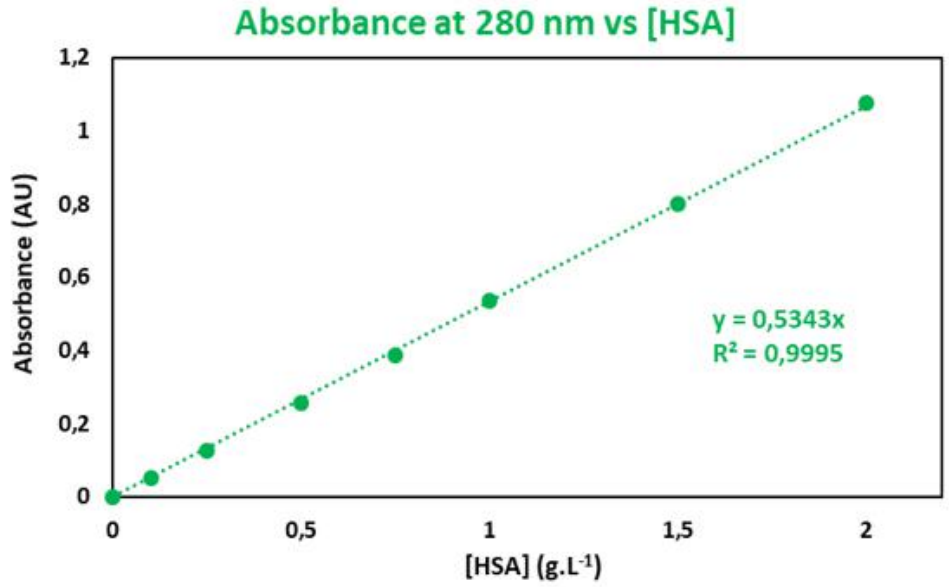

SI-Figure 5. Calibration curve of the absorbance obtained at 280 nm by UV-visible spectroscopy as function of HSA concentration.

2. ATR spectra of PS-b-PEO copolymers and those of HSA and IgG proteins

The ATR spectra that allowed to determine the characteristic peaks of the pure PS-b-PEO and those of the proteins (HSA and IgG) are shown in SI-Figure 6 and SI-Figure 7 respectively.

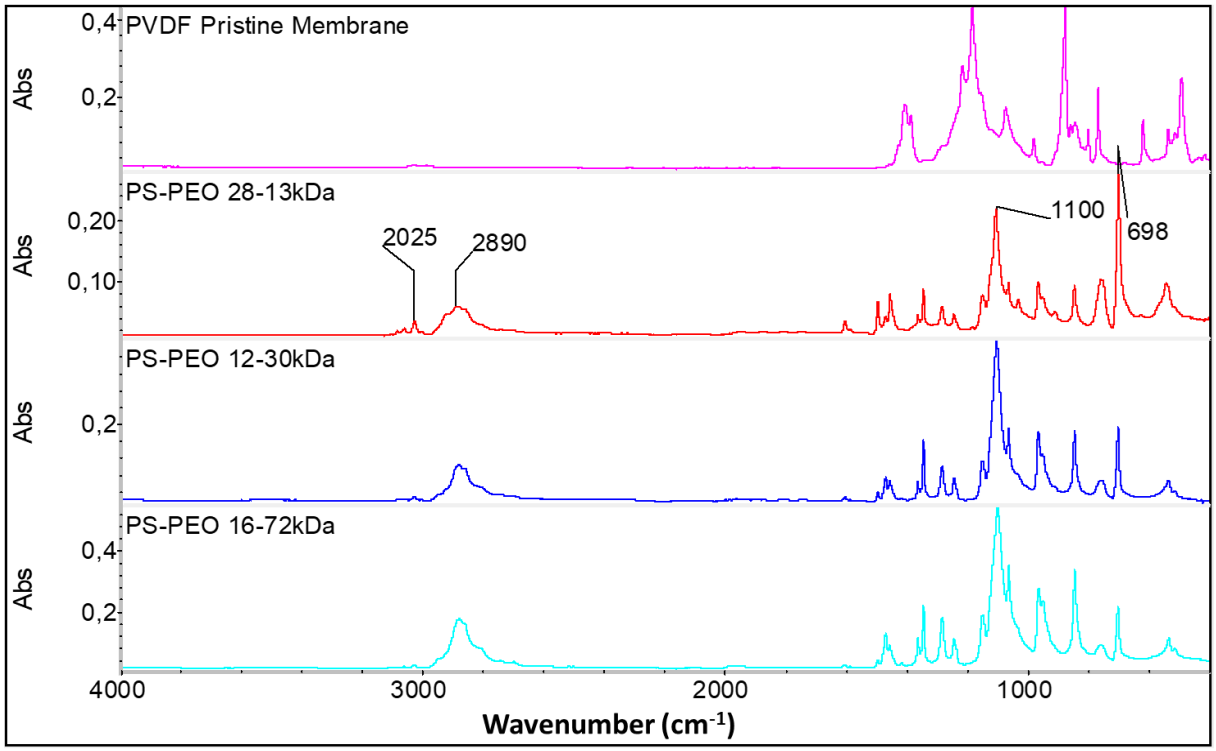

SI-Figure 6. ATR spectra the pure PS-b-PEO copolymers.

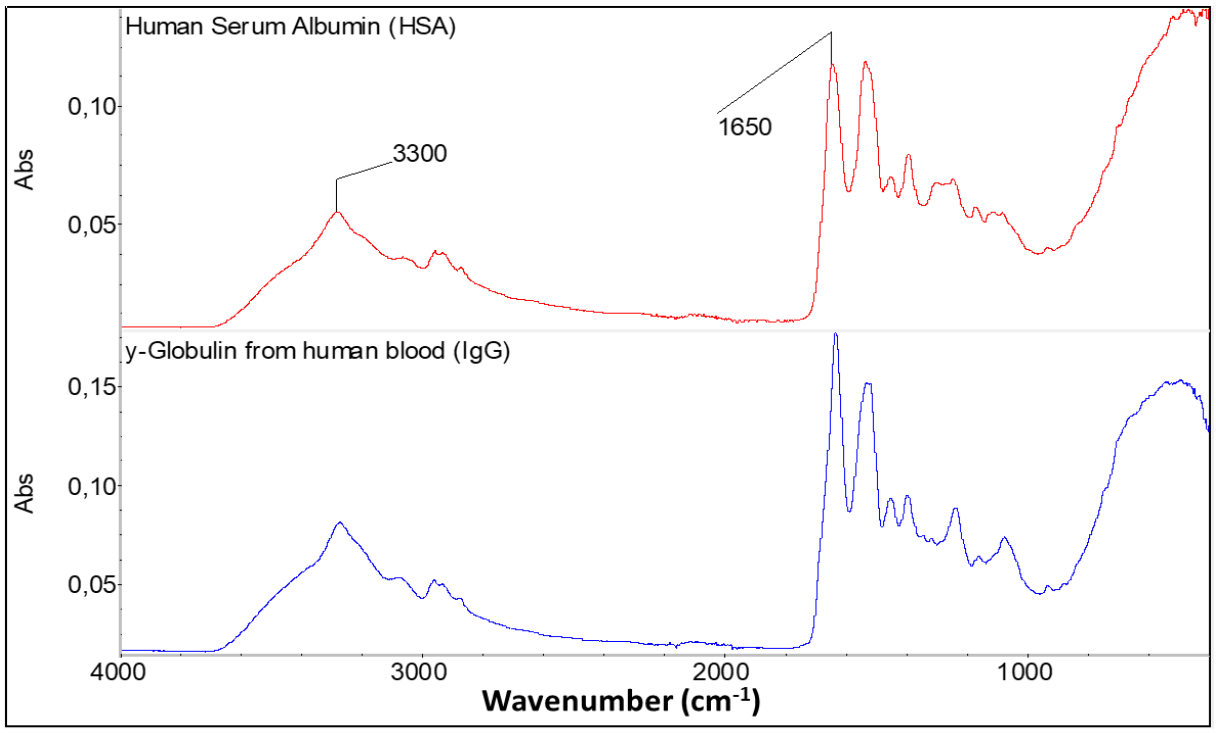

SI-Figure 7. ATR spectra obtained on the pure HSA powder and pure IgG powder.

3. Python code used for FTIR mapping analysis

The Python code that allowed to convert the color-coded maps with different rainbow scales into maps coded with same grey scale and permitted then to evaluate the mean intensities for the chosen peaks is given below.

```
%matplotlib inline
import matplotlib.pyplot as plt
import scipy.misc
import matplotlib.image as mpimg
import numpy as np
img = mpimg.imread('map name')
Imax=1.5 (#maximum of intensity obtained form the color-coded map)
#print(img)
#print (img)
plt.imshow(img)
plt.show()
lx, ly, g = img.shape
print ('lx =',lx,'ly =',ly)

# Crop image
y1=0
y2=470 (#size of the map)
x1=0
x2=470 (#size of the map)
dy=y2-y1
dx=x2-x1
crop = img[y1:y2, x1:x2]
plt.imshow(crop)
print ('min =',np.min(crop),'max =',np.max(crop))

#transformation en niveau de gris
rainbow = plt.cm.rainbow
rainbow._init()
lut = rainbow._lut[..., :]
z = crop - lut[:, None, None, :]
z *= z
d = z.sum(axis=-1)
imgg = d.argmin(axis=0)
f, (ax0, ax1, ax2) = plt.subplots(1, 3)

ax0.imshow(crop, cmap=plt.cm.gray)
ax1.imshow(imgg, cmap=plt.cm.gray)
ax2.imshow(imgg, cmap=plt.cm.rainbow)
gray_min=np.min(imgg)
gray_max=np.max(imgg)
plt.show()

print ('Gray min =',gray_min,'Gray max =',gray_max)

#Crop en 4 images
s=220
decalx=10
plt.imshow(imgg, cmap=plt.cm.rainbow)
plt.plot([decalx,decalx,s+decalx,s+decalx,decalx],
         [decalx,s+decalx,s+decalx,decalx,decalx])
```

```
plt.plot([dx-s-decalx,dx-s-decalx,dx-decalx,dx-decalx,dx-s-decalx],
         [decalx,decalx+s,decalx+s,decalx,decalx])
plt.plot([decalx,s+decalx,s+decalx,decalx,decalx],
         [dy-s-decalx,dy-s-decalx,dy-decalx,dy-decalx,dy-s-decalx])
plt.plot([dx-s-decalx,dx-decalx,dx-decalx,dx-s-decalx,dx-s-decalx],
         [dy-s-decalx,dy-s-decalx,dy-decalx,dy-decalx,dy-s-decalx])
plt.show()
cropA = imgg[decalx:s+decalx, decalx:s+decalx]
cropC = imgg[dy-s-decalx:dy-decalx, decalx:s+decalx]
cropB = imgg[decalx:s+decalx, dx-s-decalx:dx-decalx]
cropD = imgg[dy-s-decalx:dy-decalx, dx-s-decalx:dx-decalx]
f, ((ax1, ax2), (ax3, ax4)) = plt.subplots(2, 2)
ax1.imshow(cropA, cmap=plt.cm.gray, vmin=gray_min, vmax=gray_max)
ax1.set_title("A")
ax2.imshow(cropB, cmap=plt.cm.gray, vmin=gray_min, vmax=gray_max)
ax2.set_title("B")
ax3.imshow(cropC, cmap=plt.cm.gray, vmin=gray_min, vmax=gray_max)
ax3.set_title("C")
ax4.imshow(cropD, cmap=plt.cm.gray, vmin=gray_min, vmax=gray_max)
ax4.set_title("D")
plt.show()
print ('A Gray mean =',round(np.mean(cropA),2), 'Gray min =',np.min(cropA),
       'Gray max =', np.max(cropA),'Gray std =', round(np.std(cropA),2))
print ('B Gray mean =',round(np.mean(cropB),2), 'Gray min =',np.min(cropB),
       'Gray max =', np.max(cropB),'Gray std =', round(np.std(cropB),2))
print ('C Gray mean =',round(np.mean(cropC),2), 'Gray min =',np.min(cropC),
       'Gray max =', np.max(cropC),'Gray std =', round(np.std(cropC),2))
print ('D Gray mean =',round(np.mean(cropD),2), 'Gray min =',np.min(cropD),
       'Gray max =', np.max(cropD),'Gray std =', round(np.std(cropD),2))
```

```
f, ((ax1, ax2), (ax3, ax4)) = plt.subplots(2, 2)
ax1.imshow(cropA, cmap=plt.cm.gray)
ax1.set_title("A")
ax2.imshow(cropB, cmap=plt.cm.gray)
ax2.set_title("B")
ax3.imshow(cropC, cmap=plt.cm.gray)
ax3.set_title("C")
ax4.imshow(cropD, cmap=plt.cm.gray)
ax4.set_title("D")
plt.show()

yerr = [np.std(cropC)*Imax/255,np.std(cropD)*Imax/255,np.std(cropA)*Imax/255,
        np.std(cropB)*Imax/255]
plt.errorbar(["C","D","A","B"] #(operating conditions),
        [np.mean(cropC)*Imax/255,np.mean(cropD)*Imax/255,
         np.mean(cropA)*Imax/255,np.mean(cropB)*Imax/255], yerr=yerr, fmt='x')

plt.xlabel("investigated parameter")
plt.ylabel("mean intensity of investigated peak (xx $cm^{-1}$)")

print (np.mean(cropC)*Imax/255,np.mean(cropD)*Imax/255,np.mean(cropA)*Imax/255,
       np.mean(cropB)*Imax/255)
print (np.std(cropC)*Imax/255,np.std(cropD)*Imax/255,np.std(cropA)*Imax/255,
       np.std(cropB)*Imax/255)
```

D. Scientific communications and publication

- C. Merzougui, P. Roblin, P. Aimar, P. Bacchin, C. Causserand. **Poster**. Functionalized membrane bio-interface to control blood protein behaviour: polyelectrolyte-protein interaction investigated using Small Angle X-ray Scattering (SAXS). November 28 – December 2, 2021. **Euromembrane2021**, Copenhagen, Denmark.
- C. Merzougui, P. Roblin, P. Aimar, C. Causserand, P. Bacchin. **Poster**. Blood proteins interactions with polymers. 2-5 November, 2021. **GDR SLAMM**, Biarritz, France.
- C. Merzougui, P. Roblin, P. Aimar, C. Causserand, P. Bacchin. **Poster**. Small angle X-ray scattering (SAXS) to investigate interaction of HSA protein with PAA polyelectrolyte. 8-9 April, 2021. **Geneva Colloids**, Geneva, Switzerland.
- C. Merzougui, P. Roblin, P. Aimar, C. Causserand, P. Bacchin. **Oral presentation**. HSA-PAA complex formation as explored by small angle X-ray scattering (SAXS). January 19th, 2021. **GDR SLAMM**, Rennes, France.
- C. Merzougui, P. Roblin, P. Aimar, C. Causserand, P. Bacchin. **Poster**. HSA-PAA complex formation as explored by small angle X-ray scattering (SAXS). 6-9 December, 2020. **10th International Colloids Conference**, Palma, Spain.
- C. Merzougui, P. Roblin, C. Causserand, P. Bacchin, A. Venault, Y. Chang, P. Aimar, J.Y. Lai. **Oral presentation**. Probing polymer-protein interactions by small angle X-ray Scattering. 28-29 June, 2019. **International Membrane Conference in Taiwan**, Taipei, Taiwan.

Soft Matter

PAPER

View Article Online
View Journal

Cite this: DOI: 10.1039/d0sm01221a

Pearl-necklace assembly of human serum albumin with the poly(acrylic acid) polyelectrolyte investigated using small angle X-ray scattering (SAXS)†

Charaf E. Merzougui,*[a] Pierre Roblin,*[a] Pierre Aimar,[a] Antoine Venault,[b] Yung Chang,[b] Christel Causserand[a] and Patrice Bacchin[a]

Received 3rd July 2020,
Accepted 21st September 2020

DOI: 10.1039/d0sm01221a

rsc.li/soft-matter-journal

In this comprehensive study, the interaction of human serum albumin (HSA) with poly(acrylic acid) (PAA) was explored using small angle X-ray scattering (SAXS) combined with chromatography. The results revealed the formation of a complex between HSA macromolecules and PAA chains but solely under some specific conditions of the ionic strength and pH of the medium. In fact, this binding was found to take place only at pH close to 5 and at low ionic strength (0.15 M). Otherwise, for a higher pH and a salt concentration of 0.75 M the HSA–PAA complex tends to dissociate completely showing the reversibility of the complexation. The assessment of the influence of the HSA/PAA molar ratio on the radius of gyration of the complex suggests that 4 HSA molecules could bind to each 100 kDa PAA chain. In addition, the Porod volume evaluation for the same range of the HSA/PAA ratio confirms this assumption. Finally, an all-atom SAXS modelling study using the BUNCH program was conducted to find a compatible model that fits the HSA–PAA complex scattering data. This model allows us to portray the HSA/PAA complex as a pearl-necklace assembly with 4 HSA molecules on the 100 kDa PAA chain.

Introduction

Interactions between proteins and polymeric surfaces, whether linear (polyelectrolyte brushes)[1,2] or spherical (functional nanoparticles),[3–5] have received growing attention over the past few decades. Many processes involve this phenomenon in several fields and for versatile applications, such as protein separation,[5,6] drug delivery,[7,8] ligand uptake,[9] enzyme immobilization,[10] and antibacterial encapsulation,[11] among many other applications in chemistry and biology.[12]

The design of biomaterial and medical devices is among the fields in which this interaction is relevant.[13,14] Biomaterials are often used for the treatment of diseases such as cardiac failure, but also in medical applications such as wound healing, deep skin injury repair, dentistry or orthopedics.[15] In many cases, these biomaterials have direct contact with blood. One of the fastest growing areas for biomaterials is the development of new systems for controlled and targeted drug delivery. For example, suitable advanced membrane technologies could be proposed to address several critical needs related to blood cells screening and the concentration of the growth factors stored inside the granules of platelets and expressed after their activation. These growth factors are used to enhance the wound healing process of diabetic ulcers. For that, the architecture of the membrane biointerface at the nanoscale is often customized by grafting on it some functional groups such as poly(acrylic acid) (PAA). It is a negatively charged bioactive polymer in aqueous medium which is widely used to modify polymeric surfaces for drug release and many other applications.[16] One of them is the enhancement of platelet adhesion, especially when it is conjugated to proteins such as fibrinogen. However, nonspecific interactions between other blood components and polymers used for interface modification could hamper the capture of platelets. Among these blood components, human serum albumin (HSA) is an abundant plasma protein ([HSA] ≈ 42 mg mL^{-1} in blood[17]) that maintains the pH and osmotic pressure of blood and transports some molecules in the blood. This protein is able to decrease platelets adhesion and activation on a solid surface by being adsorbed onto that particular surface.[18] Therefore, with the purpose of designing functionalized membrane surfaces to selectively separate thrombocytes from other blood cells, the control of these nonspecific interactions is required.

According to the literature, a number of protein–polyelectrolyte complexes have been studied under a variety of

[a] Laboratoire de Génie Chimique, Université de Toulouse, CNRS, INPT, UPS, Toulouse, France. E-mail: merzougui@chimie.ups-tlse.fr, roblin@chimie.ups-tlse.fr
[b] R&D Center for Membrane Technology, Chung Yuan Christian University, Chung Li, Taiwan

† Electronic supplementary information (ESI) available. See DOI: 10.1039/d0sm01221a

View Article Online
Paper Soft Matter

physicochemical conditions *via* several analytical techniques.[19,20] Concerning the complexes of serum albumin and polymers, the interaction of bovine serum albumin (BSA) with spherical polyelectrolyte brushes in solution was evidenced using small angle X-ray and neutron scattering (SAXS and SANS).[21,22] Interactions between BSA and planar synthesized poly(acrylic acid) were also the subject of a dedicated work.[23] Furthermore, the binding of HSA with small polyelectrolyte brushes of PAA (with 25 repeating units only),[25] and with dendritic polyglycerol sulfate,[26] has also been discussed using isothermal calorimetry (ITC) data. In fact, it has been proved that only one HSA is bound per chain of PAA 1.8 kDa. Then, for a pH maintained at 7.2, a study on the effect of salt concentration revealed that this binding was dominated by an attractive electrostatic potential between the two solutes.[24] Using total internal reflection fluorescence (TIRF) spectroscopy, it has also been proven that negatively charged BSA is strongly adsorbed on planar PAA (278 AA units $\approx$ 20 kDa) at a low ionic strength and pH $>$ 5 due to electrostatic interactions.[26] However, the current knowledge does not allow us to determine the exact stoichiometry of polyelectrolyte–protein complexes for a larger polymer and whether it is correlated to the size of the polyelectrolyte.

In the present study, we used SAXS combined with chromatography to assess the affinity of HSA to bind to a larger PAA (100 kDa) to check out the formation of multiprotein–polymer complexes compared to the 1HSA–1PAA binding reported in the literature using a smaller polyelectrolyte.[24] First, as a starting point for further experiments with polymers, the structure of native HSA was examined in phosphate buffer solution. Then, the HSA/PAA complexation was studied in media with different ionic strengths or pH in order to find the conditions leading to an attractive interaction. After that, a detailed study modeling the Porod volume was conducted to determine the stoichiometry of the (*n*HSA–PAA) complex formed. For this purpose, the influence of the HSA/PAA molar ratio on the complex size (radius of gyration and Porod volume) was assessed. Eventually, a compatible model has been found using the BUNCH program[27] to fit the scattering data of the HSA–PAA complex. It allowed us to propose an all-atom pearl necklace model that describes the structure of the complex at the ionic strength and pH mentioned above, and it also validated the proposed stoichiometry.

Experimental section

Materials and sample preparation

Human serum albumin (HSA, lyophilized powder, $\geq$96% agarose gel electrophoresis) with a molecular weight of 66 478 g mol^{-1} and poly(acrylic acid) (PAA) with a molecular weight around 100 000 g mol^{-1} (35 wt% in H_2O) were purchased from Sigma-Aldrich and used as received.

HSA powder was dissolved in PBS 1$\times$ (0.012 M phosphate buffer solution at pH 7.4, ionic strength = 0.137 M) to obtain a stock solution of 50 g L^{-1} HSA (750 μM), from which samples of lower concentration were prepared. In the same way, the polymer solutions were prepared through dilution in PBS 1$\times$ buffer from a stock PBS solution of 100 g L^{-1} PAA (1 mM).

For the investigation of the native HSA structure in solution and the HSA–PAA interaction, the concentration of HSA was set at 5 g L^{-1} to avoid repulsion between particles which can distort the measured intensity at small angles. The pH effect was studied using different buffer solutions at 0.1 M (TRIS base at pH 8, HEPES at pH 7, MES at pH 6, a mixture of sodium citrate di-hydrate and citric acid at pH 4–5). As for the influence of ionic strength, the salt concentration was adjusted by adding the required amounts of a 4 M NaCl solution.

Then, all samples, whether protein free, polymer free or a mixture of both, were stirred using a Thermo Scientific mini centrifuge (mySPIN 12) at 10 000 rpm for 2 minutes at least, to ensure good dissolution of the solutes, before being pipetted into the sample holder for the SAXS measurement. When not in use, the samples were stored at 4 °C in a refrigerator.

Chromatography measurement

The chromatography unit used consisted of an Agilent 1260 Infinity system connected to a UV-vis detector set at a wavelength of 280 nm. Analyses were performed using an Agilent Bio Sec-3 (3 μm, 4.6 $\times$ 300 mm^2, 300 Å) size exclusion column at room temperature. In a typical analytical run, 50 μL of a 75 μM protein solution was injected, and PBS 1$\times$ was used as the mobile phase for protein structure investigation at a flow rate of 0.4 mL min^{-1}. As for the protein–polymer complexation study, a 75 μM HSA + 50 μM PAA solution was injected and a PBS solution containing 50 μM PAA was used as the mobile phase.

SAXS measurement

SAXS measurements were performed at Laboratoire de Génie Chimique, Toulouse, on the XEUSS 2.0 bench equipped with a copper internal source (GeniX3D) that produces an X-ray beam with an energy of 8 keV and a flux of 30 $\times$ 10^6 ph. mm^2 s^{-1} with a beam size of 500 $\times$ 500 μm^2. The SAXS bench is equipped with an HPLC online (Agilent 1260 Infinity) connected to the SAXS cell allowing the addition of a purification step *via* size exclusion chromatography. In the direct injection mode, that is, without the size exclusion chromatography step, 50 μL of the sample was pipetted from the sample holder maintained at a constant temperature (20 °C) using a circulating water bath and injected to the measurement cell placed under vacuum to limit air absorption. Data were collected on a 150 $\times$ 150 mm^2 DECTRIS detector (Pilatus 1M) with a sample to detector distance of 1216 mm. The scattering intensity $I(q)$ determined experimentally is expressed as a function of the scattering vector q (in Å^{-1}) resulting from a photon of wavelength λ scattering off the sample at an angle 2θ.

$$q = \frac{4\pi \sin(\theta)}{\lambda} \quad (1)$$

Each scattering curve reported in this paper is an average of at least 6 measurements on the same sample, and each SAXS measure corresponds to a data collection time of 1800 s. Scattering curves were recorded within the range

View Article Online
Soft Matter Paper

$0.005 < q < 0.5$ Å^{-1}. Finally, the actual solute scattering intensity $I(q)$ was obtained by subtracting the buffer solution contribution from the total SAXS signal.

Porod volume calculation

From SAXS experiments, it is possible to obtain the Porod volume of an object from the Porod invariant Q:[28]

$$V_{obj} = \frac{2\pi^2 I(0)}{Q} \times \frac{1-\phi}{S(0)} \quad (2)$$

When the dispersion is diluted the volume fraction $\phi \rightarrow 0$, $S(0) \rightarrow 1$ and the Porod volume can be determined by knowing the zero angle intensity $I(0)$ and Q.

Q is called the Porod invariant because its value does not depend on the structure but on the volume fraction and the contrast between two phases $\Delta\rho$:

$$Q = \int_0^\infty q^2(I(q) - K)\mathrm{d}q = 2\pi^2\phi(1-\phi)r_e^2(\Delta\rho)^2 \quad (3)$$

where K is a constant defined to ensure the asymptotic intensity decay proportional to q^{-4} at higher angles.[29]

The value of Q can be roughly obtained from the integration of the Kratky plot (classically with a limited integration boundary at $q = 0.25$) by considering $K = 0$:

$$Q = \int_0^{0.25} q^2 I(q)\mathrm{d}q \quad (4)$$

When the intensity decreases too slowly at large q (less than q^{-3}) as for polymeric systems[30] it is much more accurate to integrate the original equation after determining the constant K, whereby the constant K is calculated from the Porod asymptote $I(q)q^4$ *versus* q^4 at higher angles. In these calculations, the asymptote has been always determined for the same range of q between 0.3 and 0.445 with a homemade code to maintain the control of the calculation. The code is given with the plots showing the determination of K (Fig. 4 and 5) in the ESI,† SI-2, as well as the corrected dimensionless Kratky plot obtained by subtracting K from $I(q)$ (Fig. 6 in the ESI,† SI-2). It can be seen that the subtraction of the asymptote K leads to a curve that tends to zero for high q which then allows a good integration of the invariant Q.

Results and discussion

Study of single HSA

The structure of native HSA was first examined in a 0.012 M phosphate buffer solution at pH 7.4, and the obtained SAXS scattering intensities were compared to those calculated from the crystal data of HSA on the Protein Data Bank (6EZQ). In order to guarantee the absence of aggregates in the investigated samples, an Agilent chromatographic system was coupled upstream of the SAXS.

Fig. 1 shows that the experimental SAXS spectrum from purified commercial HSA (blue line) matches very well the calculated intensity from the crystal structure (red line), evidencing that the HSA used for this study is correctly folded at 75 μM in the PBS buffer condition. These preliminary results validate the use of HSA as a template to study the protein polymer interaction. Under these conditions we can expect that SAXS will be precise enough to sense an interaction between HSA and PAA.

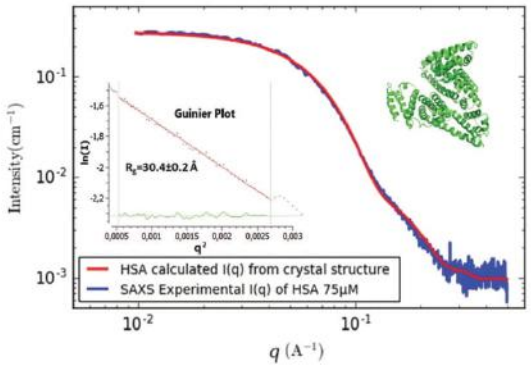

Fig. 1 Experimental SAXS scattering intensity $I(q)$ of 75 μM HSA (blue line) compared to the SAXS intensity calculated with CRYSOL from the HSA crystal structure 6EZQ (red curve). The inset presents the Guinier plot ($\ln I(q)$ *vs.* q^2, red line) with the residual (green curve) that allows the determination of radius of gyration using Primus. The HSA 3D structure is shown as a cartoon representation created using PyMOL software.

The radius of gyration R_g of HSA was then evaluated by fitting using Foxtrot or Primus.[28,31] Both software programs consider the Guinier approximation that allows the determination of R_g from the slope of the linear fit at low q of $I(q)$ *vs.* q^2 (Fig. 1), as it gives the forward scattering intensity $I(0)$ from the intercept based on the following equation:

$$\lim_{q\to 0} I = I_0 \exp\left(-\frac{1}{3}q^2 {R_g}^2\right) \quad (5)$$

The result yields approximately 30 Å (30.4 ± 0.2 Å), which is almost equal to what was found with R_g (30.2 ± 0.4 Å) in a SAXS study for HSA with the same purity, *i.e.* >96%.[17]

Likewise, the Porod volume and molecular weight were estimated using Primus that considers the Porod law (ESI,† SI-2) and found to be around 100 000 Å^3 and 64.5 kDa, respectively. These results seem to be consistent with the molecular weight of HSA (66.5 kDa), which validates the use of Primus to evaluate such parameters in further experiments.

HSA–PAA interaction

The characterization of a single protein was then followed by assessing the interactions between HSA and the polyelectrolyte chains. For that, we first studied the effect of an increase in PAA concentration on the SAXS scattering intensity for an HSA/PAA molar ratio ranging from 0 (protein alone as a reference) to a molar ratio of 3/2. As shown in Fig. 2, starting from 40 μM of PAA with 75 μM HSA, a strong change in the signal at small angles is observed, which could be due to the formation of an HSA–PAA complex, while at intermediate and high values of q the SAXS curves remain almost unchanged by the complexation. Indeed, the evolution of the slope P of the corresponding power law $I(q) = q^{-P}$ shows, that at intermediate angles (0.1 to 0.2 Å^{-1}),

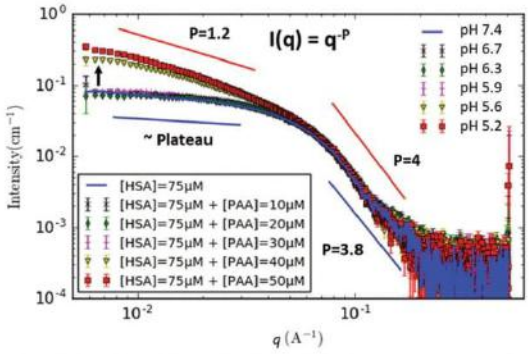

Fig. 2 Scattering intensities of the HSA–PAA mixture and pH evolution for [HSA] = 75 μM as a function of PAA concentration ([PAA] = 0 to 50 μM). Evolution of the slope of the power law $I(q) = q^{-P}$ corresponding to small and intermediate angles.

P slightly varies from 3.8 for single HSA and the mixture of HSA + 10, 20 and 30 μM PAA, to 4 when increasing the PAA concentration to 40 and 50 μM (Fig. 2). These results indicate the same type of surface despite the big change in the general shape shown by an increase in the slope at small angles (0.005 to 0.05 $Å^{-1}$). In fact, the difference is more obvious, where the slope is going from almost a tray ($P = 0.3$) for single HSA to a slope of 1.2 when adding 50 μM PAA, which corresponds to the slope of an elongated object.[32]

PAA, despite being in PBS buffer, strongly influences the pH of the solution. Thus, we can suppose that the change in the SAXS curve could be correlated to a pH variation rather than to an effect of the concentration of PAA (explicitly discussed later in the paper).

In order to confirm that the change in the SAXS signal at small angles is due to the formation of a new object being an HSA–PAA complex, we compared the SAXS curves from the HSA alone at 75 μM (blue line), the PAA alone at 60 μM (green line), the mixture of both with the same initial concentration (yellow line) and the sum (red line) of the SAXS signals of HSA at 75 μM and PAA at 60 μM (Fig. 3A).

For the first three curves, the data were processed with GNOM[33] to determine biophysical parameters such as the radius of gyration R_g and the maximal distance D_{max} using the autocorrelation function $P(r)$. This function was calculated through an indirect Fourier transformation applied to the scattering intensity $I(q)$ using the following equation:

$$P(r) = \frac{r^2}{2\pi r_e^2}\int_0^\infty q^2 I(q)\frac{\sin(qr)}{qr}\mathrm{d}q \qquad (6)$$

The pair distribution function refers to the distribution of electrons averaged over the radius r. It entirely depends on the shape and size of the particle and vanishes at their maximum electron pair distance (D_{max}). The radius of gyration can be then derived from $P(r)$ using the following expression:

$$R_g^2 = \frac{\int_0^{D_{max}} r^2 P(r)\mathrm{d}r}{2\int_0^{D_{max}} P(r)\mathrm{d}r} \qquad (7)$$

This alternative estimate of R_g makes use of the whole scattering curve and is much less sensitive to interactions or to the presence of a small fraction of oligomers. The results of the radius of gyration (29.7 Å for HSA and 110.3 Å for the complex) extracted from $P(r)$ were almost the same as those obtained by fits from the Guinier plot (30.4 Å for HSA and 108.9 Å for the complex). The Porod volumes (V_p) of HSA and the complex were also evaluated. For a flexible system such as polymer chains in solution it is difficult to evaluate the exact V_p. All parameters are reported in the table attached to Fig. 3A. Although the curves are calibrated in cm^{-1}, it is impossible to directly determine the mass concentration of the hetero-complex from $I(0)$ because we do not know either the association stoichiometry or precisely the experimental specific volume and contrast of the PAA.

As observed in Fig. 3A, the SAXS curve of HSA is consistent with a 3D object with a large plateau at small angles and a typical decrease at intermediate angles, whereas PAA exhibits a behavior similar to a flexible polymer in solution (a large decrease following a power law $I(q) = q^{-P}$ with P being close to 1.7 which corresponds to polymers with local rigidity).[34]

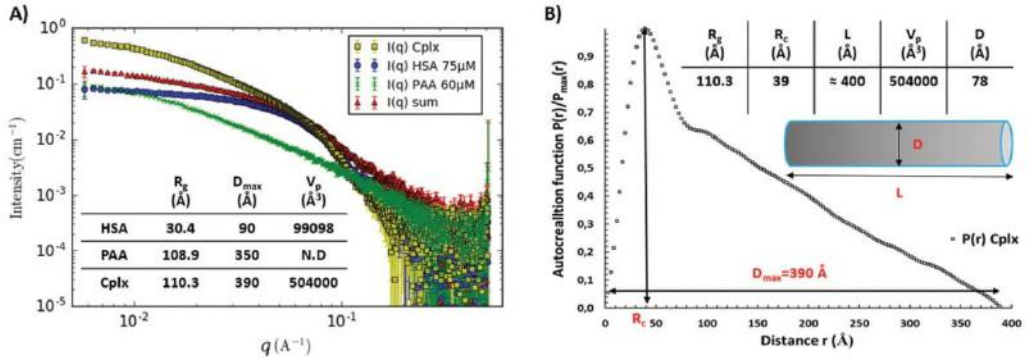

Fig. 3 (A) Scattering intensities of [HSA] = 75 μM (blue curve), [PAA] = 60 μM (green curve), the mixture of HSA and PAA at the same concentration (yellow curve) and the sum of both contributions without any interaction (red curve); the table summarizes the radius of gyration, the maximal distance and the Porod volumes of HSA, PAA and the complex. (B) Autocorrelation function determined with GNOM of the complex; the table summarizes the biophysical parameters extracted from the SAXS data of the complex.

View Article Online
Soft Matter Paper

The SAXS curve obtained for the complex presents a combination of properties of HSA and PAA. It shows a constant decrease at small angles and the same signal of HSA starting from 0.05 $Å^{-1}$. The direct comparison with a linear combination of HSA and PAA SAXS curves (the sum curve in Fig. 3A) under the same conditions of concentration reflecting the case without interactions between both partners discloses clearly that the observed SAXS curve corresponds to the creation of a new object resulting from the interactions between HSA and PAA.

The evaluation of R_g and V_p shows that the complex is five times larger than HSA alone but the difficulty to evaluate correctly the Porod volume of PAA (in the complex) or its contribution to the measured $I(0)$ does not allow the numbers of HSA and PAA forming the complex to be given directly. The form of the autocorrelation function corresponding to the complex in Fig. 3B shows a skewed distribution with a clear maximum at small distances corresponding to the radius of the cross-section R_c (R_c = 39 Å from $P(r)$, Fig. 3B). This distribution is typical of elongated objects such as cylinders, rather than corresponding to amorphous aggregates.[35] With these considerations, the length L of this cylinder can be calculated using the following relationship: $L = (12 \cdot R_g^2 \cdot R_c^2)^{0.5}$. The diameter of the cylinder, the calculated length L and all evaluated parameters are summarized in the table attached to Fig. 3B. The value of the calculated length (404 Å) is consistent with the maximal distance (390 Å) determined with the $P(r)$ calculation. One can assume that the complex of HSA/PAA-100 kDa exhibits a behavior in solution equivalent to a solid cylinder measuring around 400 Å in length and 78 Å in diameter.

To validate this hypothesis predicting the formation of a defined object instead of amorphous aggregates, solutions of HSA–PAA were flowed in various mobile phases through a size exclusion chromatography column (ESI,† SI-1). The chromatographic profiles were then compared to that of the single HSA detected mainly at 7.74 min with a small amount of dimers at 6.9 min (Fig. 4).

In fact, in a PBS mobile phase (without PAA) at pH 7.4, a peak at 7.7 min of retention time was obtained, corresponding to the molecular weight of HSA alone. This experiment shows that the complex can be dissociated in a dilute medium of PAA, illustrating the reversibility of the complex formation. On the other hand, if 50 μM of PAA is added to the mobile phase, the pH decreases to 5.2 and the elution profile is modified with a strong shift of the elution peak towards high molecular weights (Fig. 4). This observation proves that the protein is no longer single in the solution but bound to the PAA chains. The Gaussian shape of the peak eluted at 5.8 min corresponds to a profile of a unique object in solution and not to a continuous distribution of mass such as in aggregates.

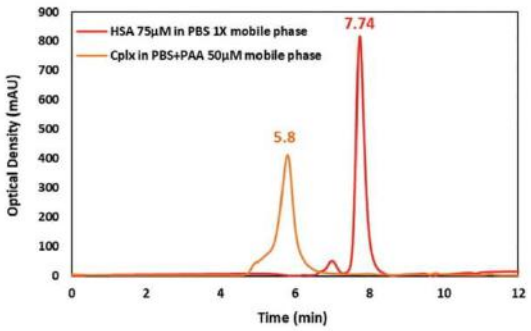

Fig. 4 Comparison of chromatographic profiles for 75 μM HSA in the PBS 1× mobile phase (red peak) and for the (75–50 μM) HSA–PAA mixture in the PBS + 50 μM PAA solution mobile phase (orange peak).

These experiments were run at PBS ionic strength (0.137 M) and at a pH controlled by the PAA concentration, ranging from 5.2 to 7.4 as mentioned above (Fig. 2). Since the pH remains higher than the HSA isoelectric point (4.7) and knowing that PAA exhibits a pK_a of 4.5, we expect repulsive forces that keep them away from each other, which is because they both theoretically bear negative charges. Yet, the adsorption of HSA molecules on PAA chains is found to occur. Attractive interactions between a polyelectrolyte and a protein having the same net charge were reported by several authors.[20,36–38] Since the proteins can carry both positive and negative charges, this binding that was found to occur in our study could be due to the attractive electrostatic potential between the positively charged patches on the surface of HSA and the negatively charged chains of PAA, which should be the operative force that overcomes the repulsion forces. A detailed ITC study performed on the binding between HSA with a negative overall charge and a negatively charged PAA[24] shows the same behavior between the two solutes, where each HSA molecule has been found to bind to one PAA chain, causing an increase in the system entropy. It has been explained by the action of the HSA surface positive charges as a multivalent counterion for the polyelectrolyte.

Other works in which experiments and dynamics computer simulations were performed addressed more deeply such a phenomenon between proteins and polyelectrolytes.[39–41] They showed a large binding affinity between charged patchy proteins and like-charged polyelectrolyte brushes despite having the same net charge. It has been shown that the strongest attraction of typical proteins at the brush surface is driven by multipolarity, Born energy (self-energy), and counterion-release contributions, which dominate locally over the monopolar and steric repulsions.

Ionic strength and pH effect on HSA/PAA complexation

For the study of ionic strength and pH effects, [HSA] was set at 75 μM and [PAA] at 50 μM (pH ~ 5 remains controlled by the polymer concentration), where the complexation was observed, while the ionic strength was varied from 0.137 M to 1 M by adding the required amount of a 4 M NaCl solution.

The data obtained and reported below (Fig. 5A) reveal a decrease in scattering intensity with an increase in ionic strength. The curves are obviously moving down, especially at medium and small angles (0.005 to 0.1 $Å^{-1}$), changing the slope, to collapse for ionic strengths of 0.75 M and 1 M with the theoretical sum (plotted as a red line) of two independent signals without any interaction (signal of HSA 75 μM + signal of PAA 50 μM) obtained at I = 0.137 M. This finding confirms the previous assumption and

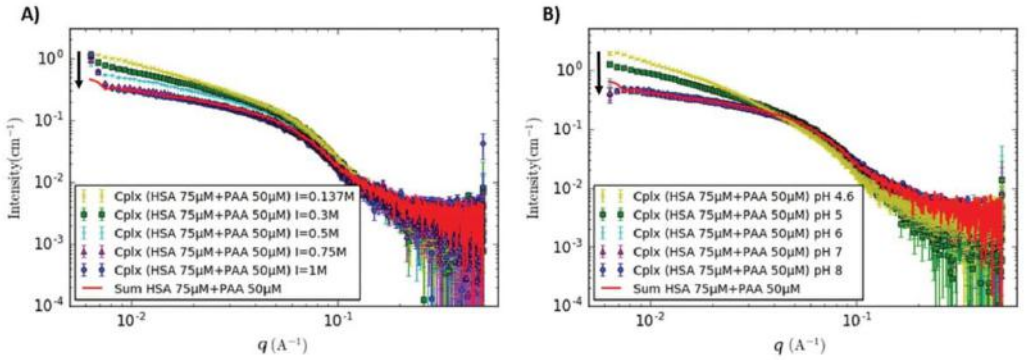

Fig. 5 Scattering intensities of the HSA–PAA mixture for [HSA] = 75 µM and [PAA] = 50 µM (A) as a function of ionic strength (I = 0.137 to 1 M) for pH ≈ 5 and (B) as a function of pH (pH = 4.6 to 8) for I = 0.137 M.

bears out the fact that the binding of HSA–PAA is due to electrostatic interactions.

Afterwards, the salt concentration was set at 0.137 M and the pH was varied from 8 to 4.6 using different buffer solutions. As shown in Fig. 5B, the decrease in pH down to 5 promotes the formation of the complex whereas at pH > 5 the complex is dissociated giving the same SAXS signal as a mix of two independent contributions. These experiments show the key roles of pH and ionic strength on complex formation correlated to the charge distribution of amino acid forming the binding pocket of HSA and to the charge density of the PAA. Decreasing the pH allows the repulsive forces to be reduced until the initiation of the attractive potential between the positive charges carried on HSA and the negative polyelectrolyte chains. However, at pH lower than 5 (pH 4.6), the obtained SAXS signal (Fig. 5B) is significantly different (slope P = 1.5) from that of a macromolecular complex (slope P = 1.2). Since the drop of pH to 4.6 cannot sufficiently alter the net charge of the protein (isoelectric point 4.7) to create phase separation, one can consider that HSA starts to unfold and form aggregates because it undergoes a form transition between pH 5.0 and 3.5.[42]

In order to determine the best conditions of complex formation, SAXS measurements for a matrix of conditions were performed where the ionic strength was varied from 0 to 0.75 M for each of the pH values: 5, 6 and 7. As the major effects are observable at small angles due to the increase in size when the complex appears, we decided to probe the changes by evaluating the radius of gyration determined from the Guinier law for each condition. Although the PAA and the complex have close R_g values (R_g ≈ 110 Å), the average value of R_g was found to be around ≈50 Å when the HSA and PAA do not interact, which is much lower than that of the complex. The data are plotted in Fig. 6. One can notice that the radius of gyration values for free PAA or single HSA, which were found to be around 110 Å and 30 Å, respectively, do not depend on the pH.

The pH in the range of 6–7 does not affect the radius of gyration of the mixture HSA + PAA, which was found to be approximately 50 Å for all the salt concentrations investigated. This observation highlights the fact that HSA–PAA binding does

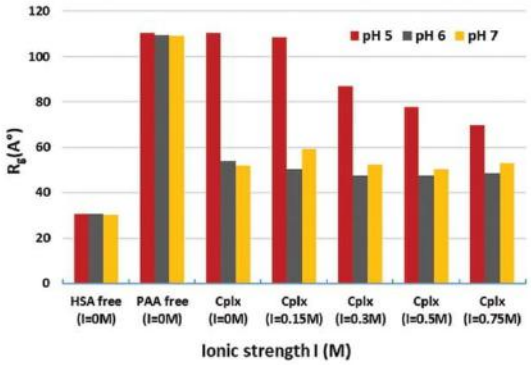

Fig. 6 Radius of gyration evolution as a function of both pH and ionic strength showing the threshold needed for the complexation phenomenon to occur ([HSA] = 75 µM; [PAA] = 50 µM; pH = 5 to 7 and I = 0 to 0.75 M).

not take place under these conditions. Since the radius of gyration obtained here through fitting is an average of the R_g value of HSA and that of PAA, it makes sense to obtain an average proportional to the amount of each solute in the mixture (a protein/polymer ratio of 3/2). A different behavior is observed at pH 5. In fact, increasing the ionic strength from 0 to 0.75 M has led to a decrease in R_g from 110 Å, which is almost the radius of gyration of the polymer, to 69.8 Å. This is because beyond an ionic strength of 0.15 M the HSA–PAA complex particles begin to dissociate into free HSA molecules and free PAA chains. This dissociation is not complete at 0.75 M and some complex particles are still in there since the obtained R_g (69.8 Å) is still higher than the average value (≈50 Å) found when the HSA and PAA do not interact. This outcome confirms the previous results (Fig. 5), suggesting that a complete dissociation of the complex takes place between 0.75 M and 1 M.

We conclude from this study that the complex is stable at pH 5 and a salt concentration below 0.15 M. As mentioned previously, we tested the stability of the complex in HPLC with elution buffers at different pH and a constant salt

View Article Online
Soft Matter Paper

concentration (I = 0.137 M) in the presence as well as the absence of PAA. The results show a dissociation of the complex for pH higher than 5 (ESI,† SI-1). The absence of PAA in the medium also promotes the dissociation, suggesting a large value of the dissociation constant, which requires the presence of PAA in the buffer to form the complex.

We henceforth know the conditions that lead to the assembly of HSA–PAA complexes in bulk. Therefore, this study constitutes a first knowledge brick to tune these reversible interactions between long-chain PAA grafted onto a membrane surface and HSA. Controlling the ionic strength and pH should enable the regulation of these interactions, promoting or preventing their formation. In fact, to enhance the platelet capture on PAA, a low salt concentration and pH > 5 should be used to prevent the adsorption of HSA on PAA. Now that the conditions of complex formation are controlled, the stoichiometry of complexation can be investigated.

Determination of the complex stoichiometry (PAA–*n*HSA)

In order to determine the number of proteins that could bind to each polymer chain, SAXS experiments were performed by setting the concentration of PAA at 50 μM and varying the HSA concentration between 75 and 600 μM. In other words, the [HSA]/[PAA] molar ratio ranged from 1.5 to 12. The experiments were performed at pH 5 and the salt concentration of I = 0.15 M to ensure complexation.

For a HSA concentration lower than 225 μM, the SAXS curve increases without any significant change of slope at small and intermediate angles (0.005 to 0.1 $Å^{-1}$ Fig. 7). This shift of the curves corresponds to an increase in the concentration of the complex, considering that the contribution of PAA is negligible, compared to that of the complex (*cf.* Fig. 3A). Given the ratio of Porod volumes between HSA and the complex of R = 1 : 5, it is expected to have several HSA molecules per chain of PAA. Such behavior in solution would suggest that the binding mechanism of HSA to PAA is cooperative, without intermediates depending on the concentration of HSA.

When the HSA concentration is close to 225 μM, the signal does not increase anymore with the concentration. Beyond 225 μM, the signal changes at small angles, with a decrease

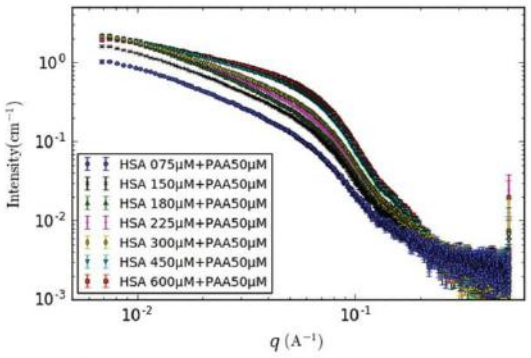

Fig. 7 Scattering profiles of the HSA–PAA mixture as a function of the HSA amount ([HSA] = 75 to 600 μM; [PAA] = 50 μM; pH = 5 and I = 0.15 M).

Table 1 Evolution of the radius of gyration as well as the Porod volume for the HSA–PAA mixture as a function of the molar ratio ([PAA] = 50 μM; [HSA] = 75–600 μM)

[HSA] μM	75	75	150	180	225	300	450	600
*n*HSA/PAA	Free HSA	1.5	3	3.6	4.5	6	9	12
R_g (±3 Å)	30.4	108.3	107	110.1	108.6	90.6	81	74.1
$V_p \times 10^3$ ($Å^3$)	99.1	428	502	500	491	400	305	239

in R_g and $I(0)$ values. At large angles, one can observe a change in the SAXS profile. This change is due to an accumulation of free HSA in the medium and eventually the measured signal is a combination of the signal of all PAA molecules involved in the complexes and that of the unbound HSA.

Table 1 summarizes the values of R_g and Porod volumes for each HSA/PAA ratio.

From the R_g values reported in Table 1, it can be concluded that the attachment of proteins to the polymer chains has taken place on all the polyelectrolyte chains available for HSA/PAA molar ratios ranging between 3.6 and 4.5.

To support this hypothesis, the Porod volume was evaluated for different HSA/PAA molar ratios. From SAXS experiments it is possible to obtain the Porod volume of an object from the Porod invariant Q as shown in the experimental section (the plots are shown in the ESI,† SI-2).

The calculated Porod volumes (reported in Table 1) exhibit the same behavior as the radius of gyration. For a HSA/PAA molar ratio of 3.6, the Porod volume is found to be around 500×10^3 $Å^3$ which represents the Porod volume of the complex (Fig. 3). Then, we notice that increasing the HSA concentration reduces the volume to 239×10^3 $Å^3$ for a molar ratio of 12. This makes sense because, after the saturation of all PAA chains, the excess of HSA contributes to the average of the Porod volume.

On the other hand, a complexation model has been developed to describe the evolution of the Porod volume for the same range of HSA/PAA molar ratios, taking into account the following complexation reaction:

$$n\text{HSA} + 1\text{PAA} \rightarrow 1\text{complex (PAA–}n\text{HSA)}$$

where n is the number of HSA molecules in each complex particle.

Thus, for a given initial $[\text{HSA}]_0/[\text{PAA}]_0$ molar ratio, it is possible to define [HSA], [PAA] and [c] as the molar concentrations in the mixture during the complexation progress of HSA, PAA and the complex, respectively. It is also possible to determine the relative volume fraction of each solute i in the mixture (ESI,† SI-3) as follows:

$$\varphi_i = \frac{N_{\text{Avo}} \cdot [i] \cdot V_i}{\phi} \quad (8)$$

where ϕ is the volume fraction of the mixture of solutes in solution and is expressed as

$$\phi = N_{\text{Avo}}([\text{c}]V_{\text{c}} + [\text{HSA}]V_{\text{HSA}} + [\text{PAA}]V_{\text{PAA}}) \quad (9)$$

where V_c, V_{HSA}, and V_{PAA} are the volumes of a molecule of the complex, HSA and PAA, respectively. These volumes were estimated using Primus from the SAXS spectra of single solutes

View Article Online
Paper Soft Matter

and found to be 500×10^3, 100×10^3 and 50×10^3 Å^3 for the complex, HSA and PAA, respectively.

Accordingly, the Porod volume can be estimated using a theoretical model. According to the literature, when a dispersion is made of n kinds of particles of volume V_i and number N_i, for a dilute dispersion $S(0) = 1$, the average volume can be written as follows (O. Spalla eqn (54)):[30]

$$V_M = \frac{\sum_i^n N_i V_i^2}{\sum_i^n N_i V_i} \quad (10)$$

The Porod volume of the mixture can then be written as a function of the relative volume fraction of solute, φ_i:

$$V_M = \frac{\sum_i^n \varphi_i V_i}{\sum_i^n \varphi_i} = \sum_i^n \varphi_i V_i \quad (11)$$

$$V_M = \varphi_c V_c + \varphi_{HSA} V_{HSA} + \varphi_{PAA} V_{PAA} \quad (12)$$

Porod volume calculations, whether from SAXS experiments or from the theoretical model, were performed using a code written in Python (ESI,† SI-2).

The results show that a complex model containing 4 HSA molecules with 1 PAA chain gives a better fit than those run assuming 3 or 5 HSA molecules per PAA (Fig. 8), which corroborates the binding stoichiometry proposed previously. As a matter of fact, when the initial $[HSA]_0/[PAA]_0$ ratio is below 4, the mixture is composed of PAA and of the HSA–PAA complex. The Porod volume then increases quickly when increasing the HSA ratio, from that of PAA to that of the complex. For a $[HSA]_0/[PAA]_0$ ratio of 4, one can consider that there is only the complex (PAA–4HSA) in the mixture and that the SAXS data provide access to the Porod volume of the complex. When $[HSA]_0/[PAA]_0$ is larger than 4, the mixture is composed of the complex plus some free HSA.

The complexation model (ESI,† SI-3) can then explain the decrease in the mean Porod volume due to the presence of non-associated HSA in addition to the HSA–PAA complex.

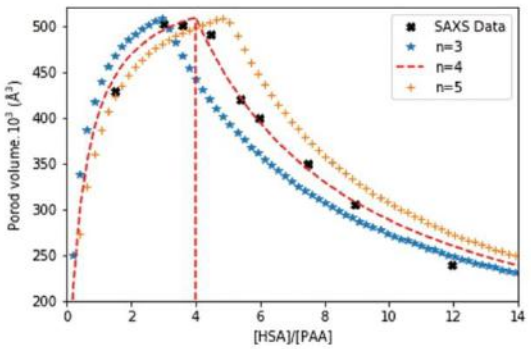

Fig. 8 Porod volume evolution as a function of the initial [HSA]/[PAA] ratio using the experimental SAXS data and calculation from the complexation model for different stoichiometry coefficients n.

Since the stoichiometry of the complex has now been determined, the amount of HSA that could be adsorbed on PAA of the same size grafted onto a membrane interface can be estimated if the amount of the grafted polyelectrolyte is known.

Investigation of the HSA–PAA complex structure

According to the analysis of the autocorrelation function $P(r)$, we can fit the data at small and medium q (less than 0.2 Å^{-1}) using a cylinder of axial length close to 400 Å and diameter equal to 78 Å. Thus, the cylinder body was tested to fit the experimental $I(q)$ value of the HSA–PAA complex using SasView (ESI,† SI-4). This model can provide information on the global shape of the complex, but provides no structural information on the internal organization of the complex. To propose a model that could be compatible with the SAXS data, we used an approach based on rigid bodies molecular modelling, completing the missing parts with dummy residues (BUNCH). The atomic structure of HSA can be used as a template for rigid bodies and the PAA polymer forms the missing part. As shown by Ballauff and coworkers,[24] PAA can interact with HSA in a pocket charged positively, giving a starting point to lock a portion of PAA at the surface of HSA. These portions of the HSA–PAA complex are connected to each other as a pearl necklace. The rest of the PAA is flexible and the conformation can be modified using the program. The program BUNCH[27] works directly with the residues of proteins rather than with different types of polymers. However, the chemical structure of PAA is close to a peptide's residue and the PAA polymer can be transformed into a poly-glycine chain. As both chains present a difference in mass ($\Delta = 1.26$), the individual form factor of the dummy residues is increased in the BUNCH program to compensate for this default of mass. In total, the 100 kDa PAA chain can be modelled with a poly-glycine chain containing 1389 residues.

During the molecular modelling process against SAXS data, the position and orientation of individual HSA are free and the conformation of the polymer chain is modified in order to describe the space occupied by the PAA. The result obtained is an all-atom model compatible with SAXS data reflecting a possible organization of the complex in solution. Interestingly, the complex forms an elongated structure as a cylinder with a non-specific orientation of the HSA. The absence of a correlation peak in the data suggests that HSA does not present a periodic or partially aligned structure in the complex. This model proposes a globally flexible organization in alternative layers composed of HSA and unfolded PAA without frozen structures (Fig. 9). Many tests have been performed with different templates and all converge to the same organization with some variations in the position or orientation of HSA. However, the distance between two monomers of HSA always ranges between 80 and 100 Å. Besides, the distance between the extremities of the complex remains constant, which was found to be 414 Å (Fig. 9). These results are consistent with the length of the complex previously evaluated, whether from $P(r)$ or from the fit of the experimental $I(q)$ value of the complex performed using SasView (ESI,† SI-4).

View Article Online
Soft Matter Paper

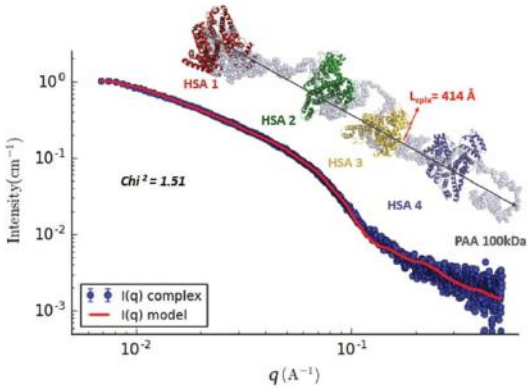

Fig. 9 Superimposition of the SAXS data of the HSA–PAA complex and those of the all atom compatible model calculated using the BUNCH program. The SAXS scattering intensity for the HSA–PAA complex is indicated with dotted thick blue circles and the model with a red line.

Conclusion

An assessment of the HSA protein interaction with the PAA polyelectrolyte has been presented in this study combining SAXS and chromatography. The study of the HSA–PAA interactions revealed a complexation phenomenon of protein molecules with the polymer chains. Tests on the effect of the ionic strength showed that this HSA–PAA binding is chiefly an electrostatic interaction, where attractive and repulsive interactions compete. Decreasing the pH to 5 allowed the negative overall charge of the protein to be reduced until the electrostatic attraction between the PAA chains and the positive patches on the protein dominated. Besides, this complexation was found to be reversible: the HSA–PAA complex tended to dissociate once put in a diluted medium (without PAA) or at a pH greater than 5. That known, it is now possible to control the interactions between HSA and PAA at the membrane interface by changing the physicochemical conditions (pH, ionic strength).

An evaluation of the complex size suggests the attachment of several protein molecules to each polymer chain. The effect of the ratio of the protein concentration to the polymer concentration was also explored, which revealed that 4 HSA molecules could be bound to each 100 kDa PAA chain. A complexation model was proposed, which allowed us to describe the Porod volume of the mixture for different HSA/PAA ratios. From this model, it could be possible to quantify the adsorbed amount of HSA on PAA of the same size grafted onto a membrane surface.

A SAXS modelling study aimed at describing the complex structure was also conducted. The cylinder body was found to fit well the experimental SAXS scattering intensities giving an idea of the global shape of the complex, but without providing any structural information. Finally, an all-atom pearl necklace model was developed using the BUNCH program to better describe the final structure of the complex.

It would be interesting in the future to evaluate the stoichiometry of complexation with different sizes of PAA. It would also be interesting to assess the reproducibility of this complexation between HSA and PAA grafted onto a membrane surface under the different physiochemical conditions discussed in this article.

Author contributions

The manuscript was written through contributions of all authors. All authors have given approval to the final version of the manuscript.

Conflicts of interest

The authors declare no competing financial interest. There are no conflicts of interest to declare.

Acknowledgements

The authors would like to acknowledge the Agence Nationale de la Recherche (MOST-ANR International Program: ANR 17-CE08-0041) for financial support, the FERMaT Federation FR3089 for providing the Small Angle X-ray Scattering laboratory facility. This work benefited from the use of the SasView application (https://www.sasview.org), originally developed under NSF award DMR-0520547. SasView contains code developed with funding from the European Union's Horizon 2020 research and innovation programme under the SINE2020 project (grant agreement No. 654000).

References

1 W. Senaratne, L. Andruzzi and C. K. Ober, Self-Assembled Monolayers and Polymer Brushes in Biotechnology: Current Applications and Future Perspectives, *Biomacromolecules*, 2005, **6**(5), 2427–2448.
2 W. M. de Vos, P. M. Biesheuvel, A. de Keizer, J. M. Kleijn and M. A. Cohen Stuart, Adsorption of the Protein Bovine Serum Albumin in a Planar Poly(Acrylic Acid) Brush Layer As Measured by Optical Reflectometry, *Langmuir*, 2008, **24**(13), 6575–6584.
3 K. Henzler, A. Wittemann, E. Breininger, M. Ballauff and S. Rosenfeldt, Adsorption of Bovine Hemoglobin onto Spherical Polyelectrolyte Brushes Monitored by Small-Angle X-Ray Scattering and Fourier Transform Infrared Spectroscopy, *Biomacromolecules*, 2007, **8**(11), 3674–3681.
4 N. Welsch, Y. Lu, J. Dzubiella and M. Ballauff, Adsorption of Proteins to Functional Polymeric Nanoparticles, *Polymer*, 2013, **54**(12), 2835–2849.
5 S. Wang, K. Chen, Y. Xu, X. Yu, W. Wang, L. Li and X. Guo, Protein Immobilization and Separation Using Anionic/Cationic Spherical Polyelectrolyte Brushes Based on Charge Anisotropy, *Soft Matter*, 2013, **9**(47), 11276–11287.
6 K. W. Mattison, I. J. Brittain and P. L. Dubin, Protein-Polyelectrolyte Phase Boundaries, *Biotechnol. Prog.*, 1995, **11**(6), 632–637.

7 A. Pourjavadi and Z. M. Tehrani, Mesoporous Silica Nanoparticles with Bilayer Coating of Poly(Acrylic Acid-Co-Itaconic Acid) and Human Serum Albumin (HSA): A PH-Sensitive Carrier for Gemcitabine Delivery, *Mater. Sci. Eng., C*, 2016, **61**, 782–790.
8 M. Das, S. Mardyani, W. C. W. Chan and E. Kumacheva, Biofunctionalized PH-Responsive Microgels for Cancer Cell Targeting: Rational Design, *Adv. Mater.*, 2006, **18**(1), 80–83.
9 S. Yu, B. Kent, C. J. Jafta, A. Petzold, A. Radulescu, M. Schuchardt, M. Tölle, M. van der Giet, W. Zidek and M. Ballauff, Stability of Human Serum Albumin Structure upon Toxin Uptake Explored by Small Angle Neutron Scattering, *Polymer*, 2018, **141**, 175–183.
10 H. Chen and Y.-L. Hsieh, Enzyme Immobilization on Ultrafine Cellulose Fibers via Poly(Acrylic Acid) Electrolyte Grafts, *Biotechnol. Bioeng.*, 2005, **90**(4), 405–413.
11 L. Rastogi and J. Arunachalam, Synthesis and Characterization of Bovine Serum Albumin–Copper Nanocomposites for Antibacterial Applications, *Colloids Surf., B*, 2013, **108**, 134–141.
12 P. Dubin, J. Bock, R. Davis, D. N. Schulz and C. Thies, *Macromolecular Complexes in Chemistry and Biology*, Springer Science & Business Media, 2012.
13 A. E. Nel, L. Mädler, D. Velegol, T. Xia, E. M. V. Hoek, P. Somasundaran, F. Klaessig, V. Castranova and M. Thompson, Understanding Biophysicochemical Interactions at the Nano-Bio Interface, *Nat. Mater.*, 2009, **8**(7), 543–557.
14 Q. Wei, T. Becherer, S. Angioletti-Uberti, J. Dzubiella, C. Wischke, A. T. Neffe, A. Lendlein, M. Ballauff and R. Haag, Protein Interactions with Polymer Coatings and Biomaterials, *Angew. Chem., Int. Ed.*, 2014, **53**(31), 8004–8031.
15 S. Bhat and A. Kumar, Biomaterials and Bioengineering Tomorrow's Healthcare, *Biomatter*, 2013, **3**(3), e24717.
16 T. Tarvainen, T. Nevalainen, A. Sundell, B. Svarfvar, J. Hyrsylä, P. Paronen and K. Järvinen, Drug Release from Poly(Acrylic Acid) Grafted Poly(Vinylidene Fluoride) Membrane Bags in the Gastrointestinal Tract in the Rat and Dog, *J. Controlled Release*, 2000, **66**(1), 19–26.
17 C. Leggio, L. Galantini and N. Viorel Pavel, About the Albumin Structure in Solution: Cigar Expanded Form versus Heart Normal Shape, *Phys. Chem. Chem. Phys.*, 2008, **10**(45), 6741–6750.
18 C. Zhang, J. Jin, J. Zhao, W. Jiang and J. Yin, Functionalized Polypropylene Non-Woven Fabric Membrane with Bovine Serum Albumin and Its Hemocompatibility Enhancement, *Colloids Surf., B*, 2013, **102**, 45–52.
19 C. L. Cooper, P. L. Dubin, A. B. Kayitmazer and S. Turksen, Polyelectrolyte–Protein Complexes, *Curr. Opin. Colloid Interface Sci.*, 2005, **10**(1), 52–78.
20 A. Basak Kayitmazer, D. Seeman, B. Baykal Minsky, L. Dubin and P. Xu, Protein–Polyelectrolyte Interactions, *Soft Matter*, 2013, **9**(9), 2553–2583.
21 S. Rosenfeldt, A. Wittemann, M. Ballauff, E. Breininger, J. Bolze and N. Dingenouts, Interaction of Proteins with Spherical Polyelectrolyte Brushes in Solution as Studied by Small-Angle x-Ray Scattering, *Phys. Rev. E: Stat., Nonlinear, Soft Matter Phys.*, 2004, **70**(6), 061403.
22 W. Wang, L. Li, K. Henzler, Y. Lu, J. Wang, H. Han, Y. Tian, Y. Wang, Z. Zhou, G. Lotze, T. Narayanan, M. Ballauff and X. Guo, Protein Immobilization onto Cationic Spherical Polyelectrolyte Brushes Studied by Small Angle X-Ray Scattering, *Biomacromolecules*, 2017, **18**(5), 1574–1581.
23 M. Topuzoğulları, N. S. Çimen, Z. Mustafaeva and M. Mustafaev, Molecular-Weight Distribution and Structural Transformation in Water-Soluble Complexes of Poly(Acrylic Acid) and Bovine Serum Albumin, *Eur. Polym. J.*, 2007, **43**(7), 2935–2946.
24 S. Yu, X. Xu, C. Yigit, M. van der Giet, W. Zidek, J. Jankowski, J. Dzubiella and M. Ballauff, Interaction of Human Serum Albumin with Short Polyelectrolytes: A Study by Calorimetry and Computer Simulations, *Soft Matter*, 2015, **11**(23), 4630–4639.
25 Q. Ran, X. Xu, P. Dey, S. Yu, Y. Lu, J. Dzubiella, R. Haag and M. Ballauff, Interaction of Human Serum Albumin with Dendritic Polyglycerol Sulfate: Rationalizing the Thermodynamics of Binding, *J. Chem. Phys.*, 2018, **149**(16), 163324.
26 O. Hollmann and C. Czeslik, Characterization of a Planar Poly(Acrylic Acid) Brush as a Materials Coating for Controlled Protein Immobilization, *Langmuir*, 2006, **22**(7), 3300–3305.
27 M. V. Petoukhov and D. I. Svergun, Global Rigid Body Modeling of Macromolecular Complexes against Small-Angle Scattering Data, *Biophys. J.*, 2005, **89**(2), 1237–1250.
28 P. V. Konarev, V. V. Volkov, A. V. Sokolova, M. H. J. Koch and D. I. Svergun, PRIMUS: A Windows PC-Based System for Small-Angle Scattering Data Analysis, *J. Appl. Crystallogr.*, 2003, **36**(5), 1277–1282.
29 M. V. Petoukhov, P. V. Konarev, A. G. Kikhney and D. I. Svergun, ATSAS 2.1 – towards Automated and Web-Supported Small-Angle Scattering Data Analysis, *J. Appl. Crystallogr.*, 2007, **40**(s1), s223–s228.
30 P. Lindner, Th. Zemb and Neutron, *X-Rays and Light. Scattering Methods Applied to Soft Condensed Matter*, New edition, North Holland, Amsterdam, Boston, 2002.
31 G. David and J. Pérez, Combined Sampler Robot and High-Performance Liquid Chromatography: A Fully Automated System for Biological Small-Angle X-Ray Scattering Experiments at the Synchrotron SOLEIL SWING Beamline, *J. Appl. Crystallogr.*, 2009, **42**(5), 892–900.
32 M. H. J. Koch, P. Vachette and D. I. Svergun, Small-Angle Scattering: A View on the Properties, Structures and Structural Changes of Biological Macromolecules in Solution, *Q. Rev. Biophys.*, 2003, **36**(2), 147–227.
33 D. I. Svergun, Determination of the Regularization Parameter in Indirect-Transform Methods Using Perceptual Criteria, *J. Appl. Crystallogr.*, 1992, **25**(4), 495–503.
34 B. Chu and B. S. Hsiao, Small-Angle X-Ray Scattering of Polymers, *Chem. Rev.*, 2001, **101**(6), 1727–1762.
35 D. I. Svergun and M. H. J. Koch, Small-Angle Scattering Studies of Biological Macromolecules in Solution, *Rep. Prog. Phys.*, 2003, **66**(10), 1735–1782.
36 X. Xu, S. Angioletti-Uberti, Y. Lu, J. Dzubiella and M. Ballauff, Interaction of Proteins with Polyelectrolytes:

Comparison of Theory to Experiment, *Langmuir*, 2019, **35**(16), 5373–5391.

37 E. Seyrek, P. L. Dubin, C. Tribet and E. A. Gamble, Ionic Strength Dependence of Protein-Polyelectrolyte Interactions, *Biomacromolecules*, 2003, **4**(2), 273–282.

38 Y. Xu, M. Mazzawi, K. Chen, L. Sun and P. L. Dubin, Protein Purification by Polyelectrolyte Coacervation: Influence of Protein Charge Anisotropy on Selectivity, *Biomacromolecules*, 2011, **12**(5), 1512–1522.

39 C. Yigit, J. Heyda, M. Ballauff and J. Dzubiella, Like-Charged Protein-Polyelectrolyte Complexation Driven by Charge Patches, *J. Chem. Phys.*, 2015, **143**(6), 064905.

40 C. Yigit, J. Heyda and J. Dzubiella, Charged Patchy Particle Models in Explicit Salt: Ion Distributions, Electrostatic Potentials, and Effective Interactions, *J. Chem. Phys.*, 2015, **143**(6), 064904.

41 C. Yigit, M. Kanduč, M. Ballauff and J. Dzubiella, Interaction of Charged Patchy Protein Models with Like-Charged Polyelectrolyte Brushes, *Langmuir*, 2017, **33**(1), 417–427.

42 M. Dockal, D. C. Carter and F. Rüker, Conformational Transitions of the Three Recombinant Domains of Human Serum Albumin Depending on PH, *J. Biol. Chem.*, 2000, **275**(5), 3042–3050.

Blood proteins interactions with coated polymer interfaces

The selective separation of blood proteins and cells is of a major importance to address some target diseases and for several medical applications such as wound healing. The challenge is to provide the most efficient and cost-effective technology that can ensure that. Among many other technologies, membranes processes have been revealed as promising techniques. However, their nonspecific interactions with proteins make them prone to biofouling, which in turn limits their application in biomedical fields. Therefore, the aim of this work is to design tailored membrane for blood proteins screening via surface modification. This latter is performed by coating onto the membrane surface some functional groups such as polystyrene-poly acrylic acid (PS-PAA) and polystyrene-poly ethylene glycol (PS-PEG) copolymers, either to promote a specific interaction with target proteins or to reduce their non-specific interaction. First, the potential interactions that could take place between PAA, PEG brushes and some abundant proteins in plasma such as human serum albumin (HSA) and ɣ-globulin (IgG) have been investigated in solution using Small Angle X-ray Scattering (SAXS) combined to chromatography. Thus, PAA has been found to form complexes with HSA in some specific physicochemical conditions of pH and ionic strength. This HSA-PAA binding has then been revealed to be reversible depending on the pH and the ionic strength of the medium and its stoichiometry was shown to be related to the PAA size. Whereas IgG did not exhibit the same behaviour as HSA towards PAA, it was found to be partially aggregated in our conditions. PEG did not display any interaction with both proteins. After that, Fourier Transform Infrared spectroscopy (FTIR) mapping showed that surface modification of the membranes by copolymers coating was successful, although the distribution of copolymer was heterogeneous over the membrane surface. The static adsorption of HSA onto membranes coated with PS-PAA was found to be also correlated to the pH and ionic strength as it was in solution, while that of IgG was not. Then, the adsorption of HSA onto a membrane coated with PS-PEG has been shown to be mitigated. Eventually, filtration experiments disclosed the same trend of HSA adsorption in dynamic mode even though the membrane permeability was reduced by the increase of the size of the copolymers brushes deposited onto the surface. Overall, this study enabled us to understand the behaviour of some abundant blood proteins in contact of some functional groups either in solution or at the interface of a modified membrane.

Keywords: interactions, blood proteins, polymers, membrane surface modification, SAXS, FTIR.

Interactions des protéines sanguines avec interfaces polymères modifiées

La séparation sélective des protéines et des cellules sanguines est d'une importance capitale pour traiter certaines maladies cibles et pour plusieurs applications médicales telles que la cicatrisation des plaies. Le défi consiste à fournir la technologie la plus efficace et la plus rentable qui puisse garantir cette séparation. Parmi de nombreuses autres technologies de séparation, les technologies membranaires se sont révélées être prometteuses. Cependant, leurs interactions non spécifiques avec les protéines les rendent vulnérables au bio-colmatage, ce qui limite leur application dans le domaine biomédical. Par conséquent, l'objectif de ce travail est de concevoir une technologie membranaire adaptée pour le dépistage des protéines sanguines en utilisant la modification de surface. Cette dernière est réalisée en déposant certains groupements fonctionnels sur la surface de la membrane, tels que des copolymères polystyrène-poly acrylique acide (PS-PAA) et polystyrène-polyéthylène glycol (PS-PEG), soit pour favoriser une interaction spécifique avec des protéines cibles ou pour réduire leur interaction non spécifique. Dans un premier temps, les interactions potentielles qui pourraient avoir lieu entre les brosses de PAA, PEG et certaines protéines abondantes dans le plasma telles que la sérum-albumine humaine (HSA) et la ɣ-globuline (IgG) ont été étudiées en solution en utilisant la Diffusion des rayons-X aux petits angles (Acronyme anglais : SAXS) combinée à la chromatographie. Ainsi, nous avons constaté que le PAA forme des complexes avec l'HSA dans certaines conditions physico-chimiques spécifiques de pH et de force ionique. Cette liaison HSA-PAA s'est ensuite révélée réversible en fonction du pH et de la force ionique du milieu, et il a été démontré que sa stœchiométrie était liée à la taille du PAA. En revanche, l'IgG n'a pas présenté le même comportement que l'HSA vis-à-vis du PAA, mais elle s'est avérée être partiellement agrégée. Quant au PEG, il n'a montré aucune interaction avec les deux protéines. Ensuite, la cartographie par spectroscopie infrarouge à transformée de Fourier (FTIR) a confirmé le succès de la modification de surface par dépôt de copolymères sur la surface de la membrane, bien que la distribution du copolymère y soit hétérogène. L'adsorption statique de l'HSA sur les membranes revêtues de PS-PAA s'est avérée également corrélée au pH et à la force ionique comme elle l'était en solution, alors que celle de l'IgG ne l'était pas. Ensuite, il a été démontré que l'adsorption de l'HSA sur la membrane recouverte de PS-PEG était réduite. Enfin, les expériences de filtration ont révélé la même tendance à l'adsorption de l'HSA en mode dynamique, même si la perméabilité de la membrane était réduite par l'augmentation de la taille des brosses de copolymères déposées sur la surface.

Globalement, cette étude nous a permis de comprendre le comportement de certaines protéines sanguines abondantes au contact de certains groupes fonctionnels que ce soit en solution ou à l'interface d'une membrane modifiée.

Mots clés : interactions, protéines sanguines, polymères, modification de surface des membranes, SAXS, FTIR.